

**DEVELOPMENT OF A MULTI-DIRECTIONAL DIRECT SIMPLE SHEAR  
TESTING DEVICE FOR CHARACTERIZATION OF THE CYCLIC SHEAR  
RESPONSE OF MARINE CLAYS**

A Dissertation

by

CASSANDRA JANEL RUTHERFORD

Submitted to the Office of Graduate Studies of  
Texas A&M University  
in partial fulfillment of the requirements for the degree of

DOCTOR OF PHILOSOPHY

May 2012

Major Subject: Civil Engineering

Development of a Multi-directional Direct Simple Shear Testing Device for  
Characterization of the Cyclic Shear Response of Marine Clays

Copyright 2012 Cassandra Janel Rutherford

**DEVELOPMENT OF A MULTI-DIRECTIONAL DIRECT SIMPLE SHEAR  
TESTING DEVICE FOR CHARACTERIZATION OF THE CYCLIC SHEAR  
RESPONSE OF MARINE CLAYS**

A Dissertation

by

CASSANDRA JANEL RUTHERFORD

Submitted to the Office of Graduate Studies of  
Texas A&M University  
in partial fulfillment of the requirements for the degree of

DOCTOR OF PHILOSOPHY

Approved by:

Chair of Committee,	Giovanna Biscontin
Committee Members,	Charles Aubeny
	Marcelo Sanchez
	William Bryant
Head of Department,	John Niedzwecki

May 2012

Major Subject: Civil Engineering

**ABSTRACT**

Development of a Multi-directional Direct Simple Shear Testing Device for  
Characterization of the Cyclic Shear Response of Marine Clays. (May 2012)

Cassandra Janel Rutherford B.S., Texas A&M University;

M.S., Texas A&M University

Chair of Advisory Committee: Dr. Giovanna Biscontin

This dissertation describes the development of a new multi-directional direct simple shear testing device, the Texas A&M Multi-directional Direct Simple Shear (TAMU-MDSS), for testing marine soil samples under conditions, which simulate, at the element level, the state of stress acting within a submarine slope under dynamic loading. Prototype testing and an experimental program to characterize the response of marine clays to complex loading conditions are presented.

The work is divided into four major components: 1) Equipment Development: Design and construction of a prototype multi-directional direct simple shear testing device (TAMU-MDSS) that addresses the limitations of previous devices. 2) Support systems: selection of control software, development of data acquisition system and design of back pressure systems for direct pore pressure measurements. 3) Prototype Testing: performance of the TAMU MDSS system and testing of strain-control and stress-control capabilities. 4) Experimental Testing: characterize the response of marine clays to monotonic, dynamic and random loads.

The two-directional monotonic, cyclic, circular and figure-8 tests demonstrated the undrained shear strength increases with increasing initial shear stress,  $\tau_c$  (i.e, slope), for shearing in the same direction (equivalent to downhill). The strength decreases for shearing in the direction opposite to the initial stress (shearing uphill). The response is as brittle for shearing in the same direction as the shear stress applied during consolidation ( $\tau_c$ ) and ductile for shearing opposite to  $\tau_c$ . These findings have important implications for the stability of the slope, predicting that forces acting downward in the slope direction will need to mobilize less strain to reach peak strength and initiate failure.

This information provides insight into the behavior of marine soils under complex loading conditions, and provides high quality laboratory data for use in constitutive and finite element model development for analysis of submarine slopes.

## **DEDICATION**

This dissertation is dedicated to my family and husband who have supported me through times of frustration, exhaustion, and exhilaration.

## ACKNOWLEDGEMENTS

I would like to gratefully thank my advisor, Dr. Giovanna Biscontin, for all her support and help completing this work. I would also like to thank the members of my dissertation committee, Dr. Charles Aubeny, Dr. Marcelo Sanchez and Dr. Bill Bryant, for their advice and recommendations during the course of my doctoral work. I am also thankful for the conversations and mentorship of Dr. Niall Slowey. Thank you to Dr. Jim Brooks and Dr. Bernie Bernard of TDI-Brooks International for the opportunities they have provided me for working offshore and managing the onshore geotechnical lab.

I would also like to thank Vishal Dantal and Dr. Youjeng Deng for their help with the x-ray diffraction analyses, and Maddy Madhuri for conducting the TEM imaging. Without the technical and mechanical expertise of Mike Linger and Charles Pivonka, the TAMU-MDSS would have never have worked. I also want to express my gratitude to all geotech graduate students, specifically Michelle Bernhardt, for helping me relax after many frustrating days and nights in the lab. I thank all of them.

To my family, Jay and Sandra Rutherford, Jayson and Christy Rutherford and my nephew, Britain, thank you for encouraging me to continue to work towards my goals and enjoy life. Finally, to my husband, Josh Peschel, thank you for taking this journey with me. I could have never done it without you.

The TAMU-MDSS was designed and machined by James Cox and Sons, Inc. of Colfax, CA. The Gulf of Mexico cores were donated by TDI-Brooks Intl. This research was supported by the National Science Foundation CAREER Award CMMI-0449021.

## NOMENCLATURE

$\alpha$	angle of orientation of consolidation shear stress ( $\tau_c/\sigma'_p$ )
$a_v$	coefficient of compressibility
$b$	pore water pressure parameter ( $\Delta u/\Delta\sigma$ ) for undrained isotropic loading
$C_\alpha$	coefficient of secondary compression
$C_c$	compression index
$CK_\alpha$	consolidation under shear stress at angle $\alpha$
$CK_o$	consolidation under $K_o$ conditions
$C_r$	recompression index
CSR	cyclic stress ratio, normalized amplitude cyclic shear stress ( $\tau_{cyc}/\sigma'_p$ )
$CSR_{max}$	maximum cyclic stress ratio
$c_v$	coefficient of consolidation
$\delta$	angle between the direction of shearing and zero degrees
$\Delta u$	excess pore water pressure
$e$	void ratio
$e_o$	initial void ratio
$\varepsilon_v$	vertical strain
$\varepsilon_{vol}$	volumetric strain
$\gamma$	engineering shear strain, magnitude of displacement normalized by height of sample ( $\Delta h/h_o$ )



$\gamma_{avg}$	average shear strain
$\gamma_c$	consolidation shear strain
$\gamma_{cyc}$	cyclic shear strain
$\gamma_T$	total unit weight
$\gamma_w$	unit weight of water
$\gamma_x, \gamma_y$	shear strain magnitude in x or y direction
GOM	Gulf of Mexico
$G_{max}$	maximum shear modulus
$G_s$	specific gravity
k	permeability
$K_\alpha$	stress conditions simulating sloping ground
$K_o$	coefficient of lateral earth pressure at rest for normally consolidated soils, stress conditions simulating level ground
LVDT	linear variable differential transducer
$m_v$	coefficient of volume change
NGI	Norwegian Geotechnical Institute
OCR	overconsolidation ratio
psi	pounds per square inch
$r_u$	normalized pore water pressure ( $\Delta u/\sigma'_p$ )
$\sigma'_p$	preconsolidation pressure
$\sigma'_n$	effective normal stress

$\sigma'_{vc}$	effective vertical stress, confining stress at which the sample has been consolidation prior to shearing
$\sigma'_{vo}$	initial effective vertical stress
SHANSEP	Stress History and Normalized Soil Engineering Properties
$s_u$	undrained shear strength
t	time
TAMU-MDSS	Texas A&M University Multi-directional Direct Simple Shear
$\tau_c$	initial shear stress
$\tau_{cyc}$	cyclic shear stress
$\tau_f$	shear stress at failure
$\tau_x, \tau_y$	shear stress in x or y direction
$\tau_{x \max}, \tau_{y \max}$	maximum shear stress in x or y direction
v	Poisson's ratio
w	water content
$w_L$	liquid limit
$w_P$	plastic limit

## TABLE OF CONTENTS

	Page
ABSTRACT .....	iii
DEDICATION .....	v
ACKNOWLEDGEMENTS .....	vi
NOMENCLATURE.....	vii
TABLE OF CONTENTS .....	x
LIST OF FIGURES.....	xiii
LIST OF TABLES .....	xx
1. INTRODUCTION.....	1
1.1 Scope of Work.....	4
1.2 Research Objectives .....	4
1.3 Dissertation Outline.....	6
2. BACKGROUND.....	8
2.1 Submarine Slopes .....	8
2.2 Simple Shear Testing .....	15
2.3 Previous Multi-directional Simple Shear Testing Devices .....	18
2.4 Measured Soil Response .....	24
2.5 Conclusions .....	27
3. DESCRIPTION OF TAMU-MDSS .....	28
3.1 Overview of TAMU-MDSS Simple Shear Equipment.....	28
3.1.1 Backpressure and Cell Pressure Systems .....	33
3.1.2 Specimen .....	35
3.1.3 Multi-axis Load Cell .....	36
3.2 Hydraulic Power Supply .....	37
3.3 Computer Control and Data Acquisition.....	38
3.4 Conclusions .....	43

	Page
4. EXPERIMENTAL EVALUATION OF THE TAMU-MDSS .....	44
4.1 Friction and Cross-coupling of Loading Tables.....	44
4.2 Constant Stress Testing of Vertical and Horizontal Loads .....	55
4.3 TAMU-MDSS Loading Path Evaluation .....	58
4.4 Comparison of Multi-axis Load Cell and Measurements of Torque ...	69
4.5 Evaluation of the Backpressure System and Chamber.....	75
4.6 Conclusions .....	76
5. GULF OF MEXICO CLAYS .....	78
5.1 Sampling of Gulf of Mexico Clay.....	79
5.2 Geology of Gulf of Mexico Clay .....	82
5.3 Multi-sensor Core Logger Profiles.....	82
5.4 Geotechnical Engineering Properties of Gulf of Mexico Clay .....	86
5.4.1 Natural Water Content and Index Classification.....	86
5.4.2 Miniature Vane Shear Strength.....	88
5.4.3 Grain Size Distribution and Specific Gravity .....	88
5.5 Clay Mineralogy.....	91
5.6 Transmitting Electron Microscopy (TEM).....	94
5.7 Constant Rate of Strain Consolidation.....	101
5.8 Triaxial Testing .....	105
5.9 Previous Testing on Gulf of Mexico Marine Clay.....	108
6. MULTI-DIRECTIONAL DIRECT SIMPLE SHEAR BEHAVIOR OF GULF OF MEXICO CLAYS .....	110
6.1 Testing Procedures .....	110
6.2 Consolidation .....	112
6.3 Undrained Shear Tests .....	114
6.3.1 Monotonic Tests.....	115
6.3.2 Cyclic Tests.....	118
6.3.3 Circular Tests .....	121
6.3.4 Figure-8 Tests.....	125
6.4 Conclusions .....	128
7. SUMMARY AND CONCLUSIONS.....	129
7.1 Summary .....	129
7.2 Recommendations for Future Work.....	130
7.2.1 TAMU-MDSS Device.....	130

	Page
7.2.2 Multi-directional Testing of Gulf of Mexico Clays .....	130
REFERENCES .....	132
APPENDIX A SIMPLE SHEAR TESTING OF CLAYS .....	138
APPENDIX B TAMU-MDSS DEVICE TEST PROCEDURES .....	146
APPENDIX C GULF OF MEXICO MARINE CLAY TEST RESULTS.....	156
APPENDIX D MATLAB DATA REDUCTION AND PROCESSING CODE .....	176
VITA .....	189

## LIST OF FIGURES

FIGURE	Page
1.1 Complex loading paths (Modified from Kammerer, 2001) .....	2
2.1 Possible triggering mechanisms of submarine slope failures (After <a href="http://www.ngi.no/en/Geohazards/Research/Offshore-Geohazards/">http://www.ngi.no/en/Geohazards/Research/Offshore-Geohazards/</a> ) .....	11
2.2 Submarine slumps identified on the Sigsbee Escarpment (After Young et al., 2003a) .....	13
2.3 Static and cyclic loading conditions for level and sloping ground .....	13
2.4 Stress conditions related to direction of slope (After Boulanger and Seed, 1995).....	14
2.5 Cambridge DSS device and NGI direct simple shear device (After Franke et al., 1979).....	16
2.6 Comparisons of stress conditions in (a) triaxial and (b) simple shear test (After Kammerer, 2001).....	17
2.7 Examples of tests that can be used to determine strength along different sections of a failure surface for embankments and shallow foundations (After Lacasse et al., 1988) .....	19
2.8 Gyrotory simple shear apparatus (After Casagrande, 1976) .....	20
2.9 Two-directional simple shear apparatus (After Ishihara and Yamazaki, 1980).....	21
2.10 MIT Multi-directional simple shear device (After DeGroot, 1989).....	22
2.11 University of California, Berkeley bidirectional cyclic simple shear device (UCS-2D) (After Boulanger and Seed, 1995) .....	23
2.12 Photograph of the University of California, Berkeley bidirectional cyclic simple shear device (After Kammerer et al., 1999) .....	23
2.13 Digitally-controlled simple shear (DC-SS) (After Duku et al., 2007) .....	25

FIGURE	Page
2.14 Photographs of DC-SS showing (a) overview of device, (b) close-up view of tri-post frame, and (c) sample with top and bottom cap (After Duku et al., 2007) .....	25
3.1 Photograph and schematic of TAMU-MDSS device .....	30
3.2 Mounting of sample in TAMU-MDSS .....	30
3.3 Horizontal tables and horizontal load cells .....	32
3.4 Plan view showing TAMU-MDSS coordinate axes .....	32
3.5 Idealized schematic of backpressure system .....	33
3.6 Photographs of backpressure system (a) side view of backpressure system (b) Top view of backpressure system.....	34
3.7 Schematic and photos of multi-axis load cell.....	36
3.8 Hydraulic power supply .....	37
3.9 Layout for control system components of TAMU-MDSS device .....	39
3.10 Data acquisition boards .....	40
4.1 Frictional resistance on the horizontal tables for monotonic tests for a rate of (a) 5%/hr and (b) 50%/hr .....	46
4.2 (a) Stroke and (b) frictional resistance for cyclic tests in the x-direction at frequencies of 0.1 Hz and 1 Hz .....	48
4.3 (a) Stroke and (b) frictional resistance for cyclic tests in the y-direction at frequencies of 0.1 Hz and 1 Hz .....	49
4.4 (a) Stroke and (b) frictional resistance for circular tests at frequencies of 0.1 Hz and 1 Hz .....	50
4.5 (a)Stroke and (b) frictional resistance for figure-8 tests at frequencies of 0.2 Hz and 1 Hz in x-direction.....	51

FIGURE	Page
4.6 Cross-coupling of horizontal tables in (a) x-direction at 1 Hz, (b) x- direction at 0.1Hz, (c) y-direction at 1 Hz, and (d) y-direction at 0.1 Hz .....	54
4.7 Rubber sample installed in TAMU-MDSS .....	55
4.8 (a) Horizontal load in x-direction, (b) vertical load in during x-direction constant test .....	56
4.9 (a) Horizontal load in y-direction, (b) vertical load during y-direction constant load test .....	57
4.10 Plots of monotonic tests on rubber sample in x-direction at (a) 5%/hr and (b) 50%/hr .....	61
4.11 Plots of monotonic tests on rubber sample in y-direction at (a) 5%/hr and (b) 50%/hr .....	62
4.12 Plots of cyclic tests on rubber sample in x-direction at (a) 0.1 Hz and (b) 1 Hz.....	64
4.13 Plots of cyclic tests on rubber sample in y-direction at (a) 0.1 Hz and (b) 1 Hz.....	65
4.14 Plots of circular tests on rubber sample at (a) 0.1 Hz and (b) 1 Hz .....	66
4.15 Plots of figure-8 tests on rubber sample in x-direction at (a) 0.1 Hz and (b) 1 Hz.....	67
4.16 Plots of figure-8 tests on rubber sample in y-direction at (a) 0.1 Hz and (b) 1 Hz.....	68
4.17 Torque measurements for monotonic tests in (a) x-direction and (b) y-direction.....	70
4.18 Torque measurements for (a) $CK_o$ and (b) $CK_\alpha$ cyclic tests in x-direction .....	71
4.19 Gap formed between cap and rubber sample .....	72



FIGURE	Page
4.20 Torque measurements for circular tests (a) $CK_{\alpha}$ horizontal load in positive x-direction and (b) $CK_{\alpha}$ horizontal load in negative x-direction and positive y-direction .....	73
4.21 Torque measurements for figure-8 tests (a) $CK_{\alpha}$ horizontal load in positive x-direction and (b) $CK_{\alpha}$ horizontal load in negative x-direction.....	74
4.22 Chamber pressure lag time .....	76
5.1 R/V Brooks McCall.....	79
5.2 TDI-Brooks International jumbo piston coring system (After <a href="http://www.tdi-bi.com">www.tdi-bi.com</a> ).....	80
5.3 (a) Jumbo piston core rig ready for deployment (b) Jumbo piston core rig in deployment .....	81
5.4 Locations of jumbo piston cores from Gulf of Mexico (Madhuri, 2011) .....	83
5.5 Photograph of multi-sensor core logger .....	84
5.6 MSCL profiles of bulk density, compressional velocity and porosity from GOM-core1 (Madhuri, 2011) .....	85
5.7 Natural water content with depth for GOM-core1 (Madhuri, 2011).....	87
5.8 Atterberg limits for GOM-core1 samples plotted on Casagrande's plasticity chart .....	89
5.9 Miniature vane shear strengths with depth for GOM-core1 (Madhuri, 2011) .....	90
5.10 Hydrometer analysis from four sections of GOM-core1 (Madhuri, 2011) .....	91
5.11 Bulk XRD analysis comparisons of sample 1 and sample 2.....	93
5.12 XRD analysis magnesium and potassium saturation - sample 1.....	95
5.13 XRD analysis magnesium and potassium saturation - sample 2.....	96

FIGURE	Page
5.14 TEM micrograph showing halloysite in the center of chlorite.....	99
5.15 TEM micrograph showing chlorite interspersed with folded smectite layers .....	99
5.16 TEM micrograph showing dispersion of the clay plates.....	100
5.17 TEM micrograph showing moire fringes on muscovite mineral or mica ..	100
5.18 Casagrande’s graphical method to determine pre-consolidation pressure (Madhuri, 2011) .....	102
5.19 CRS plot of effective stress vs strain .....	103
5.20 CRS plot of effective stress vs void ratio.....	104
5.21 Normalized effective stress paths from CK <sub>0</sub> U-C/E testing (Madhuri, 2011) .....	106
5.22 Normalized effective stress paths from CIU-C/E testing (Madhuri, 2011) .....	107
5.23 Results of consolidated undrained direct simple shear tests (After Young et al., 2003b) .....	109
6.1 CK <sub>α</sub> consolidation loading scheme. ....	113
6.2 Complex loading paths used in experimental testing program .....	115
6.3 Monotonic test results (a) stress paths, (b) stress-strain curves, and (c) pore pressure ratio.....	117
6.4 GOM-5 CK <sub>0</sub> cyclic test results (a) stress path, (b) stress-strain curve, (c) pore pressure ratio, and (d) shear strain with cycles.....	119
6.5 Cyclic tests (a) development of pore pressures, (b) accumulation of plastic strains .....	120
6.6 GOM-10 CK <sub>0</sub> circular test results (a) shear stress pattern, (b) shear strain in x and y-directions, (c) pore pressure ratio, and (d) shear strain with cycles.....	123

FIGURE	Page
6.7 Circular tests (a) development of pore pressures, (b) accumulation of plastic strains x-direction, (c) accumulation of plastic strain y-direction ..	124
6.8 GOM-13 CK <sub>0</sub> figure-8 test results (a) shear stress pattern, (b) shear strain in x and y-directions, (c) pore pressure ratio, and (d) shear strain with cycles.....	126
6.9 Figure-8 tests (a) development of pore pressures, (b) accumulation of plastic strains in x-direction, and (c) accumulation of plastic strain in y-direction .....	127
A.1 (a) General strain state; (b) Simple shear strain state (After Biscontin, 2001) .....	138
A.2 Schematic distribution of non-uniform distribution (a) of shear stresses from absence of complementary shear stress on the ends of the sample; (b) of normal stresses on the top and bottom faces of a sample in the simple shear device (After Airey et al., 1985) .....	140
A.3 Stress distribution on the principal third for a constant volume test on kaolin in the Cambridge simple shear device (a) Principal third load cells; (b) Normal and (c) shear stresses ( $\alpha$ is the shear distortion $\gamma_{xy}$ ) (after Airey and Wood, 1987). .....	142
A.4 Comparison constant volume and undrained test results (After Dyvik et al., 1987).....	144
A.5 Comparison of specimens using different saturation conditions (After Kammerer et al., 1999).....	145
C.1 Results for all CK <sub>0</sub> consolidated tests .....	159
C.2 Results for all CK <sub><math>\alpha</math></sub> consolidated tests.....	159
C.3 GOM-1 CK <sub>0</sub> monotonic x-direction 5%/hr $\delta = 0^\circ$ .....	160
C.4 GOM-2 CK <sub><math>\alpha</math></sub> monotonic x-direction 50%/hr $\delta = 0^\circ$ .....	161
C.5 GOM-3 CK <sub><math>\alpha</math></sub> monotonic x-direction 5%/hr hr $\delta = 0^\circ$ .....	162
C.6 GOM-4 CK <sub><math>\alpha</math></sub> monotonic x-direction 5%/hr $\delta = 180^\circ$ .....	163

FIGURE	Page
C.7 GOM-5 $CK_o$ cyclic x-direction, 0.1 Hz, $\tau_{cyc}/\sigma'_p = 0.2$ , $\delta = 0^\circ$ .....	164
C.8 GOM-6 $CK_\alpha$ cyclic x-direction, 0.1 Hz, $\tau_{cyc}/\sigma'_p = 0.2$ , $\delta = 0^\circ$ .....	165
C.9 GOM-7 $CK_\alpha$ cyclic x-direction , 0.1 Hz, $\tau_{cyc}/\sigma'_p = 0.15$ , $\delta = 0^\circ$ .....	166
C.10 GOM-8 $CK_\alpha$ cyclic x-direction, 0.1 Hz, $\tau_{cyc}/\sigma'_p = 0.2$ , $\delta = 90^\circ$ .....	167
C.11 GOM-9 $CK_\alpha$ cyclic x-direction, 0.1 Hz, $\tau_{cyc}/\sigma'_p = 0.15$ , $\delta = 90^\circ$ .....	168
C.12 GOM-10 $CK_o$ circular 0.1Hz, $\tau_{cyc}/\sigma'_p = 0.2$ .....	169
C.13 GOM-11 $CK_\alpha$ circular 0.1Hz, , $\tau_{cyc}/\sigma'_p = 0.2$ .....	170
C.14 GOM-12 $CK_\alpha$ circular 0.1Hz, $\tau_{cyc}/\sigma'_p = 0.15$ .....	171
C.15 GOM-13 $CK_\alpha$ figure-8, 0.1 Hz x-direction, $\tau_{cyc}/\sigma'_p = 0.2$ , $\delta = 0^\circ$ .....	172
C.16 GOM-14 $CK_o$ figure-8, 0.1 Hz x-direction, $\tau_{cyc}/\sigma'_p = 0.2$ , $\delta = 0^\circ$ .....	173
C.17 GOM-15 $CK_\alpha$ figure-8, 0.1 Hz x-direction, $\tau_{cyc}/\sigma'_p = 0.15$ , $\delta = 0^\circ$ .....	174
C.18 GOM-16 $CK_\alpha$ figure-8, 0.1 Hz x-direction, $\tau_{cyc}/\sigma'_p = 0.2$ , $\delta = 90^\circ$ .....	175

## LIST OF TABLES

TABLE	Page
2.1 Summary of published submarine slides (After Edgers and Karlsrud, 1982).....	10
3.1 Data acquisition used in TAMU-MDSS .....	41
3.2 List of TAMU-MDSS transducers .....	42
4.1 Summary of table tests for frictional resistance .....	53
4.2 Summary of rubber testing .....	59
5.1 Summary of representative sample testing.....	90
5.2 Summary of constant rate of strain consolidation tests.....	101
6.1 Summary of GOM samples tested in TAMU-MDSS. ....	111
6.2 $CK_{\alpha}$ consolidation loading schedule .....	114
C.1 Summary of Gulf of Mexico specimens .....	157
C.2 Consolidation information for all tests on Gulf of Mexico clays.....	158

## 1. INTRODUCTION

Today, approximately 3 billion people, about half of the world's population, live within 120 miles of a coastline. By 2025, this figure is predicted to double. In many coastal regions, geohazards are a major threat costing lives, disrupting infrastructure and destroying livelihoods. Coastal communities can be impacted directly by geohazards, such as submarine slope failures, through retrogressive failures, or by tsunamis generated by the failed mass movements.

Due to the world's growing oil and natural gas consumption, companies are venturing farther into deepwater, drilling deeper than ever in their quest for energy. As exploration and production moves off the shelf to the continental slope, there is an increased concern over submarine slope failures leading to possible damage to offshore structures, pipelines, anchoring systems, and telecommunication lines. An important aspect of risk assessment for offshore structures and submarine infrastructure is an evaluation of nearby submarine slope stability.

Most experimental results in the literature for fine grained soils concentrate on one-dimensional response, both for monotonic and cyclic tests. Although the traditional direct simple shear device has been used to investigate cyclic loading effects on marine clay, it does not allow for complex loading conditions, which often contribute to the failure on submarine slopes. Analysis and modeling of submarine slope stability require

---

This dissertation follows the style of *Journal of Geotechnical and Geoenvironmental Engineering*.

knowledge of numerous soil parameters and relies on the selection of appropriate shear strength values. Understanding the interaction between the initial shear stress, representing the slope, and the multi-directional shaking due to earthquake or storm loading has only been recognized as an important factor in the last few years (DeGroot, 1989; Boulanger and Seed, 1995; Biscontin, 2001; Kammerer, 2001). The initial static driving force on the slope (Figure 1.1) is combined with the dynamic loading by storms and earthquakes to create complex loading paths. Therefore, the ability to apply complex stress or strain paths is important to fully study the shear response of marine clays on submarine slopes.

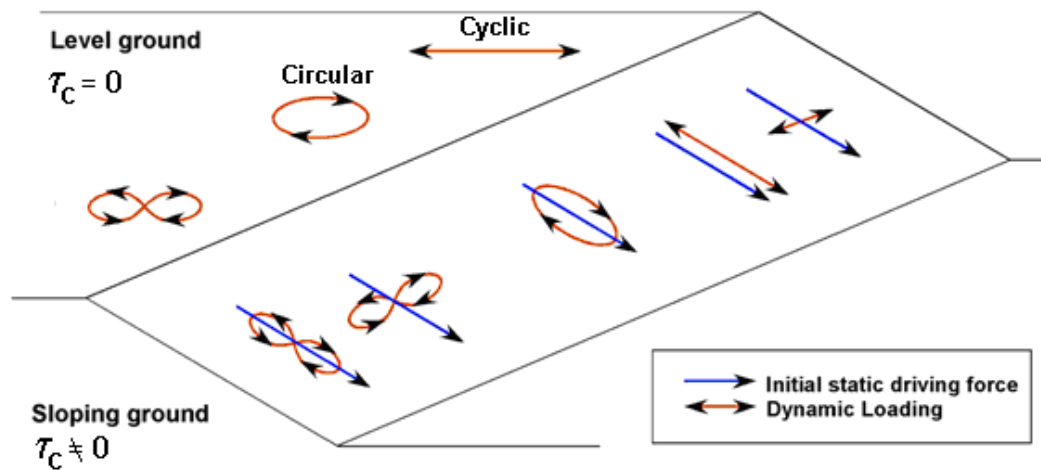


**Fig. 1.1.** Complex loading paths (Modified from Kammerer, 2001).

Very few multi-directional simple shear devices have been developed (Casagrande and Rendon, 1978; Ishihara and Yamazaki, 1980; Boulanger et al., 1993; DeGroot et al., 1996; Duku et al., 2007). However, these devices have limitations including top-bottom cap rocking, sample size restrictions, no backpressure control systems, limited testing amplitude and frequencies, and measurable friction between the horizontal loading tables. A discussion of each device is presented in Section 2.3. A new multi-directional simple shear device (TAMU-MDSS) was developed to provide high quality experimental test data at a wide range of amplitudes and cyclic frequencies for characterizing soil response more fully and for use in constitutive and finite element model development for analysis of submarine slopes.

One of the primary challenges in studying submarine landslides is the lack of information about the properties of these soils. Because offshore soil sampling is expensive, published experimental information on marine clays from offshore is limited. Most marine clay testing in the research literature is conducted on marine deposits that are now onshore and easily accessible such as Boston Blue Clay (BBC) and San Francisco Young Bay Mud (YBM). However, due to the depositional environment and mechanisms, the stress history for these soils differs from that of offshore marine sediments.

The characterization of actual offshore marine deposits is important since the depositional environment, depositional mechanics, and stress history strongly influence the structure of the deposit and consequently their mechanical response. Limited multi-directional monotonic and cyclic testing has been conducted on BBC (DeGroot, 1989;



Torkornoo, 1991) and YBM samples (Biscontin, 2001). No multi-directional simple shear testing on actual offshore marine clays is available in the literature.

### **1.1 Scope of Work**

This dissertation describes the development of a new multi-directional direct simple shear testing device, the Texas A&M Multi-directional Direct Simple Shear (TAMU-MDSS), for testing marine soil samples under conditions, which simulate, at the element level, the state of stress acting within a submarine slope under dynamic loading. Prototype testing and an experimental program to characterize the response of marine clays to complex loading conditions is presented.

### **1.2 Research Objectives**

The two main objectives of this research are 1) to design and develop a shear testing device with the capabilities to test marine clays in stress conditions as applied on submarine slopes, and 2) to conduct an experimental program with the device on Gulf of Mexico marine clays to investigate the undrained shear response of level versus sloping ground conditions.

The research consists of four major components: 1) equipment design and construction; 2) development of support systems; 3) extensive testing of capabilities of new device; and 4) analysis and synthesis of the results of an experimental testing program.

1. Equipment Development: Design and construction of a prototype multi-directional direct simple shear testing device (TAMU-MDSS) that will address the limitations including: top-bottom cap rocking; sample size

flexibility; control of back pressure system; reproduce sinusoidal and broadband command signals across a wide range of frequencies; and amplitude and decrease friction between horizontal tables.

2. Support systems: Selection of control software that allows for high frequency control and high precision for small displacements; development of data acquisition system for high accuracy; and connection for multiple transducers; design of back pressure systems for direct pore pressure measurements; control of cell pressure and installation of a multi-directional load cell.

3. Prototype Testing: The performance of the TAMU MDSS system will be evaluated using both monotonic and cyclic input motions and testing of strain-control and stress-control capabilities.

4. Experimental Testing: Sampling of marine samples; characterize the response of marine clays to monotonic, cyclic, circular and figure-8 strain and load paths; evaluate the effect of strain rate and study pore pressure generation during multi-directional loading.

The development of a new multi-directional direct simple shear testing device allows for the investigation of the response of marine clays to two dimensional loading paths. This information provides insight into the behavior of marine soils under complex loading conditions and high quality laboratory data for use in constitutive and finite element model development for analysis of submarine slopes.

### **1.3 Dissertation Outline**

The research outlined above is presented in seven sections. Section 2 describes the importance of analysis of submarine slope stability and the loading associated with submarine slopes. The relevance of simple shear testing for the characterization of marine clays to dynamic loading and measured soil response is discussed. A review of existing direct simple shear devices and their limitations is presented. A discussion of the important issues related to simple shear testing is provided in Appendix A.

The design and development of the Texas A&M University Multi-directional Direct Simple Shear device (TAMU-MDSS) is described in Section 3. This section includes the description of the backpressure system, chamber, and the measurement of forces and strains. The section also covers the control and data acquisition equipment and reduction and processing of the data. Detailed information on the procedures is located in Appendix B.

Section 4 describes the methods and procedures for evaluation of the capabilities of the TAMU-MDSS. Results from tests on rubber samples, cross-coupling analysis and harmonic testing are included.

The sampling procedures and basic geotechnical engineering properties of the Gulf of Mexico clay samples are presented in Section 5. Results from two preliminary testing studies are also presented. Eight constant rate of strain consolidation tests were conducted at various depths and varying strain rates. Eighteen  $K_o$  and isotropic triaxial tests were also conducted on the Gulf of Mexico samples (Madhuri 2011). X-ray diffraction results and transmitting electron microscopy images are presented.

The results from the TAMU-MDSS experimental program on Gulf of Mexico marine clay are presented in Section 6. The experimental program was conducted to provide information on the behavior of marine clays under stress conditions representative of soils within submarine slopes. In particular, the difference in the response of level versus sloping ground conditions was investigated. Monotonic and cyclic tests to study the effect of consolidation stress history and direction of anisotropy were conducted. Complex load patterns such as circular and figure-8 were also carried out at different shear stress ratios. Detailed information from the tests is located in Appendix C.

Section 7 presents a synthesis of the results of the experimental program. The section concludes with recommendations for future work with the TAMU-MDSS. The code for data reduction is provided in Appendix D.

## **2. BACKGROUND**

With the increase in the demand of oil and natural gas, exploration and production has continued to move deeper from the easily accessible continental shelf to deepwater reservoirs off the continental slope. With these advances come additional risks due to possibility of submarine slope failures damaging pipelines, offshore structures, anchoring systems and telecommunications cables. Analysis and modeling of nearby submarine slope stability has become an important aspect of the risk analysis for offshore structures and seabed infrastructure. The characterization of the undrained shear response of these soils to complex loading is required for the constitutive modeling and finite element analysis of the submarine slopes.

### **2.1 Submarine Slopes**

Submarine slope failures, also known as submarine landslides, are soil mass movements that can result in sediment transport across the continental shelf and into the deep ocean. A submarine landslide is initiated when the downwards driving stress exceeds the resisting stress of the seafloor slope material. Two main characteristics differentiate submarine from aerial slope failures: 1) their large size and volume of sediment carried, and, 2) the extremely shallow slopes of the failures. Evidence has shown that failures have occurred on slopes as low as 1-4 degrees (Lewis, 1971). Edgers and Karlsrud (1982) provide information on known submarine slides summarized in Table 2.1.

The evaluation of submarine slope stability can be complex due to the large number of possible triggering mechanisms and difficulty in collecting information regarding the mass movements (Figure 2.1). Some hypothesized causes of submarine slope failures include: 1) presence of weak geological layers; 2) oversteepening of the slope due to erosion; 3) overpressure due to rapid accumulation of sedimentary deposits on the slope; 4) high pore pressure and groundwater seepage; 5) volcanic island growth; 6) glacial loading; 7) earthquakes; 8) storm wave loading and dynamic loading from hurricanes; and 9) gas hydrate dissociation (Hampton et al., 1996).

Dynamic loading such as earthquakes and storm wave loading have been identified as causes of large slope failures. One of the largest submarine slope failures historically recorded was triggered by an earthquake on the Grand Banks, Newfoundland in 1929 creating a submarine landslide that severed trans-Atlantic communication cables almost 600 km away (Heezen and Ewing, 1952; Hampton et al., 1996) and resulted in a tsunami which killed 28 people (Fine et al., 2005). A submarine landslide triggered by an earthquake offshore Papua New Guinea in 1998 created a tsunami killing about 2000 people (Tappin et al., 2001). In 1969, offshore platforms in the Gulf of Mexico were damaged due to slope failures caused by twenty-meter high waves associated with Hurricane Camille (Bea, 1971).

Large-scale submarine slope failures have been observed near the Mississippi Delta in the Gulf of Mexico (Coleman and Garrison, 1977) and along the Sigsbee Escarpment. Prior and Coleman (1978) reported slide failures on the Mississippi Delta front on slopes with an average inclination of 0.5 degrees. For submarine slopes near

**Table 2.1.** Summary of published submarine slides (After Edgers and Karlsrud, 1982).

Slide	Year	V (m <sup>3</sup> )	L (km)	H (m)	L/H	Soil Type	Triggering mechanisms	References
1. Bassein	Ancient	700-900 x 10	215	2200	98		S, EQ	Moore et al., 1976
2. Storegga	Ancient	800 x 10	>160	1700	94		EQ?	Bugge et al., 1979
3. Grand Banks	1929	760 x 10	>750	5000	152	Sand/silt	EQ	Heezen and Ewing, 1952
4. Spanish Sahara	Ancient	600 x 10	700	3100	226	Grav. cl. sand	S	Embley, 1976
5. Rockall	Ancient	296 x 10	5	700	>19.3		S	Roberts, 1972
6. Walvis Bay S.W. Africa	Ancient	90 x 10	250	2100	119			Emery et al., 1975
7. Messina	1908	>> 10 <sup>4</sup>	>220	3200	>69	Sand/silt	EQ	Ryan and Heezen, 1965
8. Orleansville	1954	>> 104	100	2600	38		EQ	Heezen and Ewing, 1955
9. Ice Bay/Malaspina	Ancient	32 x 10	12	80	150	Clayey silt	EQ	Carlson, 1978
10. Cooper River	Ancient	24 x 109	8	45	94	Silt/sand	S	Carlson and Molnia, 1977
11. Ranger	Ancient	20 x 109	37	800	46	Clayey and sandy silt	S (EQ)	Normark, 1974
12. Mid. Alb. Bank	Ancient	19 x 109	5.3	600	9	Silty clay	EQ, S	Hamoton et al., 1978
13. Wil. Canyon	Ancient	11 x 10	60	2800	21.4	Silty clay and silt	S	McGregor and Bennet, 1977
14. Kidnappers	Ancient	8 x 10	11	200	55	Sandy silt	EQ (?)	Lewis, 1971
15. Kayak	Ancient	5.9 x 10	18	150	120	Clayey silt	S, EQ	Carlson and Molnia, 1977
16. Paoanui	Ancient	1 x 109	7	200	35	Silt/sand	EQ (?)	Lewis, 1971
17. Mid. Atl. Cont. Slope	Ancient	4 x 109	3.5	300	11.7	Silty clay	S	Knebel and Carson, 1979
18. Magdalena R.	1935	3 x 108	24	1400	17		S	Heezen, 1956, Menard, 1964
19. California	Ancient	2.5 x	3.5	150	23	Clayey and sandy silt	EQ (?)	Edwards et al., 1980
20. Suva, Fiji	1953	1.5 x 10	110	1800	61	Sand	EQ	Houtz and Wellman, 1962
21. Valdez	1964	7.5 x 10	1.28	168	7.6	Gravelly silty sand	EQ	Coulter and Migliaccio, 1966
22. Orkdalsfjord	1930	2.5 x 107	22.5	500	45	Sand/silt	M	Bjerrum, 1971
23. Sokkelvik	1959	106-107	>5	100	>50	Quick clay sand?		Braend, 1961
24. Sandnesjoen	1967	105-106	1.2	180	7		M	Karlsrud, 1979
25. Helsinki harbor	1936	6 x 103	0.4	11	13	Sand/silt	M	Andresen and Bjerrum, 1967

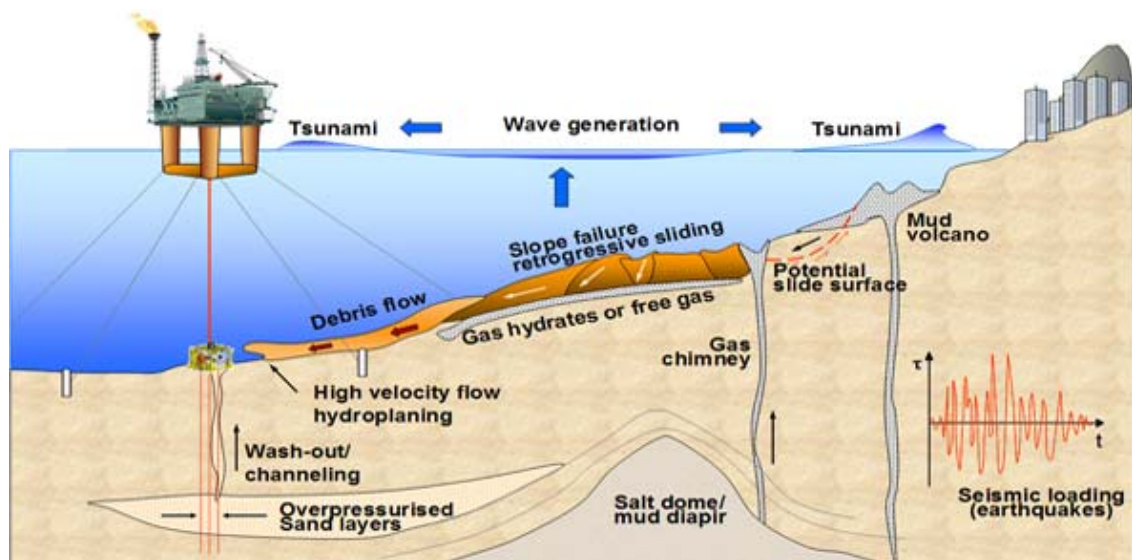


**Fig. 2.1.** Possible triggering mechanisms of submarine slope failures  
(After <http://www.ngi.no/en/Geohazards/Research/Offshore-Geohazards/>).

river deltas, the deposition rate is faster than the rate of consolidation and the new material can trigger localized gravity failures in the weak, unconsolidated sediments. On the continental shelf, the deposition rate is low, the sediments are usually fine silts and clays and are allowed to gain sufficient strength. Theoretically the slopes are stable under gravity loads; however, submarine slope failures have been observed on the Sigsbee Escarpment over the last 25,000 years and have been attributed to seismic loading (Frydman et al., 1988) or wave loading (Schapery and Dunlap, 1978). A variety of mass movement features such as translational slides, rotational slumps, and debris flows have been identified (Figure. 2.2). The complex topography of the seafloor in this region is caused mainly by salt dynamics that has resulted in the formation of large salt domes, basins, and canyons (Bryant et al., 1990; Bryant et al., 1991). The walls



of these features are steep slopes, and in some cases, the inter-basin and inter-canyon slopes exceed 25 degrees (Young et al. 2003a).

Slope instability is a direct potential threat to subsea infrastructure, pipelines and anchor systems on the slope and is, therefore, a key concern in most geohazard studies. Recent advances have been made in understanding the nature and processes of submarine landslides through the use of seafloor mapping technology. Hazard maps of the continental slopes offshore Oregon, California, the Texas/Louisiana Gulf Coast, and New Jersey/Maryland have been created (McAdoo and Watts, 2004). Understanding the response of the soil and the submarine slope to dynamic loading is an important aspect to accurate hazard maps.

Soils on sloping ground surfaces are subjected to initial static driving shear stresses, which the soil must resist in order to maintain stability of the slope (Figure 2.3). For level ground conditions, there are no driving shear stresses and, consequently, there are no initial static shear stresses acting on horizontal planes within the ground. The earthquake shaking of a slope produces multi-directional components of dynamic loading generally assumed as upward propagating horizontal shear waves (Figure 2.4). The horizontal shear waves can be subdivided into two orthogonal components which act in the transverse (parallel to the dip direction of the slope) and longitudinal (perpendicular to the dip direction of the slope). The static stresses prior to seismic loading on the slope are the vertical effective stress ( $\sigma'_{vc}$ ) and the shear stress ( $\tau_s$ ) in the direction of the slope. During seismic loading, an additional cyclic shear stress ( $\tau_{cyc}$ ) is

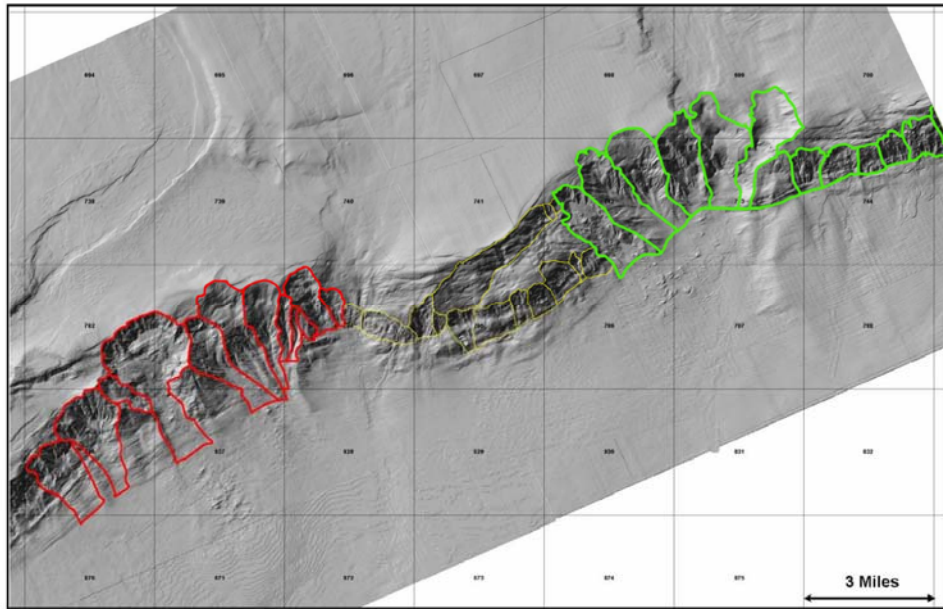


**Fig. 2.2.** Submarine slumps identified on the Sigsbee Escarpment (After Young et al., 2003a).

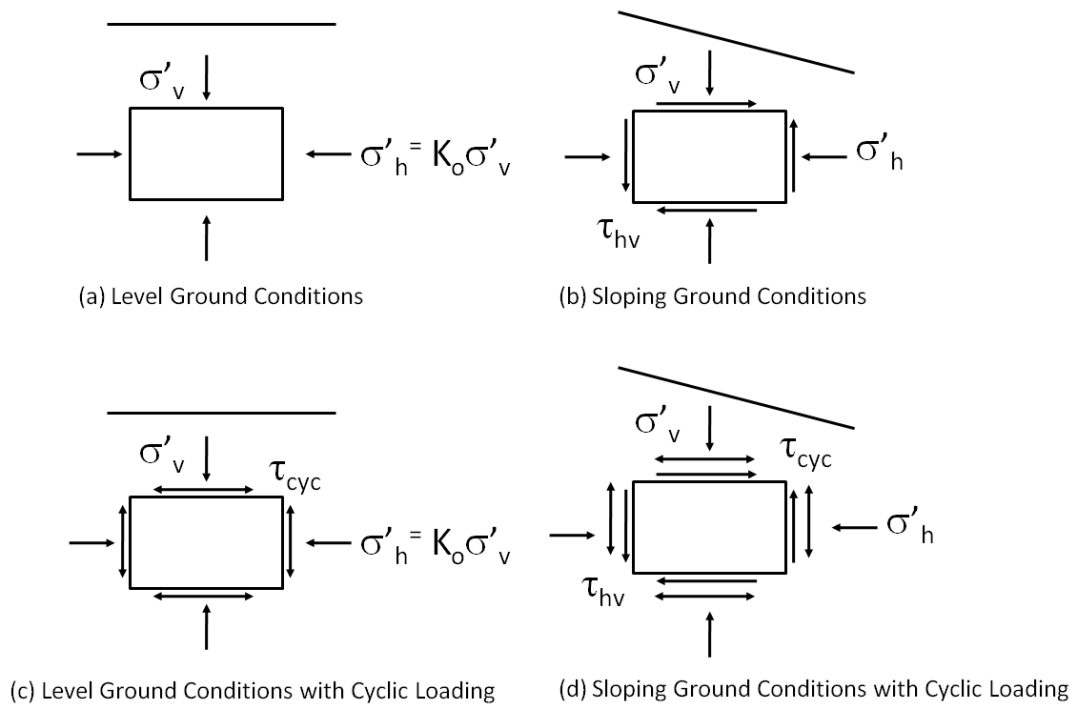
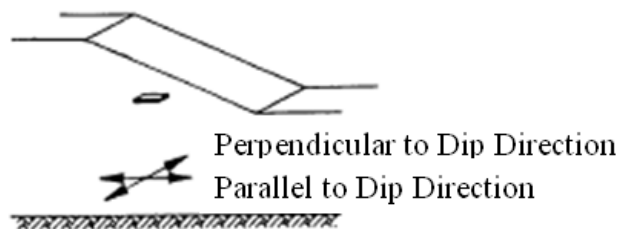
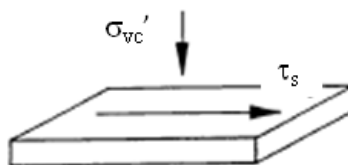


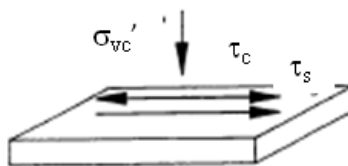
**Fig. 2.3.** Static and cyclic loading conditions for level and sloping ground.



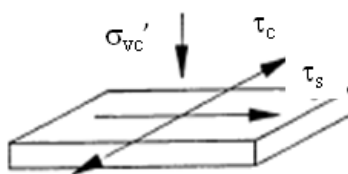
(a) Orthogonal Components of Seismic Loading of Sloping Ground



(b) Static Stress Conditions on Horizontal Planes Prior to Seismic Loading



(c) Dynamic Stress Conditions on Horizontal Planes for Seismic Loading Parallel to the Dip Direction on the Slope



(d) Dynamic Stress Conditions on Horizontal Planes for Seismic Loading Perpendicular to the Dip Direction of the Slope

**Fig. 2.4.** Stress conditions related to direction of slope  
(After Boulanger and Seed, 1995).

applied to the slope in the direction parallel and perpendicular to the dip direction on the slope.

The undrained shear strength is an important parameter required for analysis and modeling of slope stability. Because shear strength varies according to the state of stress associated with the soil's failure mechanism and the strain rate, the selection of the appropriate experimental laboratory tests is imperative. Given the large size of submarine landslides, the failure surface of a submarine slope can be realistically described by simple shear conditions along a large portion of length (Bjerrum and Landva, 1966).

## **2.2 Simple Shear Testing**

The direct simple shear (DSS) apparatus, developed in 1936 by Royal Swedish Geotechnical Institute, was the first device capable of deforming a soil specimen in simple shear (Kjellman, 1951). Two types of DSS devices have evolved from the original 1936 apparatus (Figure 2.5): the Cambridge device designed by Roscoe (1953) and the Norwegian Geotechnical Institute (NGI) device created by Bjerrum and Landva (1966). Extensive comparisons and reviews of the advantages and limitations of each device are available in the literature (Lucks et al., 1972; Shen et al., 1978; Saada et al., 1982; Vucetic and Lacasse, 1982; Budhu, 1985; Amer et al., 1987; Airey and Wood, 1987; Budhu and Britto, 1987; Boulanger et al., 1993).

Historically, DSS devices have been used to study embankments, design pile shafts, study liquefaction of sand and assess the cyclic behavior of pile foundations. One advantage of the DSS test over the triaxial test is that it allows the principal stresses to

rotate during shearing, while the specimen is kept in a plane strain condition (Figure 2.6). Criticisms of the DSS apparatus are mainly due to its inability to impose uniform normal and shear stresses to a test specimen. A discussion of the important issues related to simple shear testing such as state of stress at failure, failure conditions, and constant volume versus constant height testing is provided in Appendix A.

Numerous analytical, numerical and experimental studies (Finn et al. 1971; Lucks et al. 1972; Prevost and Hoeg, 1976; Saada and Townsend, 1981; Finn et al., 1982) have been conducted to determine the importance of the stress non-uniformity on the measured soil response. However, as shown by Shen et al. (1978), the uniformity of the shear stress distribution in a sample improves as the specimen height–diameter ratio

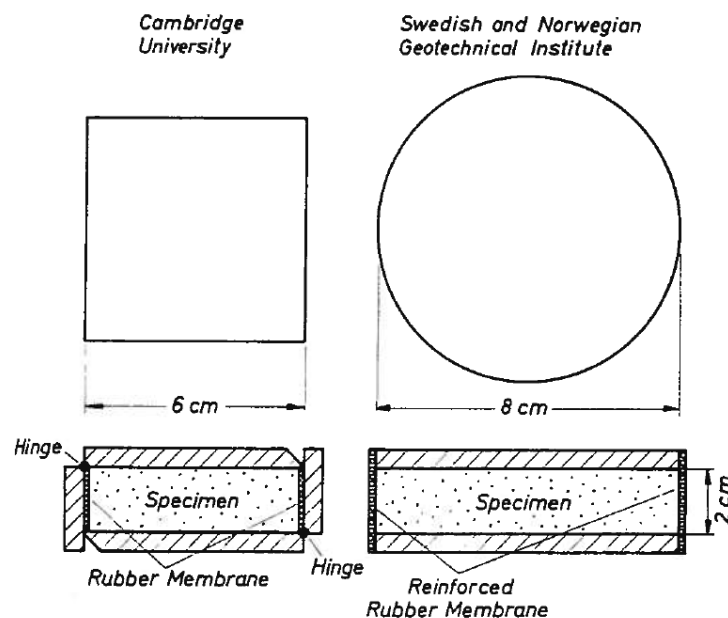
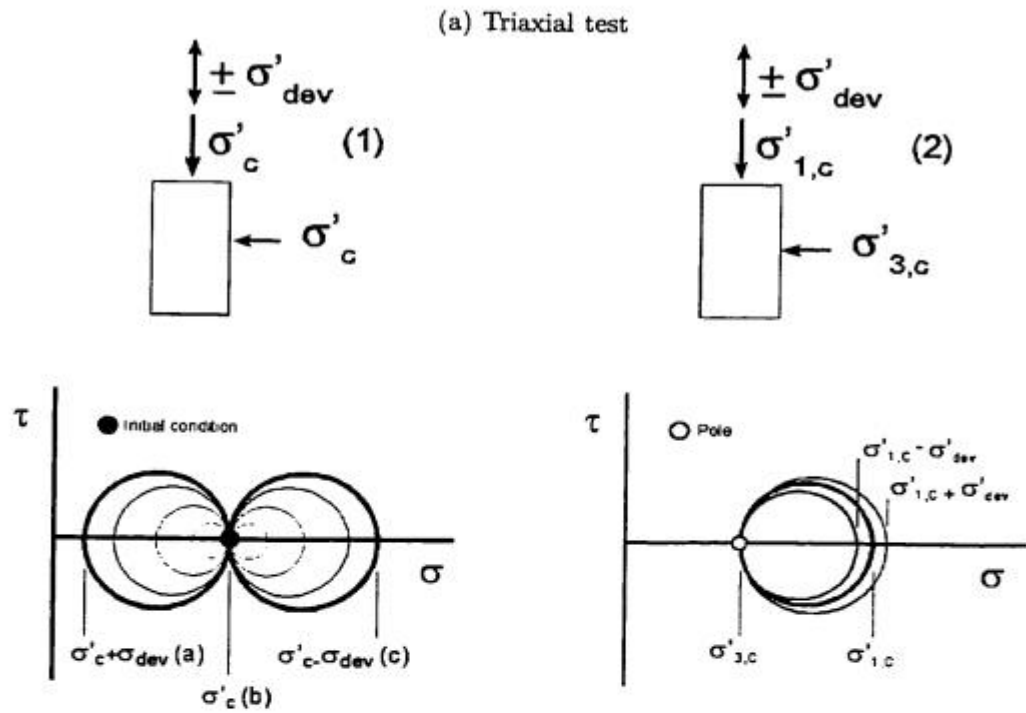


**Fig. 2.5.** Cambridge DSS device and NGI direct simple shear device (After Franke et al., 1979).



Stresses during triaxial tests consolidated (1) isotropically and (2) with initial driving shear stress consolidation

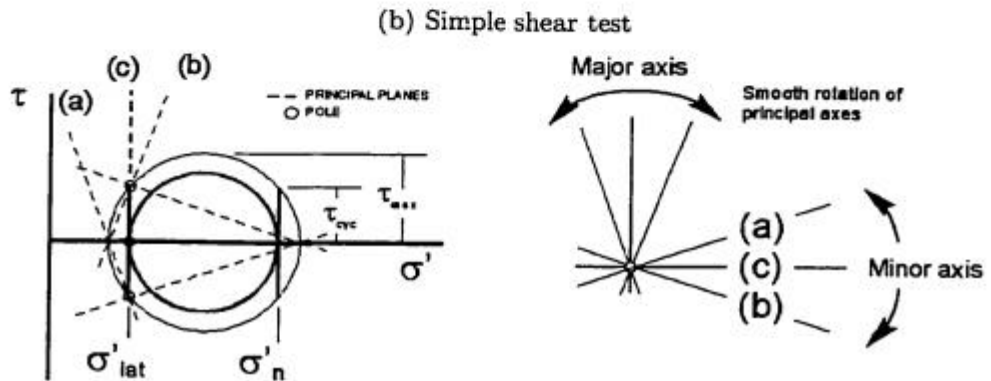


Fig. 2.6. Comparisons of stress conditions in (a) triaxial and (b) simple shear test (After Kammerer, 2001).

decreases, percent of wire-reinforcement increases, elastic modulus of the soil decreases, Poisson's ratio of the soil decreases and applied horizontal displacement increases. Even with the limitations of the DSS to implement ideal simple shear boundary conditions, the uniformity of stresses and strains is better in the DSS than in a standard triaxial apparatus due to the considerable bulging of the sample that may occur as the test approaches failure (Airey and Wood, 1987). Although the traditional DSS device has been used to investigate cyclic loading effects on marine clay (Andersen et al., 1980; Azzouz et al., 1989; McCarron et al., 1995), it does not allow for complex loading conditions, which often contribute to the failure on submarine slopes (Figure 2.7).

### **2.3 Previous Multi-directional Simple Shear Testing Devices**

Cyclic loading tests in DSS were limited to single axis shear loading until Casagrande and Rendon (1978) and Ishihara and Yamazaki (1980) developed multi-directional direct simple shear apparatuses. Both devices were developed to study the liquefaction behavior of sands and, although they provide unique abilities, both have their own limitations. Liquefaction studies use DSS testing since earthquake waves can be simplified as vertically propagating horizontal shear waves.

The gyratory simple shear apparatus (Figure 2.8) designed by Casagrande and Rendon (1978) can conduct uni-directional cyclic direct shear tests and gyratory shear test in which the top of the sample rotates through 360 degrees. However, this device is only able to apply one horizontal shear force which could not be varied during a test. This limitation would prevent the ability to conduct undrained shear tests at a constant rate of strain.

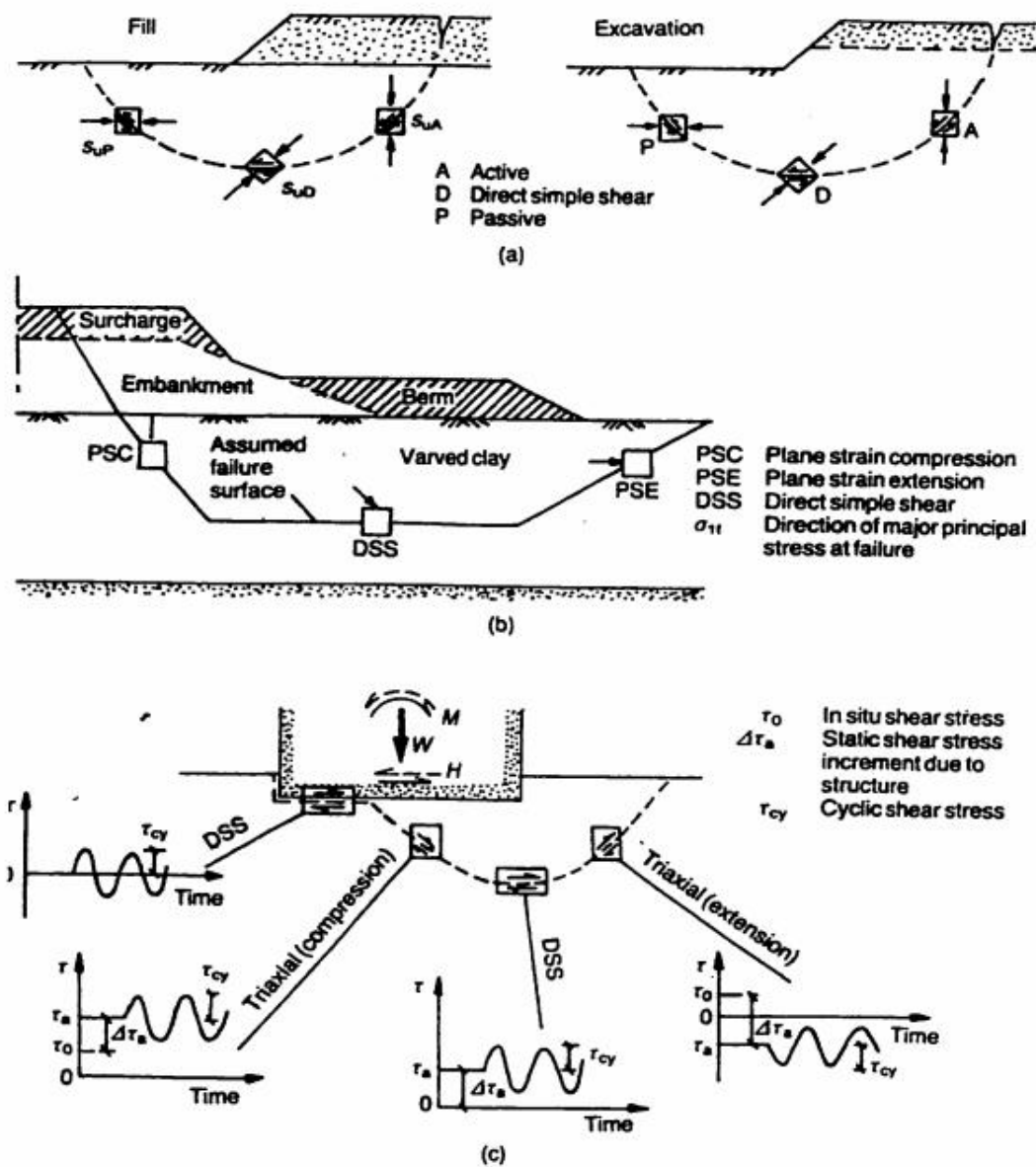


**Fig. 2.7.** Examples of tests that can be used to determine strength along different sections of a failure surface for embankments and shallow foundations (After Lacasse et al., 1988).



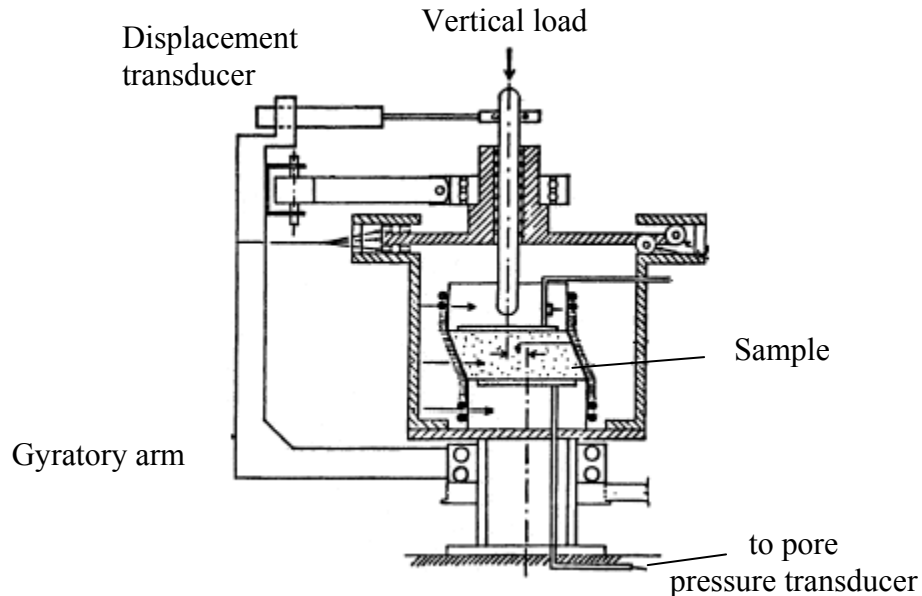


**Fig. 2.8.** Gyrotory simple shear apparatus  
(After Casagrande, 1976).

The two-directional simple shear apparatus (Figure 2.9) developed at the University of Tokyo by Ishihara and Yamazaki (1980) is capable of applying two horizontal cyclic shear forces to the top of circular samples in two mutually perpendicular directions. The device can conduct multi-directional loading but the horizontal forces must act perpendicular to one another. Therefore, only angles of 0, 90 and 180 degrees between the horizontal shear forces can be applied. Both circular and elliptic loading is possible.

Other multi-directional simple shear devices have been developed to overcome limitations of the gyrotory and two-directional simple shear apparatuses. DeGroot (1989)

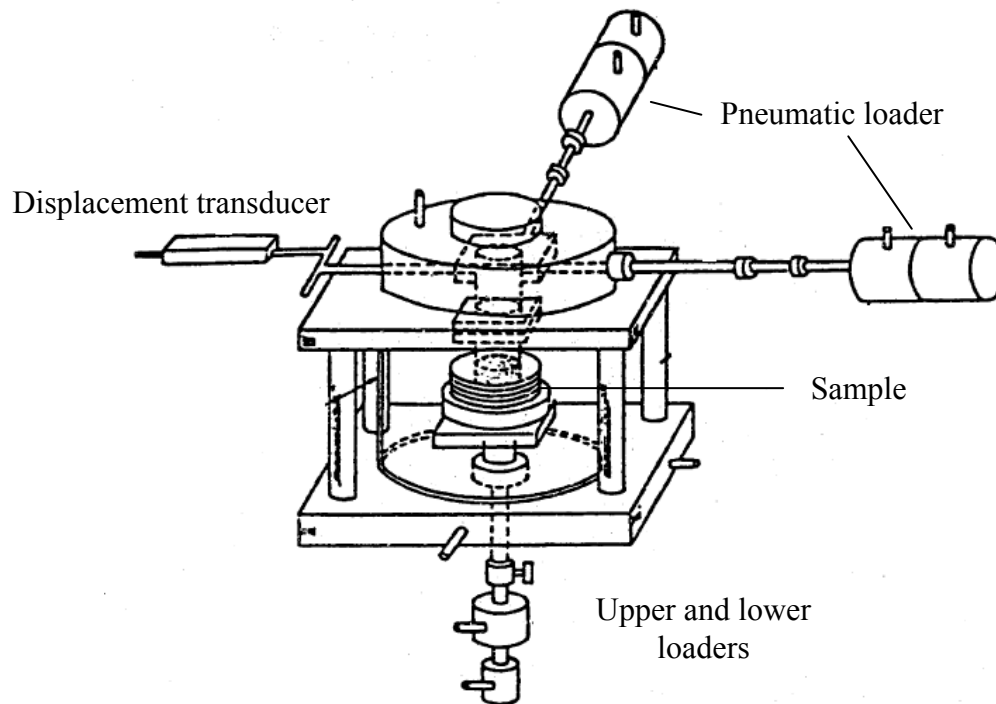


**Fig. 2.9.** Two-directional simple shear apparatus  
(After Ishihara and Yamazaki, 1980).

developed a new multidirectional direct simple shear (MDSS) testing device for testing soil samples under conditions which simulate, at the element level, the state of stress acting within the foundation soil of an offshore Arctic gravity structure (Figure 2.10). Although providing the ability to apply both a vertical stress and a horizontal shear stress to the sample during consolidation, the MDSS created new limitations. Corrections for frictional resistance between horizontal shear force plates and rotation of the top cap during application of applied horizontal shear force were issues. The MDSS also has limited angles in which the horizontal shear forces can be applied and can only change directions of loading between phases of test.

The University of California, Berkeley bidirectional cyclic simple shear device (UCS-2D) described Boulanger et al. (1993) significantly reduced mechanical compliance issues that caused relative top-base cap rocking in earlier devices and provided chamber pressure control which allows back pressure saturation (Figures 2.11 and 2.12). However, due to the pneumatic loading systems the UCS-2D is unable to apply earthquake-like broadband loading at rapid displacement rates.

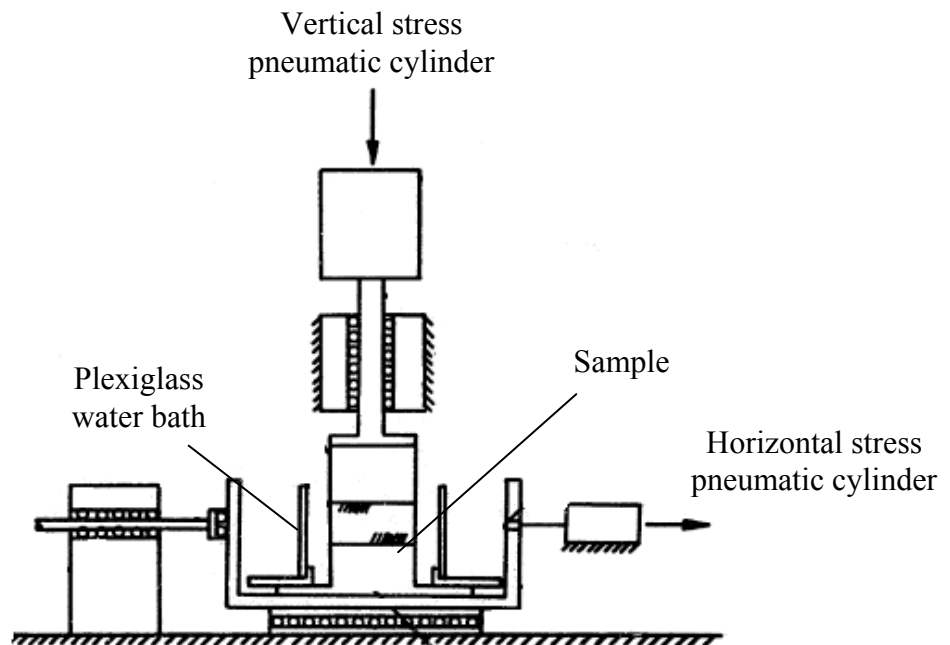


**Fig. 2.10.** MIT Multi-directional simple shear device (After DeGroot, 1989).

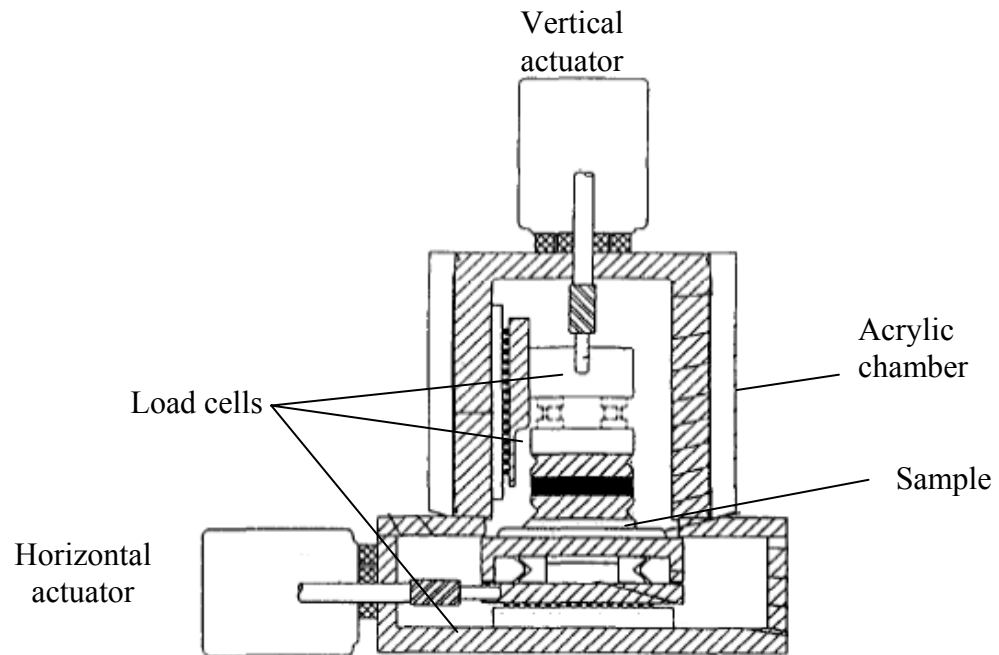


**Fig. 2.11.** University of California, Berkeley bidirectional cyclic simple shear device (UCS-2D) (After Boulanger and Seed, 1995).



**Fig. 2.12.** Photograph of the University of California, Berkeley bidirectional cyclic simple shear device (After Kammerer et al., 1999).

The digitally-controlled simple shear (DC-SS) (Duku et al., 2007) incorporated a servo-hydraulic actuation and true digital control to overcome control limitations of previous multi-directional simple shear devices (Figures 2.13 and 2.14). The DC-SS is able to reproduce sinusoidal and broadband command signals across a wide range of frequencies and amplitudes, however has limited control for small displacements.

Although each of the existing multi-directional simple shear devices was developed to overcome some previous limitations they retain a number of limitations including top-bottom cap rocking, no back pressure control systems, limited testing amplitude and frequencies, and measurable friction between the horizontal loading tables. The TAMU-MDSS is necessary to provide high quality experimental test data at a wide range of amplitudes and frequencies for use in constitutive and finite element model development for analysis of submarine slope.

## **2.4 Measured Soil Response**

One of the primary challenges in studying submarine landslides is the lack of information about the properties of these soils in situ. Because offshore soil sampling is expensive, published experimental information on marine clays from offshore is limited. Most marine clay testing in the research literature is conducted on marine deposits that are now onshore and easily accessible such as Boston Blue Clay (BBC) and San Francisco Young Bay Mud (YBM). However, due to the depositional environment and mechanisms, the stress history for these samples differs from offshore marine sediments.

A very limited number of two-directional monotonic and cyclic tests on clays are available and the results are sometimes contradictory (Biscontin, 2001; DeGroot et. al.,

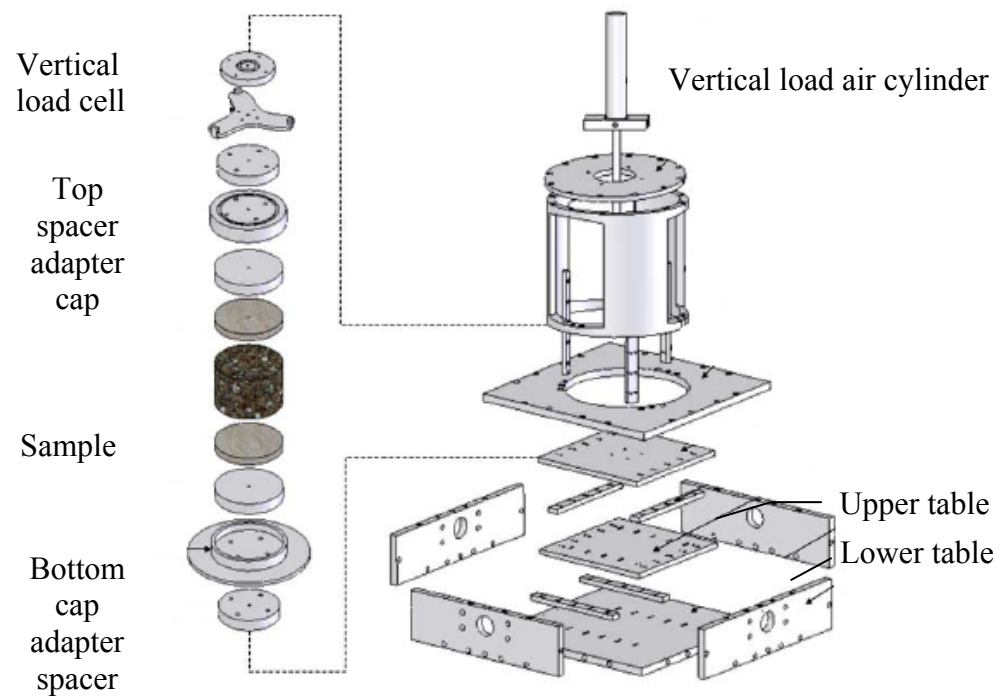


**Fig. 2.13.** Digitally-controlled simple shear (DC-SS) (After Duku et al., 2007).

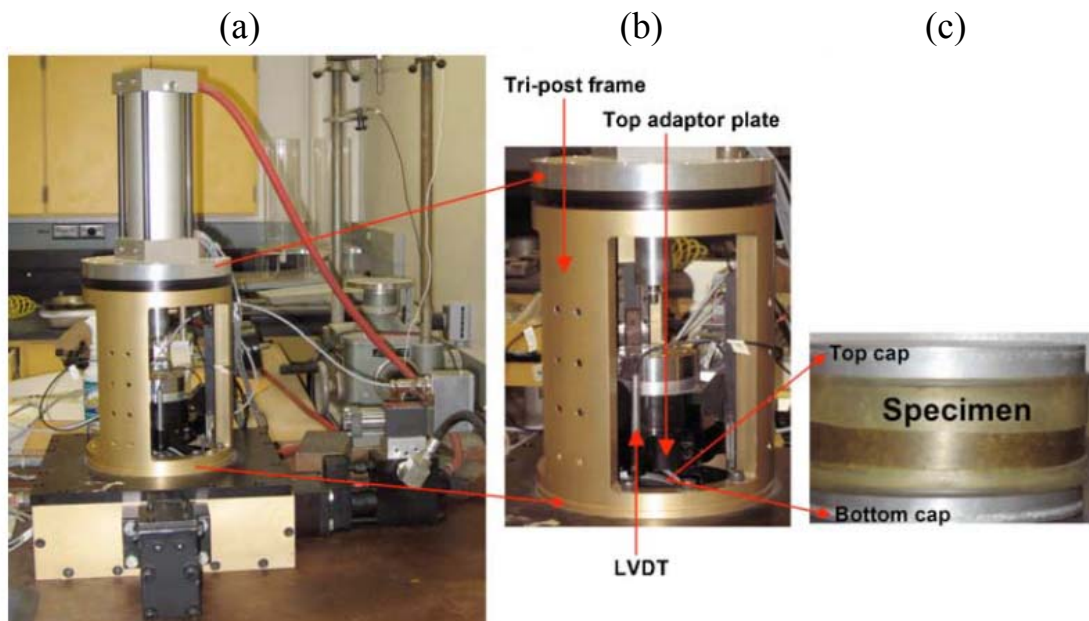


**Fig. 2.14.** Photographs of DC-SS showing (a) overview of device, (b) close-up view of tri-post frame, and (c) sample with top and bottom cap (After Duku et al., 2007).

1996). Results from simple shear testing on BBC (Ladd and Edgers, 1972; Malek, 1987; DeGroot, 1989) and YBM (Rau, 1999; Biscontin, 2001) have demonstrated the undrained shear strength increases with increasing initial shear stress,  $\tau_c$  (i.e, slope), for shearing in the same direction (equivalent to downhill). The strength decreases for shearing in the direction opposite to the initial stress (shearing uphill). The response is brittle for shearing in the same direction as the shear stress applied during consolidation ( $\tau_c$ ) and ductile for shearing opposite to  $\tau_c$ .

These findings have important implications for the stability of the slope, predicting that forces acting downward in the slope direction will need to mobilize less strain to reach peak strength and initiate failure. During cyclic stress controlled tests with no initial shear stress ( $\tau_c = 0$ ) simulating level ground, the cyclic strains are symmetrically centered around the zero strain axis, with full reversal at each cycle. When  $\tau_c \neq 0$  (simulating a slope) an average shear strain accumulates during the tests and the maximum and minimum shear strains are not centered around the zero strain axis.

The characterization of actual offshore marine deposits is important since the depositional environment, depositional mechanics and stress history strongly influence the structure of the deposit and consequently their mechanical response. Limited multi-directional monotonic and cyclic testing has been conducted on BBC (DeGroot, 1989; Torkornoo, 1991) and YBM samples (Biscontin, 2001). No multi-directional simple shear testing on actual offshore marine clays is available in the literature.

## 2.5 Conclusions

Analysis and modeling of submarine stability slopes require knowledge of numerous soil parameters and relies on the selection of appropriate shear strength values. However, most experimental results in the literature for fine grained soils concentrate on one-dimensional response, both for monotonic and cyclic tests. Although the traditional direct simple shear device has been used to investigate cyclic loading effects on marine clay, it does not allow for complex loading conditions, which often contribute to the failure on submarine slopes.

Understanding the interaction between the initial shear stress, representing the slope, and the multi-directional shaking due to earthquakes or storm loading has only been recognized as an important factor in the last few years (DeGroot, 1989; Boulanger and Seed, 1995; Biscontin, 2001; Kammerer, 2001). Very few multi-directional simple shear devices have been developed (Casagrande and Rendon, 1978; Ishihara and Yamazaki, 1980; Boulanger et al., 1993; DeGroot et al., 1996; Duku et al., 2007). However, these devices have reported issues such as top-bottom cap rocking, sample size restrictions, no back pressure control systems, limited testing amplitude and frequencies, and measurable friction between the horizontal loading tables.



### 3. DESCRIPTION OF TAMU-MDSS

The Texas A&M Multi-directional Simple Shear (TAMU-MDSS) device was developed to experimentally simulate, at the element level, the stress conditions within a submarine slope subjected to cyclic loading. The new device allows for the investigation of the response of marine clays to shear rate effects, frequencies, and multi-directional loading paths. This prototype provides the ability to apply a large range of shear stresses and complex loading paths, such as figure-8 and circular patterns, to a cylindrical soil sample confined by a wire-reinforced membrane. The load and torque experienced by the sample is directly measured by a multi-axis load cell installed above the sample. Backpressure saturation of the sample is possible due to the ability to apply pressure in the chamber and backpressure to the water lines. The TAMU-MDSS system consists of three components: the direct simple shear testing equipment, the computer and data acquisition console and the hydraulic power supply (Figure 3.1).

#### 3.1 Overview of TAMU-MDSS Simple Shear Equipment

The testing equipment allows loading along three independent axes, two perpendicular horizontal directions (X-axis and Y-axis) to allow any stress or strain paths in the horizontal plane, and a third in the vertical direction (Z-axis). Special care was taken with the design of the support for the top assembly to minimize compliance and increase stiffness in order to eliminate the rocking motion observed for other types of multi-directional simple shear testing devices. Instead of a tri-post frame used in the DC-SS, the TAMU-MDSS design incorporates a four column support frame. The top

assembly is mounted on the four column support frame using low friction bearing sleeves.

Loads are applied to the top assembly by a hydraulic actuator mounted at the top of the device. The TAMU-MDSS can also apply cyclic loading in the z-axis, allowing the device to be used as a cyclic triaxial testing device with some modification to the sample caps and attachments. The vertical loads are transmitted to the sample through the top assembly attached to a vertical load cell (Figure 3.2). The maximum vertical capacity of the vertical load cell is  $\pm 1.1$  kN (250 lbf) with  $\pm 0.04\%$  static error band and hysteresis.

Vertical confinement is provided by end caps with embedded porous stones allowing drainage. The fine porous stones are recessed into the cap with a tight fit but can be removed for cleaning. The stones can be saturated for undrained tests. Drainage lines are connected to both caps leading to the backpressure system. The caps are held tightly in position by the top and bottom assembly adapters. The top cap is attached to the top assembly using a circular clamp. The bottom cap is secured to the bottom assembly by tightening two bolts in the “t” shaped bracket which allows a measure of movement before tightening. This feature is provided to avoid shearing the specimen if caps are slightly misaligned. Once the specimen is secured, the LVDTs record the initial position. Step by step procedures for sample installation are provided in Appendix B.

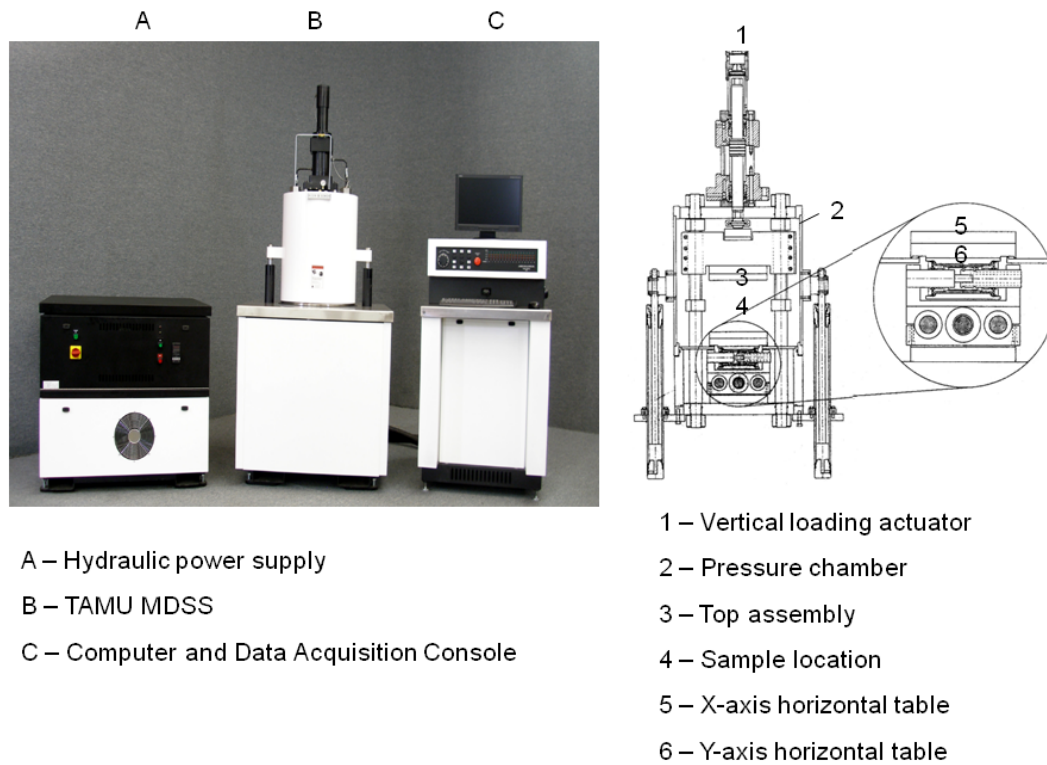


**Fig. 3.1.** Photograph and schematic of TAMU-MDSS device.

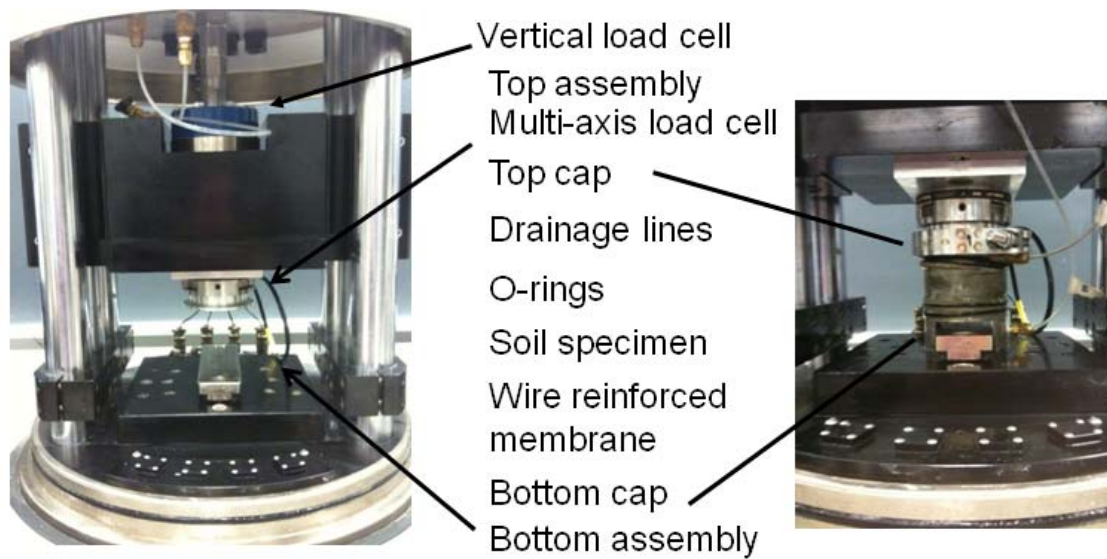


**Fig. 3.2.** Mounting of sample in TAMU-MDSS.

Horizontal shear loads are applied to the bottom assembly by two independently controlled horizontal tables (Figure 3.3). The horizontal loads are applied by actuators and recorded by two load cells. The maximum horizontal capacity for each load cell is  $\pm 1.1$  kN (250 lbf) for both x and y directions. The maximum actuator stroke in the x and y direction is  $\pm 5.0$  cm (1.97 in). The bottom of the sample can move in any direction as a result of a custom-built layered system consisting of two track and table elements aligned perpendicularly to each other (Figure 3.3). The top horizontal table (x-direction) is mounted using low-friction track bearings directly on lower table (y-direction). The lower table also moves on the low-friction track bearings attached to the base of the device. This design allows for independent control of each horizontal table allowing for the creation of any strain and stress-controlled loading path. An evaluation of possible cross-coupling of the two horizontal tables is discussed in section 4. The coordinate axes, as shown in Figure 3.4, are used for reference in describing the direction of the displacements and applied forces.

In the TAMU-MDSS, the sample can deform vertically and in any horizontal direction. The horizontal deformation takes place with the bottom of the sample moving relative to the top. The top assembly and top cap are held fixed against horizontal displacement. Deformations are monitored with linear variable distance transformers (LVDTs) mounted on the load frame and horizontal tables. The vertical displacement transducer is a Macrosensor AC model PR 812-2000 LVDT with a range of  $\pm 50$  mm. The two horizontal displacement transducers mounted to the horizontal tables are Solartron AC LVDT's gage type stroke  $\pm 10.0$  mm.

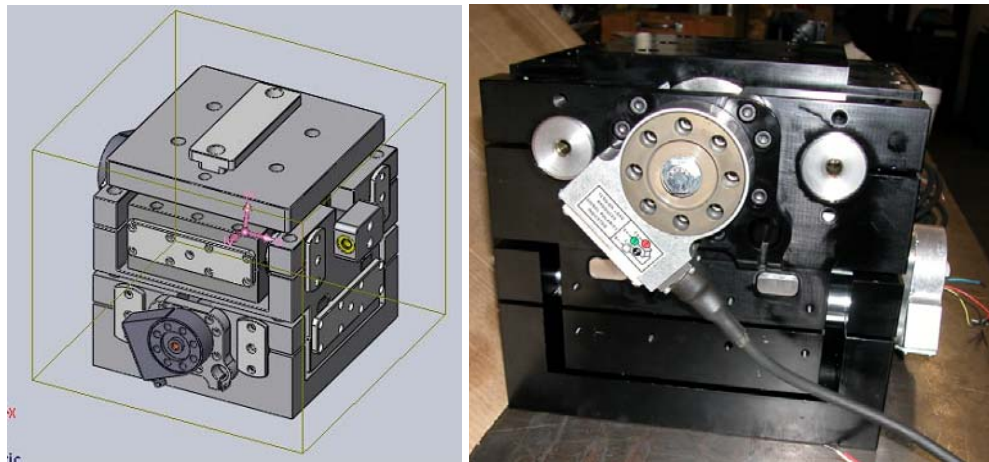


**Fig. 3.3.** Horizontal tables and horizontal load cells.

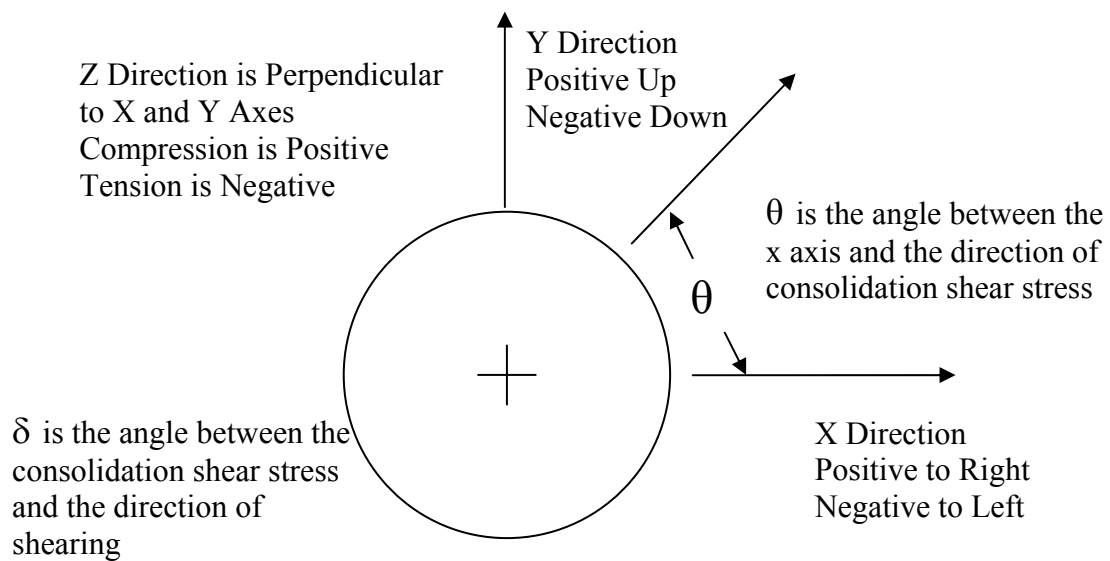


**Fig. 3.4.** Plan view showing TAMU-MDSS coordinate axes.

### 3.1.1 Backpressure and Cell Pressure Systems

Most simple shear devices are unable to perform truly undrained testing with direct measurement of pore pressure because they do not allow full saturation of the sample. In the TAMU MDSS, both backpressure and cell pressure can be independently measured and controlled. The pressure chamber is rated for a maximum air pressure of 861.8 kPa (125 psi). The chamber pressure transducer is a Honeywell model FP2000 transducer with a range of 50psi and an accuracy of  $\pm 0.10\%$  FS.

Two differential pressure transducers are used in the backpressure system to measure the excess pore pressure and volume change of sample (Figures 3.5 and 3.6). The excess pore pressure transducer referred as the “effective transducer” is a Honeywell model FP2000 wet/wet pressure transducer with a range of 50 psi and an accuracy of  $\pm 0.10\%$  FS. The volume change transducer is a Honeywell model FP2000 wet/dry pressure transducer with a range of 10 inch water and an accuracy of  $\pm 0.10\%$ .

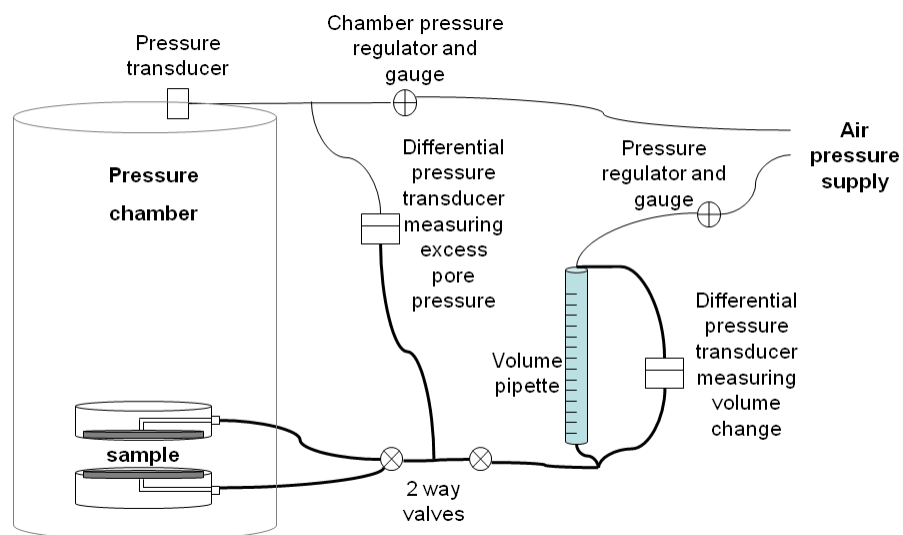


**Fig. 3.5.** Idealized schematic of backpressure system.

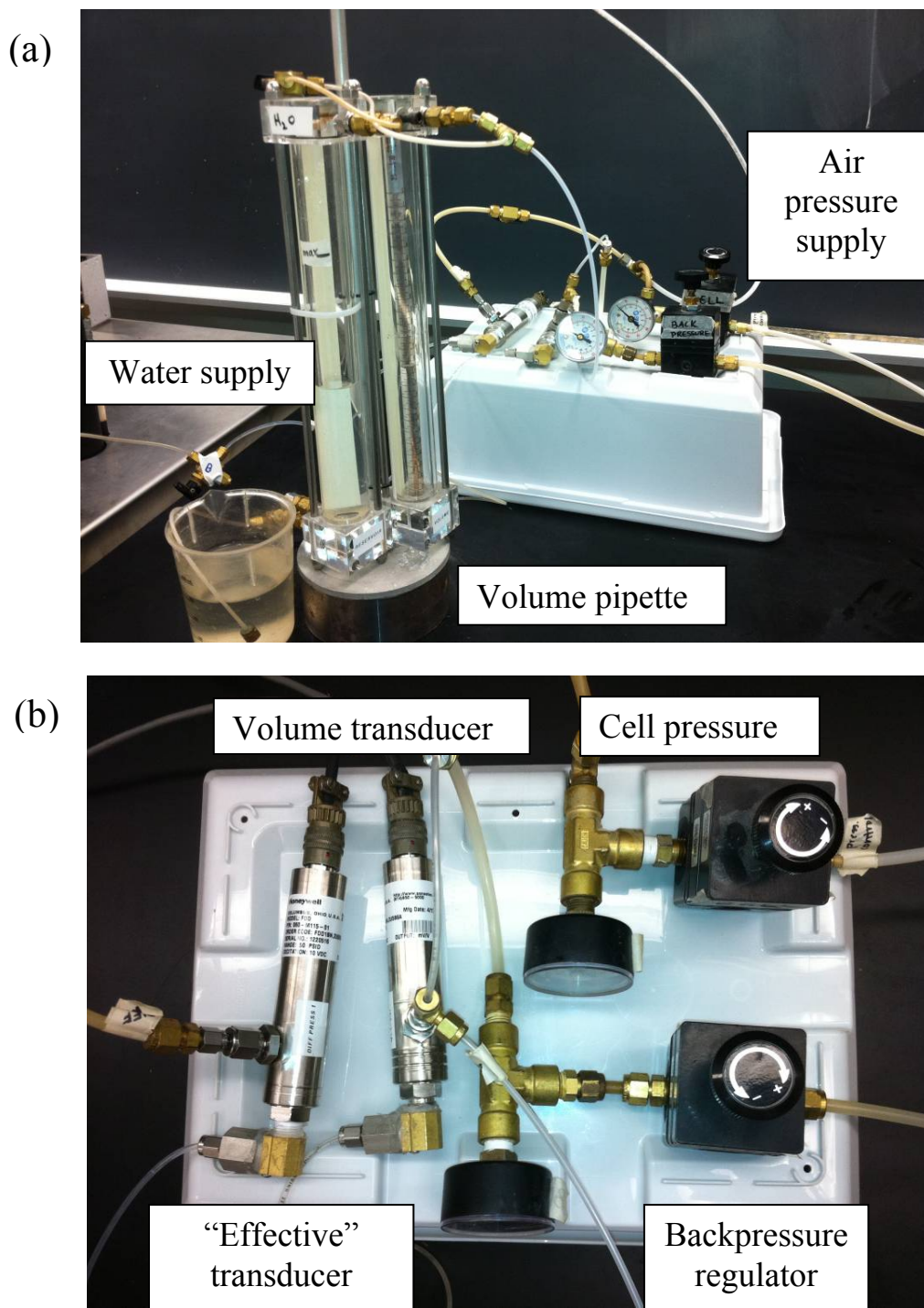


**Fig. 3.6.** Photographs of backpressure system (a) side view of backpressure system (b) top view of backpressure system.

### **3.1.2 Specimen**

The device can accommodate specimens up to a diameter of 100 mm (4 in), larger than the more typical size of 70 mm (2.8 in) and resulting in more uniform stress distribution (Vucetic and Lacasee, 1982; Finn et al., 1982). Larger samples up to 150 mm (6 in) can be tested with minor modifications to the sample mounting brackets. Similar to the NGI simple shear device, the samples are circular and maintain constant cross-sectional area by using a wire-reinforced membrane.

As discussed in Section 2.3, the diameter to height ratio was selected as 4 to minimize the effects of non-uniform stress distribution along the top and bottom of the sample due to the lack of complementary shear stress on the lateral boundaries of the sample.

The wire-reinforce latex membrane is manufactured by Geonor for the NGI shear device. The standard sized membrane with a specimen area of 50 cm<sup>2</sup> is used. A wire-stiffness of  $c = 1.0$  is used in an effort to match the average stiffness properties of the soil. The reinforcement in these membranes is constant wire with a diameter of 0.015 cm, a Young's modulus of  $1.55 \times 10^6$  kg/cm<sup>2</sup>, and a tensile strength of 5800 kg/cm<sup>2</sup> (Dyvik, 1981). The wire is wound at 20 turns per centimeter of membrane height (0.05 cm center to center spacing). A chamber pressure lower than the anticipated lateral pressure in the samples is applied to minimize the load carried by the wires in the reinforced membrane. The use of the reinforced membrane prevents direct measurement of the lateral confining pressure because the amount of stress that the wire carries is unknown. The membrane is assumed to have negligible lateral deformation and



therefore the samples are consolidated under  $K_o$  conditions. Cell pressure can also be used to enforce  $K_o$  conditions following procedures outline in Boulanger et al. (1993). Backpressure procedures are described in more detail in Appendix B.

### 3.1.3 Multi-axis Load Cell

One of the main improvements of the TAMU-MDSS over similar devices is the multi-axis load cell installed directly above the sample to increase accuracy and reduce the influence of compliance (Figure 3.7). The transducer has a sensing range of  $\pm 2$  kN (450 lbf) in the vertical axis and  $\pm 0.67$  kN (150 lbf) in the horizontal axes. The torque applied to the specimen can be measured within a range of  $\pm 0.068$  kN-m (600 lbf-in) in all three directions. The data acquisition system for the multi-axis load cell is through a separate laptop using Labview software. Six channels, three forces and three torques, are recorded with time.

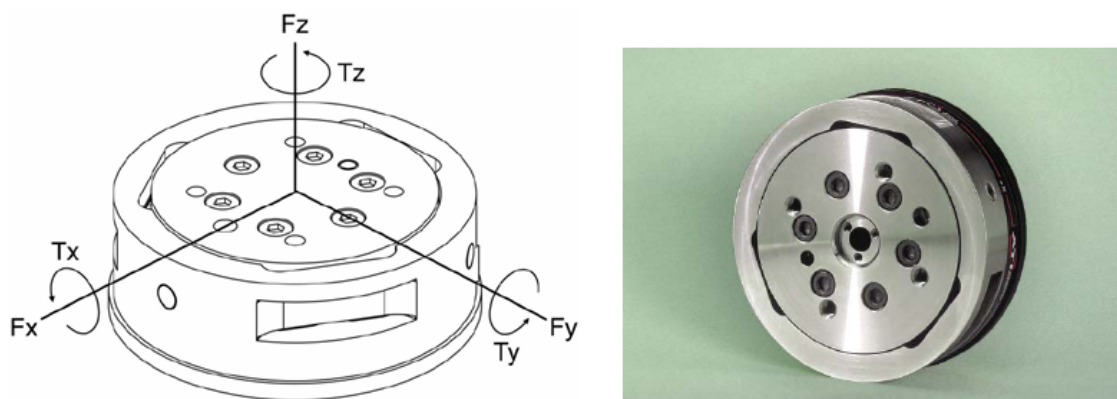


**Fig. 3.7.** Schematic and photos of multi-axis load cell

### 3.2 Hydraulic Power Supply

A servo-hydraulic control system (Figure 3.8) is used to allow for frequencies up to 20 Hz and more reliable control. The hydraulic power supply (Model CS7580-D) system was designed specifically for laboratory use. Standard hydraulic power supplies using fixed or variable displacement piston pumps run at a constant rotations per minute (RPM). The noise level and heat generated remains virtually constant. However, the CS7580-D system varies the pump RPM in relation to demand. When variable lower flow rates are required, the motor speed slows to the minimum rotation required to maintain the programmed pressure. This concept reduces energy cost up to 50%, lowers operating temperatures and runs 30-40% quieter than other hydraulic units. For additional noise reduction, the pumping system is enclosed in an acoustically dampened outer cabinet.



**Fig.3.8.** Hydraulic power supply.

### 3.3 Computer Control and Data Acquisition

The Automated Testing System (ATS) software package (Sousa and Chan, 1991) was chosen for control of the closed-loop system. ATS provides control signals to servo-valve drivers for the hydraulic actuators and the chamber pressure controller (Figure 3.9). Voltage from the LVDTs, load cells and pressure transducers are acquired from the data acquisition board by ATS through a data acquisition board (National Instruments PCI-6703).

The 16-bit board allows high sampling resolution and analog-to-digital and digital-to-analog processing allowing the system to record data and control servo-valves. ATS can sample all 16 input channels (Figure 3.10 and Table 3.1) and then update the output commands sent to the selected servos at a rate selected by the user of either 500, 1000 or 2000 times per second. All components of the data acquisition system are summarized in Table 3.2. The control system uses a PD (Proportional-Derivative) control algorithm. Gains for the PD control system are determined by manual tuning. ATS allows for either manual or automatic control of each output channel using any input channel as the feedback to be controlled.

A number of pre-programmed control signals, called tests, are available on ATS. Ramp tests are used to change feedback channel from one value to another at a specified constant rate of change. Cyclic tests are used to produce a sinusoidal wave of specified amplitude, frequency and mean value, while wave tests are used to reproduce a wave form which the user specifies by providing a digitized data file describing one cycle of the wave. Each test can be applied to a specific feedback channel and multiple tests can

be combined to control different channels simultaneously. Tests using all three servos valves can be conducted in parallel allowing complex loading patterns such as circular and figure-8. The ability to specify the feedback channel allows versatility in running either strain or stress controlled tests.

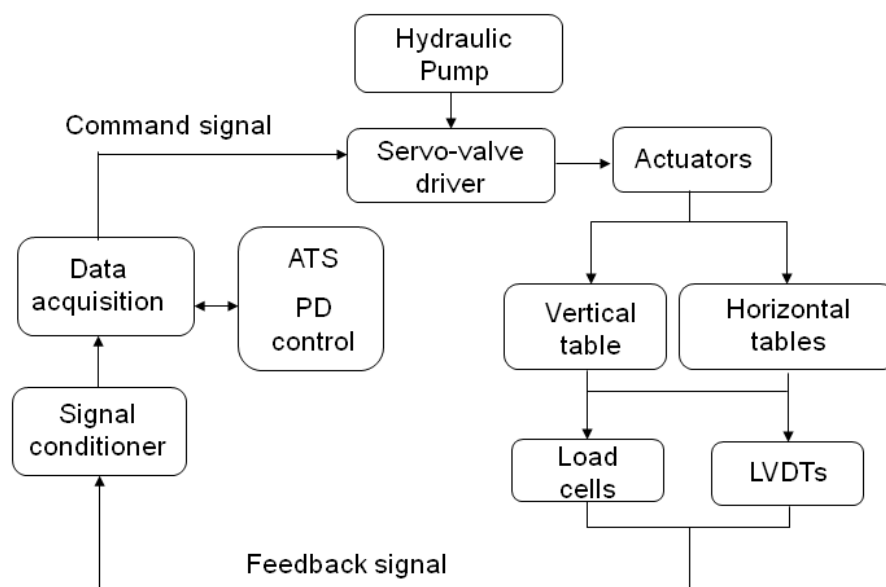


**Fig. 3.9.** Layout for control system components of TAMU-MDSS device.



**Fig. 3.10.** Data acquisition boards.

**Table 3.1** Data acquisition used in TAMU-MDSS.

Channel No.	Channel Name	Instrument
0	Zstroke	Vertical LVDT
1	Zload	Vertical load cell
2	Xstroke	X direction LVDT
3	Xload	X direction load cell
4	Ystroke	Y direction LVDT
5	Yload	Y direction load cell
6	“Effective”	Differential pressure transducer
7	Cell	Pressure transducer
8	Empty	-
9	Volume	Differential pressure transducer
10	Empty	-
11	Signal conditioning	-
12	Empty	-
13	SV2	Servo y direction
14	SV1	Servo x direction
15	SVO	Servo z direction

**Table 3.2** List of TAMU-MDSS transducers.

Transducer	Measured Quantity	Model and Sensitivity
Vertical LVDT	Axial deformation	Macrosensors General Purpose AC-Operated LVDT Position Sensor Model PR812-2000 Range $\pm 50.0$ mm $\pm 0.25\%$ FS
Vertical load cell	Vertical load	Interface Model 1010 Fatigue rated load cell Capacity: 250 lbf $\pm 0.03\%$ FS
X direction Horizontal LVDT	Shear deformation x-direction	Solartron AC LVDT gage type Range: $\pm 10.0$ mm $\pm 0.2\%$ FS
X direction Load cell	Load in x-direction	Straincert Universal Load Cell. Capacity: 250 lbf Nonlinearity $\pm 0.10\%$ FS
Y direction Horizontal LVDT	Shear deformation y-direction	Solartron AC LVDT gage type Range: $\pm 10.0$ mm $\pm 0.2\%$ FS
Y direction Load cell	Load in y-direction	Straincert Universal Load Cell. Capacity: 250 lbf Nonlinearity $\pm 0.10\%$ FS
Differential pressure transducer	Difference between volume and cell pressure	Honeywell FP2000 range : 50psi Accuracy $\pm 0.10\%$
Pressure transducer	Chamber pressure	Honeywell FP2000 range : 50psi Accuracy $\pm 0.10\%$
Differential pressure transducer	Volume (inches of water)	Honeywell FP2000 range: 10 inch water, Accuracy $\pm 0.10\%$

### **3.4 Conclusions**

An overview of the development and capabilities of the new Texas A&M multi-directional simple shear device has been presented. The TAMU-MDSS applies both vertical and horizontal loads to a cylindrical sample confined in a wire-reinforced membrane. The device is capable of shearing the sample in monotonic, cyclic and complex patterns under both stress and strain-control. Chamber pressure and backpressure can be applied to allow for sample saturation. Pore pressure generation during undrained shearing can be directly measured. The forces and torques applied to the sample are measured by the multi-axis load cell installed immediately above the sample. The capabilities of the TAMU-MDSS will be demonstrated in section 4 through the testing of a rubber sample.



#### **4. EXPERIMENTAL EVALUATION OF THE TAMU-MDSS**

An experimental evaluation of the TAMU-MDSS was performed to determine the full capabilities of the device. Initially, each strain-controlled test was carried out using only the horizontal tables. These tests were used to determine the friction between the tables and if the direction of the test and rate influenced the friction. Secondly, a rubber sample with dimensions similar to those of the marine clay specimens in the experimental study was used to evaluate the capabilities of the device and the repeatability of the tests. The device evaluation program has two main objectives:

1. Evaluate the kinematics of the device to ensure the TAMU-MDSS is capable of conducting strain and stress-controlled monotonic, cyclic, circular and figure-8 test patterns.
2. Verify the sample set-up procedures and data acquisition systems are working properly and produce repeatable results.

The performance of the TAMU-MDSS system was evaluated using harmonic input motions and the resulting feedback signal was recorded. To evaluate each axis independently, uni-directional tests were conducted. Cross-coupling effects between the axes were analyzed by conducting bi-directional testing and varying the signal frequencies to each horizontal table.

##### **4.1 Friction and Cross-coupling of Loading Tables**

The loads applied to the sample by the three actuators (two horizontal and one vertical) are measured by load cells mounted inside the chamber between the actuators

and the loading tables. Thus, the load cells measure both frictional and inertial loads which may not be transferred to the sample. The magnitude of the loads developed by “device friction” between the horizontal tables needs to be determined.

First, each axis of motion was evaluated on its own. A ramp monotonic command signal was sent to one of the actuators and the load and displacement of each table was recorded to access friction between the tables. Two different strain rates were conducted to determine if the friction in the system was rate dependent.

Figure 4.1 shows plots of frictional resistance for monotonic tests in the x and y-directions at strain rates of 5%/hr and 50%/hr. In monotonic loading at a rate of 5%/hr (1 mm/hr), the recorded force due to friction in the x-direction was measured to be a maximum of  $\pm 0.017$  kN (4 lbf), which corresponds to less than 3.6 kPa (0.5 psi) over a 79.75 mm (3.14 in) diameter sample. The friction in the y-direction was measured to be a maximum of  $\pm 0.017$  kN (4 lbf), which corresponds to less than 3.6 kPa (0.5 psi) for the samples. For a rate of 50%/hr (10 mm/hr), a maximum force of  $\pm 0.022$  kN (5 lbf) or 4.5 kPa (0.7 psi) was measured. Based on the measured loads in each direction and different strain rates, the frictional resistance is smaller in magnitude in the x-direction. The monotonic tests also indicate friction of the tables is mostly independent of rate for the rates which will be used in the testing program.

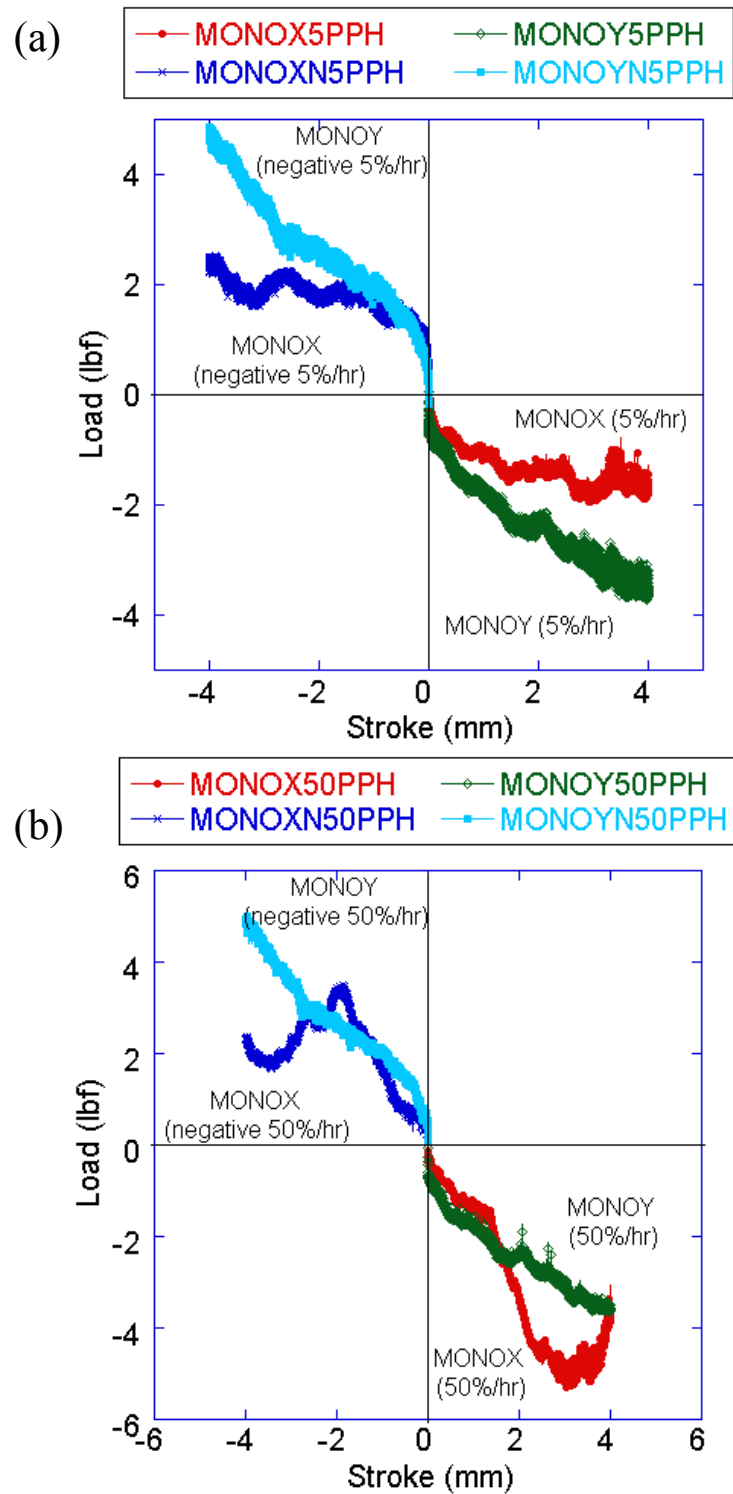


**Fig. 4.1.** Frictional resistance on the horizontal tables for monotonic tests for a rate of (a) 5%/hr and (b) 50%/hr.

Sinusoidal command signals were also sent to each axis to determine the frictional resistance for cyclic, circular and figure-8 strain controlled tests. Two amplitudes (0.1 mm and 3 mm) and two frequencies (0.1 Hz and 1 Hz) were used. Figure 4.2 and Figure 4.3 shows plots for cyclic tests in the x-direction and y-direction, respectively. For cyclic loading at both frequencies and amplitudes, the friction in the x-direction was measured to be less than 0.007 kN (1.5 lbf), which corresponds to less than 1.3 kPa (0.19 psi). The friction in the y-direction was measured to be less than  $\pm 0.178$  kN (4 lbf) or 3.6 kPa (0.5 psi). As indicated in the plots, the frictional resistance is directly related to the amplitude of the cyclic loading. As the amplitude increased from 0.1 mm to 3 mm, the load in the corresponding direction increased from 0.002 kN (0.5 lbf) to 0.004 kN (1 lbf). Increased frequency does not seem to create additional frictional resistance in cyclic loading.

Circular tests were conducted at frequencies of 0.1 Hz and 1 Hz with full strain amplitudes of 0.1 mm and 3 mm. Figure 4.4 shows plots for circular tests. The load due to friction in the x-direction was measured to be less than 0.004 kN (1 lbf) or 0.89 kPa (0.1 psi). The frictional resistance in the y-direction was measured to be less than 0.013 kN (3 lbf), which corresponds to less than 0.3 psi (2.67 kPa).

Figure-8 tests were conducted at frequencies of 0.1 Hz and 1 Hz with full strain amplitudes in the major axis of 0.2 mm and 6 mm. Figure 4.5 shows plots for figure-8 tests. The x-direction and y-direction load cells measured the friction to be less than 0.004 kN (1 lbf) or 0.89 kPa (0.1 psi). The frictional resistance measured in the y-direction was less than  $\pm 0.178$  kN (4 lbf) or 3.6 kPa (0.5 psi).

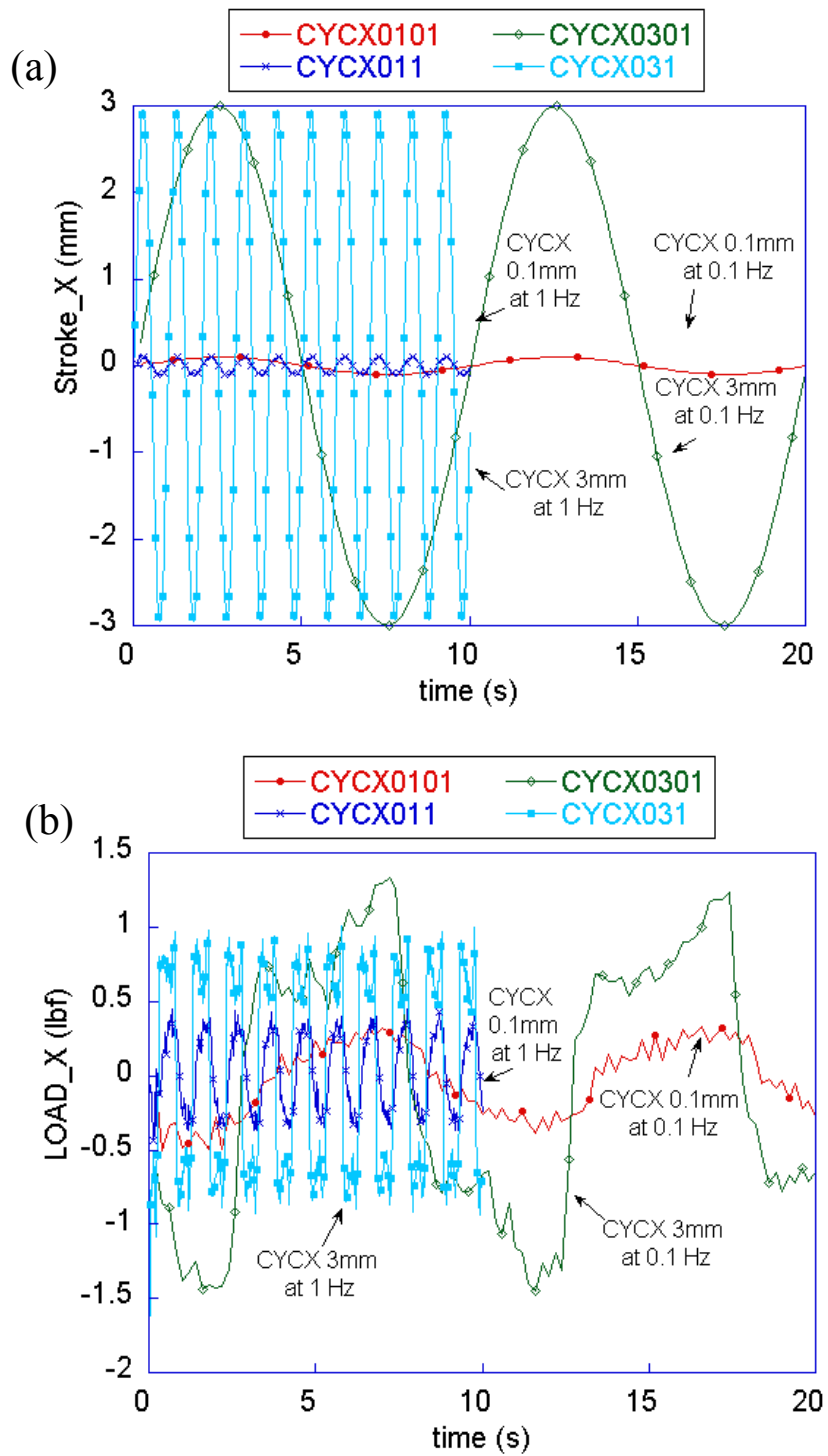


**Fig. 4.2.** (a) Stroke and (b) frictional resistance for cyclic tests in the x-direction at frequencies of 0.1 Hz and 1 Hz.

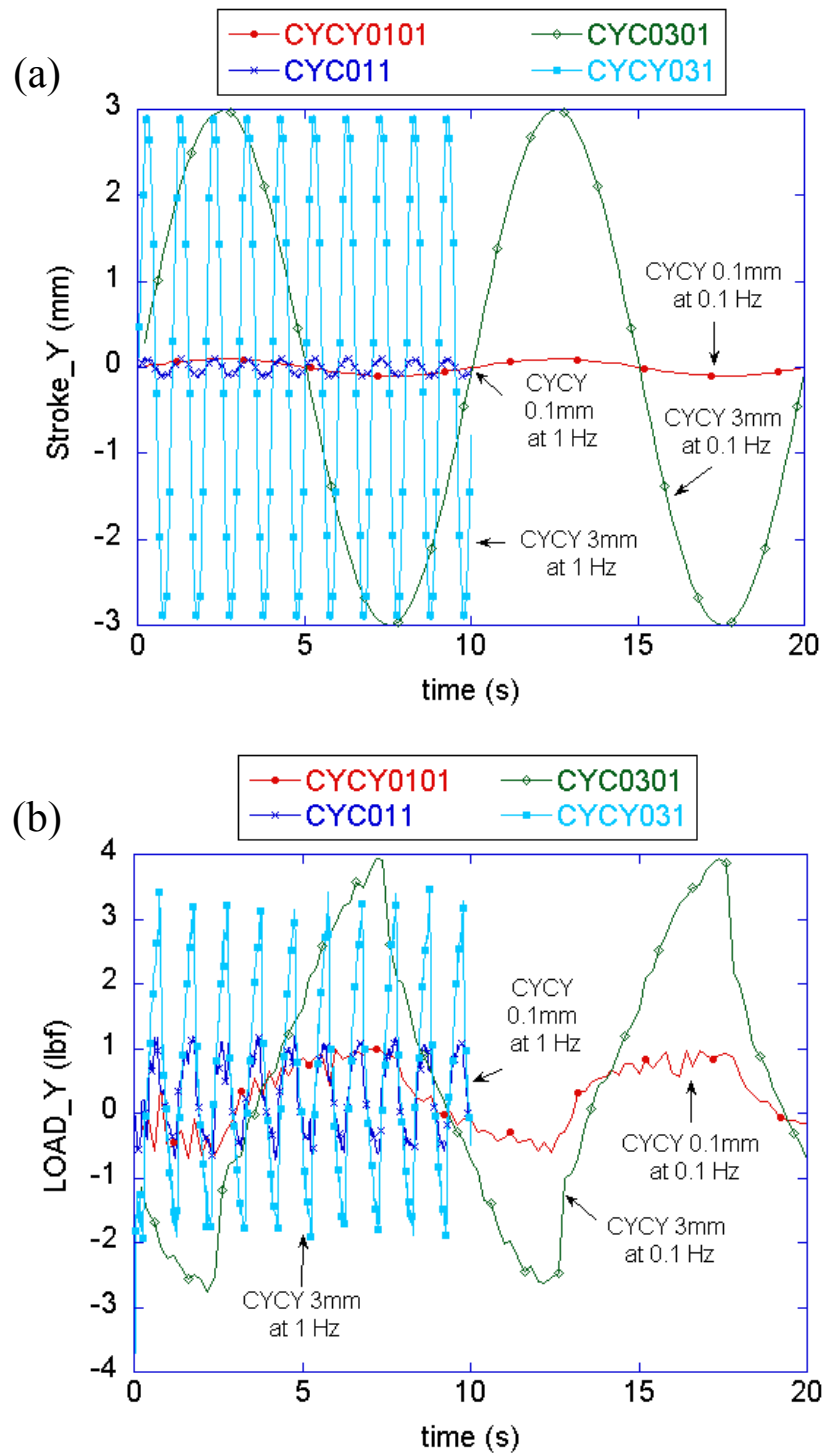


**Fig. 4.3.** (a) Stroke and (b) frictional resistance for cyclic tests in the y-direction at frequencies of 0.1 Hz and 1 Hz.

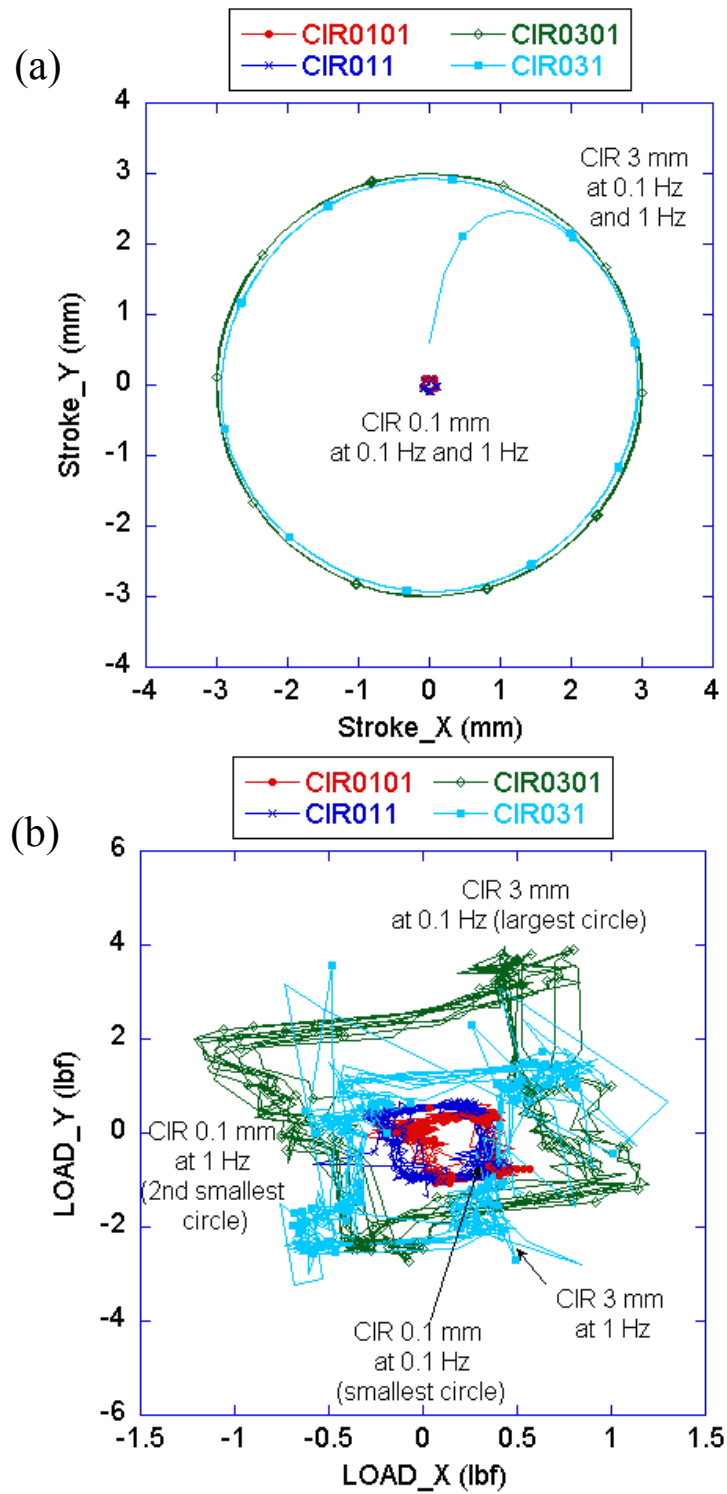


**Fig. 4.4.** (a) Stroke and (b) frictional resistance for circular tests at frequencies of 0.1 Hz and 1 Hz.

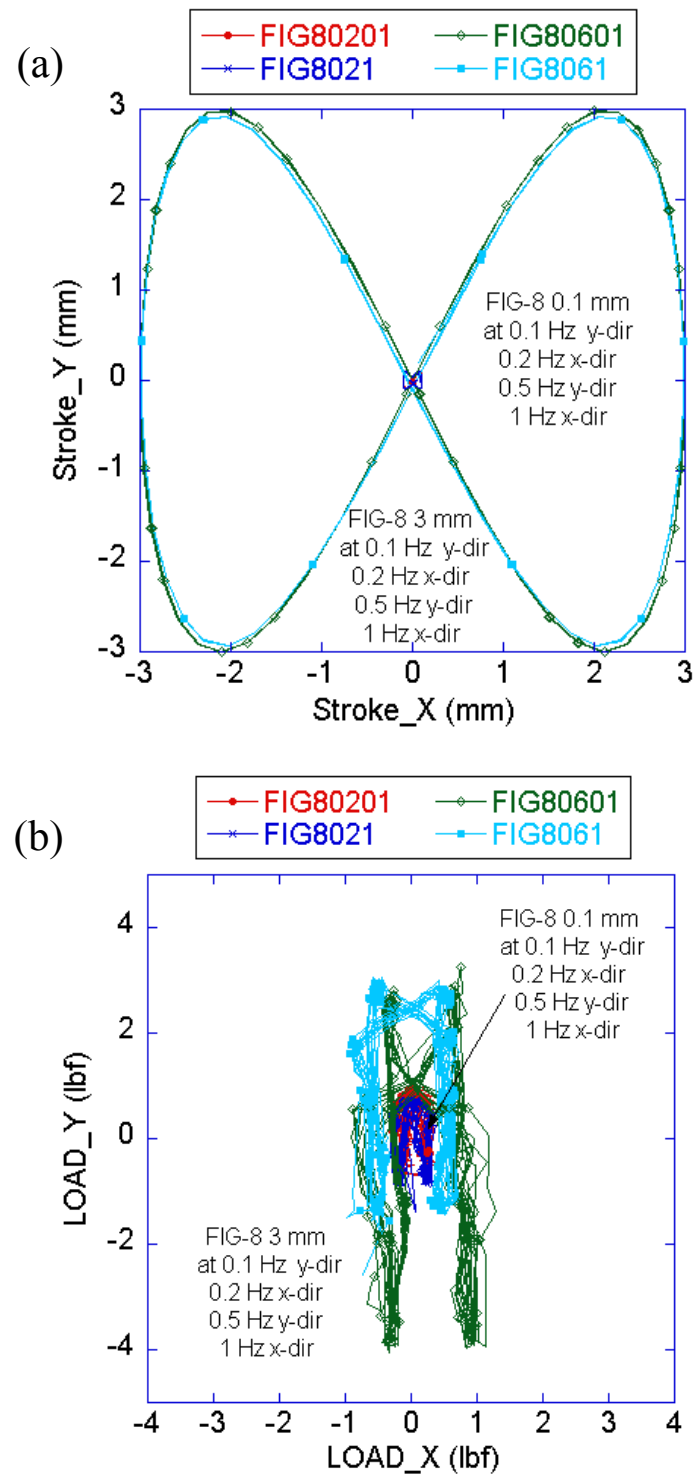


**Fig. 4.5.** (a) Stroke and (b) frictional resistance for figure-8 tests at frequencies of 0.2 Hz and 1 Hz in x-direction.

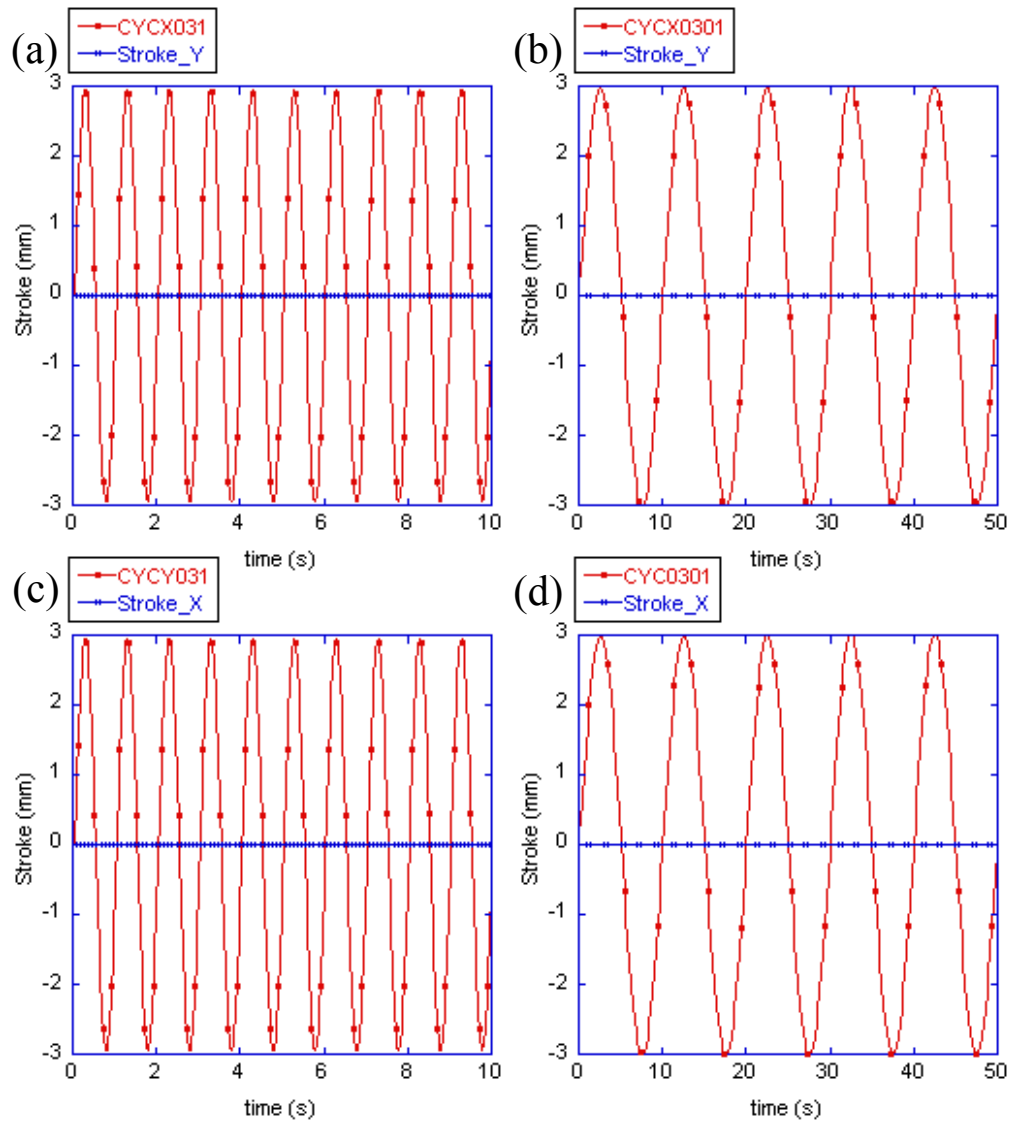


Table 4.1 summarizes the measured forces due to friction for each axis and type of table test. Lubrication prior to each test minimizes the magnitude of friction along the track bearings. The magnitude of the frictional resistance is important for the stress-controlled tests in which the horizontal table load cells measure the feedback for the control loop. However, the shear response of the sample is also measured by the multi-directional load cell installed directly above the sample.

Once each axis had been tested individually, cross-coupling effects were examined by providing a harmonic command signal to one of the tables while recording the movement of the stationary table. Cross coupling would be indicated if there is a significant movement of the stationary table when the other table is moving at different strain amplitudes and frequencies. A sine wave of strain amplitudes 0.1 mm and 3 mm at frequencies of 0.1 Hz and 1 Hz was applied to each axis. As shown in Figure 4.6, for each case, negligible movement of the stationary table was measured indicating limited cross-coupling between the horizontal tables during cyclic loading.

**Table 4.1.** Summary of table tests for frictional resistance.

No.	Test	Stroke (mm)	Rate	Max. force due to friction x-direction (lbf)	Max. force due to friction y-direction (lbf)
1	MONO	3	5%/hr or 1 mm/hr	4	4
2	MONO	3	-5%/hr or -1 mm/hr	4	4
3	MONO	3	50%/hr or 10 mm/hr	5	5
4	MONO	3	-50%/hr or -10 mm/hr	5	5
5	CYC	0.1	0.1 Hz	0.5	1.5
6	CYC	3	0.1 Hz	1.5	4
7	CYC	0.1	1 Hz	0.5	1.5
8	CYC	3	1 Hz	1	3
9	CIRR	0.1	0.1 Hz	1	1
10	CIRR	3	0.1 Hz	1	3
11	CIRR	0.1	1 Hz	0.5	0.5
12	CIRR	3	1 Hz	0.5	1
13	FIG8	0.2 x-dir 0.1 y-dir	0.2 Hz x-dir/ 0.1 Hz y-dir	0.5	1
14	FIG8	6 x-dir 3 y-dir	1 Hz x-dir/ 0.5 Hz y-dir	1	4
15	FIG8	0.2 x-dir 0.1 y-dir	0.2 Hz x-dir/ 0.1 Hz y-dir	0.5	1
16	FIG8	6 x-dir 3 y-dir	1 Hz x-dir/ 0.5 Hz y-dir	1	3



**Fig. 4.6.** Cross-coupling of horizontal tables in (a) x-direction at 1 Hz, (b) x-direction at 0.1Hz, (c) y-direction at 1 Hz, and (d) y-direction at 0.1 Hz.

## 4.2 Constant Stress Testing of Vertical and Horizontal Loads

To ensure the TAMU-MDSS could maintain constant stress in the vertical and horizontal loads, an elastic rubber sample (Figure 4.7) was subjected to each of the following: 1) a vertical load of 0.444kN (100 lbf) over 12 hours, 2) a vertical load of 0.444 kN (100 lbf) and a horizontal load in the x-direction of 0.089 kN (20 lbf) for 12 hours, and 3) a vertical load of 0.444 kN (100 lbf) and a horizontal load in the y-direction of 0.089 kN (20 lbf) for 12 hours. The results of each test are plotted in Figures 4.8 and 4.9. As shown in the plots, the vertical load fluctuates approximately 0.013 kN (3 lbf) during horizontal loading in the x and y-directions. The horizontal load fluctuates approximately 0.002 kN (0.4 lbf) in the x-direction and 0.004 kN (1 lbf) in the y-direction. These fluctuations may be due to the inherent behavior of the rubber sample to vertical and horizontal loading and not the system controls.

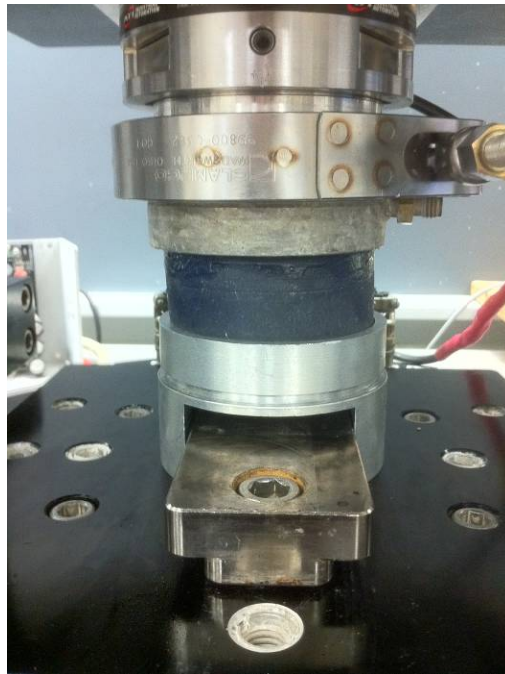


**Fig. 4.7.** Rubber sample installed in TAMU-MDSS.

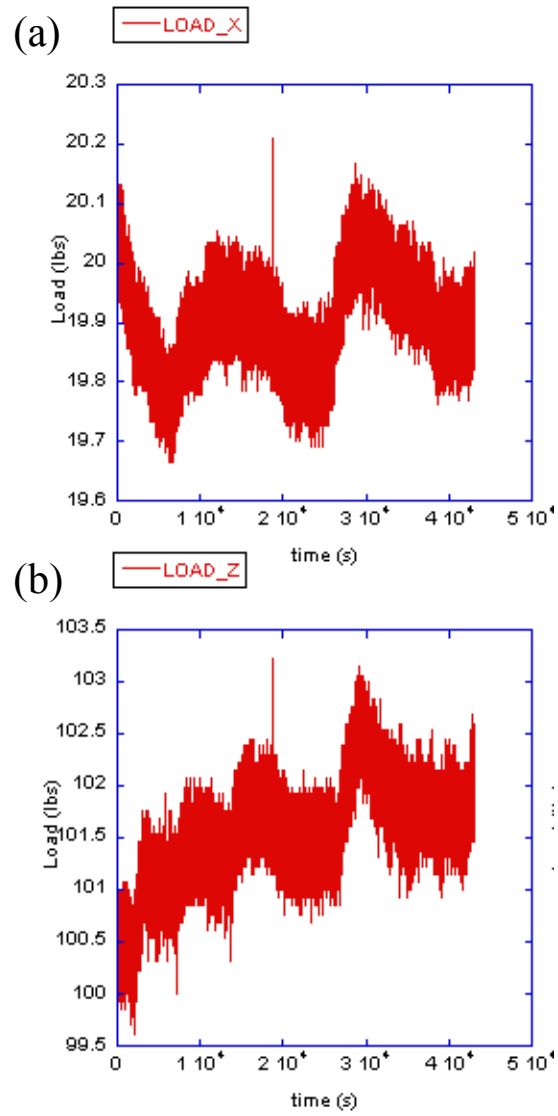


**Fig. 4.8.** (a) Horizontal load in x-direction, (b) vertical load in during x-direction constant test.

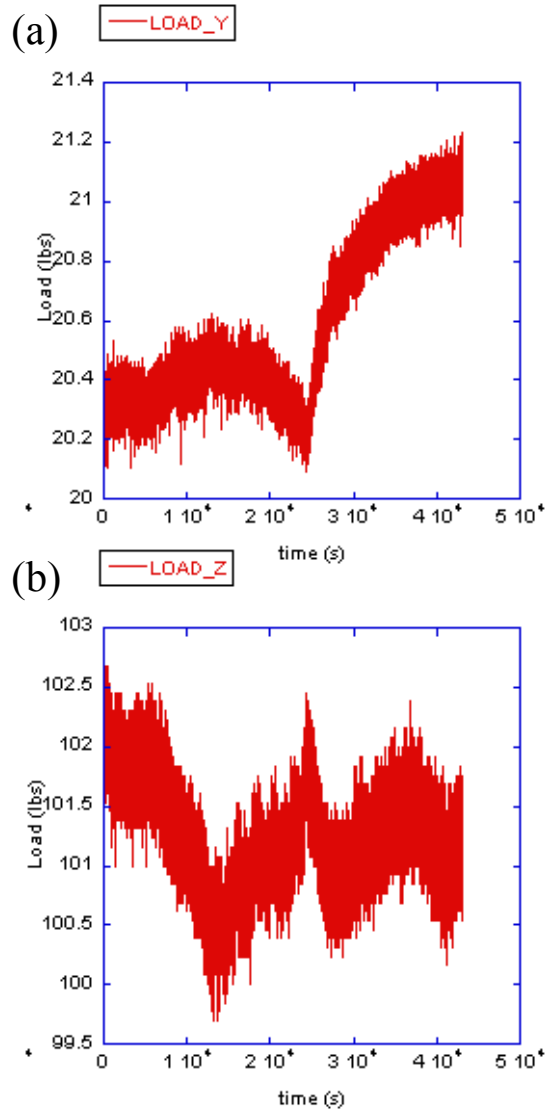


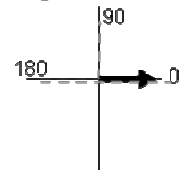
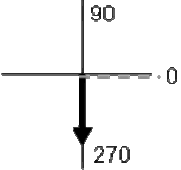
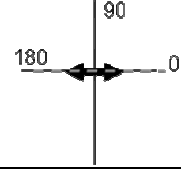
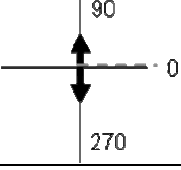
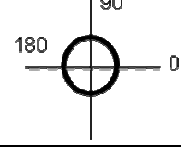
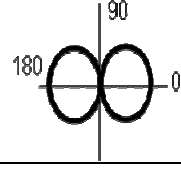
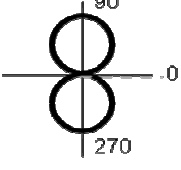
**Fig. 4.9.** (a) Horizontal load in y-direction, (b) vertical load during y-direction constant load test.

### 4.3 TAMU-MDSS Loading Path Evaluation

Fifty-eight tests were conducted on a rubber sample to assess the performance of the TAMU-MDSS. The rubber sample was subjected to the same stresses and deformations under which the marine clay specimens were tested in the experimental plan. Table 4.2 gives a summary of the tests conducted in the TAMU-MDSS on a rubber sample. In all the tests, the rubber sample was subjected to a vertical load of 0.444 kN (100 lbf). For  $CK_{\alpha}$  type tests, a horizontal load of 0.089 kN (20 lbf) was applied. The angle,  $\theta$ , is the angle between the positive x-axis and the direction of the applied horizontal consolidation shear stress. Shearing for each case occurred at an angle,  $\delta$ , which is the angle between the consolidation shear stress and the direction of shearing. Twenty-nine tests were at the same rate used for the clay samples. The loading path capabilities are shown in Table 4.2. Additional tests were performed at different rates to evaluate the device at higher monotonic rates and cyclic frequencies. Eight monotonic tests were carried out at a rate of 50%/hr and twenty cyclic and multi-directional tests were conducted at a frequency of 1 Hz.

The monotonic tests were conducted to simulate both  $CK_0$  and  $CK_{\alpha}$  consolidation and subsequent shearing in each direction indicated by  $\delta$  in Table 4.2. In  $CK_0$  consolidation of the clay specimens only a vertical load is applied, while  $CK_{\alpha}$  consolidation also requires a horizontal load (as indicated by dashed line), in addition to the vertical. In both cases, lateral constraint is applied by the wire-reinforced membrane. During the evaluation with the rubber specimen, no lateral constraint is applied, but the

**Table 4.2.** Summary of rubber testing.

Plan View Test Path	Test Name	Consolidation	$\delta$ (degrees)
1-D linear path x-direction 	MONOXR-1 MONOXR-2 MONOXRa-3 MONOXRa-4 MONOXRa-5	CK <sub>o</sub> CK <sub>o</sub> CK <sub><math>\alpha</math></sub> CK <sub><math>\alpha</math></sub> CK <sub><math>\alpha</math></sub>	- - 0 90 180
1-D linear path y-direction 	MONOYR-6 MONOYRa-7 MONOYRa-8 MONOYRa-9	CK <sub>o</sub> CK <sub><math>\alpha</math></sub> CK <sub><math>\alpha</math></sub> CK <sub><math>\alpha</math></sub>	- 270 0 90
2-D cyclic path x-direction 	CYCXR-10 CYCRa-11 CYCRa-12 CYCRa-13	CK <sub>o</sub> CK <sub><math>\alpha</math></sub> CK <sub><math>\alpha</math></sub> CK <sub><math>\alpha</math></sub>	- 0 90 180
2-D cyclic path y-direction 	CYCYR-14 CYCYRa-15 CYCYRa-16 CYCYRa-17	CK <sub>o</sub> CK <sub><math>\alpha</math></sub> CK <sub><math>\alpha</math></sub> CK <sub><math>\alpha</math></sub>	- 270 90 180
Circular path 	CIRR-18 CIRRa-19 CIRRa-20 CIRRa-21	CK <sub>o</sub> CK <sub><math>\alpha</math></sub> CK <sub><math>\alpha</math></sub> CK <sub><math>\alpha</math></sub>	- 0 90 180
Figure-8 path x-direction 	FIG8XR-22 FIGXRa-23 FIGXRa-24 FIGXRa-25	CK <sub>o</sub> CK <sub><math>\alpha</math></sub> CK <sub><math>\alpha</math></sub> CK <sub><math>\alpha</math></sub>	- 0 90 180
Figure-8 path y-direction 	FIGYR-26 FIGYRa-27 FIGYRa-28 FIGYRa-29	CK <sub>o</sub> CK <sub><math>\alpha</math></sub> CK <sub><math>\alpha</math></sub> CK <sub><math>\alpha</math></sub>	- 270 0 90



loading pattern – vertical load only for  $K_o$  and vertical and horizontal load for  $K_\alpha$  – remains the same. Due to the addition of the horizontal load, there is an initial displacement in the x-direction or y-direction as illustrated in Figures 4.10 and 4.11.

The first two tests (MONOXR-1 and MONOXR-2) were  $CK_o$  type and sheared at a rate of 5%/hr to 3 mm displacement. The tests were compared to determine if the device was able to repeat the same strain controlled test. As shown in Figure 4.9, the plot of the x-stroke with time for each test is the same.  $CK_\alpha$  type tests (MONOXRa-3, MONOXRa-4, MONOXRa-5) were simulated by applying a horizontal shear stress in the positive x-direction ( $\theta = 0^\circ$ ). For monotonic tests, both downhill ( $\delta = 0^\circ$ ), across the slope ( $\delta = 90^\circ$ ), and uphill ( $\delta = 180^\circ$ ) shearing directions were tested.

The following examples are used to illustrate the definitions of shearing downhill, across the slope and uphill. For example, MONOXRa-3 had a horizontal load of 0.089 kN (20 lbf) applied in the x-direction ( $\theta = 0^\circ$ ) and then monotonically sheared in the same direction ( $\delta = 0^\circ$ ), which simulates a downhill monotonic shearing test. For MONOXRa-4, the rubber sample was similarly subjected to a horizontal load of 0.089 kN (20 lbf) in the x-direction ( $\theta = 0^\circ$ ), however, was sheared monotonically in the positive y-direction ( $\delta = 90^\circ$ ) simulating across the slope shearing. As shown in each plot, the x-stroke has a positive offset for  $CK_\alpha$  tests due to the application of a horizontal load in the x-direction.

The tests were repeated at a rate of 50%/hr. MONOXRa-3B was stopped early to prevent overloading to the fine load cell due to the large horizontal load in the x-

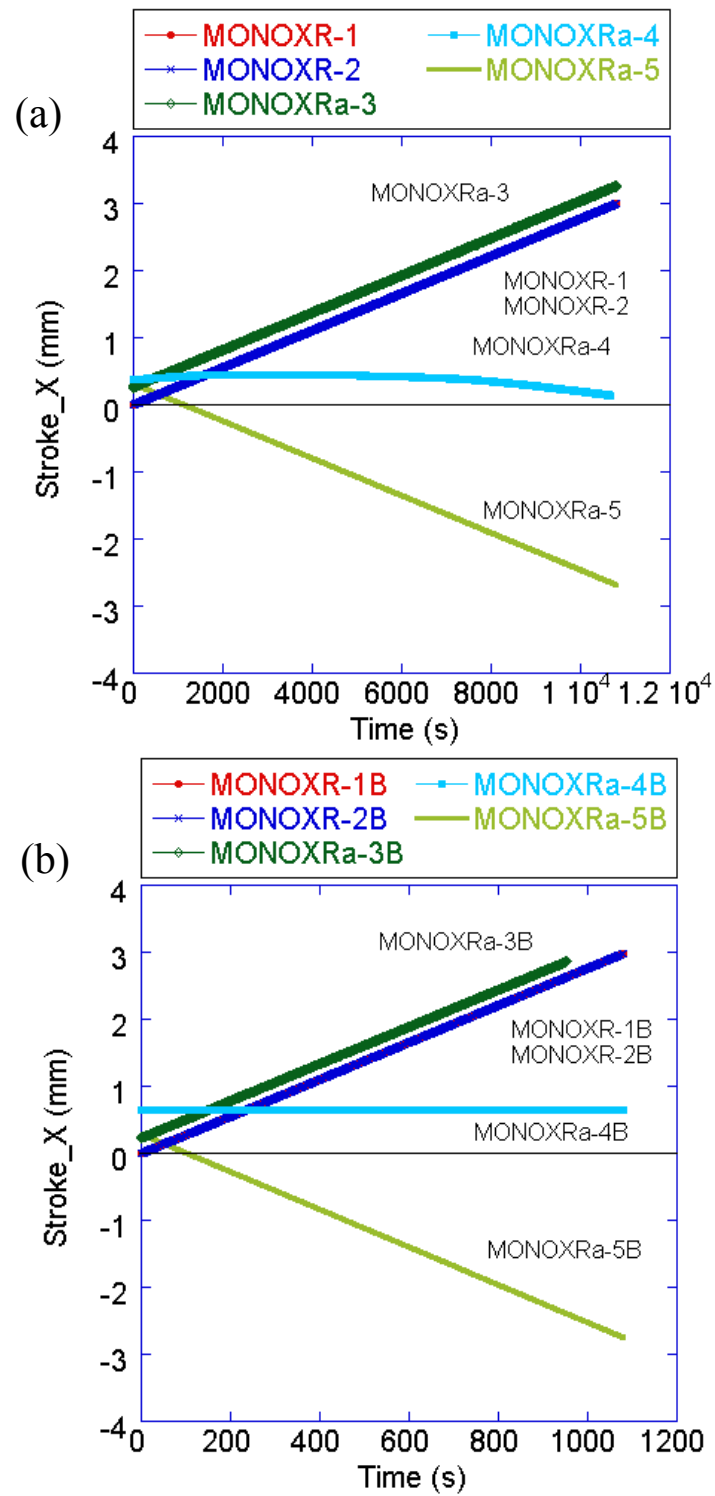


**Fig. 4.10.** Plots of monotonic tests on rubber sample in x-direction at (a) 5%/hr and (b) 50%/hr.

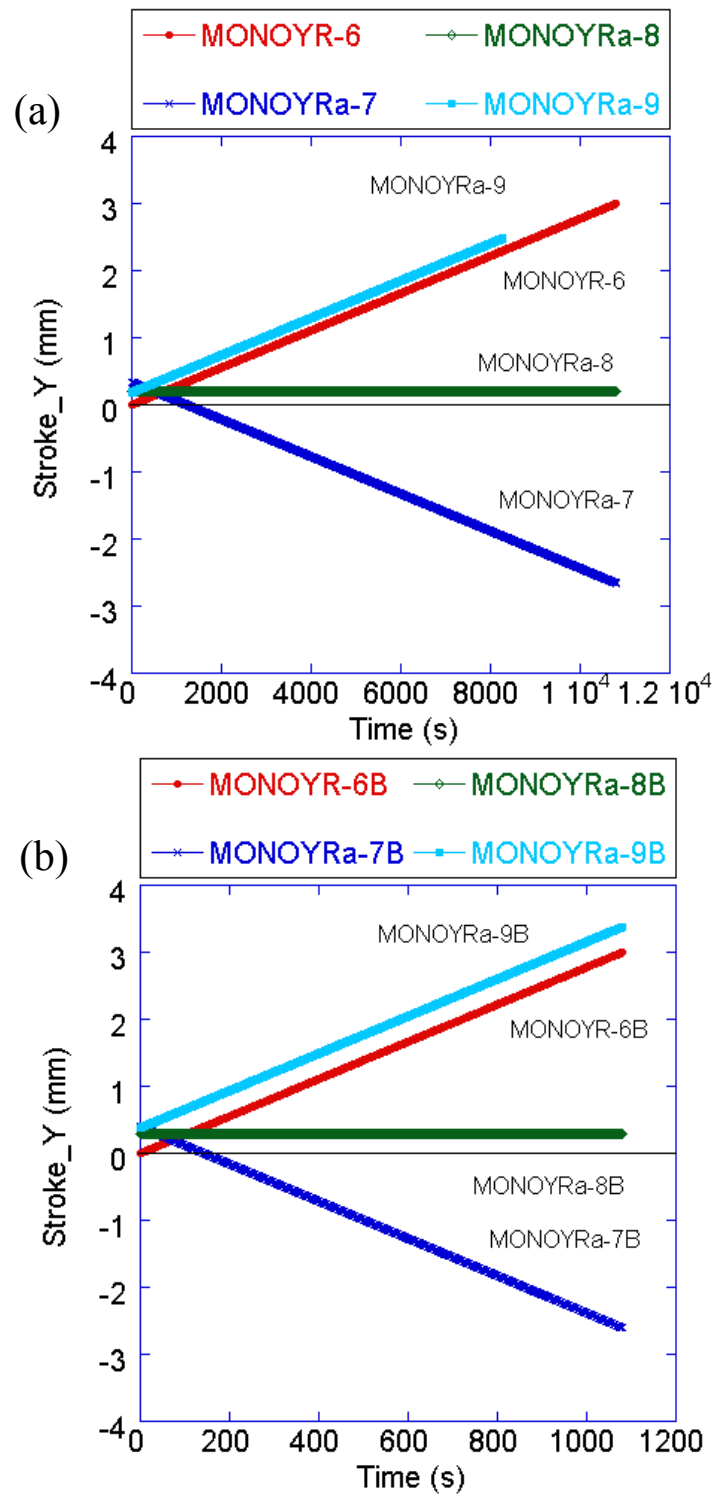


**Fig. 4.11.** Plots of monotonic tests on rubber sample in y-direction at (a) 5%/hr and (b) 50%/hr.

direction. Monotonic tests (MONOY-6, MONOYRa-7, MONOYRa-8, MONOYRa-9) at 5%/hr and 50%/hr were also conducted in the y-direction (Figure 4.10). MONOYRa-9 was stopped early due to large horizontal load in the y-direction. Similar results in both directions indicate that monotonic testing in both directions is equivalent.

An evaluation of each axis using stress-controlled cyclic loading was also conducted with the rubber sample. Cyclic tests at frequencies of 0.1 Hz and 1 Hz were carried out in both directions with a horizontal load of 20 lbf. Both  $CK_o$  and  $CK_\alpha$  type tests were simulated as discussed previously. Comparisons of the results are shown in Figures 4.12 and 4.13. These tests indicate that the TAMU-MDSS is able to conduct stress-controlled tests at various frequencies. The testing software is also able to start the shearing portion of the test with no drift of the load from the consolidation shear stress. This is shown in the tests with  $\delta = 0, 90$  and  $180$  degrees. As indicated in the figures, when shearing is applied in the perpendicular direction ( $\delta = 90^\circ$ ), the load measured in the axis in which the horizontal load is applied remains constant.

Circular and figure-8 stress controlled loading patterns were tested at both 0.1 Hz and 1 Hz. It was critical to evaluate if the device could conduct these complex load patterns for both  $CK_o$  and  $CK_\alpha$  consolidation. Figures 4.14 – 4.16 show the results of the multi-directional shearing patterns. As illustrated in the plots, the higher frequency results have larger noise, which may be due to the inherent material properties of the rubber samples, increased friction between the tables as determined earlier by the frictional resistance testing or less accurate controls at higher frequencies.

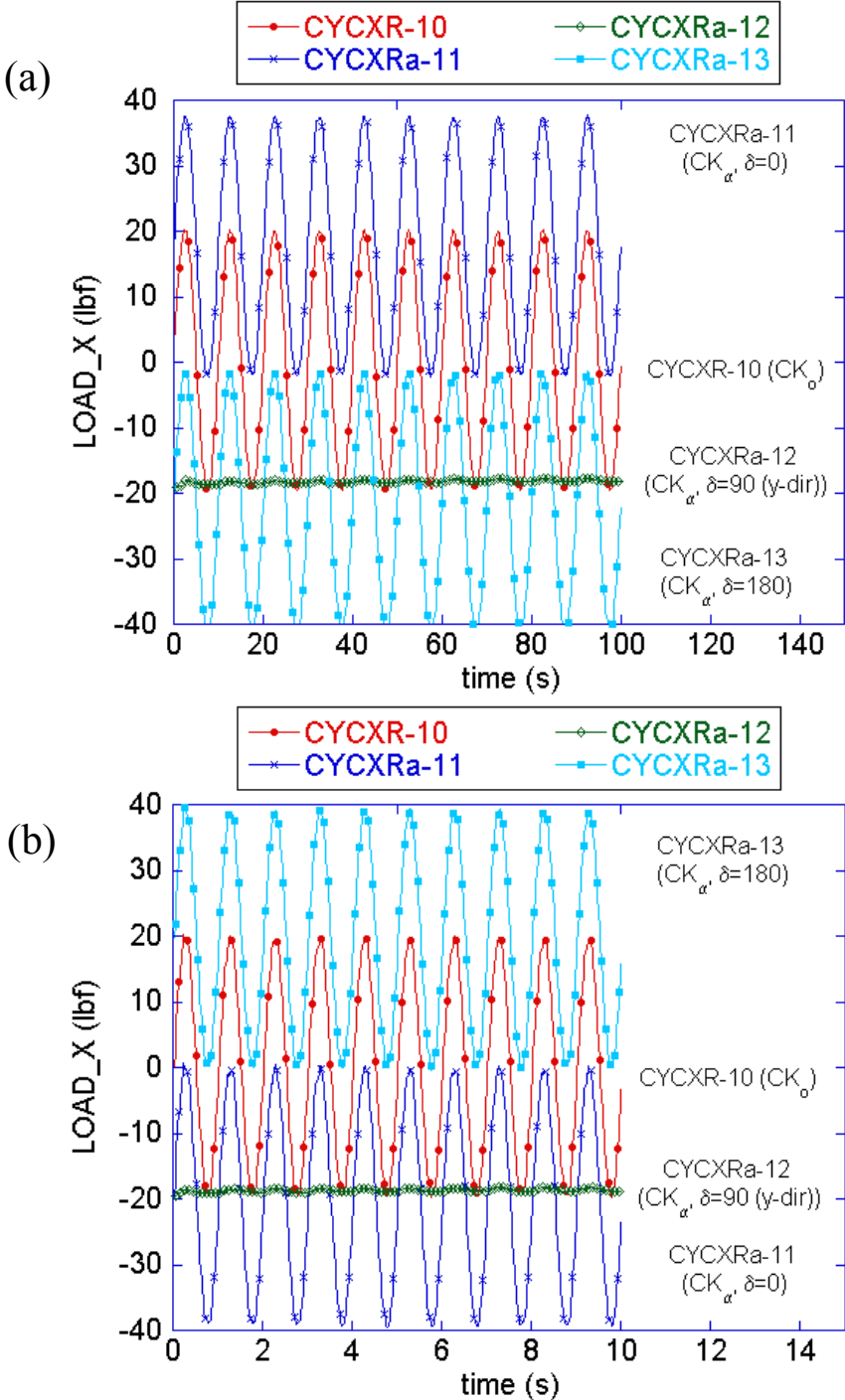


Fig. 4.12. Plots of cyclic tests on rubber sample in x-direction at (a) 0.1 Hz and (b) 1 Hz.

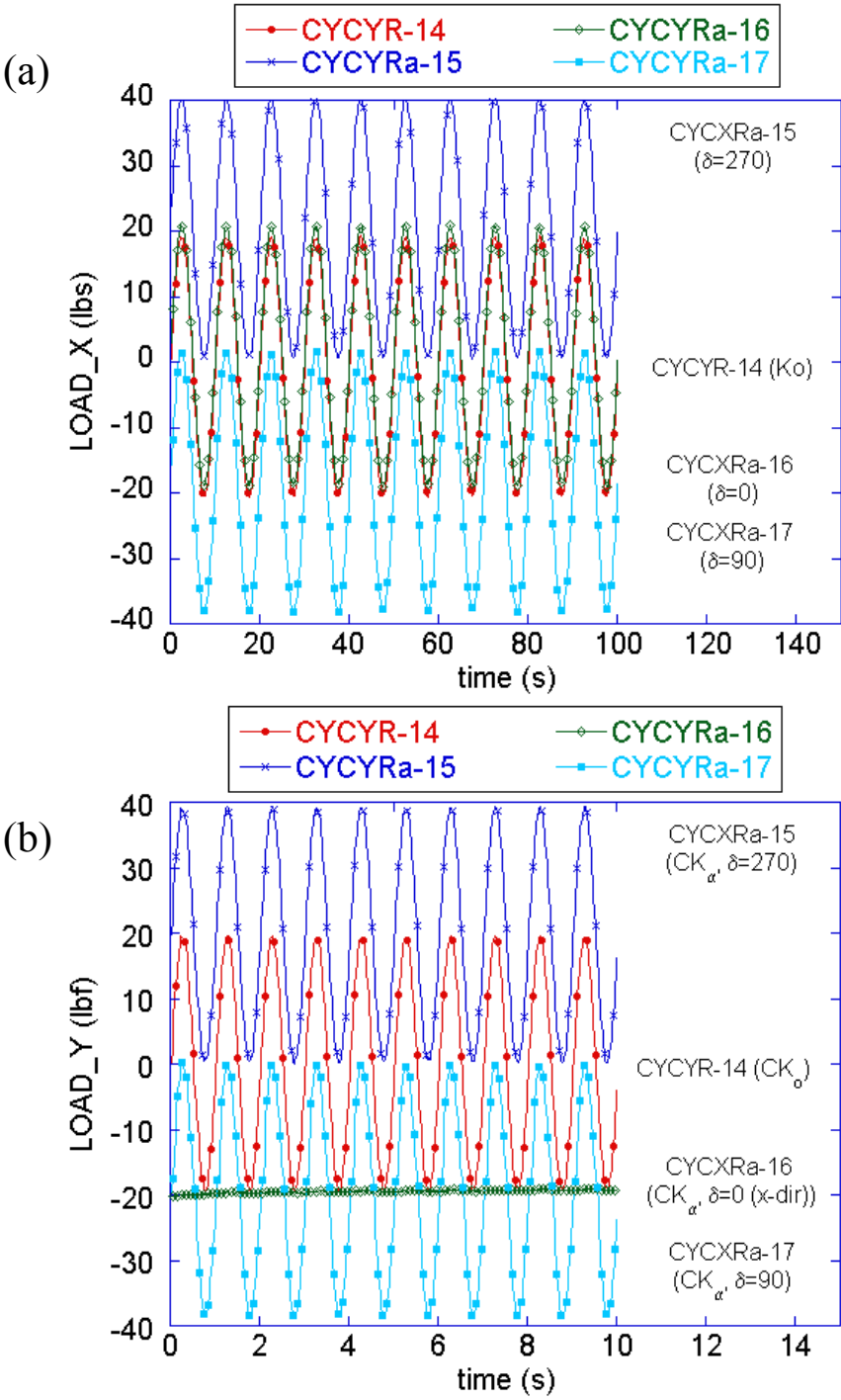
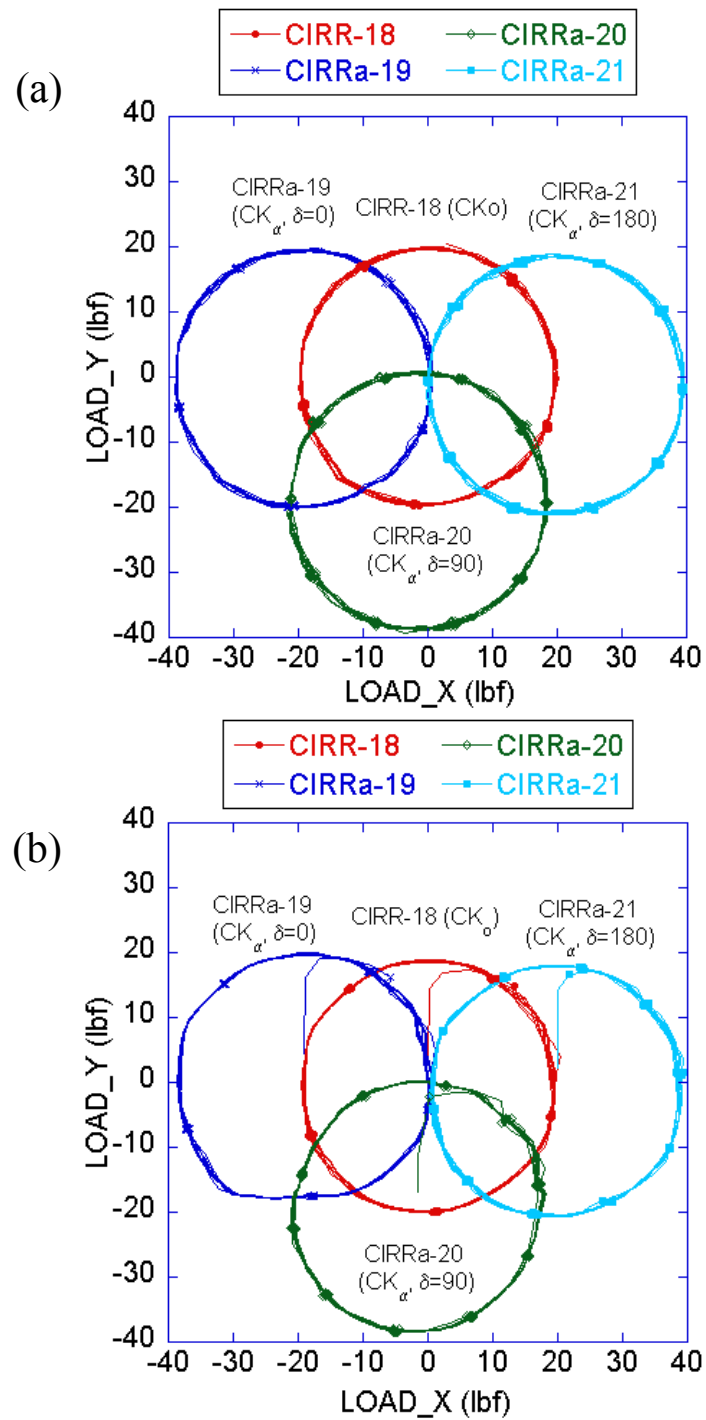
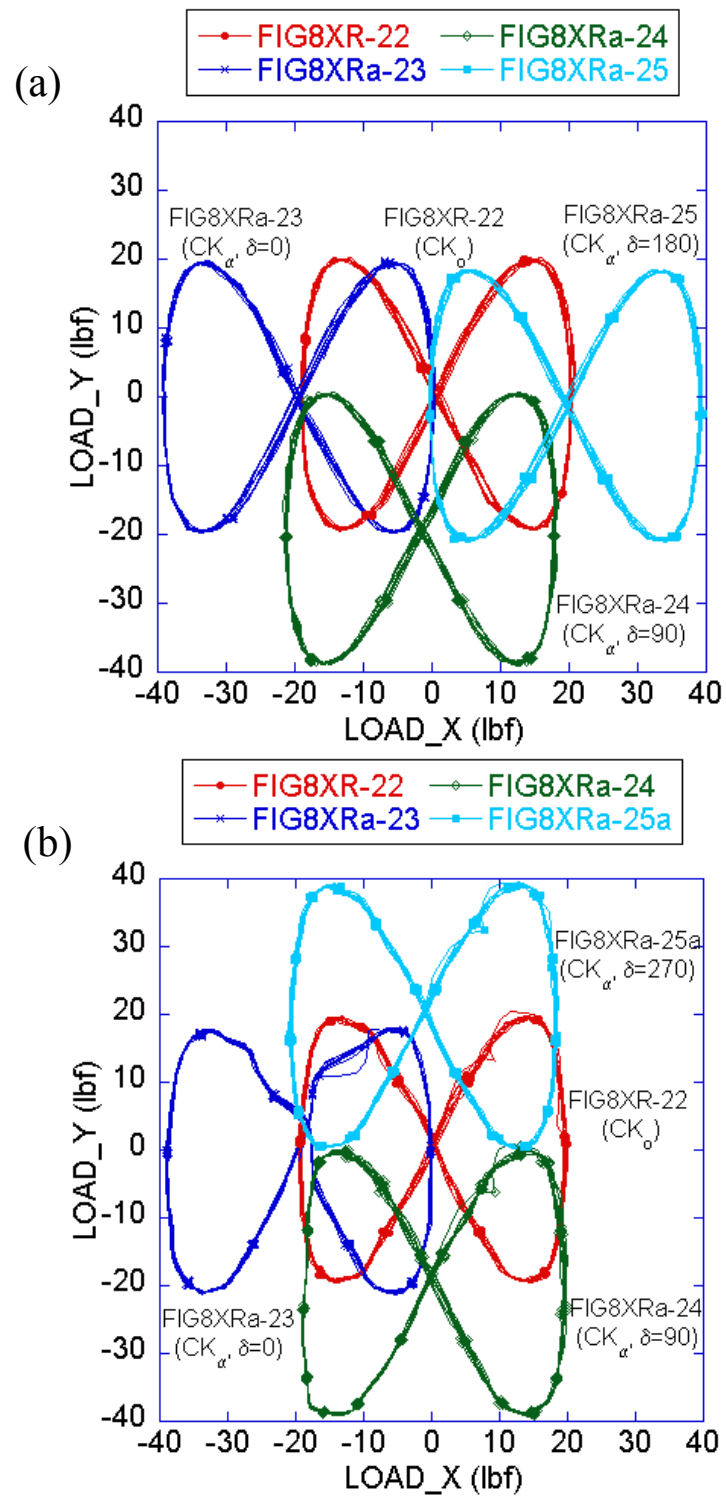


Fig. 4.13. Plots of cyclic tests on rubber sample in y-direction at (a) 0.1 Hz and (b) 1 Hz.



**Fig. 4.14.** Plots of circular tests on rubber sample at (a) 0.1 Hz and (b) 1 Hz.



**Fig. 4.15.** Plots of figure-8 tests on rubber sample in x-direction at (a) 0.1 Hz and (b) 1 Hz.



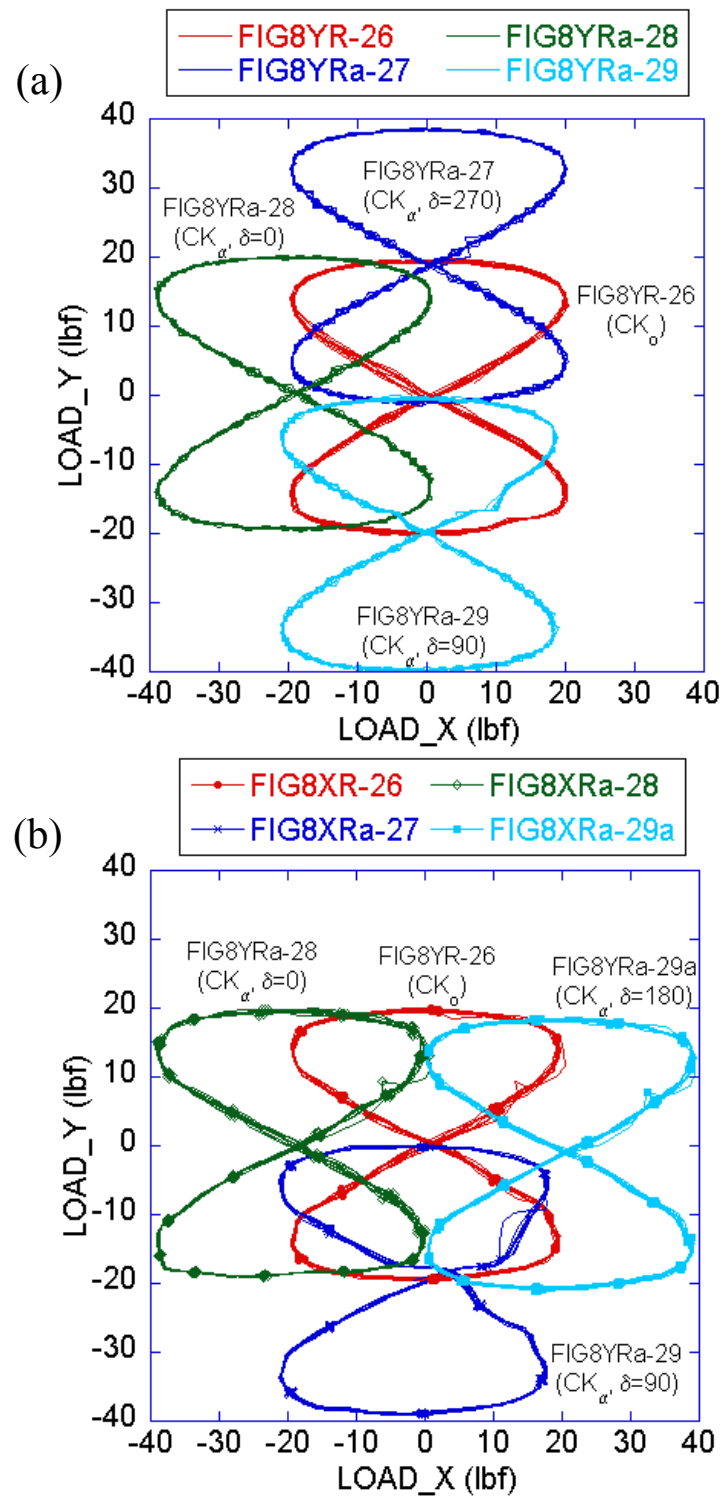


**Fig. 4.16.** Plots of figure-8 tests on rubber sample in y-direction at (a) 0.1 Hz and (b) 1 Hz.

#### **4.4 Comparison of Multi-axis Load Cell and Measurements of Torque**

The multi-axis load cell is installed directed above the sample and measures the forces and torques applied to the sample. The TAMU-MDSS vertical load cell and the multi-axis load cell were directly calibrated to each other through the use of a specially designed aluminum cylinder. The measured torques applied to the top cap can provide insight to the degree of rocking the sample is experiencing. Plots of torque compared to the load applied to the sample over time are presented in Figures 4.17 and 4.18 for the monotonic and cyclic tests. The stiffness of the rubber sample creates a large torque in the opposite direction of the loading. As the horizontal table moves monotonically, a gap is formed between the rubber sample and the sample cap along the trailing edge (Figure 4.19). The rubber sample also tilts during loading in the perpendicular direction as illustrated in the plots by the increase of torque in the perpendicular axes. Some slight rotation occurs shown by the small change in torque in the z-direction. Similar results are shown in Figure 4.20 and Figure 4.21 for circular and figure-8 tests.

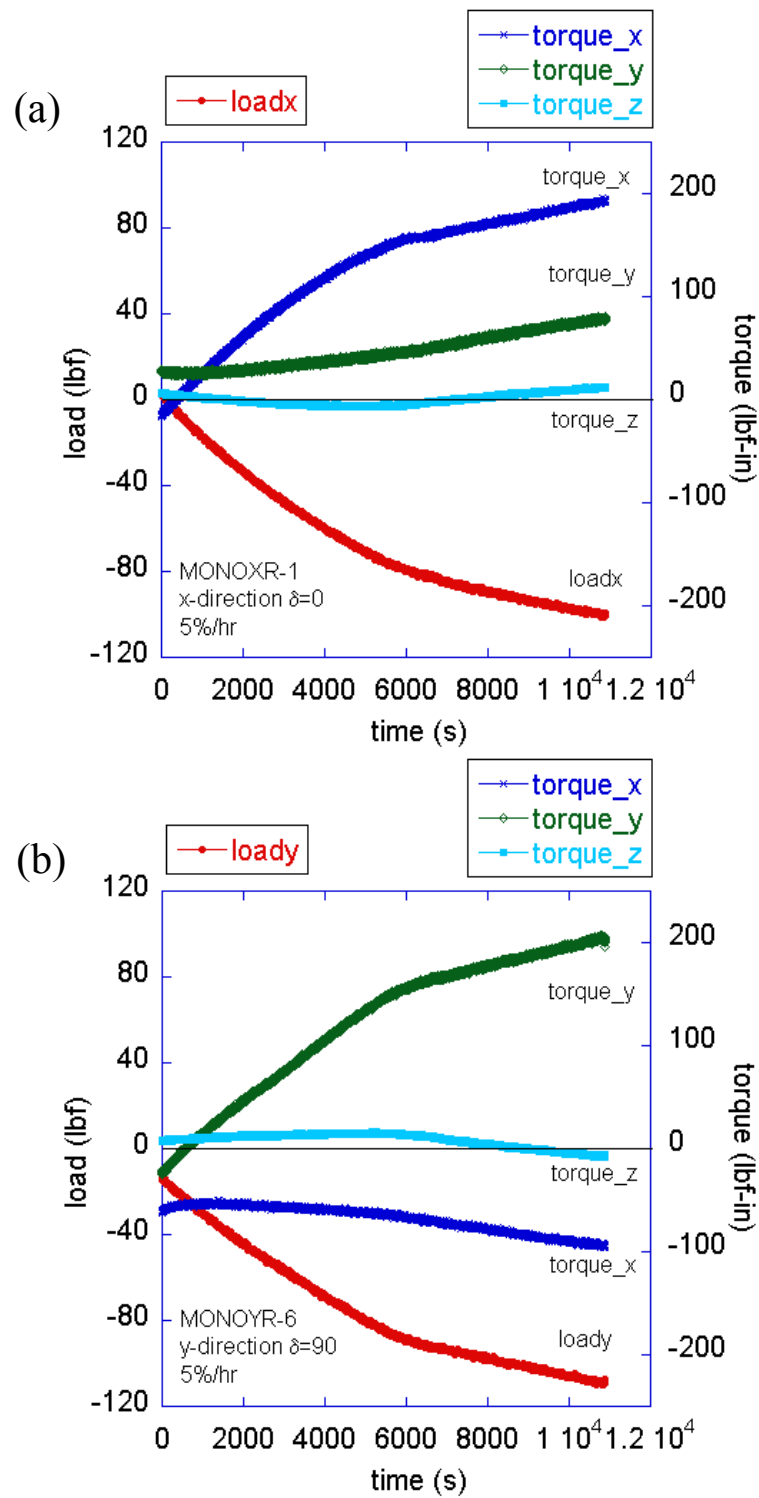


**Fig. 4.17.** Torque measurements for monotonic tests in (a) x-direction and (b) y-direction.

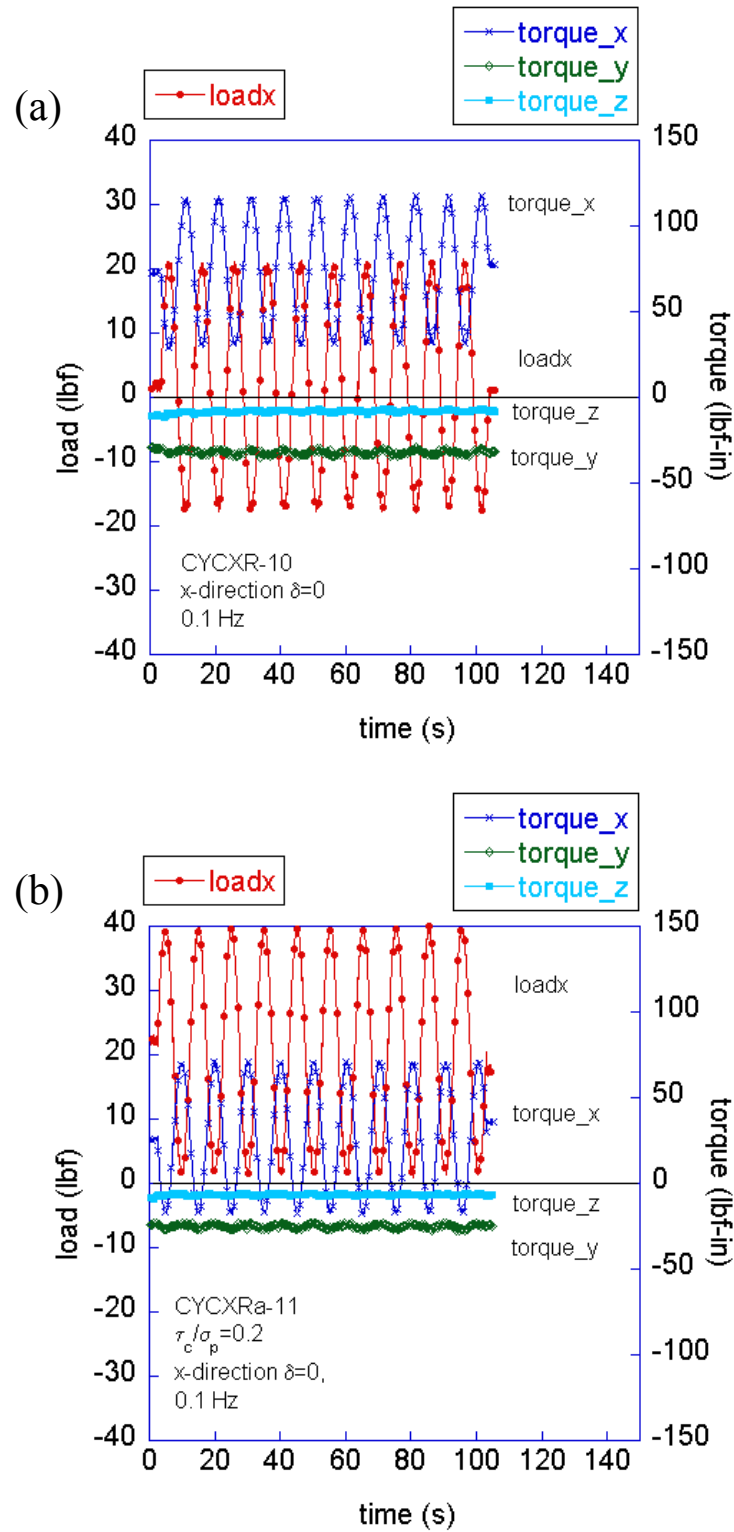


**Fig. 4.18.** Torque measurements for (a)  $CK_0$  and (b)  $CK_\alpha$  cyclic tests in x-direction.

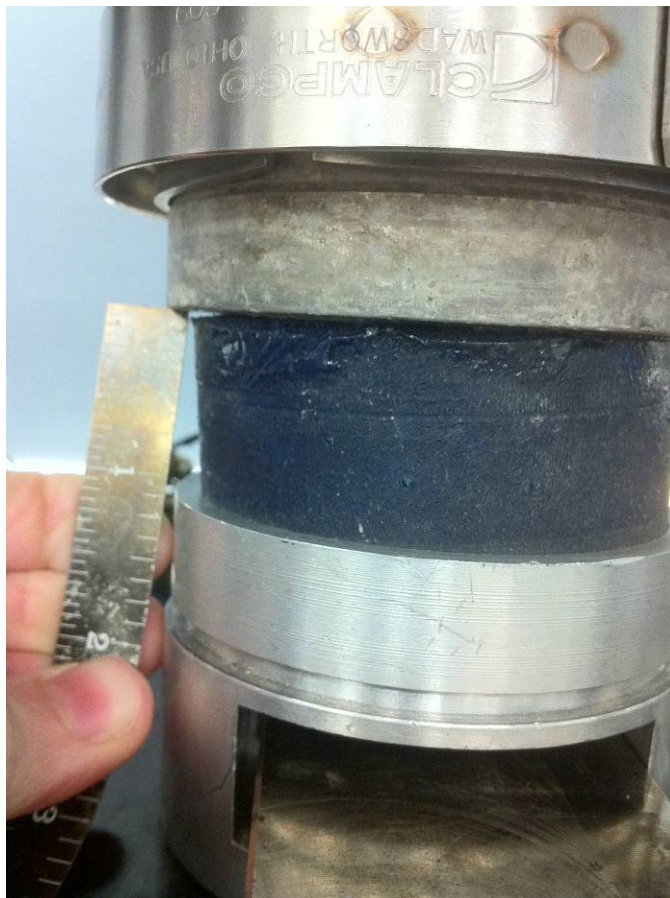


**Fig. 4.19.** Gap formed between cap and rubber sample.

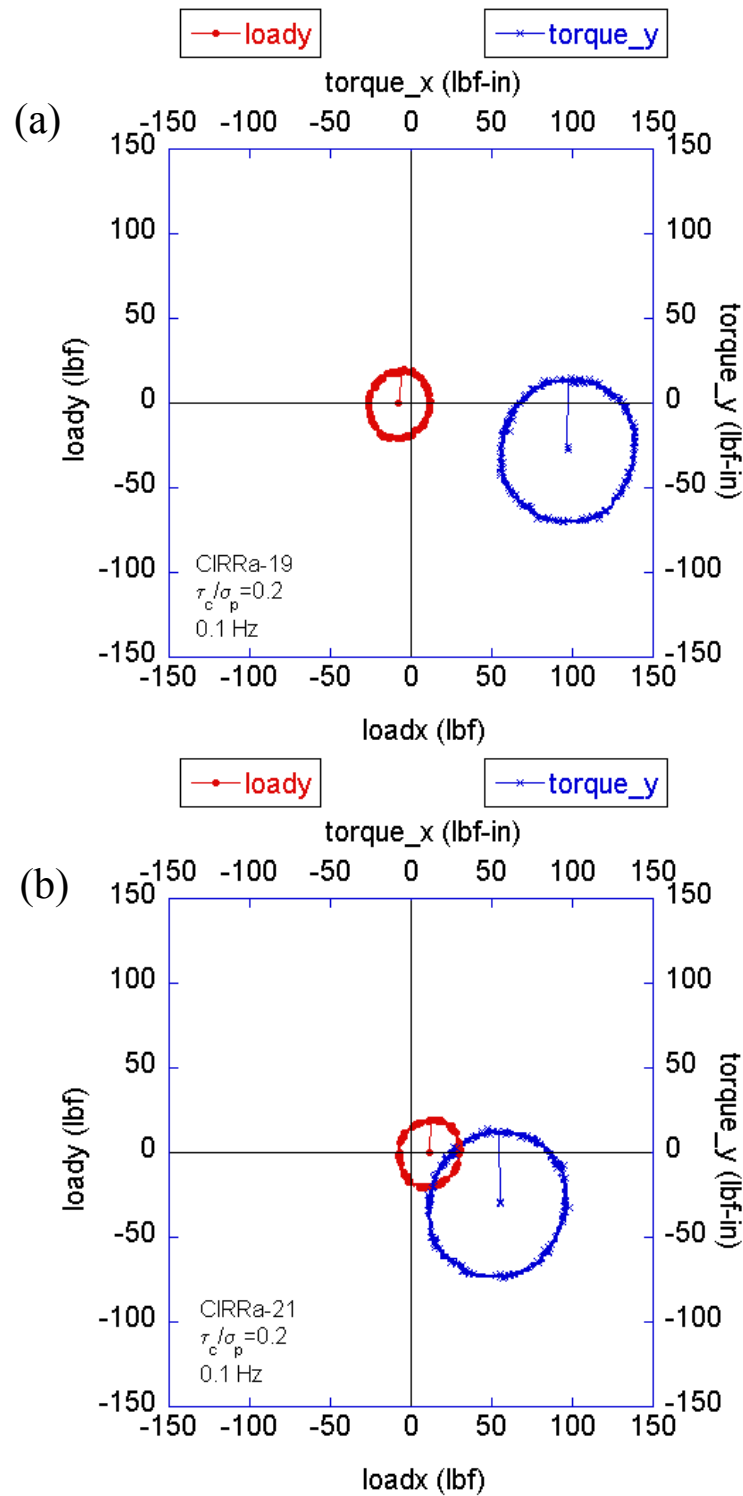


**Fig. 4.20.** Torque measurements for circular tests (a)  $CK_\alpha$  horizontal load in positive x-direction and (b)  $CK_\alpha$  horizontal load in negative x-direction and positive y-direction.

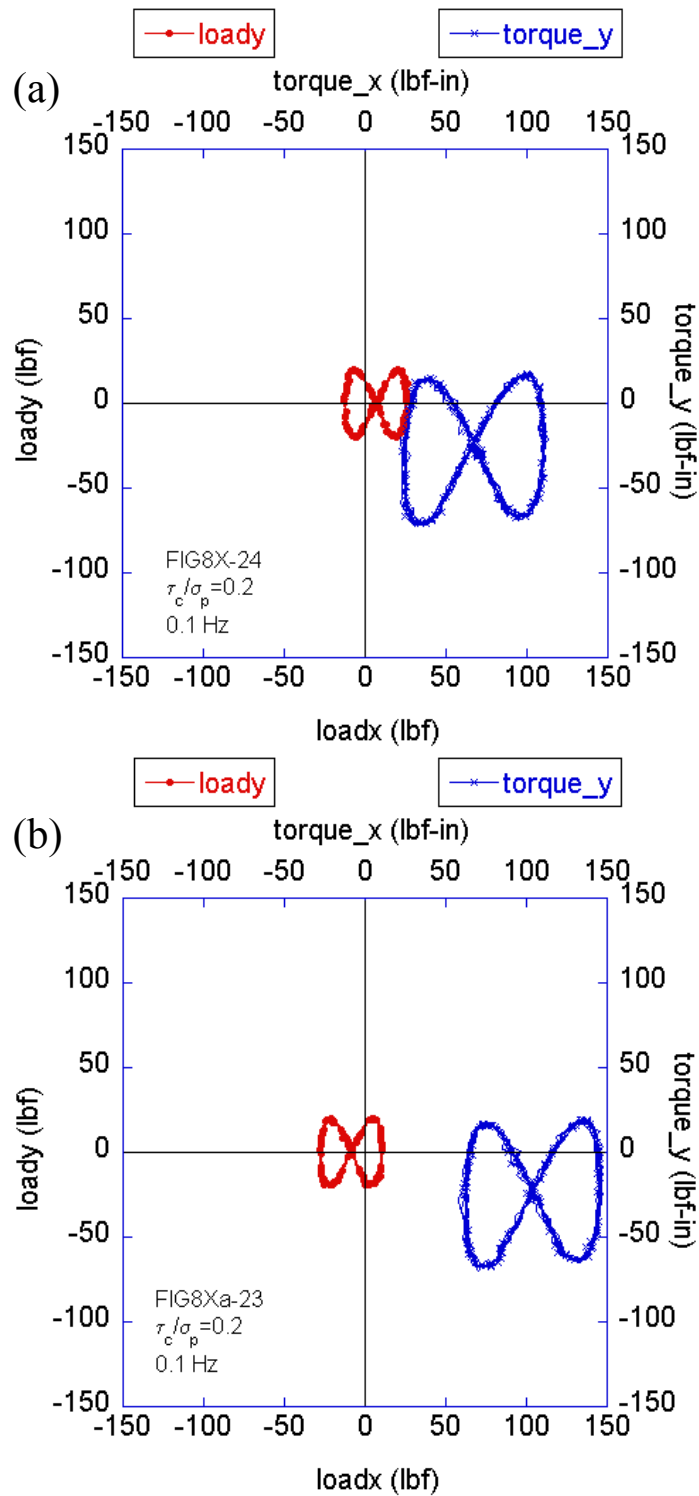


**Fig. 4.21.** Torque measurements for figure-8 tests (a)  $CK_\alpha$  horizontal load in positive x-direction and (b)  $CK_\alpha$  horizontal load in negative x-direction.

#### **4.5 Evaluation of the Backpressure System and Chamber**

Tests were conducted to evaluate possible leakage through valves, line connections and the connection through the chamber. The first test accessed the backpressure system and sample drainage lines. The sample water lines were capped creating a closed system. A pressure of 20 psi was applied through the backpressure system. The valve to the volume pipette was closed to prevent drainage and the change in pressure over time was recorded. The system has a small change in pressure over time, however, with constant application of backpressure to the volume pipette minimal pressure change occurs.

The second tests evaluated the chamber and cell pressure regulator system. A constant chamber pressure was maintained for 36 hours at a pressure of 20 psi to determine the amount of cell pressure dissipation over time. The chamber maintains a constant pressure and does not leak. A third tests was conducted to evaluate the time it takes the chamber to fill to the same pressure set by the regulator. The backpressure regulator was fully open and set to zero psi. The cell pressure was increased by 5 psi every 5 minutes. The chamber pressure was recorded by the cell pressure transducer over the duration of the test. As indicated in Figure 4.22, there is a lag between application of the cell pressure and the measurement of the chamber pressure by the pressure transducer installed in the top of the chamber. However, with small incremental chamber pressure increases during back saturation, the lag does not directly affect the specimen.



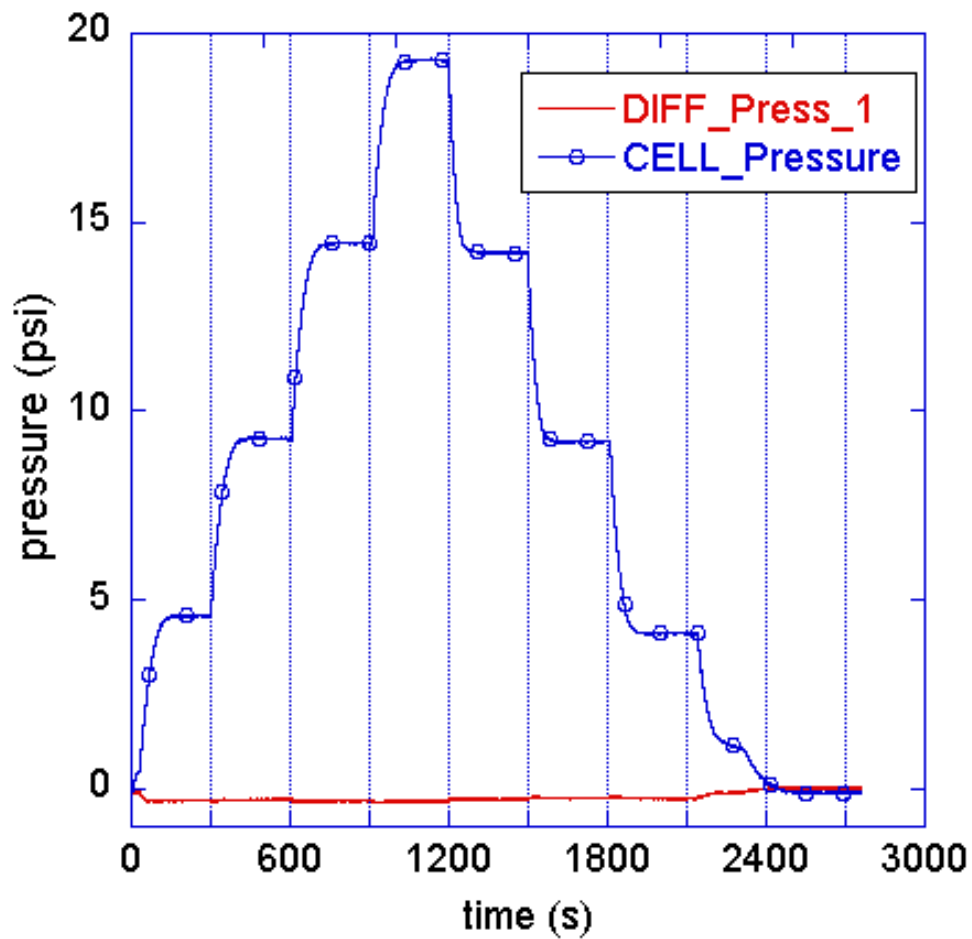


**Fig. 4.22.** Chamber pressure lag time.

#### 4.6 Conclusions

An experimental evaluation of the TAMU-MDSS was conducted to determine the full capabilities and limitations of the device. Strain-controlled tests were used to determine the force due to friction between the horizontal tables. It was determined that the friction depended on both rate and direction. A majority of the experimental plan tests for Gulf of Mexico marine clays will be conducted in the x-direction since this axis had a lower amount of friction in comparison with the y-direction.

Rubber sample tests were used to verify the TAMU-MDSS testing software and device were able to apply both strain and stress-controlled monotonic, cyclic, circular and figure-8 test patterns. The device is capable of performing tests at various frequencies, however, it shows evidence of increased noise either due to friction or control issues at higher frequencies. Therefore, the initial cyclic and multi-directional tests will be performed at a frequency of 0.1 Hz. Forces and torque measurements from the multi-axis load cell showed the rubber sample tilted and rotated during shearing, however, this may be due to the material properties of the rubber sample. The influence of tilt and twist was studied when conducting the Gulf of Mexico marine clay tests (Section 6).

Finally, the backpressure system was shown to be capable of maintaining pressure during the duration of the test. Some fluctuations from the house pressure can be an issue for maintaining the chamber and backpressure higher than 20 psi, however, at 20 psi, the fluctuations are minimal.

## 5. GULF OF MEXICO CLAYS

This section presents the sampling and results from basic and advanced characterizations of the Gulf of Mexico marine clay samples. Geotechnical engineering properties are of critical importance for the analysis and design of seafloor processes and operations such as evaluation of slope stability and the design of anchors and foundations. One of the primary challenges in studying submarine landslides is the lack of information about the properties of these soils in situ. Because offshore soil sampling is expensive, published experimental information on marine clays from offshore is limited. Most marine clay testing in the research literature is conducted on marine deposits that are now onshore and easily accessible such as Boston Blue Clay (BBC) and San Francisco Young Bay Mud (YBM). However, due to the depositional environment and mechanisms, the stress history for these samples differs from that of offshore marine sediments.

Marine clays on the continental shelf and slope differ from traditionally tested fine grained sediments in three important aspects: depositional environment, depositional mechanisms, and stress history. Because the structure of the deposits and the mechanical response to loading can be influenced by these factors, the samples used in the experimental plan are undisturbed marine soils. However, not only is collecting offshore samples expensive and requires specialized equipment, high quality undisturbed samples require great expertise.

## 5.1 Sampling of Gulf of Mexico Clay

The Gulf of Mexico samples were collected in and around the Green Canyon near the Sigsbee Escarpment in October 2007 on the Research Vessel Brooks-McCall operated by TDI-Brooks International (Figure 5.1). The 100 mm (4 in) diameter cores were taken using the jumbo piston core system at approximately 1000-1300 meters of water depth. Approximately 30 sites were sampled on varying degrees of slope.



**Fig. 5.1.** R/V Brooks McCall.

A jumbo piston corer uses the "free fall" of the coring rig to achieve a greater initial force on impact than gravity coring (Figure 5.2). A sliding piston inside the core barrel is used to reduce inside wall friction with the sediment and to assist in the evacuation of displaced water from the top of the core. TDI-BI vessels are equipped with 30 meter 4" Jumbo Piston cores (JPC) that can be collected at depths in excess of 4,000 meters. The JPC utilizes a cantilevered deployment platform over the stern of the vessel

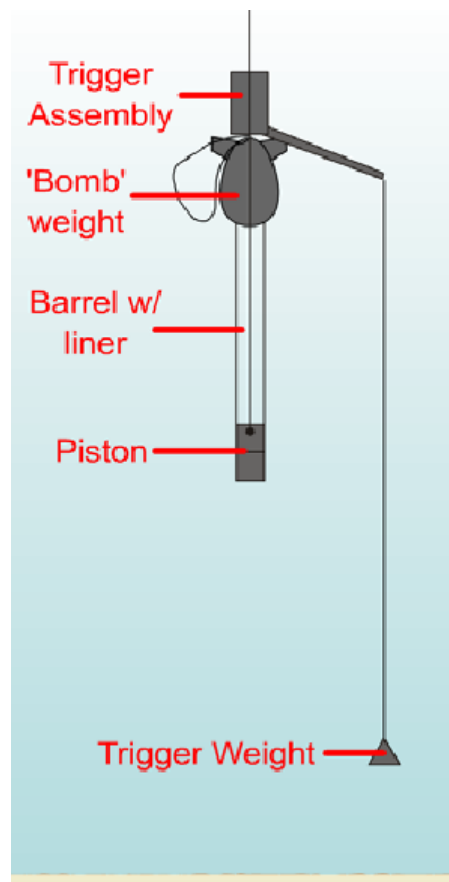


**Fig. 5.2.** TDI-Brooks International jumbo piston coring system (After [www.tdi-bi.com](http://www.tdi-bi.com)).

with a rail and capture bucket assembly placed on the deck of the vessel directly beneath the stern A-frame (Figure 5.3). The JPC consists of a 4,000  $\text{lb}_f$  weight stand, a 4" core barrel, a mechanical trigger, standard schedule 40 PVC liner, a cutting shoe, and a foil core catcher.

The cores were cut into 1 meter long sections, labeled, wax sealed, capped and stored vertically. Some cores were tested with a laboratory miniature vane on the vessel and the top 7-8 cm (3 in) were bagged for additional geotechnical testing onshore.

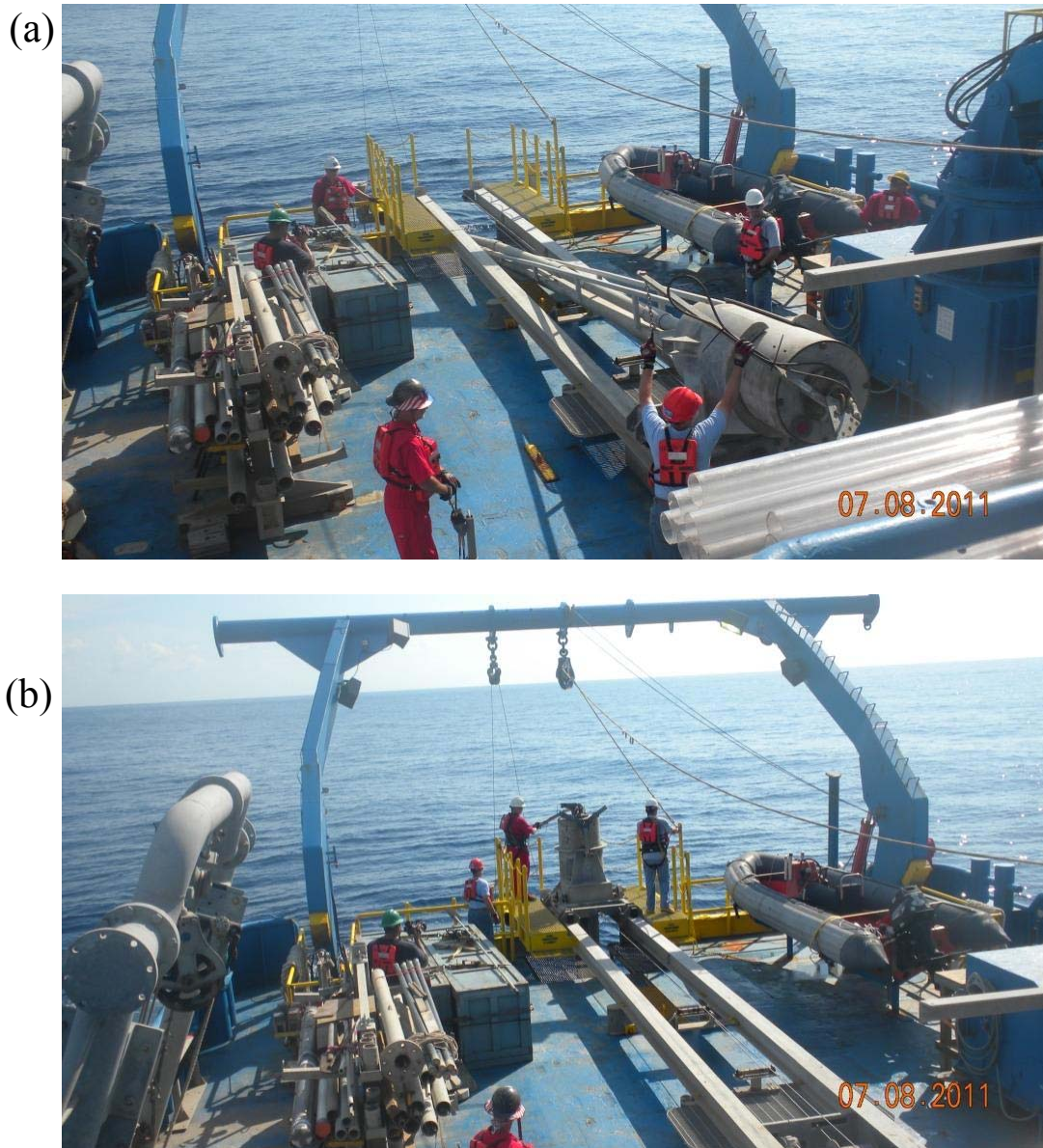


**Fig. 5.3.** (a) Jumbo piston core rig ready for deployment (b) Jumbo piston core rig in deployment

Processed core sections were stored in an air conditioned room on the vessel pending their careful offload at the next port call. These sections were then transported by enclosed truck to on-shore laboratories for further geotechnical testing.

## **5.2 Geology of Gulf of Mexico Clay**

The Southern Green Canyon (Figure 5.4) lies along the Sigsbee Escarpment in the Gulf of Mexico. Al-Khafaji et al. (2003) describe the geology of the lower continental slope as consisting of uniform surficial deposits of highly plastic Holocene clays overlying older, stiffer, less plastic, Pleistocene clays. The Sigsbee Escarpment consists of stiff clays that have been exposed by slides and slumps. These sediments have also experienced uplift by the underlying salt and erosion caused by bottom currents. The upper continental rise consists of uniform deposits of highly plastic clays with a thin drape of Holocene clays (Jeanjean et al, 2003; Slowey et al, 2003).

## **5.3 Multi-sensor Core Logger Profiles**

The core samples were scanned using a GEOTEK Multi-sensor core logger (MSCL) (Figure 5.5). A conveyor system moves the sensor array, which scans the core as it passes. The conveyor is driven by a stepper motor which can position a core to an accuracy of better than 0.5 mm. The computer controlling the conveyor also controls the sensors, so that all data are automatically correlated. The computer also measures the length of each core section and can automatically subtract the thickness of the end caps, allowing the sections to follow sequentially, producing an unbroken stream of data.

The MSCL can handle core sections up to 1.5 m long and 15 cm in diameter, and can sample at 1-mm intervals. The logger is equipped with a <sup>137</sup>Cs gamma source in a

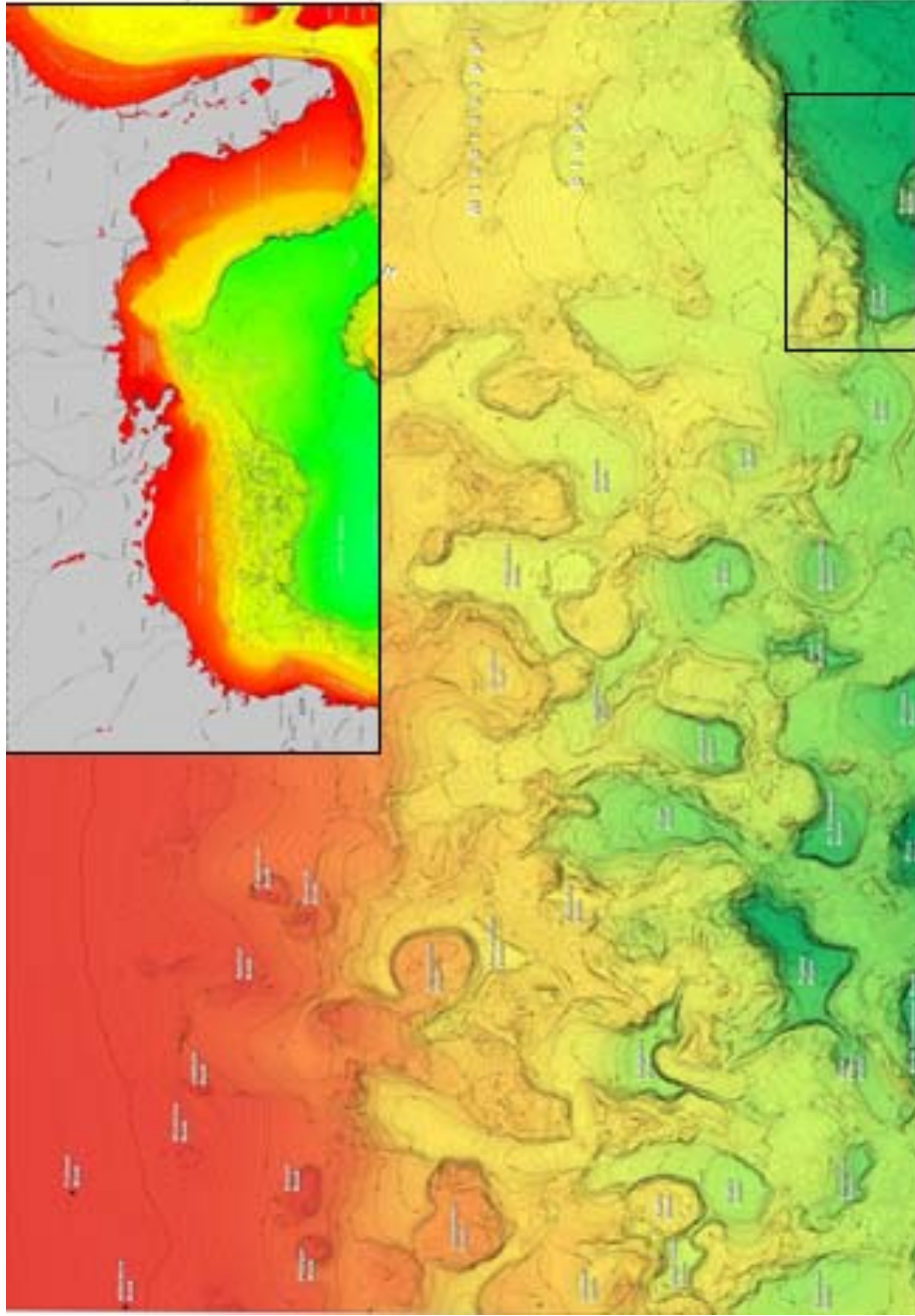


**Fig. 5.4.** Locations of jumbo piston cores from Gulf of Mexico (Madhuri, 2011).





**Fig. 5.5.** Photograph of multi-sensor core logger.

lead shield for determining bulk density, with a resolution of 1%. The logger is also equipped with 250-500 kHz piezo-electric ceramic transducers for measuring P-wave velocity, which are spring-loaded against the sample and accurate to 0.2%. Core diameter measurements are taken using rectilinear displacement transducers, with a resolution of 0.05 mm (sleeved core). Data recorded includes p-wave velocity, bulk density, porosity and moisture content.

Figure 5.6 shows the MSCL data for GOM-core1 which was used in the experimental testing program. GOM-core1 was sampled from a water depth of 1,310 m beneath mean sea level. The core had a total length of 13.46 m. The p-wave velocity was used to locate samples within the core liner with a minimal amount of disturbance. The end of the core sections were not used because of possible disturbance due to storage, transportation, oxidation and changes in water content. The p-wave velocities measured

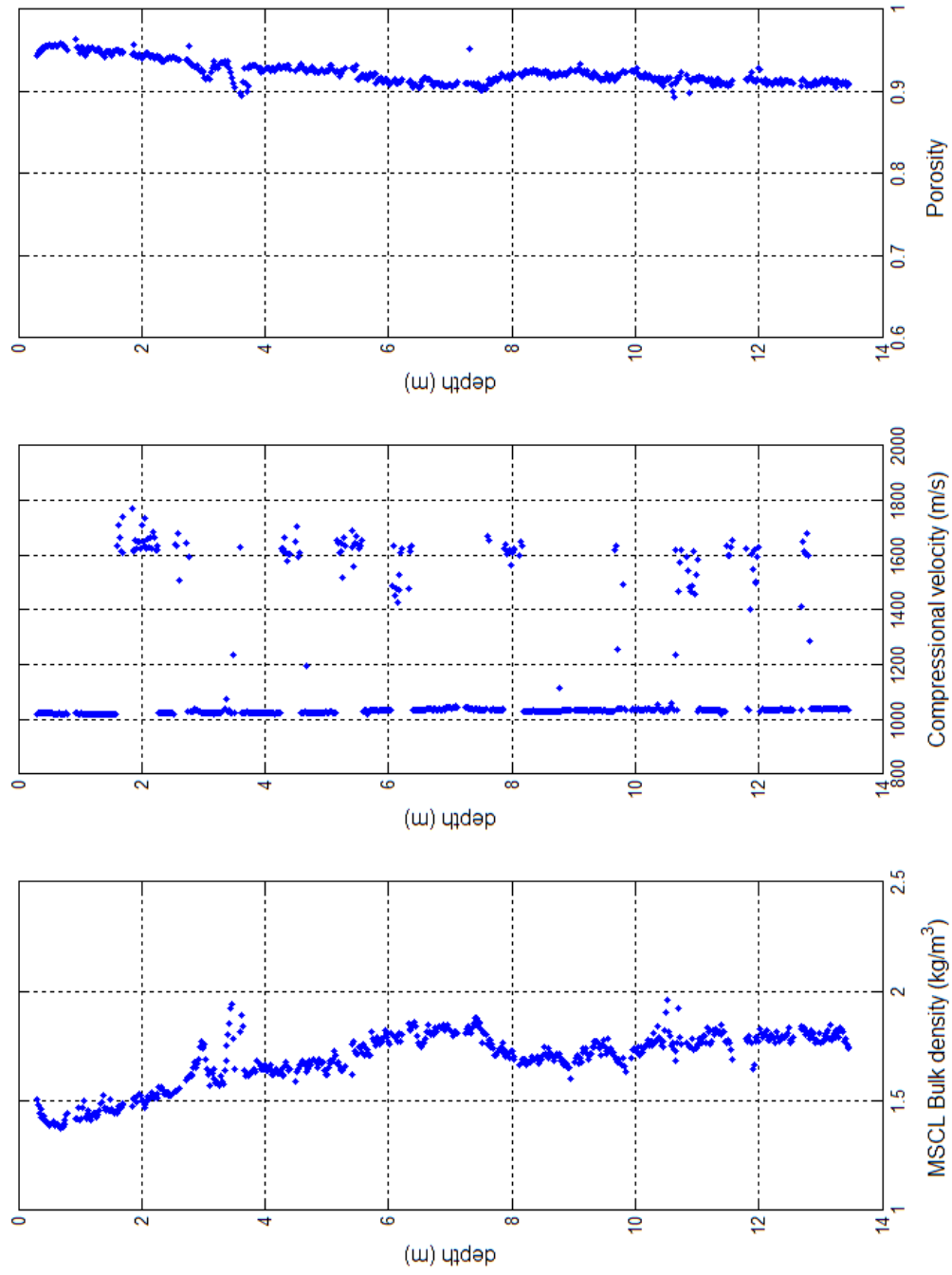


**Fig 5.6.** MSCL profiles of bulk density, compressional velocity and porosity from GOM-core1 (Madhuri, 2011).

within the soil were approximately 1050 m/s. Larger p-wave measurements indicate gaps in the core at location in which the core was sub-sampled for remold miniature vane tests and index testing. Locations of constant density and porosity indicate homogenous material.

#### **5.4 Geotechnical Engineering Properties of Gulf of Mexico Clay**

Classification and index testing was conducted on samples throughout GOM-core1. The natural water content and miniature vane strengths were determined from the top of each section. Atterberg limits, grain size analysis and specific gravity tests were performed on representative samples along the length of the core. Constant rate of strain consolidation and triaxial tests were also conducted on limited sections of GOM-core1.

##### ***5.4.1 Natural Water Content and Index Classification***

The natural water content was measured at the top of each section of the core. Figure 5.7 presents the water content with core depth from the mudline. As illustrated in the plot, the top 4 m of sediment has a water content higher than 100%. The water content slowly decreases from 100% to 60% between a depth of 4 m to 7 m. Below 7 m, the water content remains constant between 60%-80%. Consolidation, triaxial and direct simple shear tests were conducted on samples below 7 m because the shallower samples were too soft to trim without considerable disturbance,

As indicated in Figure 5.7, liquid and plastic limits were determined at the same locations as the natural water content. The liquid limit gradually decreases in the top 4 m from 100 to 60 and ranges from 60 to 80 below depths of 7 m. The natural water content is greater than liquid limit until approximately 6 m. The plastic limit is

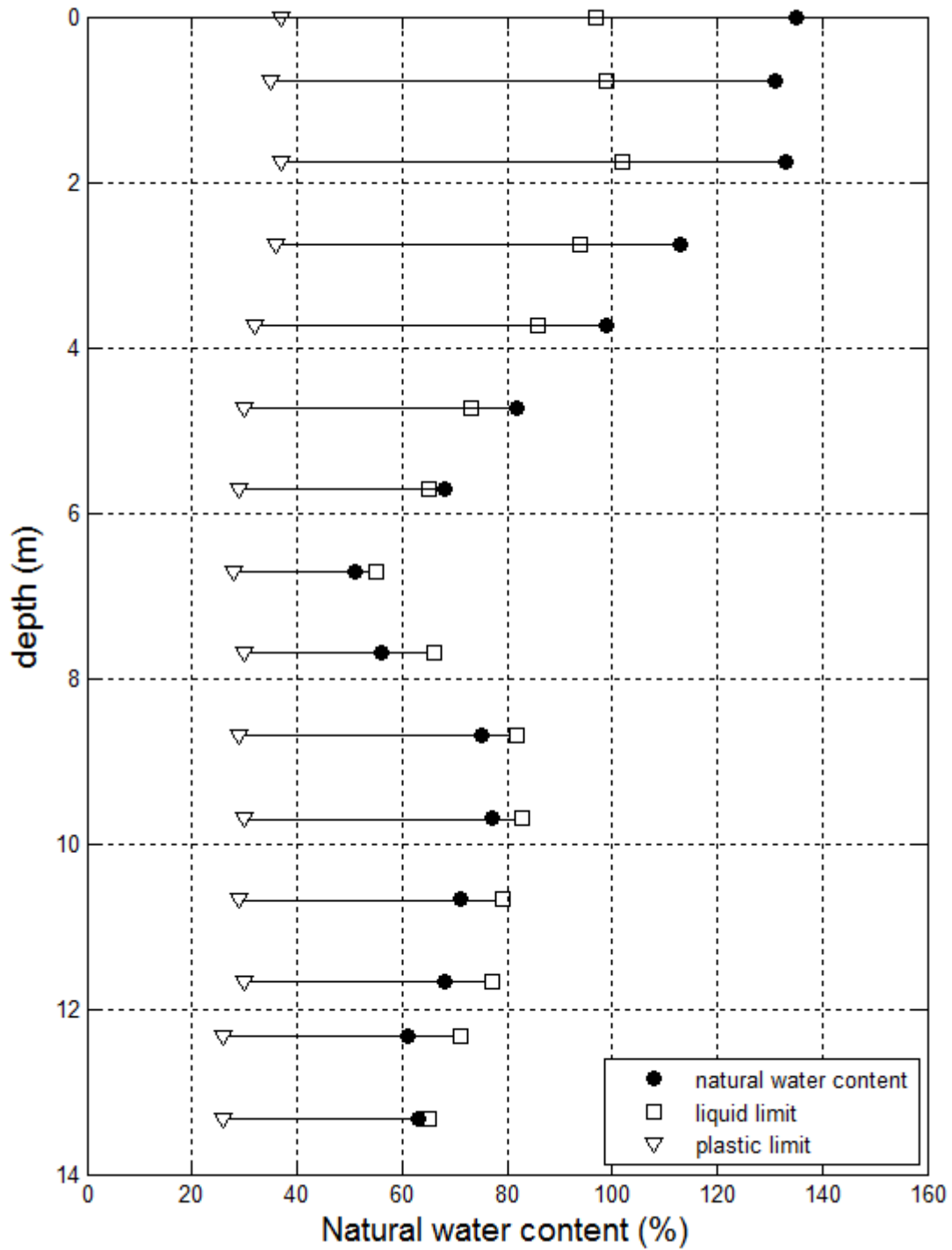


**Fig. 5.7.** Natural water content with depth for GOM-core1 (Madhuri, 2011).

approximately 36 for the first 4 m of the core and then decreases to 29 . Results of classification tests are plotted in Figure 5.8. As is typical with marine clays, the results are close to the A-line and classify the clay sample is either MH or CH.

#### ***5.4.2 Miniature Vane Shear Strength***

Laboratory miniature vane shear strength tests were conducted offshore on the tops of each section and the bottom of the last section. Figure 5.9 shows the shear strength increases gradually with depth with a maximum shear strength of 22 kPa. Samples for advanced geotechnical testing were chosen in the lower sections of the core with shear strengths of approximately 20 kPa.

#### ***5.4.3 Grain Size Distribution and Specific Gravity***

Grain size analysis and specific gravity tests were conducted on samples within the sections used for advanced geotechnical testing (Table 5.1). Hydrometer analyses were performed in accordance with ASTM D422-63(2007). As illustrated in Figure 5.10, the four hydrometer tests are consistent for the lower sections of the core. The soil consists of 84-99% fine particles of which 51-72% are clay size. Specific gravity tests were carried out in accordance with ASTM D854. The results indicate consistent material in sections 11,12, 13 and 15.

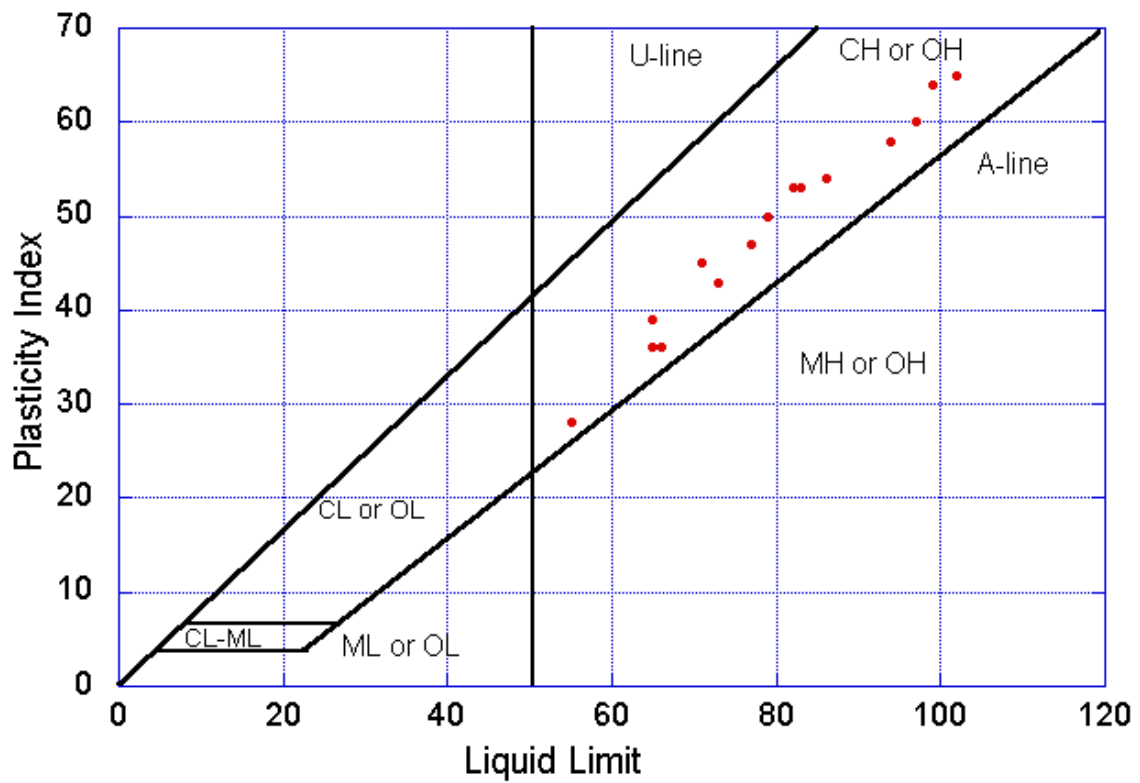


**Fig. 5.8.** Atterberg limits for GOM-core1 samples plotted on Casagrande's plasticity chart.

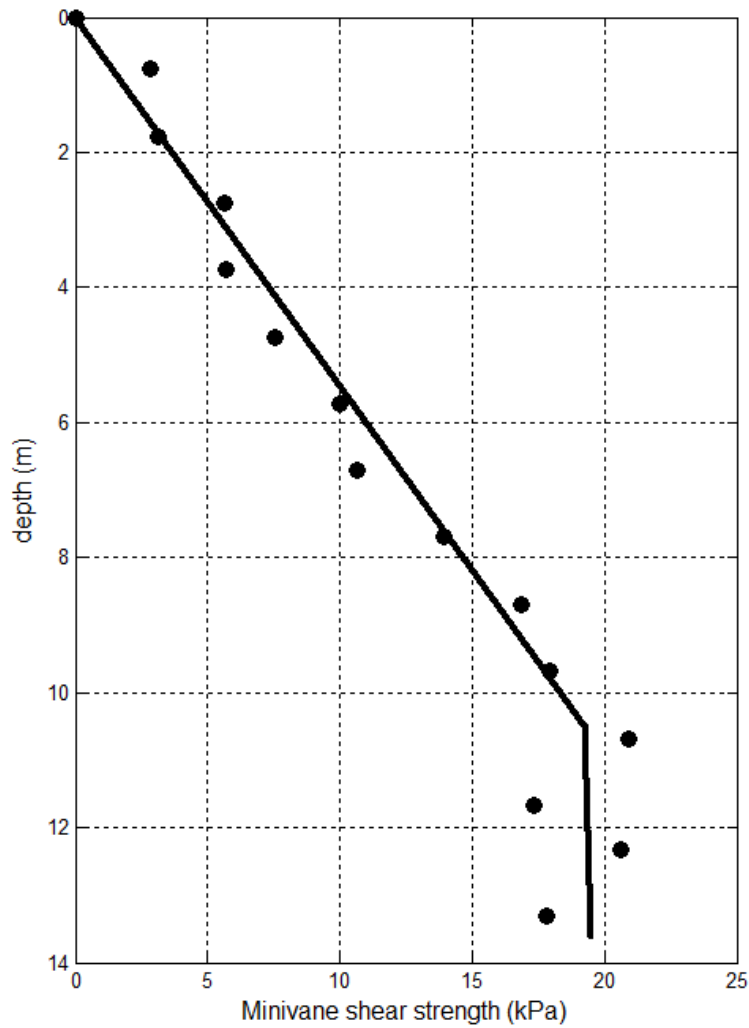


**Fig. 5. 9.** Miniature vane shear strengths with depth for GOM-core1 (Madhuri, 2011).

**Table 5.1.** Summary of representative sample testing.

Section	Depth (m)	Specific gravity	Soil Type
11	9.0 - 9.7	2.74	MH
12	9.7 - 10.6	2.76	CH
13	10.6 - 11.5	2.76	CH
15	12.2 - 13.5	2.76	CH





sample preparation required an air dry sample to be ground with a mortar and pestle using soft pressure. The sample was then passed through a 140 mesh sieve (0.104 mm) to obtain a uniform particle size of the minerals in the sample. A front loading mount method was used to prepare the sample for bulk XRD analysis. Figure 5.11 shows the bulk XRD for both samples. As indicated in the plots, the mineral composition of the two samples is similar. The samples are a mixture of seven main minerals, clinochlore (chlorite), muscovite (mica), quartz, feldspar albite, magnesium calcite, dolomite and halite. The minerals present suggest that the sample consists mainly of fine-grained sediments and does not require fractionation for the fine clay fraction.

To perform a detailed investigation of clay size Phyllosilicate minerals, different techniques such as cation exchange, organic salvation and heat treatments were used, oriented specimens dried on a flat support for XRD analysis. The two samples were then prepared using two different treatments to concentrate some mineral components and enhance the x-ray signal response. The first treatment was magnesium saturation. Magnesium was used because it highly hydrates and its presence in the interlayer of the clay minerals results in a stable complex with two water layer between each 2:1 layer of clay (Deng et al., 2009). The cation saturation is required because the d-spacings for smectite and vermiculite are highly variable without a known exchange cation. The following procedures were used for preparation of the sample using the magnesium saturation treatment. 50 mg of air-dried clay was transferred into a centrifuge tube. Approximately 2 mL of  $MgCl_2$  was added to the tube and mixed using a vortex mixer to suspend the particles. 0.5 M  $MgCl_2$  solution was then added to increase the volume



of solution to 15 mL in the centrifuge tube. The sample was shaken for 20 minutes on a shake table and then centrifuged at 2000 rpm for 10 minutes. The supernatant of the sample was removed using a pipette and then entire process was repeated two more times. The magnesium saturated clay was washed using deionized water, vortexed, and centrifuged for a total of three times. The clear fluid was removed for a final time and the remaining clay solution was pipetted onto a glass disc for analysis.

The same procedures were used for the second treatment of potassium saturation with 1 M KCl solution. The potassium is used because the large size of the cation allows the cation to migrate into interlayer in smectites and vermiculites in an unhydrated state (Deng et al., 2009). Since the samples are heat treated at 330° C and 550 ° C, two K-saturated discs are created for each clay sample. Any difference between the XRD patterns for the two different treatments reveal the presence of swelling components in the sample (Deng et al., 2009). Figures 5.12 and 5.13 shows the XRD of the fine clay for each sample. As shown in the plots, the XRD pattern reveals the presence of chlorite, mica, kaolinite, smectite, quartz, feldspar albite, and dolomite in both samples.

### **5.6 Transmitting Electron Microscopy (TEM)**

Transmission electron microscopy (TEM) was used to study dispersions of individual particles. TEM can be used for morphology and chemical analysis; however, its main advantage is the sub-micron particle viewing. Analysis can be conducted on minerals that include selected area electron diffraction (SAED), lattice fringes, and moire fringes. The electron microscope used was the JEOL 2010, where the image was projected on a fluorescent viewing screen with a digital CCD camera (Gatan ORIUS

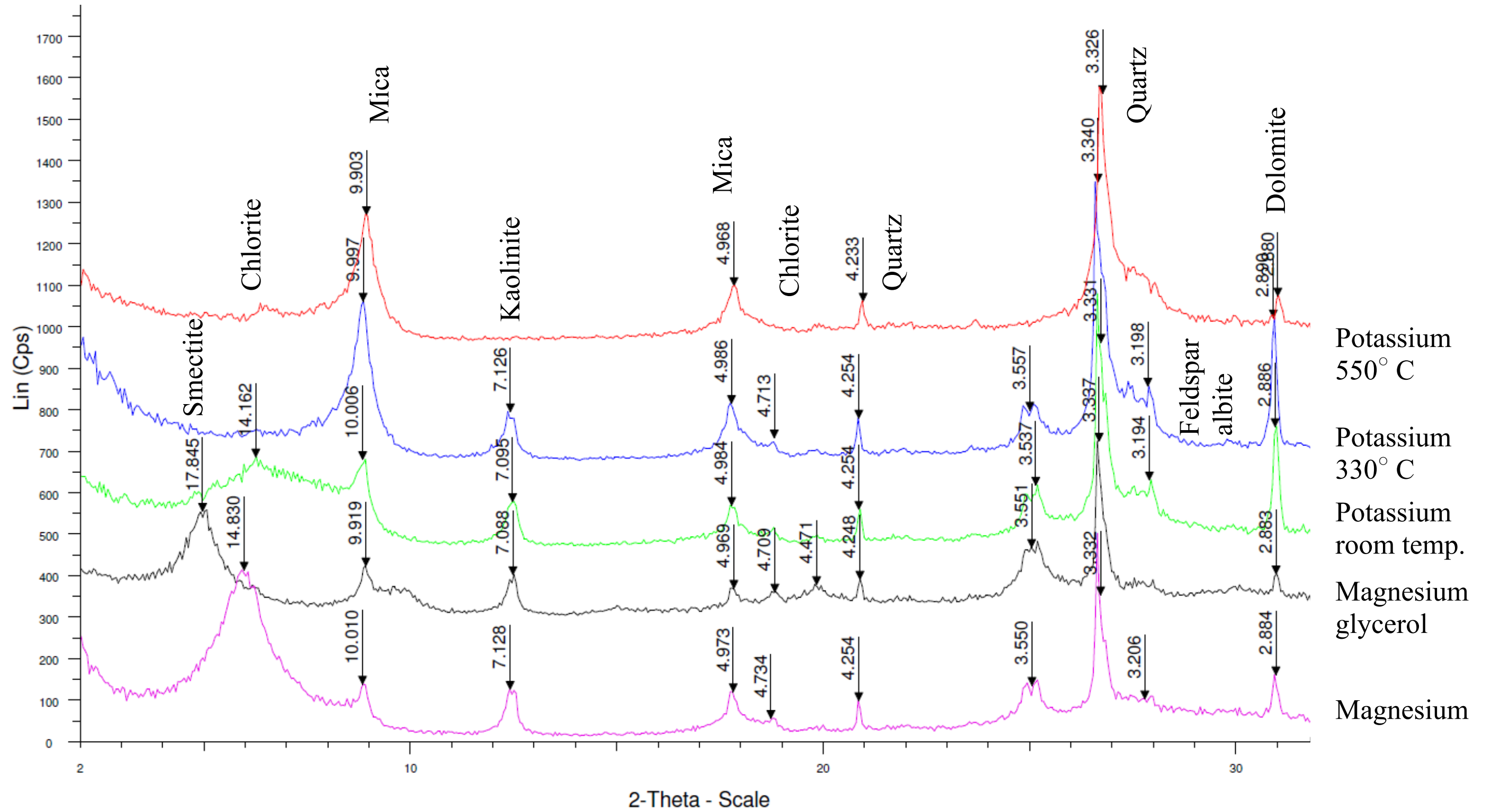


Fig. 5.12. XRD analysis magnesium and potassium saturation - sample 1.

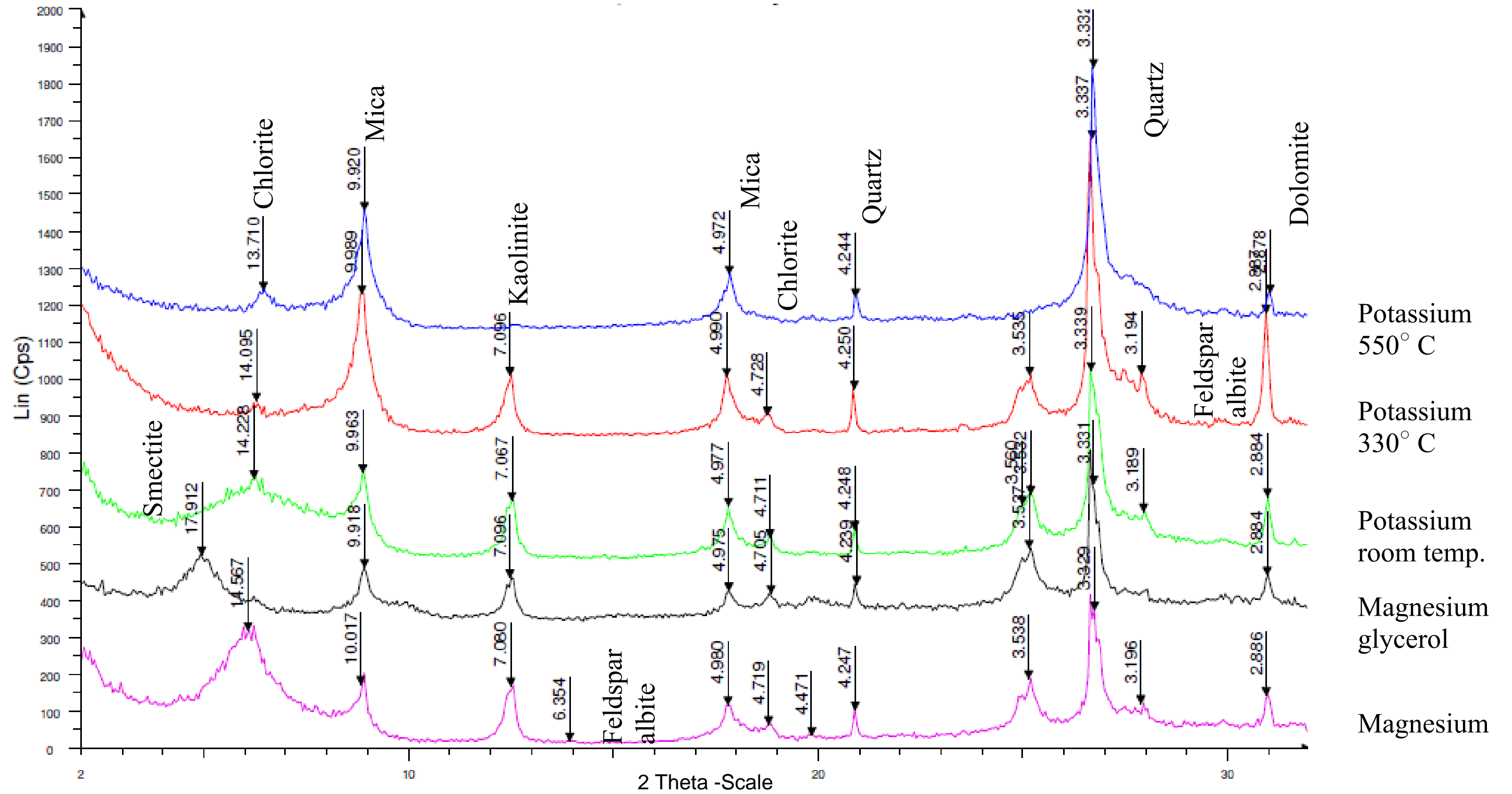


Fig. 5.13. XRD analysis magnesium and potassium saturation - sample 2.

CCD camera) beneath it and on a computer monitor. The source of the electron illumination is a small heated tungsten filament at the top of the evacuated column. Vacuum pressures on the order of  $10^{-5}$  Torr are employed. The sample must be dry and the dissipation of heat from the concentrated electron beam is by conduction through the sample and grid.

The sample clay used for TEM was prepared or dispersed in two ways. First, distilled, deionized water was used to disperse the clay, secondly, one clay sample was prepared with alcohol and water to observe the difference in the sample dispersion. An aliquot of the saturated clay sample (about 5 mg of clay) was dispersed in 10 ml of distilled, deionized water and another aliquot where 5 mg of the clay was dispersed in 10 ml of ethyl alcohol in labeled test tubes.

The diluted clay was dispersed by vigorous manual agitation of the test tubes. The test tubes were placed in an ultrasonic generator and sonicated for 3-4 min. The frequency of the ultrasonic field should be checked as very high frequencies of  $10^6$  Hz or higher can produce particle degeneration. The time allowed for sonication is also important as longer agitation times can produce heating.

After dispersion, 100  $\mu$ l of the water suspension was removed from mid-depth with a disposable pipette and placed in a smaller test tube. Using another pipette, 500  $\mu$ l of distilled deionized water was added to the suspension to dilute it. Another sample was prepared by adding 100  $\mu$ l of the suspension to 1000  $\mu$ l of water. Similarly, 100  $\mu$ l of the clay suspension in ethanol was removed from mid-depth and diluted using 500  $\mu$ l and 1000  $\mu$ l of ethanol.

These four smaller test tubes with different concentrations were then placed in the ultrasonic generator and agitated for 3-4 min. 400 mesh holey carbon grids were used to mount the clay. The carbon film was first rendered hydrophilic by ion bombardment from a glow discharge source. A droplet from each of the four small test tubes was placed onto four hydrophilic carbon support films using a light microscope. The four carbon grids were then left to dry and then placed in labeled containers ready to be used in the microscope.

Figure 5.14 shows the presence of halloysite (long tubular structure clay particle) in the center surrounded by chlorite in the background. Figure 5.15 shows chlorite interspersed with folded smectite layers or as complex interstratified grains of silica mineral in between particles of chlorite. The results of the X-ray diffraction show presence of both smectite and quartz, making the minerals shown in the image difficult to identify. Figure 5.16 shows the dispersion of the clay plates. Although the image is not entirely clear and lacks contrast, the different clay platelets can be discerned. Figure 5.17 shows moire fringes on muscovite mineral or mica.

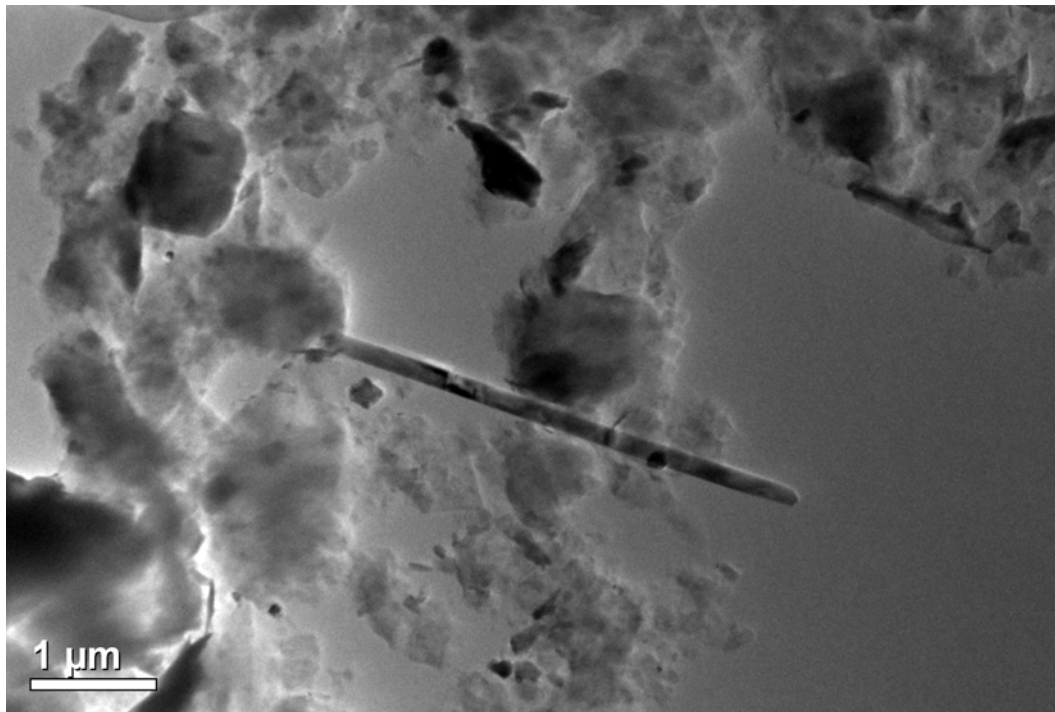


**Fig. 5.14.** TEM micrograph showing halloysite in the center of chlorite.

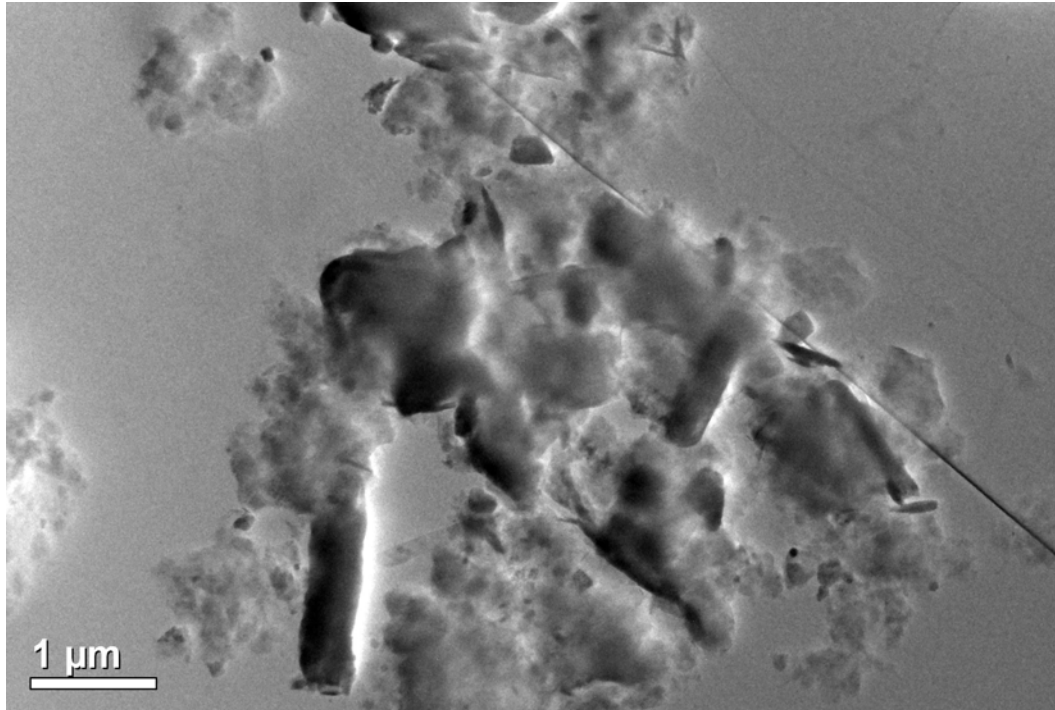


**Fig. 5.15.** TEM micrograph showing chlorite interspersed with folded smectite layers.



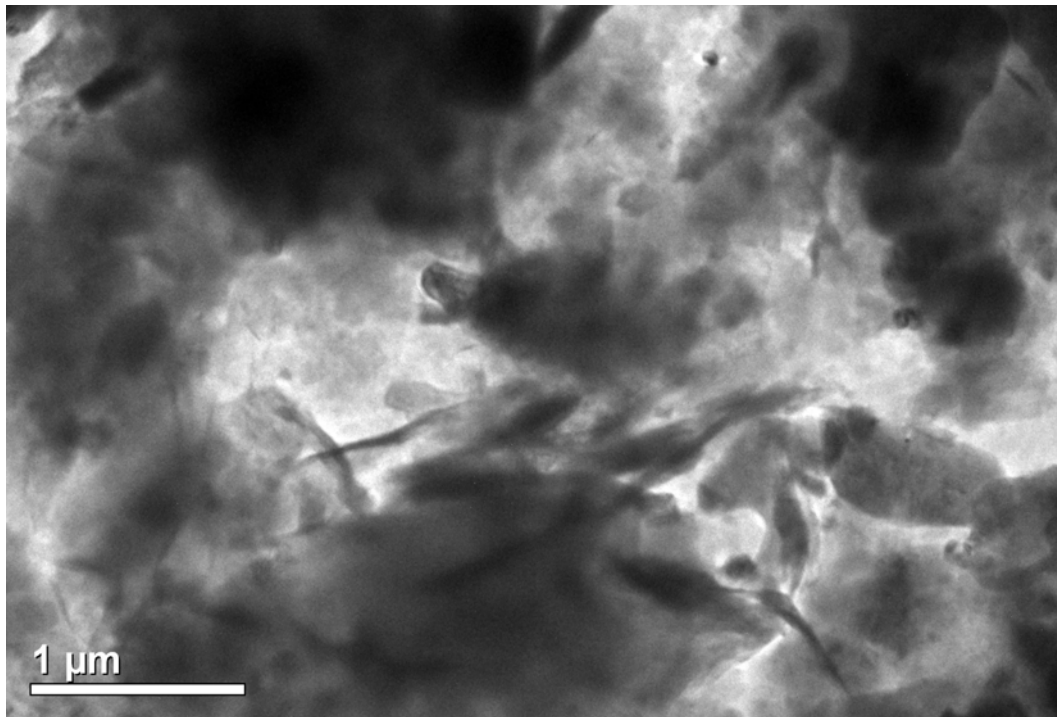


**Fig. 5.16.** TEM micrograph showing dispersion of the clay plates.

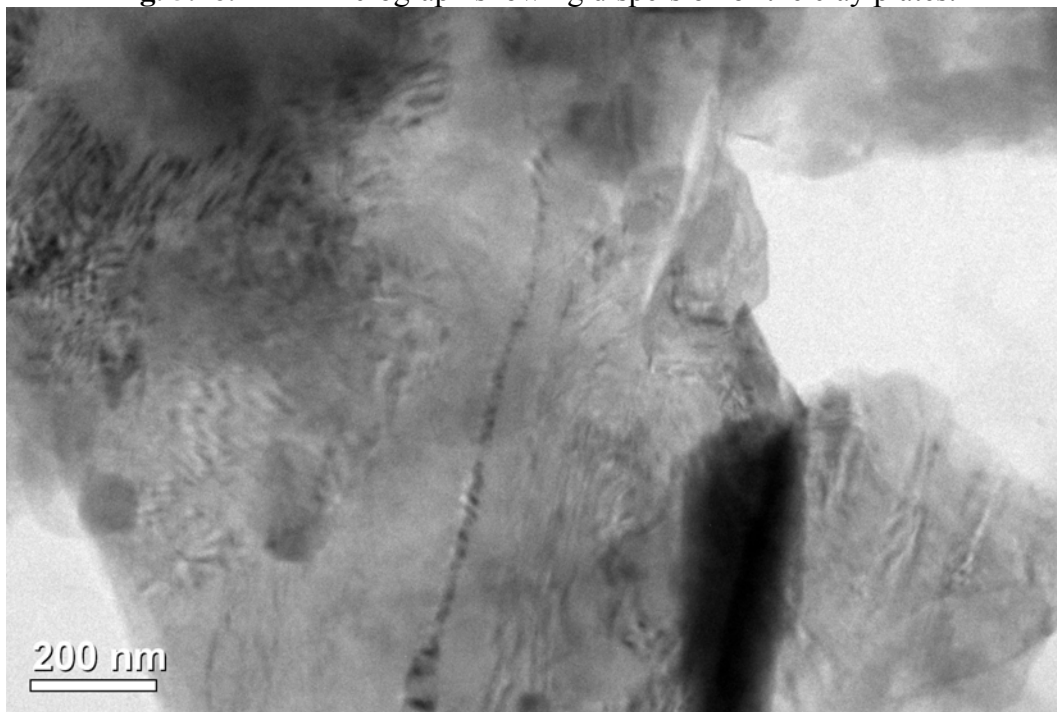


**Fig. 5.17.** TEM micrograph showing moiré fringes on muscovite mineral or mica.

### 5.7 Constant Rate of Strain Consolidation

Constant rate of strain consolidation tests were conducted on eight samples at various depths and strain rates (Table 5.2). As shown in Figure 5.18, Casagrande's graphical method was used to obtain the value of pre-consolidation pressure ( $\sigma'_p$ ). For a depth of 11.5 m, the pre-consolidation pressure was calculated to be 72 kPa. Figure 5.19 presents results of effective stress vs strain and Figure 5.20 presents results of void ratio changing over effective stress. Results indicate a compression index ( $C_c$ ) of 0.55 and a recompression index ( $C_r$ ) of 0.07 for all the curves.

**Table 5.2.** Summary of constant rate of strain consolidation tests.

Test Name	Depth (m)	Strain Rate
CRS-GOM1	13.14	7
CRS-GOM2	13.18	5
CRS-GOM3	13.23	3
CRS-GOM4	11.81	1
CRS-GOM7	11.96	2
CRS-GOM6	12.10	1.5
CRS-GOM7	12.13	1.5
CRS-GOM8	10.01	1.5

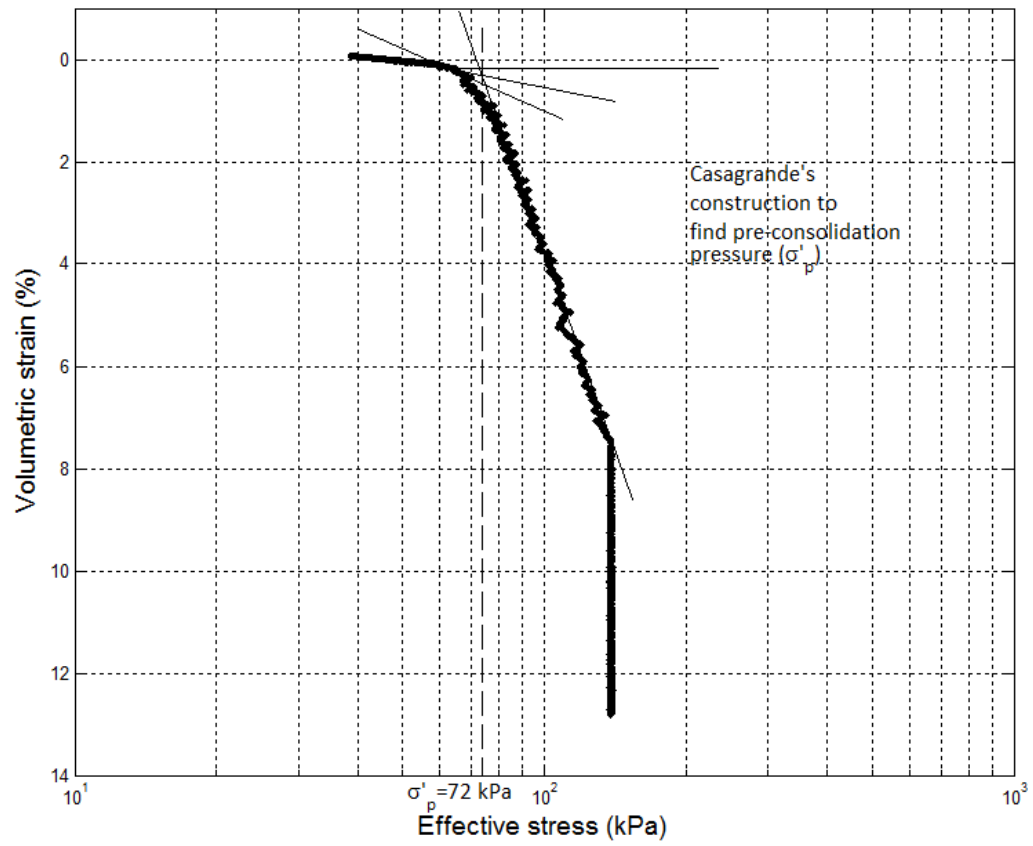


**Fig. 5.18.** Casagrande's graphical method to determine pre-consolidation pressure (Madhuri, 2011).

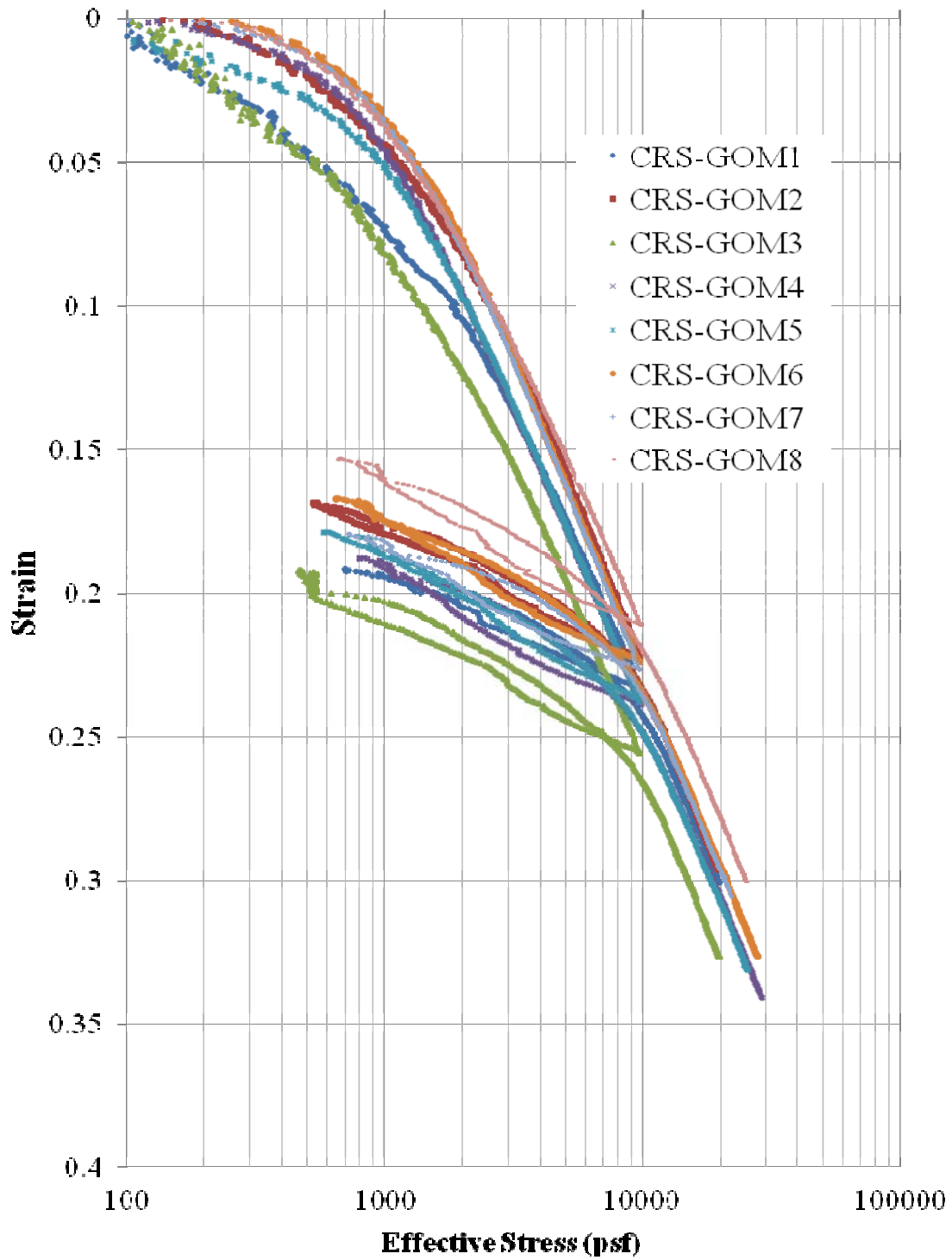
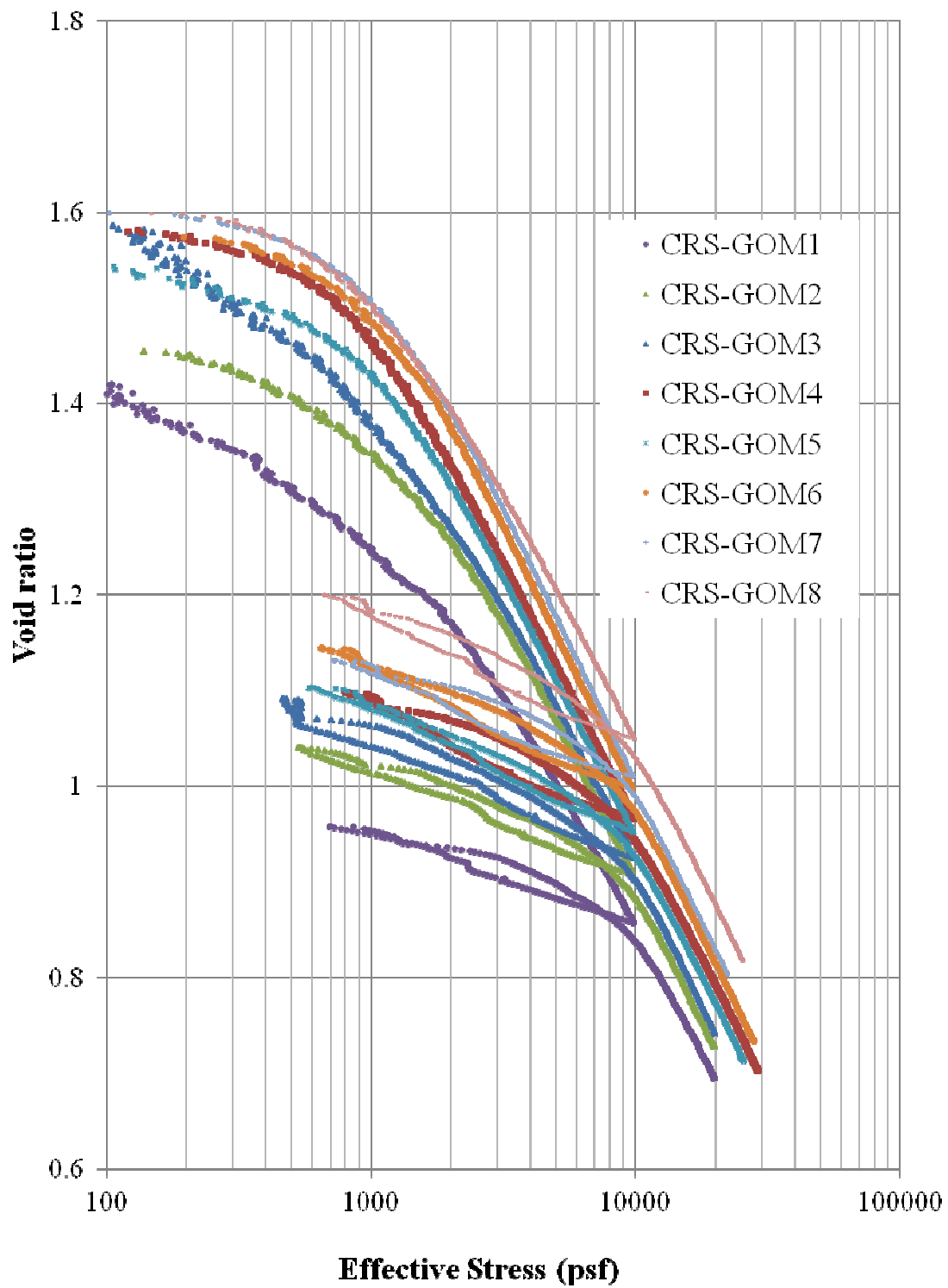


Fig. 5.19. CRS plot of effective stress vs strain.



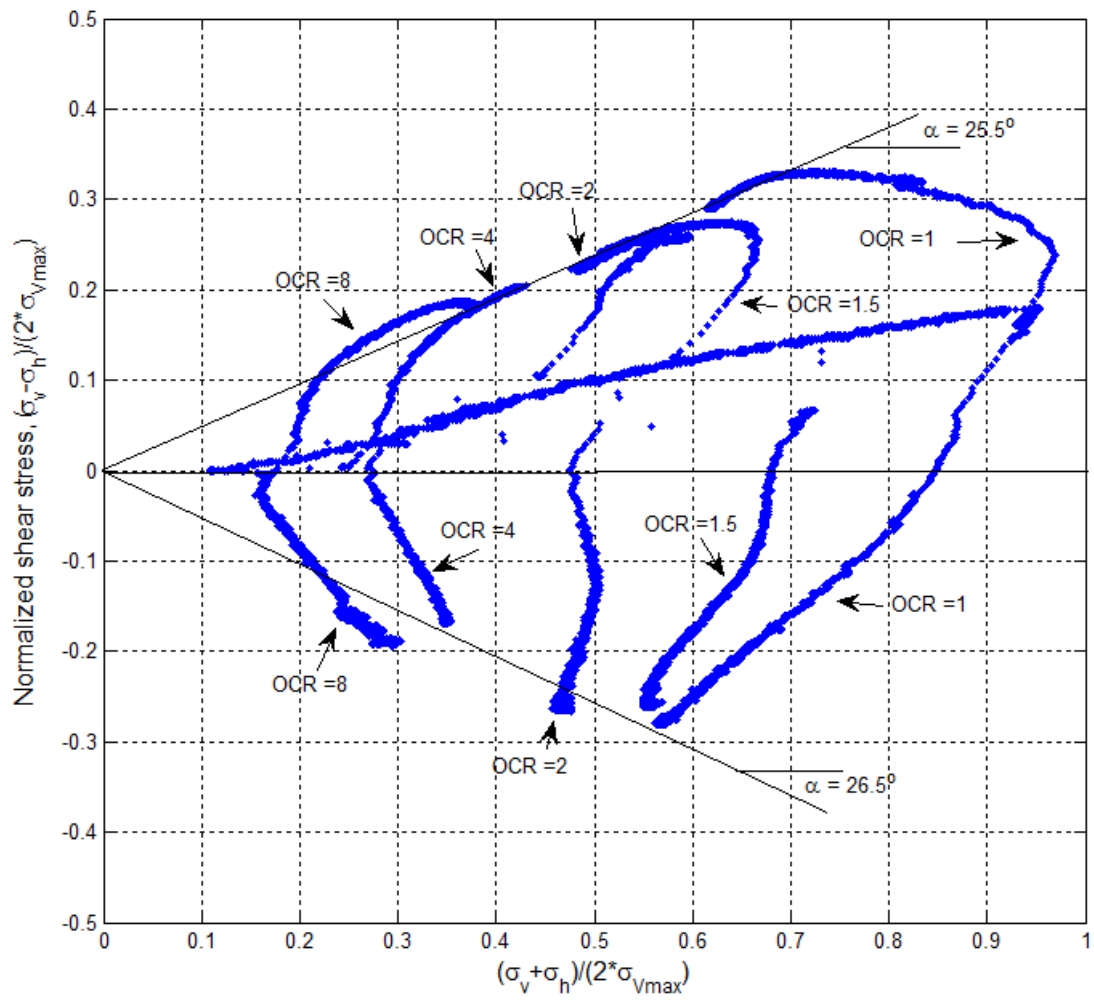
**Fig. 5.20.** CRS plot of effective stress vs void ratio.

## 5.8 Triaxial Testing

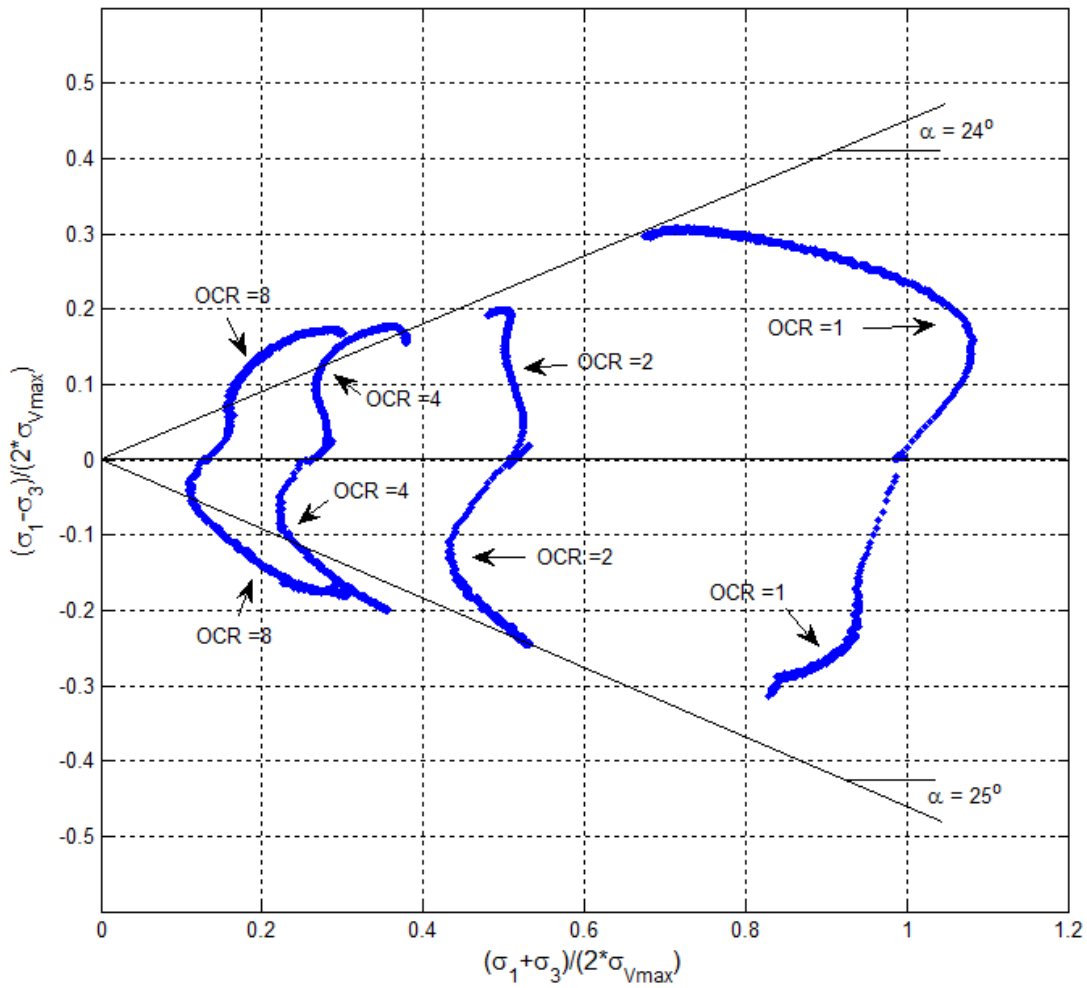
A comprehensive series of CK<sub>o</sub>U compression and tension and CIU compression and extension triaxial tests were performed on the Gulf of Mexico sample (Madhuri, 2011). Figure 5.21 presents the normalized effective stress paths for CK<sub>o</sub>U compression and extension testing. For the compression tests, the effective stress envelope at critical state is represented by a perfectly straight line at an angle of 25.5°. For the extension tests, the effective stress shear envelope at critical state is not as clear as for compression. It is best represented by a line which passes through the points of maximum shear stress with an angle of 26.5°. The friction angle ( $\phi$ ) for the compression failure envelope was found to be 28° and - for the extension failure envelope was found to be 29.5°.

Figure 5.22 presents the normalized effective stress paths for CIU compression and extension testing. For compression tests, the effective shear stress envelope at critical state is at an angle of 24°. The effective shear stress envelope for the extension tests was 25°. The friction angles for the compression and extension tests were found to be 26.4° and 27.7°.

Comparing the strengths between the CK<sub>o</sub>U-C/E tests and the CIU-C/E tests, it can be seen that the isotropic tests tend to fail at slightly lower strengths than the K<sub>o</sub> consolidated tests. Additionally, the angle for the isotropic tests in both compression and extension is less than the angles obtained from the CK<sub>o</sub>U-C/E tests.



**Fig. 5.21.** Normalized effective stress paths from CKoU-C/E testing (Madhuri 2011).



**Fig. 5.22.** Normalized effective stress paths from CIU-C/E testing (Madhuri 2011).



### **5.9 Previous Testing on Gulf of Mexico Marine Clay**

Limited monotonic direct simple shear tests results of Gulf of Mexico clays are available in the literature. Young et al. (2003b) conducted consolidated undrained direct simple shear monotonic tests on Gulf of Mexico samples from the northern Garden Banks and northern Green Canyon regions. Normalized shear behavior was observed at consolidation pressures of about 2.5 times the effective consolidation pressure,  $\sigma'_{vu}$ . The ratio of peak shear strength to the effective consolidation pressure,  $S_u / \sigma'_{vu}$  ranged from 0.221 to 0.273 (Figure 5.23).

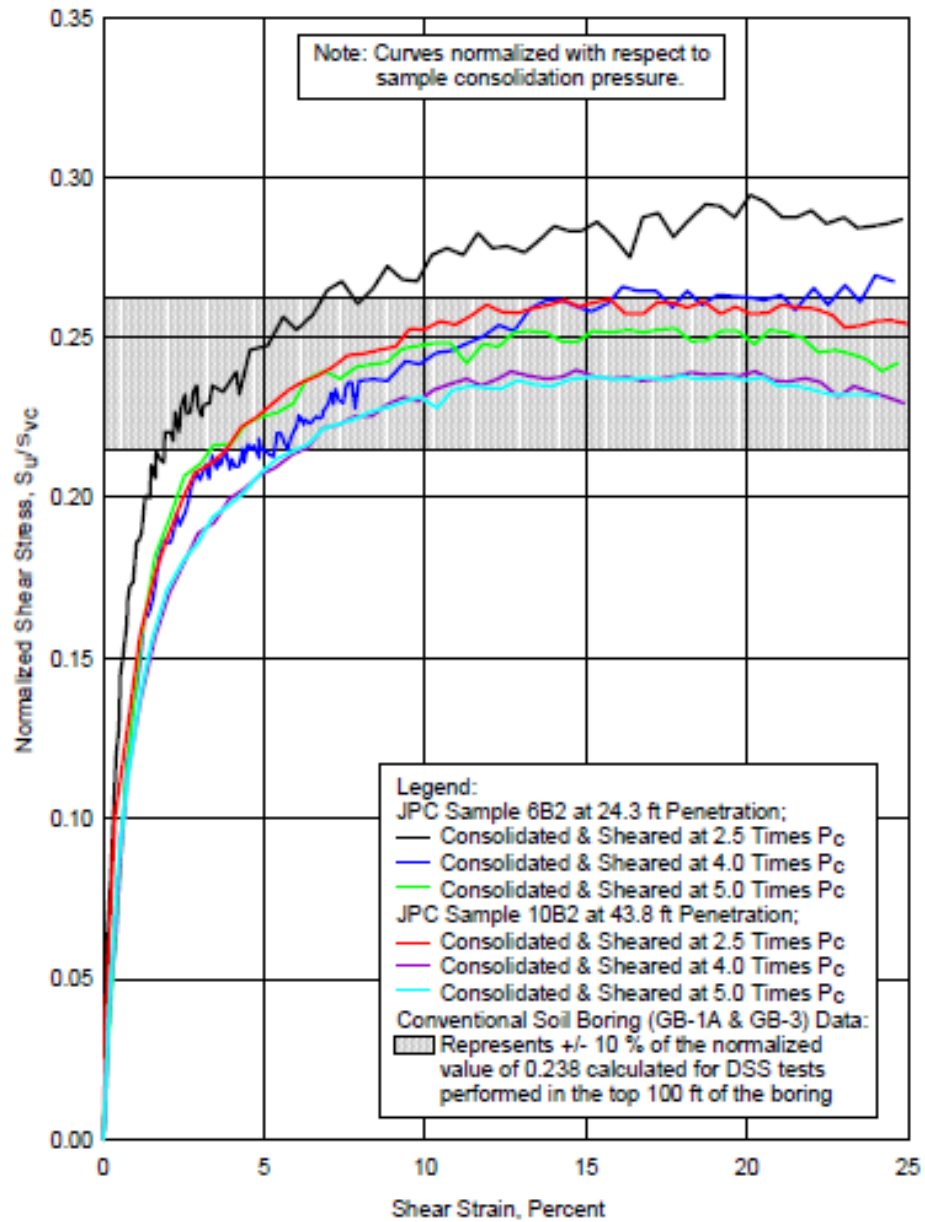


**Fig. 5.23.** Results of consolidated undrained direct simple shear tests (After Young et al., 2003b).

## **6. MULTI-DIRECTIONAL DIRECT SIMPLE SHEAR BEHAVIOR OF GULF OF MEXICO CLAYS**

An experimental test program was conducted on Gulf of Mexico clay with the objective of simulating the stress conditions within a submarine slope. Specimens were anisotropically consolidated under a vertical normal stress and horizontal shear stress and subsequently sheared undrained by application of an additional horizontal shear stress acting at an angle,  $\delta$ , relative to the consolidation shear stress. Monotonic, cyclic, circular, and figure-8 tests were conducted to simulate various loading patterns on a submarine slope subjected to dynamic loading. Table 6.1 summarizes the Gulf of Mexico specimens tested in the TAMU-MDSS.

### **6.1 Testing Procedures**

The MSCL data was used to locate specimens within the core liner with a minimum amount of disturbance. Both ends of core sections were discarded because of possible disturbance, possible oxidation and change in water content during the storage period. The cores were stored in the humidity room until testing. The location of each sample was determined and the depth was recorded. The liner of the core was marked with the depth, specimen name and an arrow indicating the orientation. The height of each specimen was approximately 20 cm. A PVC cutter was used to cut the PVC liner above and below the specimen. A wire was used to cut the soil and was then extruded using a jack or allowed to extrude due to self weight. The porous stones were saturated and filter paper was cut for both the top and bottom caps. The weight of the caps,

**Table 6.1.** Summary of GOM specimens tested in TAMU-MDSS.

Specimen	Test type	Consolidation	Rate	Cyclic shear stress ratio (CRS)	Direction of shearing $\delta$ (degrees)
GOM-1	MONO	$CK_o$	5%/hr	-	0
GOM-2	MONO	$CK_o$	50%/hr	-	0
GOM-3	MONO	$CK_\alpha$	5%/hr	-	0
GOM-4	MONO	$CK_\alpha$	5%/hr	-	180
GOM-5	CYCLIC	$CK_o$	0.1 Hz	0.20	0
GOM-6	CYCLIC	$CK_\alpha$	0.1 Hz	0.20	0
GOM-7	CYCLIC	$CK_\alpha$	0.1 Hz	0.15	0
GOM-8	CYCLIC	$CK_\alpha$	0.1 Hz	0.20	90
GOM-9	CYCLIC	$CK_\alpha$	0.1 Hz	0.15	90
GOM-10	CIRCULAR	$CK_o$	0.1 Hz	0.20	-
GOM-11	CIRCULAR	$CK_\alpha$	0.1 Hz	0.20	-
GOM-12	CIRCULAR	$CK_\alpha$	0.1 Hz	0.15	-
GOM-13	FIGURE-8	$CK_o$	0.1 Hz x-dir 0.2 Hz y-dir	0.20	0
GOM-14	FIGURE-8	$CK_\alpha$	0.1 Hz x-dir 0.2 Hz y-dir	0.20	0
GOM-15	FIGURE-8	$CK_\alpha$	0.1 Hz x-dir 0.2 Hz y-dir	0.15	0
GOM-16	FIGURE-8	$CK_\alpha$	0.1 Hz x-dir 0.2 Hz y-dir	0.20	90
GOM-17	FIGURE-8	$CK_\alpha$	0.1 Hz x-dir 0.2 Hz y-dir	0.15	90

saturated porous stones, filter paper, o-rings and membrane was recorded. The specimen was then placed on the bottom cap and transferred to the trimmer. A wire saw was used to trim the specimen to the specified diameter of approximately 79.8 mm (3.14 in) for a diameter to height ratio of 4:1. The water content and Atterberg limits were determined from trimmings. The specimen was laterally confined by a wire-reinforced membrane. O-rings and hose clamps were installed on the top and bottom cap to prevent the o-rings from moving during shearing and causing water to leak decreasing the excess pore pressure. A summary of the depth, initial and final water contents, and unit weight for each specimen is provided in Appendix C.

## **6.2 Consolidation**

Consolidation of the specimens is used to minimize the effects of sampling disturbance and load the specimen to a normally consolidated state. The wire-reinforced membrane was used to provide lateral restraint and ensure  $K_o$  conditions (Bjerrum and Landva, 1966). Back saturation of the specimen was conducted following procedures similar to those used in triaxial testing. The chamber pressure and backpressure are increases gradually keeping the difference between the two at a small value that will minimize the effective stress applied to the specimen. The specimens were backpressure saturated to a minimum B-value of 0.95. The consolidation effective stress ( $\sigma'_{vc}$ ) was selected as 83.6 kPa so that all specimens would be normally consolidated to a stress at least 1.5 times the estimated maximum past pressure. The effect of a slope was simulated by reproducing the consolidation stress history by subjecting the specimen to a consolidation shear stress ( $\tau_c$ ).

For  $CK_o$  consolidated tests, the loading increment was applied in a single step and the specimen was allowed to consolidate for 12 hours. For  $CK_\alpha$  tests, the vertical load increments were applied in three stages, with two shear load increments for each vertical (Figure 6.1). After the last increment, the specimens were allowed to consolidate for 12 hours. Table 6.2 summarizes the loading schedule.

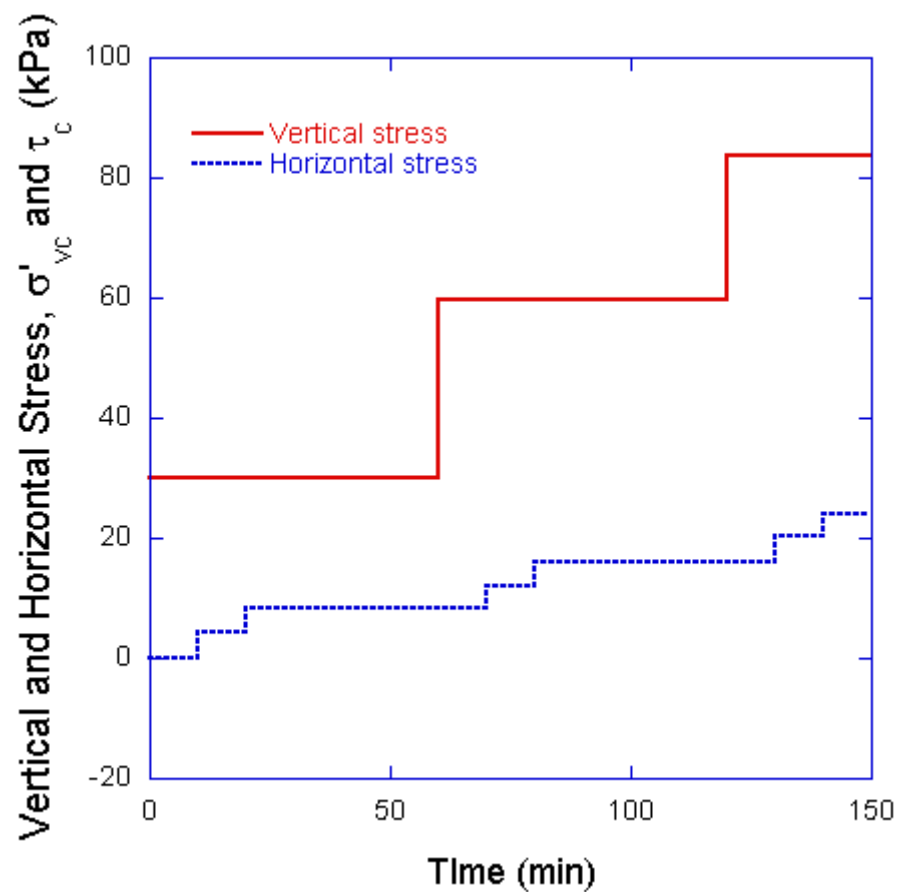


**Fig. 6.1.**  $CK_\alpha$  consolidation loading scheme.

**Table 6.2.**  $CK_{\alpha}$  consolidation loading schedule.

Time (min)	Vertical stress (kPa)	Horizontal stress (kPa)
0	29.9	0
10	29.9	4.19
20	29.9	8.37
60	59.8	8.37
70	59.8	11.96
80	59.8	16.15
120	83.6	16.15
130	83.6	20.33
140	83.6	23.92

### 6.3 Undrained Shear Tests

The testing program was aimed at characterizing the response of marine clay deposits in simple shear. The first part of the testing concentrated on establishing the response to one-dimensional monotonic and cyclic shearing of  $CK_0$  consolidated specimens, simulating level ground conditions. Results were compared with other clay tests specifically Boston Blue Clay (DeGroot, 1989) and San Francisco Young Bay Mud (Biscontin, 2011) published in the literature. The effect of the slope (simulated by  $CK_{\alpha}$  consolidation conditions) was investigated on monotonic and cyclic tests under varying stress amplitude as well as orientation on the horizontal plane (angle  $\delta$  between slope direction and loading axis). Multi-directional loading patterns such as circles and figure-8 (hourglass shape) were used to simulate simplified earthquake loading. Figure 6. 2 illustrates the stress paths used in the experimental testing program.

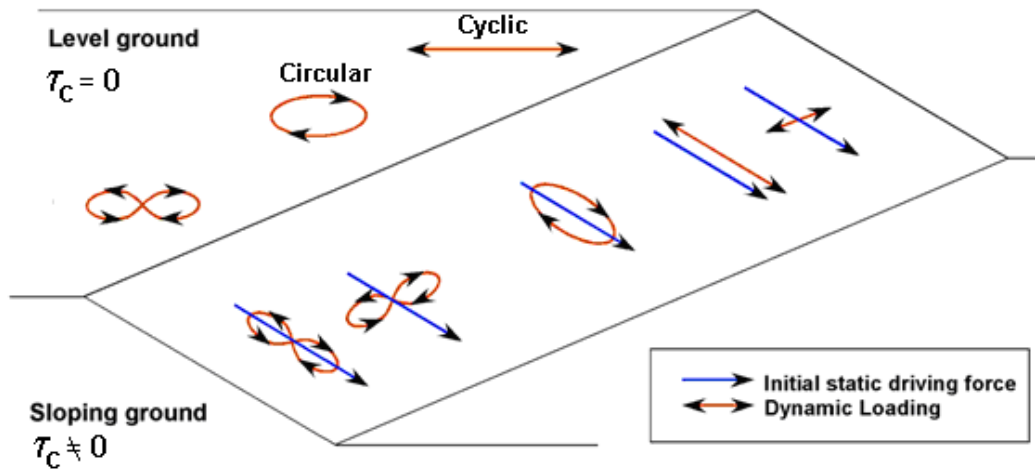


**Fig. 6.2.** Complex loading paths used in experimental testing program (Modified from Kammerer, 2001).

### 6.3.1 Monotonic Tests

Four specimens were monotonically sheared to investigate the influence of an initial shear stress ( $\tau_c$ ) on the overall behavior of the soil. Test GOM-1 was performed at  $\tau_c = 0$  ( $CK_o$  consolidation) at the standard rate of 5% strain per hour and constitutes the baseline of monotonic response for level ground. Test GOM-2 was performed at  $CK_o$  consolidation at a rate of 50%/hr for comparison of the rate effects on the shear behavior of the soil. Test GOM-3 was  $CK_\alpha$  consolidated at  $\tau_c/\sigma'_{vc} = 0.2$ , which is equivalent to a slope of  $11.3^\circ$  and then sheared at 5%/hr along the same direction as the applied consolidation shear stress simulating shearing downslope ( $\delta = 0^\circ$ ). Test GOM-4 was



also  $CK_\alpha$  consolidated at  $\tau_c/\sigma'_{vc} = 0.2$  and then sheared at 5%/hr in the opposite direction ( $\delta = 180^\circ$ ), or upslope. The tests results are summarized in Figure 6.3.

Tests GOM-1 and GOM-3 reach approximately the same condition in the stress path space, for a stress ratio  $\tau_c/\sigma'_{vc} = \psi$  of  $23.7^\circ$ , however, neither GOM-2 or GOM-4 reach the failure envelope. A normalized shear stress at large strains ranging from 0.20 to 0.38. Biscontin (2001) reported a failure envelope at  $\psi = 25^\circ$  and a normalized shear stress values approximately 0.27 for San Francisco Young Bay Mud  $K_o$  consolidated monotonically sheared at 5%/hr. Young et al. (2003b) reported consolidated undrained direct simple shear monotonic tests with normalized shear stress ratios ranging from 0.221 to 0.273 for Gulf of Mexico clays.

The complete state of stress during the tests is unknown because lack of horizontal stress measurements due to the use of the wire reinforced membrane to maintain  $K_o$  conditions during consolidation. An assumption related to the orientation of the principal stresses has to be made for the construction of the Mohr's circle. Appendix A presents the most common hypotheses for failure conditions in simple shear testing. For this work, failure criterion 1 in which the maximum horizontal shear stress is also the shear strength of the soil ( $s_u$ ) will be used.

For  $CK_\alpha$  consolidated monotonic tests (GOM-1 and GOM-2), both tests show a continuous increase in shear stress until large strains are reached. Test GOM-3, in which the specimen was strained in the same direction (downslope) as the consolidation shear stress, has a larger shear strength than the other tests and once the shear stress has reached the failure envelope continues down the failure envelope with continued shear

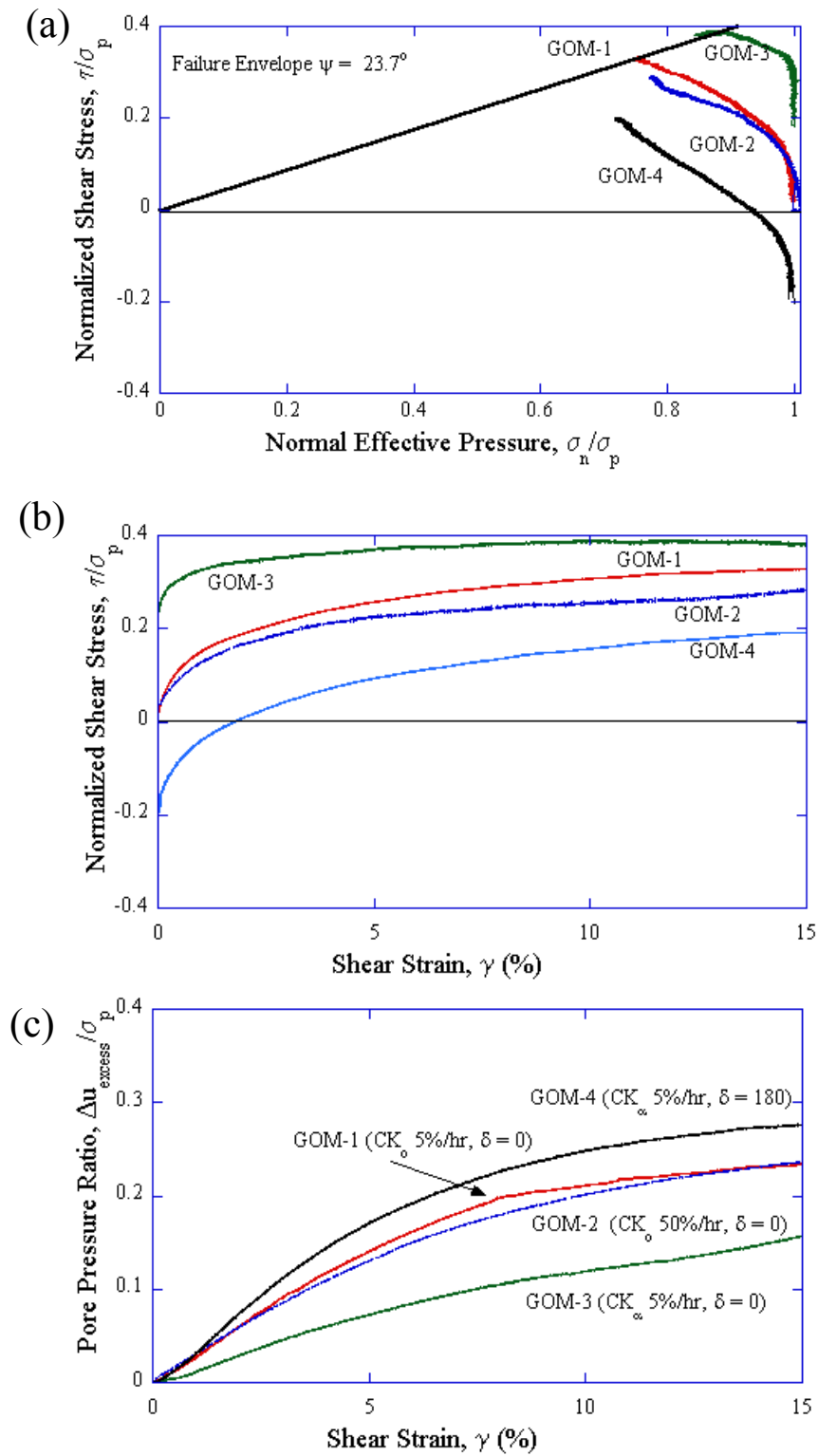


**Fig. 6.3.** Monotonic test results (a) stress paths, (b) stress-strain curves, and (c) pore pressure ratio

strain. For the upslope shearing case, GOM-4, the shear strength shows a ductile behavior and does not reach the failure envelope. Additional shear strain may be required for the shear stress to continue to the failure envelope.

### **6.3.2 Cyclic Tests**

Five specimens were consolidated and subjected to uniform cycles of shear loading at a frequency of 0.1 Hz. Test GOM-5 was  $CK_0$  consolidated and sheared at an amplitude of  $\tau_{cyc}/\sigma'_{vc}$  of 0.2. This test represents the baseline for level ground conditions in terms of the cyclic response of Gulf of Mexico clay. Figure 6.4 shows results for GOM-5.

Four specimens were  $CK_\alpha$  consolidated at  $\tau_c/\sigma'_{vc} = 0.2$ , which is equivalent to a slope of  $11.3^\circ$ . Two different cyclic stress ratios ( $CSR = \tau_{cyc}/\sigma'_{vc}$ ) of 0.15 and 0.2 were investigated. GOM-6 was  $CK_\alpha$  consolidated and sheared at a frequency of 0.1 Hz and  $\tau_{cyc}/\sigma'_{vc} = 0.2$  in the same direction as the consolidation shear stress ( $\delta = 0^\circ$ ). Similarly, GOM-7 was  $CK_\alpha$  consolidated and sheared at a frequency of 0.1 Hz at  $\delta = 0^\circ$ , however, the cyclic shear stress ratio was 0.15. GOM-8 and GOM-9 were  $CK_\alpha$  consolidated and sheared at a frequency of 0.1 Hz, however, were sheared in the perpendicular direction ( $\delta = 90^\circ$ ) of the consolidation shear stress equivalent to shearing across the slope.

The fundamental soil behavior during cyclic shearing is the development of excess pore pressure with accumulation of plastic strains as the number of cycles increases. The excess pore pressure versus the number of cycles for the two cyclic shear stress ratios (CRS) is plotted in Figure 6.5. The accumulation of plastic strains with

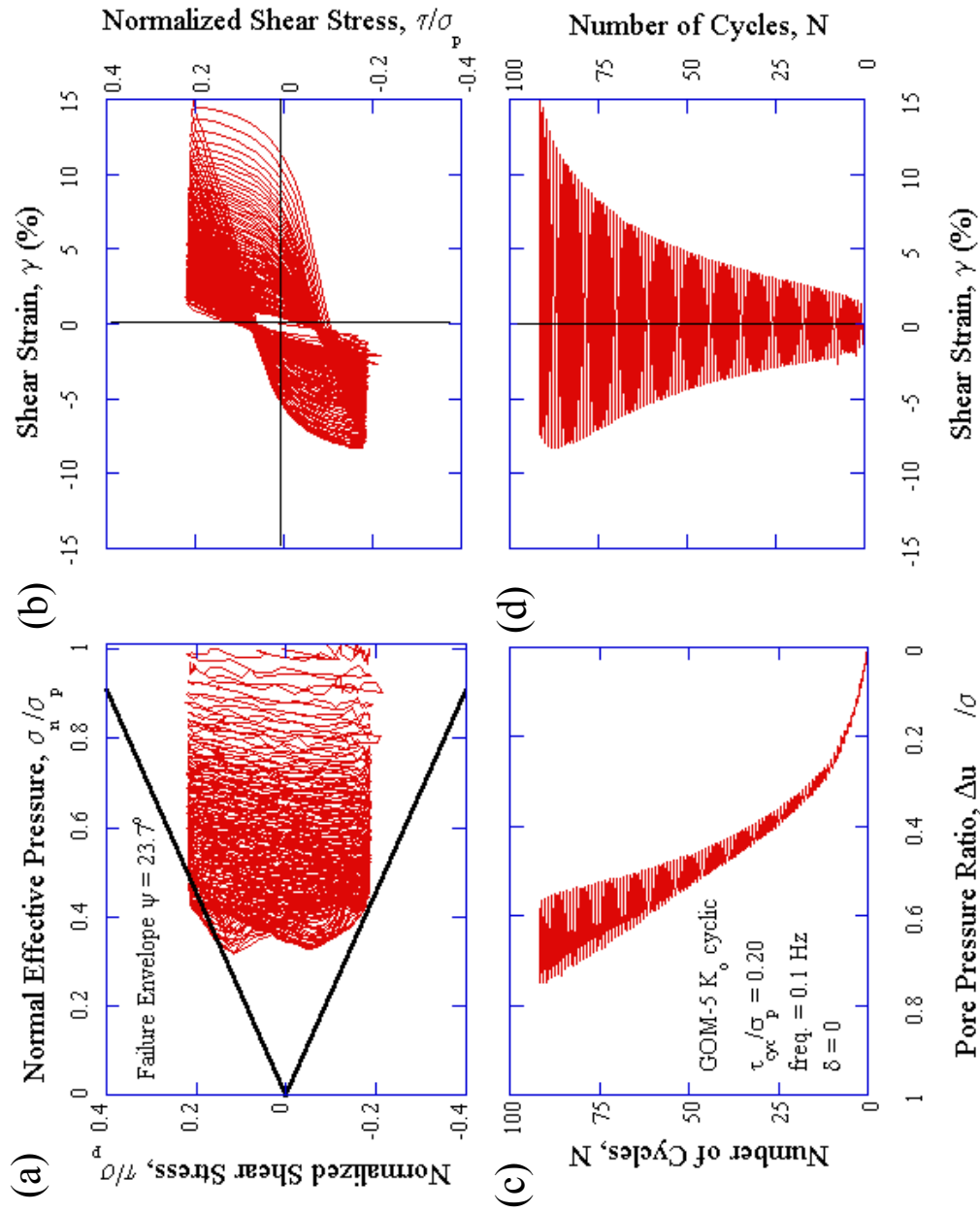


**Fig. 6.4.** GOM-5  $CK_0$  cyclic test results (a) stress path, (b) stress-strain curve, (c) pore pressure ratio, and (d) shear strain with cycles

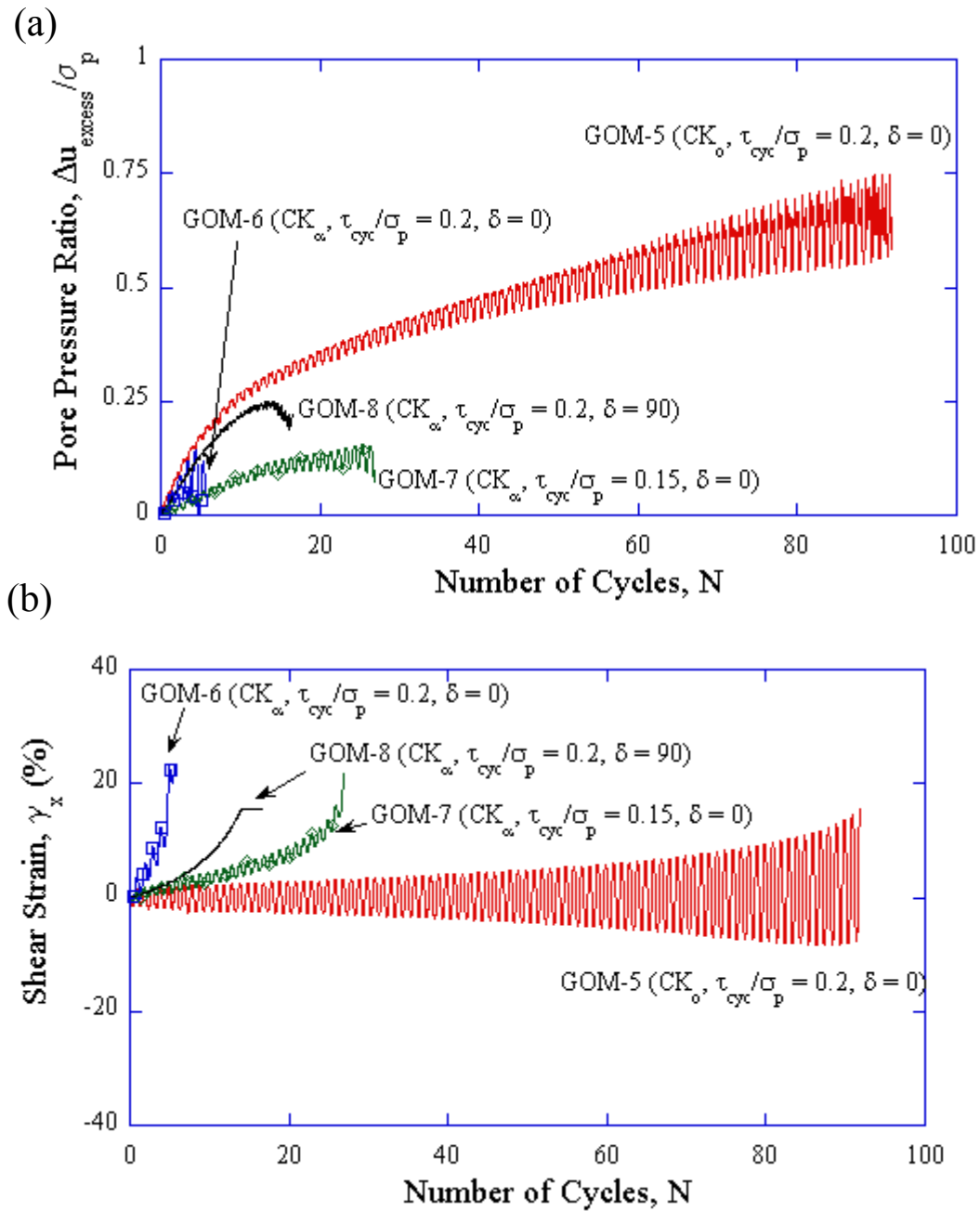


**Fig. 6.5.** Cyclic tests (a) development of pore pressures, (b) accumulation of plastic strains

progressing cycles is also plotted. The value of CRS and the application to an initial static driving stress directly influences the generation of pore pressure during the test.

For  $CK_{\alpha}$  consolidated tests (GOM-6, GOM-7, GOM-8 and GOM-9), excess pore pressure generation was significantly decreased in comparison with GOM-5 simulating level ground. Test GOM-5 reached a pore pressure ratio ( $\Delta u_{\text{excess}}/\sigma_p$ ) of approximately 0.75 while the other tests accumulated permanent strains in the downhill direction very quickly thus limiting the generation of excess pore pressure.

For tests GOM-8 and GOM-9 in which undrained shearing was performed perpendicular to the direction of the consolidation shear stress ( $\delta = 90^\circ$ ), the specimen also failed in the downhill direction. Because the stresses are loading the specimen in the same direction at the point of the test where the material is the softest, permanent displacements accumulate in the direction of the consolidation shear stress, in this case, the x-direction.

As the cyclic stress ratio increased from 0.15 to 0.20, as illustrated in tests GOM-6 and GOM-7, the rate of the accumulation of permanent strains increased and the generation of excess pore pressures also increased. Test GOM-6 at a CRS value of 0.2 accumulated shear strains over 15% in 5 cycles, whereas test GOM-7, in which the CRS value was 0.15, did not accumulated shear strains over 15% until 26 cycles.

### ***6.3.3 Circular Tests***

Due to the complexity of earthquake loading, circular load patterns were used to simplify the multi-directional shearing of the specimen. Three specimens were subjected to a circular stress loading pattern at a frequency of 0.1 Hz. GOM- 10 was  $CK_{\circ}$

consolidated and sheared at a cyclic shear stress ratio,  $\tau_{cyc}/\sigma'_{vc} = 0.2$  (Figure 6.6). This test was used as the baseline for circular shearing on level ground. Figure 6.7 compares the generation of excess pore pressure and accumulation of plastic strains with cycles for the circular tests.

Results for test GOM-10 show failure of the specimen occurs at approximately 13 cycles and moves in a positive x-direction. The pore pressure ratio was approximately 0.5. GOM-11 and GOM-12 were  $CK_{\alpha}$  consolidated and sheared at CRS of 0.15 and 0.2, respectively. Both tests accumulated permanent strains in the direction of the consolidation shear stress and generated approximately the same excess pore pressure, however, tests GOM-11 failed in 7 cycles whereas tests GOM-12 failure in 27 cycles.

Due to the symmetry of the circular tests, the shear stress values do not approach zero at any point in the tests unlike cyclic and figure-8 tests. The excess pore pressure generation for the circular tests on sloping ground are similar to the magnitudes in the  $CK_{\alpha}$  cyclic tests, however, accumulate permanent strains at a lower number of cycles.

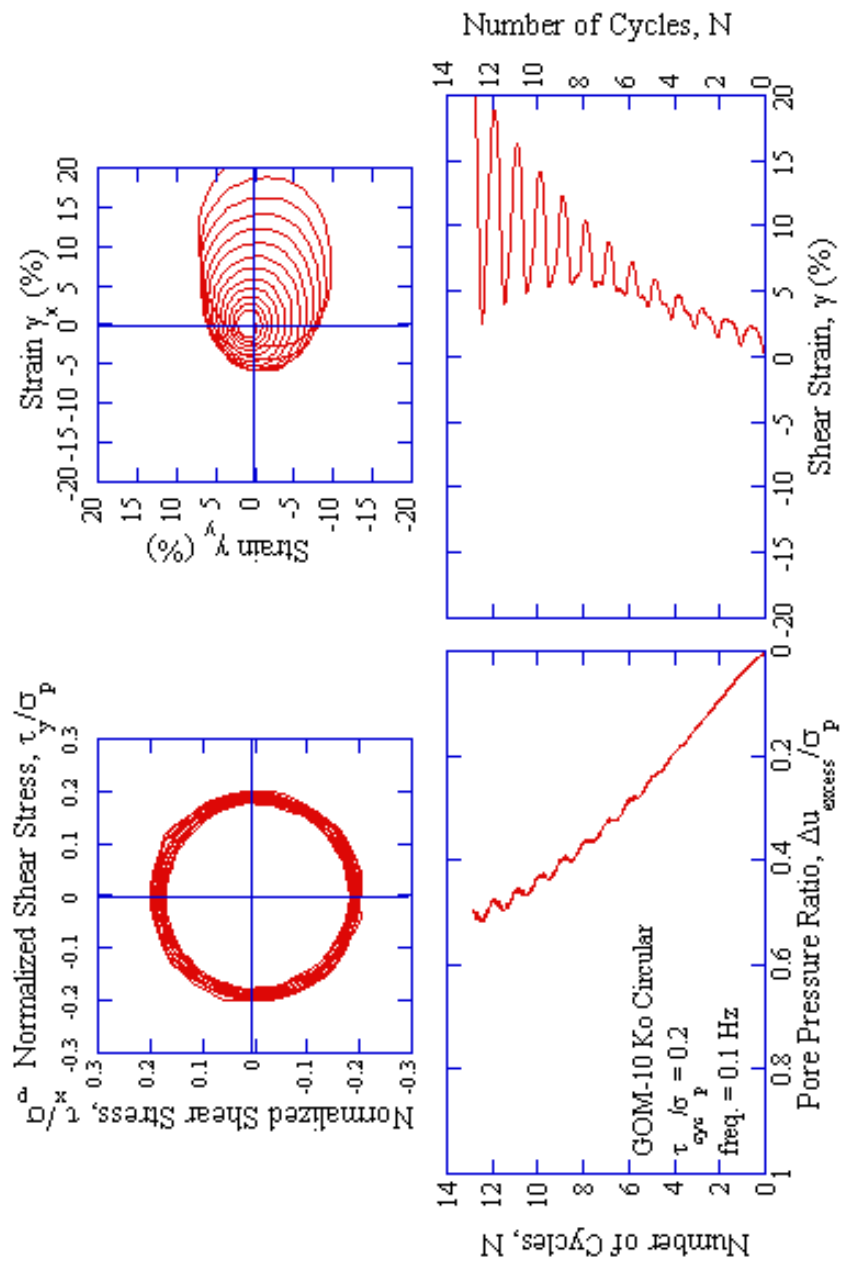


**Fig. 6.6.** GOM-10 CK<sub>o</sub> circular test results (a) shear stress pattern, (b) shear strain in x and y-directions, (c) pore pressure ratio, and (d) shear strain with cycles



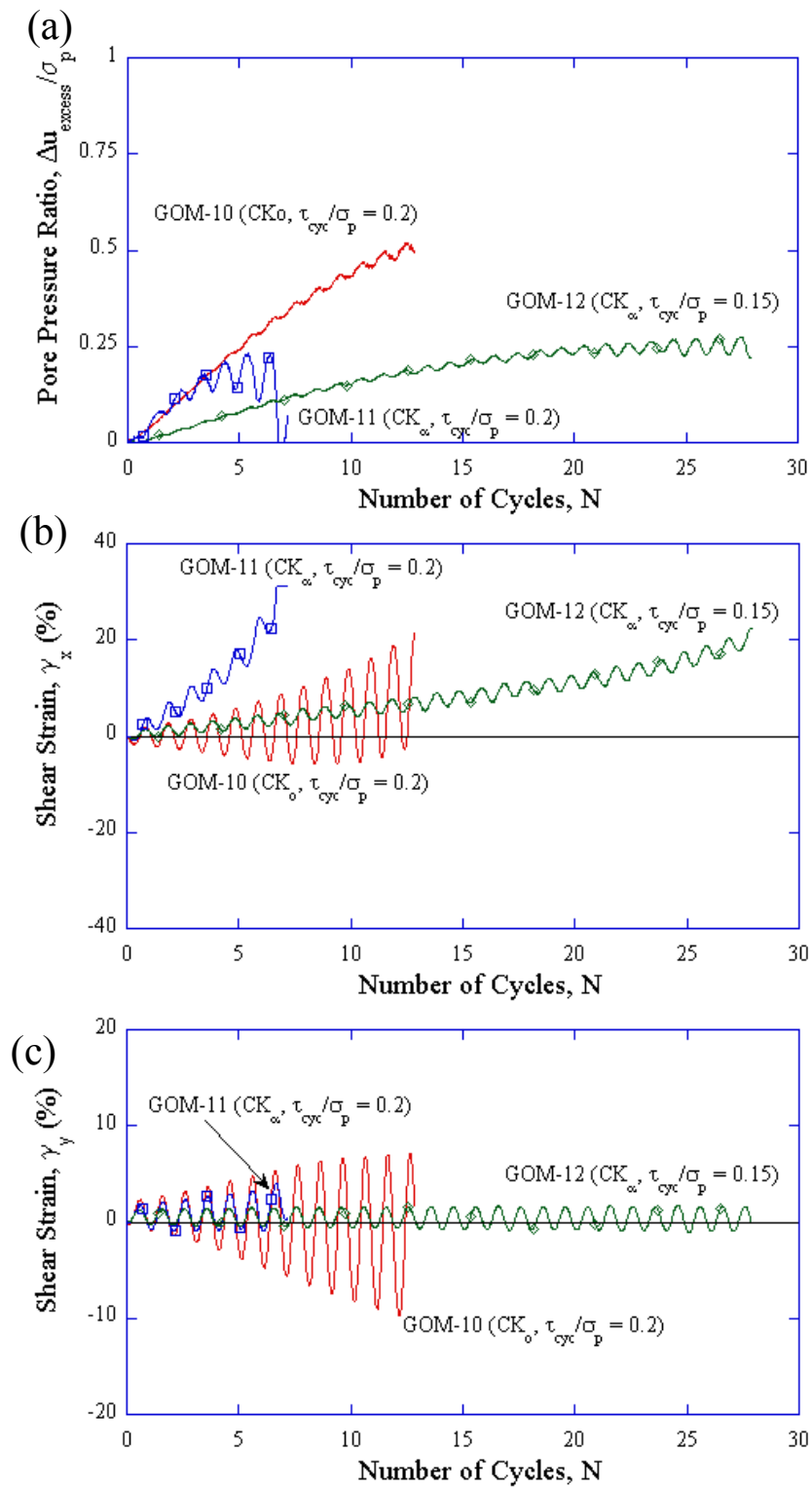
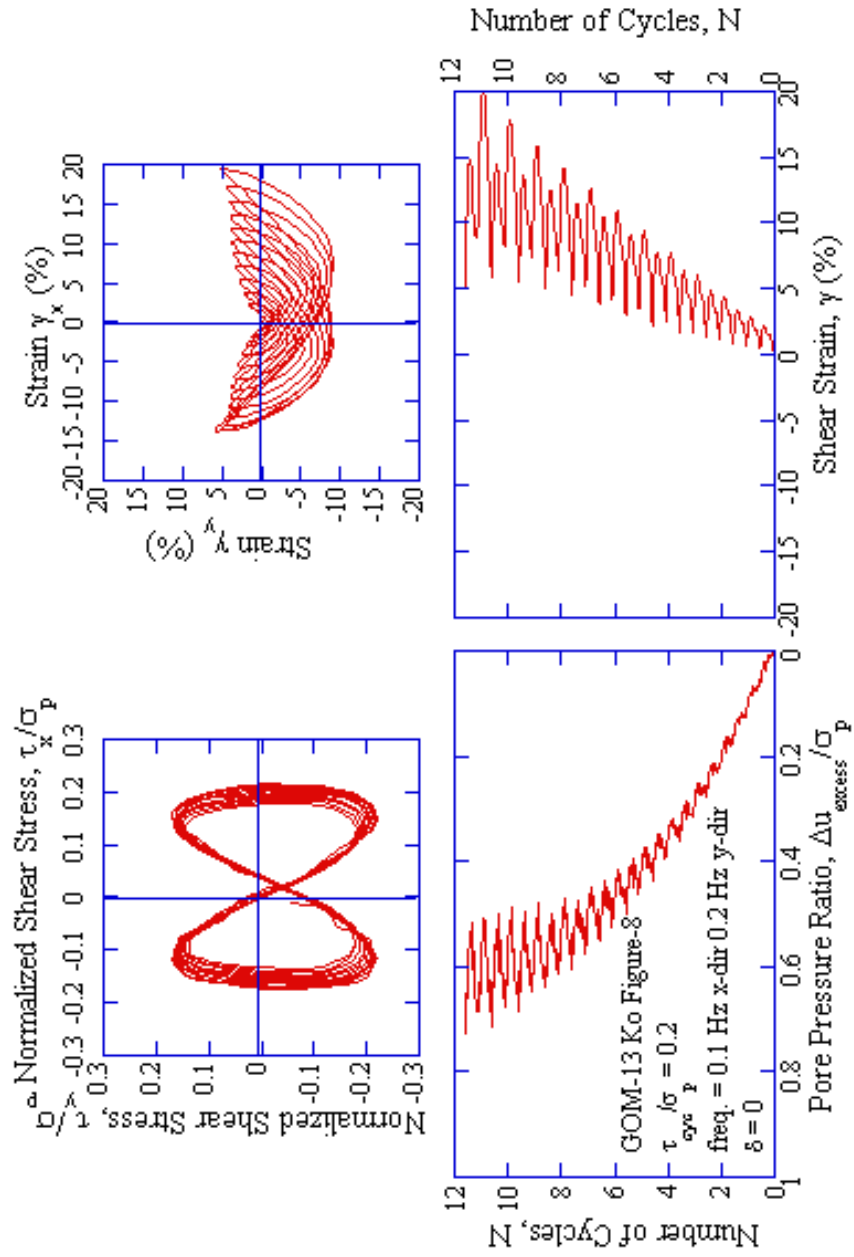


**Fig. 6.7.** Circular tests (a) development of pore pressures, (b) accumulation of plastic strains x-direction, (c) accumulation of plastic strain y-direction

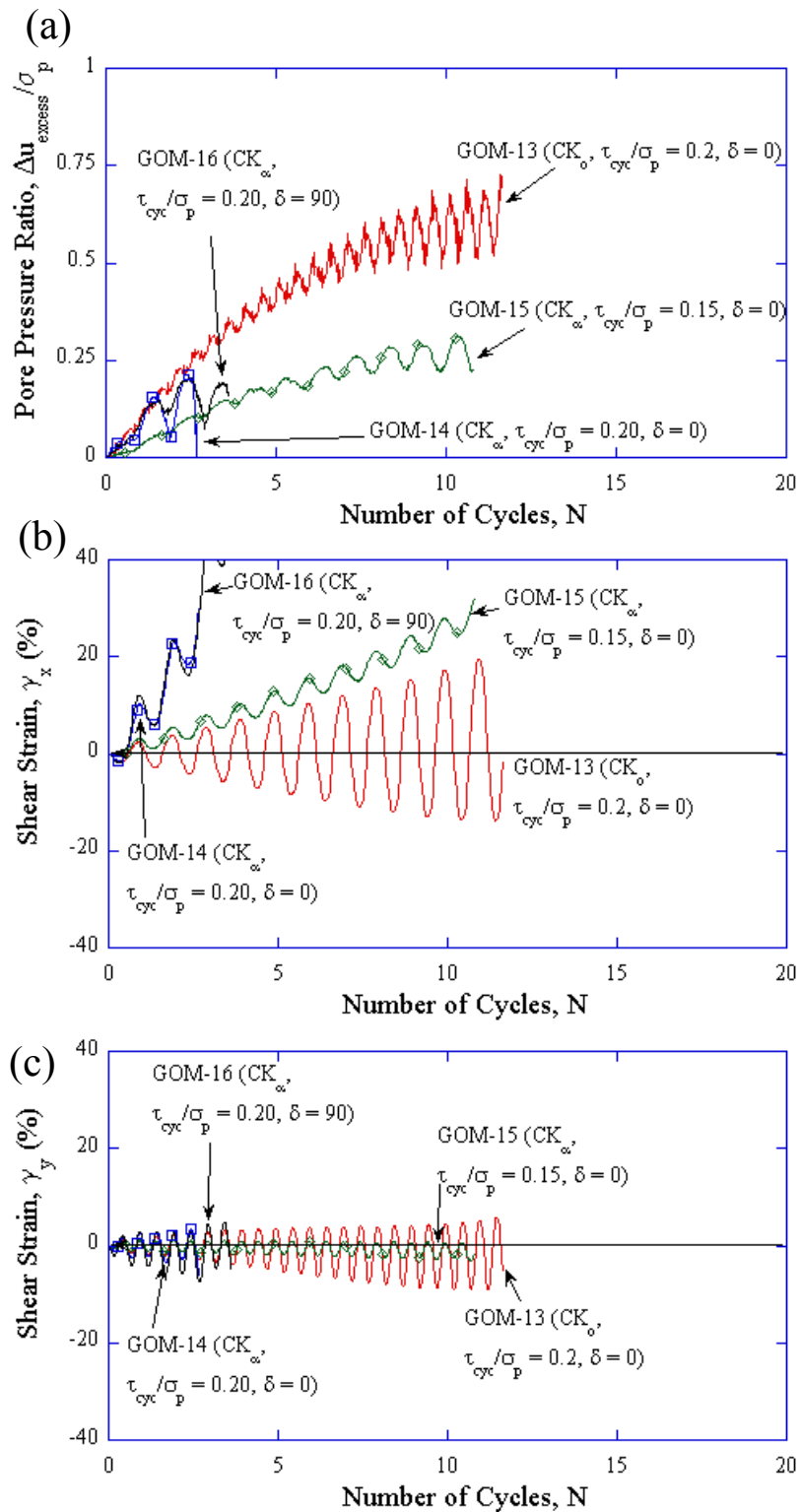
### 6.3.4 Figure-8 Tests

Figure-8 tests were used as simplified earthquake loading patterns. Five figure-8 tests were conducted at a frequency of 0.1 Hz in the x-direction and simultaneously a frequency of 0.2 Hz in y-direction. GOM-13 was  $CK_0$  consolidated and sheared at a cyclic shear stress ratio,  $\tau_{cyc}/\sigma'_{vc} = 0.2$  (Figure 6.8). This tests will be used the figure-8 baseline for level ground. Four tests (GOM-14, GOM-15, GOM-16 and GOM-17) were  $CK_\alpha$  consolidated and subjected to a figure-8 stress loading pattern at two cyclic stress ratios and in two different directions. GOM-14 and GOM-15 were sheared in the same direction as the consolidation shear stress ( $\delta = 0^\circ$ ) while GOM-16 and GOM-17 were sheared perpendicular to the consolidation shear stress ( $\delta = 90^\circ$ ). GOM-14 and GOM-16 were sheared with a cyclic stress ratio of 0.2 while GOM-15 and GOM-17 were sheared with  $\tau_{cyc}/\sigma'_{vc} = 0.15$ . Figure 6.9 compares the generation of excess pore pressure and accumulation of plastic strains with cycles for the circular tests.

Test GOM-13 simulating level ground generates the largest pore pressure ratio of approximately 0.75 which is the same magnitude as the pore pressure generation by the cyclic  $CK_0$  test GOM-5. As the CRS was decreased, the number of cycles during accumulation of permanent strains increased from 3 cycles to 11 cycles. The excess pore pressure generation for the tests simulating sloping ground generate approximately the same excess pore pressure ratios. Tests performed perpendicular to the consolidation shear stress generate more excess pore pressure than the other  $CK_\alpha$  tests, however, accumulated permanent strains in the downhill direction regardless of the cyclic shear stress ratio.



**Fig. 6.8.** GOM-13 CK<sub>o</sub> figure-8 test results (a) shear stress pattern, (b) shear strain in x and y-directions, (c) pore pressure ratio, and (d) shear strain with cycles



**Fig. 6.9.** Figure-8 tests (a) development of pore pressures, (b) accumulation of plastic strains in x-direction, and (c) accumulation of plastic strain in y-direction

## 6.4 Conclusions

Results of  $CK_0$  consolidation cyclic and multi-directional tests (GOM-5, GOM-10, and GOM-13) indicate that the largest generation of excess pore pressures occurs for specimens subjected to full stress reversals. Because of the different geometries of the stress paths, pore pressure generation is affected in different ways by the inclusion of an initial driving shear stress even if the nominal amount of stress reversal is the same.

Figure-8 tests accumulated permanent deformations in less cycles than both cyclic and circular tests due to the combination of the horizontal shear stress rotation and complete shear stress removal and reversal during loading. For tests incorporating an initial horizontal shear stress, the strains migrated in the downhill direction regardless of the orientation of the cyclic loading.

These findings have important implications for the stability of the slope, predicting that forces acting downward in the slope direction will need to mobilize less strain to reach peak strength and initiate failure. During cyclic tests with no initial shear stress ( $\tau_c = 0$ ) simulating level ground, the cyclic strains are symmetrically centered around the zero strain axis, with full reversal at each cycle. When  $\tau_c \neq 0$  (simulating a slope) an average shear strain accumulates during the tests and the maximum and minimum shear strains are not centered around the zero strain axis.

## 7. SUMMARY AND CONCLUSIONS

### 7.1 Summary

This dissertation describes the development of a new multi-directional direct simple shear testing device, the Texas A&M Multi-directional Direct Simple Shear (TAMU-MDSS), for testing marine soil samples under conditions, which simulate, at the element level, the state of stress acting within a submarine slope under dynamic loading. Prototype testing and an experimental program to characterize the response of marine clays to complex loading conditions is presented.

The work is divided into four major components: 1) Equipment Development: Design and construction of a prototype multi-directional direct simple shear testing device (TAMU-MDSS) that addresses the limitations of previous devices. 2) Support systems: selection of control software, development of data acquisition system and design of back pressure systems for direct pore pressure measurements. 3) Prototype Testing: performance of the TAMU MDSS system and testing of strain-control and stress-control capabilities. 4) Experimental Testing: characterize the response of marine clays to monotonic, dynamic and random loads.

The two-directional monotonic, cyclic, circular and figure-8 tests demonstrated the undrained shear strength increases with increasing initial shear stress,  $\tau_c$  (i.e, slope), for shearing in the same direction (equivalent to downhill). The strength decreases for shearing in the direction opposite to the initial stress (shearing uphill). The response is brittle for shearing in the same direction as the shear stress applied during consolidation

( $\tau_c$ ) and ductile for shearing opposite to  $\tau_c$ . These findings have important implications for the stability of the slope predicting that forces acting downward in the slope direction will need to mobilize less strain to reach peak strength and initiate failure. This information provides insight into the behavior of marine soils under complex loading conditions and provides high quality laboratory data for use in constitutive and finite element model development for analysis of submarine slopes.

## **7.2 Recommendations for Future Work**

### ***7.2.1 TAMU-MDSS Device***

Like other devices of its type, the TAMU-MDSS has some measureable frictional resistance between the horizontal loading plates during strain-controlled motions. An additional evaluation of the “device friction” should be conducted to determine the extent in which application of vertical load to the horizontal plates effects the measured frictional resistance. Control of the TAMU-MDSS using ATS has some limitation specifically related to the PID controls. A sensitivity analysis of the gains to specific material stiffness is required. Currently, the multi-axis load cell data acquisition is recorded on a separate system. Incorporation of all sensor measurements into one data acquisition system would be beneficial. The backpressure and cell pressure system could be automated using flow pumps and an air pressure controller to facilitate the backpressure portion of the testing.

### ***7.2.2. Multi-directional Testing of Gulf of Mexico Clays***

An experimental testing program using reconstituted samples could be conducted to compare the results with undisturbed tests conducted in this research. Specimens

could also be consolidated at different OCR to determine influence of over consolidation on behavior. The tests conducted in this experimental study focused on a single slope angle, however, testing should be carried out to determine to what extent different slope angles effect the behavior. Additionally, tests at varying cyclic frequencies and different cyclic stress ratios could be conducted to provide more insight into the multi-directional undrained shear behavior of Gulf of Mexico clays subjected to complex load patterns.



## REFERENCES

Airey, D., M. Budhu, and D. Wood (1985). "Some aspects of the behavior of soils in simple shear." *Developments in Soil Mechanics and Foundation Engineering, Stress-Strain Modeling of Soils*, Elsevier, London, U.K., Chapter 6, 185-213.

Airey, D. and Wood, D. (1987). "An evaluation of direct simple shear tests on clay." *Geotechnique*, 37(1), 25-35.

Al-Khafaji, Z. A., Young, A. G., DeGroof, W. and Humphrey, G. D. (2003). "Geotechnical properties of the Sigsbee Escarpment from deep soil borings." 2003 Offshore Technology Conference, Houston, TX, U.S.A., 5-8 May 2003. paper no. OTC 15158.

Amer, M. I., Kovacs, W. D., and Aggour, M.S. (1987). "Cyclic simple shear size effects." *J. of Geotech. Engrg.* 113(7), 693-707.

Andersen, K., Pool, J., Brown, S., and Rosenbrand, W. (1980). "Cyclic and static laboratory tests on Drammen clay." *J. of Geotech. Engrg. Div.*, 106(GT5), 499-529.

Azzouz, A., Malek, A., and M. Baligh (1989). "Cyclic behavior of clays in undrained simple shear." *J. of Geotech. Eng.* 115(5), 637-657.

Bea, R. G. (1971). "How sea floor slides affect offshore structures." *Oil and Gas J.*, 69, 88-91.

Biscontin, G. (2001). "Modeling the dynamic behavior of lightly overconsolidated soil deposits on submerged slopes." Ph.D. Dissertation, University of California, Berkeley.

Bjerrum, L. (1954). *Theoretical and experimental investigations on the shear strength of soils*. Norwegian Geotechnical Institute, Oslo, Norway.

Bjerrum, L., and Landva, A. (1966). "Direct simple-shear test on a Norwegian quick clay." *Geotechnique*, 16(1), 1-20.

Boulanger, R.W. (1990). "Liquefaction behavior of saturated cohesionless soils subjected to unidirectional and bidirectional static and cyclic simple shear stresses." Ph.D. Dissertation, University of California, Berkeley.

Boulanger, R. W. and Seed, R. B. (1995). "Liquefaction of sand under bidirectional monotonic and cyclic loading." *J. Geotech. Engrg.*, 121(12), 870-878.

- Boulangier, R.W., Chan, C. K., Seed, H. B., Seed, R.B., and Sousa, J. (1993). "A low-compliance bi-directional cyclic simple shear apparatus." *Geotech. Test. J.*, 16(1), 36-45.
- Bryant, W. R., Bryant, J. R., Feeley, M.H., and Simmons, G.R. (1990). "Physiographic and bathymetric characteristics of the continental slope, northwest Gulf of Mexico." *Geo. Mar. Letters.*, 10, 182-199.
- Bryant, W.R., Simmons, G.R., and Grin, P. (1991). "The morphology and evolution of basins on the continental slope, northwest Gulf of Mexico." *Gulf Coast Association of Geological Societies Transactions*, 41, 73-82.
- Budhu, M. (1985). "Lateral stresses observed in the simple shear apparatus." *J. of Geotech. Eng.*, 111(6), 698-711.
- Budhu, M. and Britto, A. (1987). "Numerical analysis of soils in simple shear devices." *Soils Found.*, 29(2), 31-41.
- Casagrande, A. (1976). "*Liquefaction and cyclic deformation of sands - A critical review.*" Harvard Soil Mechanics Series No. 88, Harvard University, Cambridge, MA., January.
- Casagrande, A. and Rendon, F. (1978). "Gyratory shear apparatus: Design, testing procedures." Technical Report S-78-15, Corps of Engineers Waterway Experiment Station, Vicksburg, MS.
- Coleman, J. and L. Garrison (1977). "Geological aspects of marine slope stability, northwestern Gulf of Mexico." *Marine Geotechnology* 2, 9-44.
- Deng, Y., White, G. N., and Dixon, J. B., (2009). "Soil mineralogy laboratory manual." 11th edition. Published by the authors, Department of Soil and Crop Sciences, Texas A&M University, College Station, TX 77843-2474.
- DeGroot, D. J. (1989). "The multidirectional direct simple shear apparatus with application to design of offshore arctic structures." Ph.D. Dissertation, Massachusetts Institute of Technology, Cambridge.
- DeGroot, D.J., Ladd, C.C., and Germaine, J.T. (1996). "Undrained multidirectional direct simple shear behavior of cohesive soil," *J. Geotech. Engrg.*, 122(2), 91-98.
- Duku, P.M., Stewart, J. P, Whang, D. H, and Venugopal, R. (2007). "Digitally controlled simple shear apparatus for dynamic soil testing," *Geotech. Test. J.*, 30(5), 1-10.

Dyvik, R.(1981). “Strain and pore pressure behavior of fine grained soils subjected to cyclic shear loading,” Ph.D. Dissertation, Reneesleae Polytechnic Institute, Troy.

Dyvik, R., Berre, T., Lacasse, S., and Raadim, B. (1987). “Comparison of truly undrained and constant volume direct simple shear tests.” *Geotechnique*, 37(1), 3-10.

Edgers, L. and Karlsrud, K. (1982). “Soil flows generated by submarine slides- case studies and consequences.” In *Proc. 3<sup>rd</sup> Int. Cong. On the Behavior of Off-Shore Structures*, Cambridge, MA. 2, 425-437.

Fine, I.V., Rabinovichb, A.B., Bornholdd, B.D., Thomsonb, R.E. and Kulikovb, E.A. (2005). “The Grand Banks landslide-generated tsunami of November 18, 1929: preliminary analysis and numerical modeling.” *Mar. Geol.*, 215, 45-57.

Finn, L. W. D., Pickering, D. J., and Bransby, P. L. (1971). “Sand liquefaction in triaxial and simple shear tests.” *J. Soil Mech. and Found. Div.*, 97(SM4). 639-659.

Finn, L. W. D., Bhatia, D. K., and Pickering, D. J. (1982). “The cyclic simple shear test.” *Soil mechanics – Transient and cyclic loads*, G. N. Pande and O. C. Zienkiewicz, eds., John Wiley & Sons, New York, NY, book chapter 21, 583-607.

Franke, E., Kiekbusch, M., and Schuppener, B. (1979). “A new direct simple shear device.” *Geotech. Test. J.*, 2(4), 190-199.

Frydman, S., Talesnick, M., Almagor, G., and Wiseman, G. (1988). “Simple shear testing for the study of the earthquake response of clay from the Israeli continental slope.” *Mar. Geotech.*, 7, 143-171.

Hampton, M. A., Lee, H.J. and Locat, J. (1996). “Submarine landslides.” *Reviews of Geophysics*, 34, 33-59.

Heezen, B.C. and Ewing, M. (1952). “Turbidity currents and submarine slumps, and the 1929 Grand Banks earthquake.” *American Journal of Science*, 250, 849-873.

International Centre for Geohazards. (2010). “Offshore Geohazards.”<  
<http://www.ngi.no/en/Geohazards/Research/Offshore-Geohazards/>> (Dec. 16, 2011).

Ishihara, K. and Yamazaki, F., (1980). “Cyclic simple shear tests on saturated sand in multi-directional loading.” *Soil Found.*, 20(1), 45-59.

Jeanjean, P., Hill, A., Taylor, S. (2003). “The challenges of siting facilities along the Sigsbee Escarpment in the southern Green Canyon area of the Gulf of Mexico: Framework for Integrated Studies.” Offshore Technology Conference, OTCX 15156.

Kammerer, A. (2001). "Undrained response of cohesionless soils under multidirectional cyclic simple shear conditions." Ph.D. Dissertation, University of California, Berkeley.

Kammerer, A. M., Hunt, C. E., and Riemer, M. (1999). "UC Berkeley geotechnical testing for the East Bay crossing of the San Francisco-Oakland Bay Bridge." Report No. UCB/GT/99-18, Department of Civil and Environmental Engineering, University of California, Berkeley.

Kjellman, W. (1951). "Testing the shear strength of clay in Sweden." *Geotechnique*, 2(3), 225-235.

Lacasse, S., Dyvik, R., and Hoeg, K. (1988). "Discussion on the behavior of normally consolidated clay as observed in undrained direct shear tests by Wroth (1987)." *Geotechnique*, 38(1), 144-146.

Ladd, C. C. and Edgers, L. (1972). "Consolidated-undrained direct-simple shear tests on saturated clays." Report No. 16, Department of Civil Engineering, Massachusetts Institute of Technology, Cambridge.

Lewis, K. (1971). "Slumping on a continental shelf inclined at 1 to 4." *Sedimentology*, 16, 97-110.

Lucks, A., Christian, J., Brandow, G., and Hoeg, K. (1972). "Stress conditions in NGI simple shear test." *J. of the Soil Mechanics and Found. Div.* 98 (SM1), 155-160.

Madhuri, M. (2011). "Characterization of Gulf of Mexico clay using automated triaxial testing." M.S. Thesis, Texas A&M University, College Station.

Malek, A. M. (1987). "Cyclic behavior of clay in undrained simple shearing and application to offshore tension piles." Ph.D. Dissertation, Massachusetts Institute of Technology, Cambridge.

McAdoo, B. G. and Watts, P. (2004). "Tsunami hazard from submarine landslides on the Oregon continental slope." *Mar. Geol.*, 203, 235-245.

McCarron, W. O., Lawrence, J. C., Werner, R. J., Germaine, J. T., and Cauble, D. F. (1995). "Cyclic direct simple shear testing of Beaufort Sea clay." *Can. Geotech. J.*, 32(4), 584-600.

Prevost, J. and Hoeg, K. (1976). "Reanalysis of simple shear soil testing." *Canadian Geotech. J.* 13(4), 418-429.

Prior, D. and J. Coleman (1978). "Disintegrating retrogressive landslide on very-low-angle subaqueous slopes, Mississippi delta." *Marine Geotechnology*, 3(1), 37-60.

Rau, G. A. (1999). "Evaluation of strength degradation in seismic loading of holocene bay mud from Marin County, California." Ph.D. Dissertation, University of California, Berkeley.

Roscoe, K. (1953). "An apparatus for the application of simple shear to soil samples." *Proc. of the 3<sup>rd</sup> Int. Conf. In Soil Mechanics and Foundation Engineering*, Zurich, Switzerland, 1, 186-191.

Saada, A. and Townsend, F. (1981). "State of the art: Laboratory strength testing of soils." *Laboratory shear strength of soil*, R. N. Yong and F. C. Townsend (Eds.), American Society of Testing and Materials, Philadelphia, PA, 7-77.

Saada, A. S., Fries, G., and Ker, C. C., (1982). "An evaluation of laboratory testing techniques in soil mechanics." *J. of Geotech. Engrgr.*, 123(3), 379-398.

Schapery, R. and Dunlap, W. (1978). "Prediction of storm induced sea bottom movement and platform forces." Offshore Technology Conference, Houston TX, 1789-1796.

Shen, C.K., Sadigh, K., and Herrmann, L. R., (1978), "An analysis of NGI simple shear apparatus for cyclic load testing." *Dynamic Geotechnical Testing*, ASTM STP 654, ASTM International, West Conshohocken, PA, 148-162.

Slowey, N. C., Bryant, W. R., Bean, D.A., Young, A.G., and Gartner, S. (2003). "Sedimentation in the vicinity of the Sigsbee Escarpment during the last 25,000 years." *Proc. 19<sup>th</sup> Int'l OMAE Conference*, paper no. 5045.

Sousa, J. B. and Chan, C. K. (1991). "Computer applications in the geotechnical laboratories of the University of California at Berkeley." *Geotechnical Engineering Congress*, Geotechnical Engineering Division of ASCE.

Tappin, D., Watts, P., McMurty, G., Lafoy, Y., and Matsumoto, T. (2001). "Prediction of slump generated tsunamis: the July 17, 1998 Papua New Guinea tsunami." *Prediction of underwater landslide hazards*, P. Watts, C.E. Synolakis, and J.-P. Bardet (Eds.), Balkema, The Netherlands.

TDI-Brooks International. "Welcome to TDI-Brooks International." <[www.tdi-bi.com](http://www.tdi-bi.com)> (Dec. 16, 2011).

Torkornoo, R. (1991). "Multidirectional simple shear behavior of an overconsolidated clay." Master Thesis, University of Massachusetts, Amherst.

Vucetic, M. and Lacasee, S. (1982). "Specimen size effect in simple shear test." *J. of the Geotech. Engrg Div.*, 108(GT12), 1567-1585.

Young, A.G., Bryant, W.R., Slowey, N.C., Brand, J.R., and Garnter, S. (2003a). "Age dating of past slope failures of the Sigsbee Escarpment within Atlantis and Mad Dog developments." Offshore Technology Conference, Houston TX, OTC 15204.

Young, A.G., Honganen, C.D., Silva, A.J., and Bryant, W.R. (2003b). "Comparison of geotechnical properties from large-diameter long cores and borings in deep water Gulf of Mexico." Offshore Technology Conference, Houston TX, OTC 12089.

**APPENDIX A**  
**SIMPLE SHEAR TESTING OF CLAYS**

**A.1. Stresses in the Simple Shear Device**

Simple shear conditions refers to the plane strain condition in which only the shear strain  $\gamma_{yx}$  and the vertical strain,  $\varepsilon_{yy}$ , are non-zero. The strain,  $\varepsilon_{zz}$ , and engineering strains,  $\gamma_{yx}$  and  $\gamma_{zx}$  are equal to zero. For constant volume tests, no vertical displacement occurs and  $\varepsilon_{yy}$  is also zero. However, implementation of these conditions is difficult to attain in laboratory testing devices as illustrated in Figure A.1.

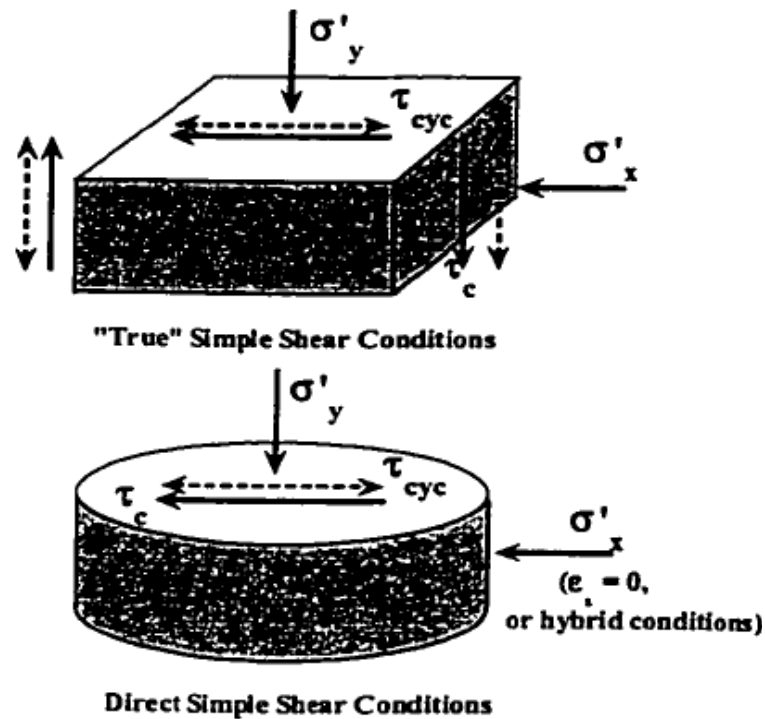


**Fig. A.1.** (a) General strain state; (b) Simple shear strain state (After Biscontin, 2001).

The idealized in-situ boundary conditions in the field require four main assumptions for direct simple shear testing. The assumption of the constant volume of the sample implies no drainage of pore pressure redistribution during loading. This assumption also implies that any shear loading imposed occurs so rapidly that drainage of the soil cannot occur. The application of a constant vertical load to the sample implies that the overburden remains constant during shearing. Assuming no lateral strain of the specimen presumes the deposit is of large horizontal extent that lateral stresses throughout the layer are such that lateral strains do not occur. Finally, the maintenance of a constant height of the sample is assumed because if the volume is constant and no lateral strains occur then the height must be also be constant.

A wire-reinforced membrane is used to maintain the boundary conditions of constant volume and no lateral strain, although, one drawback is that lateral stresses cannot be easily measured. Stacked rings have been used in some direct simple shear testing devices, however, in this research stacked rings are not used because of possible inherent mechanical restraint against multi-directional loading. By using a device with chamber pressure and direct measurements of pore pressure, constant load can be maintained during tests. Constant height is assumed since the sample has completed the consolidation phase of the testing and drainage is prevented during shearing.

A criticism of direct simple shearing testing is mainly due to the inability to impose uniform normal and shear stresses to a test specimen. Non-uniform stresses conditions (Figure A.2) in simple shear tests specimens may develop due to (Boulanger, 1990):



- 1) The lack of complimentary shear stresses on the lateral boundaries
- 2) Corner and edge effects
- 3) Non-rigid boundaries which allows stress redistribution
- 4) Pinching effects which may result from any relative rocking motions between the sample's cap and base
- 5) Consolidation which is not truly one-dimensional which in combination with the rigid top and bottom boundaries results in non-uniform radial shear stresses

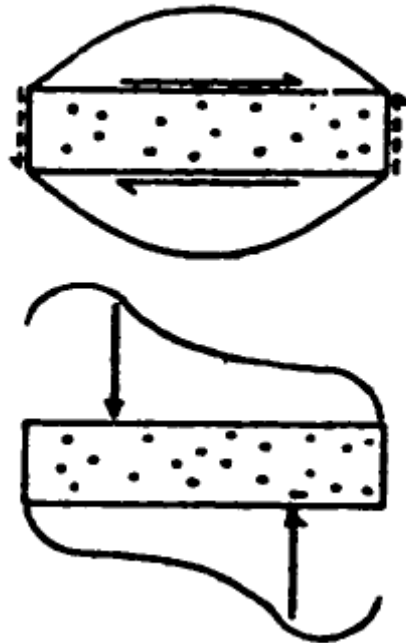


**Fig. A.2.** Schematic distribution of non-uniform distribution (a) of shear stresses from absence of complementary shear stress on the ends of the sample; (b) of normal stresses on the top and bottom faces of a sample in the simple shear device (After Airey et al., 1985).

The influence of the lack of complementary shear stresses along the lateral boundaries of circular test specimens has been investigated both experimentally (Finn et al., 1971, Finn et al., 1982, Vucetic and Lacasse, 1982, Budhu, 1985, Airey and Wood, 1984) and numerically (Roscoe, 1953. Lucks et al., 1972). Budhu (1985) presented measurements of radial normal stresses obtained by instrumented wire wrapped membranes and compared with the measurements of two orthogonal lateral normal stresses that developed at the rigid lateral boundaries of an instruments Cambridge device (cuboidal sample). Airey and Wood (1984, 1987) showed that the uniformity of stresses improves as the plasticity of the material tested increases. Typical normal and shear stress distributions measured on the center of the sample during constant volume tests are shown in Figure A.3. Analytical and numerical test results suggest that for D/H values of 4 or greater the lack of complementary shear stress affects a relatively small portion of the sample such that the average shear stresses applied to the sample are reasonably representative of the shear stresses acting over the center portion of the sample.

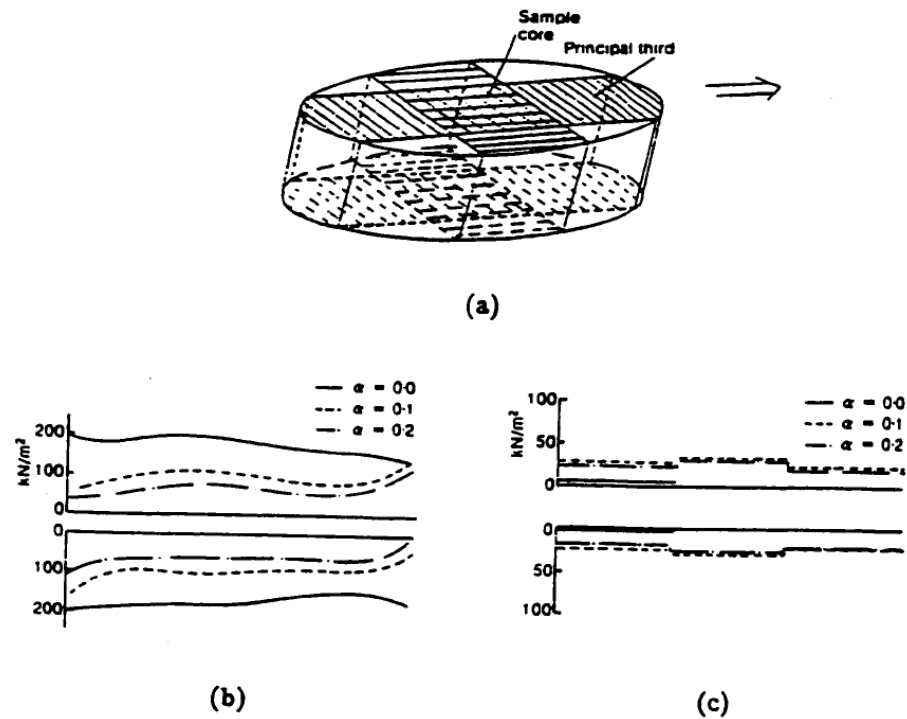


**Fig. A.3.** Stress distribution on the principal third for a constant volume test on kaolin in the Cambridge simple shear device (a) Principal third load cells; (b) Normal and (c) shear stresses ( $\alpha$  is the shear distortion  $\gamma_{xy}$ ) (after Airey and Wood, 1987).

## A.2. Undrained vs. Constant Volume Testing

Casagrande (1976) deviated from the traditional NGI method by placing the sample in a pressure cell allowing back pressure to be applied to ensure full saturation of the specimen and the direct measurement of the pore water pressure during the undrained shear test. This approach allowed for an alternative to the historical “constant volume” approach which had been introduced early on with the NGI apparatus (Taylor, 1953; Bjerrum, 1954). Constant volume of the specimen is ensured by maintaining a

constant height of the sample by changing the vertical load. The excess pore pressure is then assumed equal to the change in vertical stress.

Few existing simple shear devices have been designed to impose a chamber pressure allowing for the full saturation of the sample. Comparing direct measurements with “constant volume” results, monotonic tests by Dyvik et al. (1987) and Kammerer et al. (1999) show that the assumption that constant volume tests are equal to excess pore pressure measurements for saturated soils (Figure A.4 and A.5). No comparisons of the two methods are available in the literature for cyclic tests on saturated clays.

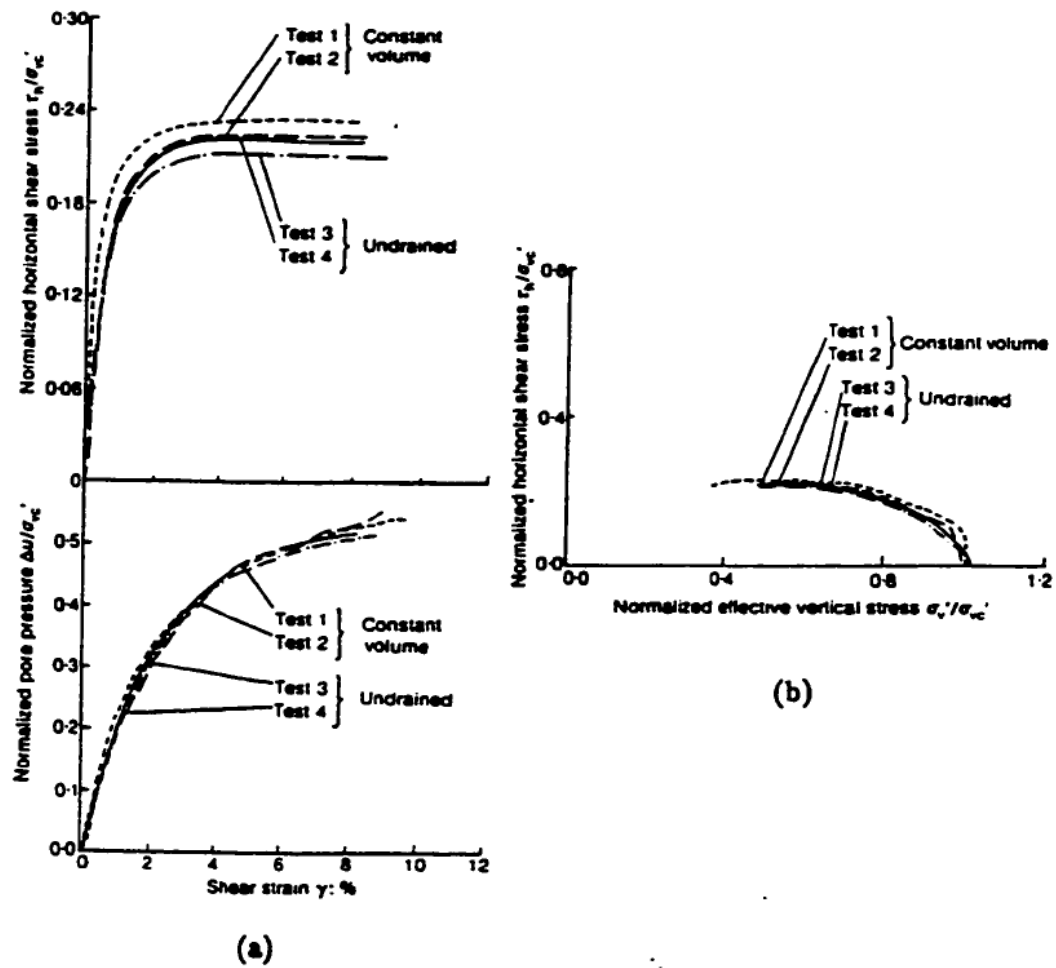
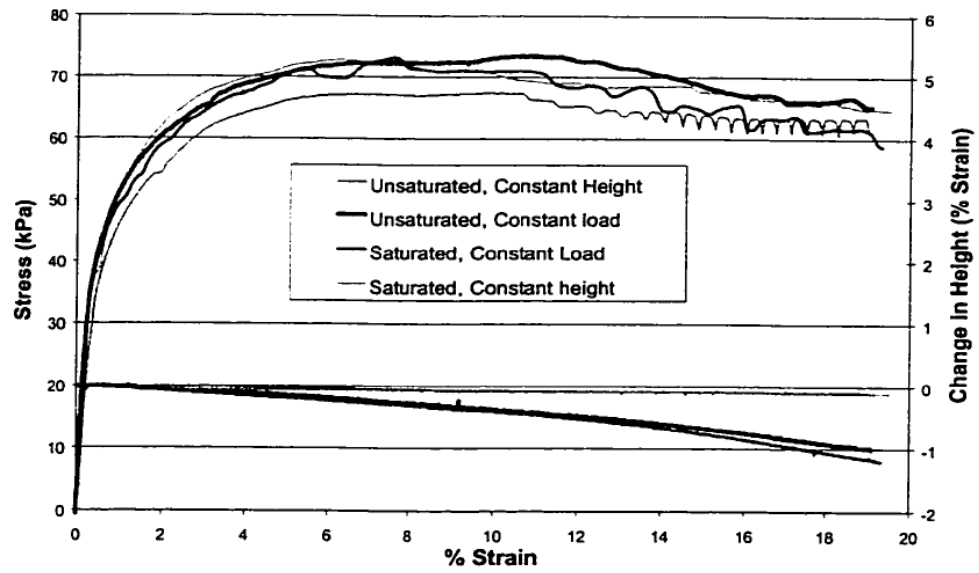


Fig. A.4. Comparison of constant volume and undrained tests results (Dyvik et al., 1987).



**Fig. A.5.** Comparison of specimens using different saturation conditions (After Kammerer et al., 1999).

## APPENDIX B

### TAMU-MDSS DEVICE TEST PROCEDURES

1 - Saturation of the caps (**Need:** caps, porous stones, de-aired water, vacuum chambers)

- De-air vacuum chamber with vacuum pump
- Pour de-aired water from the vacuum chamber into the reservoir or bowl
- Hook up the drain lines of the caps to the lines from the vacuum chamber and submerge the caps in the water (keep valve to lines closed)
- Apply house vacuum to vacuum chamber and open valve to one cap. Switch to the other cap to pull all the air out
- Take lines off from the connection closer to the caps
- Let the caps soak completely submerged

1a – Saturation of the caps (from dry condition)

- De-air water in the vacuum chamber and connect the lines
- Let water flow into the caps slowly through capillary suction
- Switch frequently

2- Preparing the sample (**Need:** core section, cm ruler, marker, pipe cutter, thin wire, glass plate, extruder, caps, o-rings, filter paper, spacer, dial gage, scale, water content cups, test information sheet, pen)

- Measure 20 mm on liner
- Use pipe cutter to cut liner
- Use wire to cut through soil
- Extrude soil from sampler (about 20 mm thick)
- Measure the caps with a spacer
- Weigh caps with membrane, clamps and 4 o-rings
- Weigh 2 water content cups (1 for trimmings and 1 for sample)

3 – Trimming the sample (**Need:** sample, caps, filter paper, trimming jig, wire saw, paper towels, wet rag, ziplok bag, moisture cup, level, scale, oven, test information sheet)

- Place sample on the filter paper and bottom cap
- Place bottom cap and sample on the trimming jig
- Position the bottom cap correctly for trimming
- Trim sample to desired diameter
- Use one trimming piece for moisture content
- Weigh trimming and cup and place in oven
- Place trimmings in labeled ziplok bag and place in moisture room

4 – Placing the membrane (**Need:** sample, caps, membrane, o-rings, square, level, dial gage, pi tape, vacuum chambers, vacuum source, test information)

- Remove sample and bottom cap from trimming jig
- Place filter paper and top cap
- Flip sample upside down to top cap
- Remove bottom cap
- Pull the wet membrane on the sample
- Use o-ring extender to stretch and place two o-rings on bottom cap
- Stretch two o-rings over extender for top cap and place around sample
- Replace top cap
- Check alignment with square and level
- Install 2-orings on top cap
- Fix o-ring location, sacrificial membranes and hose clamps
- Weigh the assembly
- Measure the height of the assembly
- Measure the diameter with pi tape
- Connect drain lines from vacuum chamber to caps
- Attach line to house vacuum
- Apply slight vacuum to top cap(about 1.5 in Hg) making sure bottom cap vacuum chamber is open
- Measure the height of the assembly
- Measure the diameter with pi tape
- Check if visible bubbles are coming out

5 – Seating the sample in the device (**Need:** assembled sample, vacuum chambers, socket wrench)

- Zero x and y axis strokes (control -> transducers -> zero units)
- Put sample into the device
- Move the sample still connected to the vacuum chamber to the device
- Little by little lower the top of the device toward the sample until there is just a small space left
- Load sample to 10lbs in vertical axis using stroke control
- Disconnect vacuum chamber from vacuum lines
- Connect water lines by wet connection (slight pressure on back pressure lines to cause constant dripping, 0.2 is enough)
- Change Z-axis from stroke control to load control and immediately manually lower the load back to 10lbs (changing to load control causes slight rise in piston)
- Check to make sure P gain is set to 100 for the remainder of the test
- Install top clamp around sample cap and fine loadcell, tighten by hand until you can no longer turn it



- Use ratchet with hexhead to tighten bottom sample cap to bar on lower plate, tighten each side equally while monitoring x and y loads to ensure they remain close to 0.0
- Record all initial readings
- Continue to backpressure steps

6 – Getting rid of the bubbles still in the sample (**Need:** cloth towel, vacuum chamber, house pressure, test information sheet)

- Flush the lines so that any bubbles are pushed out. Remember to use a towel to protect the device from the water
- Take line that is open to vacuum chamber (but no vacuum on it) and connect to one of the drainage line of the device). Make sure it is a “wet connection
- Repeat with the second line
- Select which line to get bubbles out
- Move vacuum chambers to top of chamber
- Disconnect lines and attach vacuum chambers
- Make sure that each vacuum chamber valve is open
- Using vacuum chamber attached to top and apply slight vacuum (2-5). Let stay until all bubbles make it out.
- Switch to the other vacuum chamber
- Close valves to samples
- Disconnect vacuum chambers
- Slightly increase back pressure just enough to push air out of drainage lines to the elevation of the top of the chamber
- Make a wet connection from drainage lines to valves
- Turn off pressure
- Open valves to samples
- Take LVDT measurements and initial volume measurements
- Close the chamber

7 – B value checks (**Need:** B-value check file, test information sheet, house pressure, back pressure calculation excel spreadsheet)

- Close A valve
- Close cell release valve under chamber (opened to allow oil in chamber to drain)
- Verify that nothing is in the path of the chamber as it is lowered
- Lower chamber by pushing chamber down button on the computer console
- Once chamber is completely lowered, switch metal toggle switch to on to prevent chamber from rising during test
- Increase cell pressure to 2psi and maintain the 10lbs load in the vertical direction (manually move back and forth increasing each incrementally to desired values) differential pressure goes down during this step

- Record vertical load, chamber pressure and effective stress (as indicated in the test sheet)
  - Close the b-valve and open the a-valve
  - Increase the differential pressure to 0.1
  - Open the b-valve
  - Slightly increase the back pressure to approximately 0.2 and hold for 30 min to 1 hour
  - Bring cell pressure up (~ 5 psi) until effective stress is about 10-12 kPa (1.45 – 1.75 psi) while keeping the vertical load constant (by increasing it slowly)
  - Wait until equilibrium is reached
  - Read measurements
  - Close B valve and open A valve
  - Increase backpressure until effective stress is back to slightly less than zero (~-0.2)
  - Open B valve, open A valve
  - Calculate B value check
  - Wait 10 minutes or more depending on how low B valve is
  - Close A valve
  - Check if effective stress is going up (suction: still need more time to get pore pressure down). Open A and let stand a little while.
  - Repeat B value check until you get a value over 0.95
  - Maximum house pressure is 29 psi
- 8 – Starting the consolidation (**Need:** Consolidation ATS file, test information sheet,
- When the B value check is right, let stand until re-equilibrated for the last time
  - Open ATS consolidation test file
  - Select vertical load needed to consolidated to the desired value of stress
  - Keep A valve open
  - Take LVDT readings and initial volume
  - Start data test
  - Reset column of water by opening and closing pipette/reservoir valve
  - Record ending consolidation test information on test sheet
- 9 – Starting shearing test (**Need:** Shear ATS file, test information sheet)
- Record information on test sheet
  - Make sure A valve is closed
  - Open ATS shear test file
  - Select shearing rate or shearing load needed for test
  - Take LVDT readings and initial volume
  - Start data test
  - Record ending shear test information on test sheet

10 – Removing sample from MDSS (**Need:** House pressure, assembled sample, scale, dial gage, pi tape, sample moisture content cup, test information sheet, oven)

- Open A valve
- Slowly decrease both cell pressure and back pressure maintaining a low effective stress difference (-.2 and -1.5 psi) also decreasing the total load on sample back to seating pressure of 5 lbs
- Once both cell pressure and back pressure are close to 1 psi turn off house pressure supply
- Remove line from house pressure supply
- Open chamber
- Switch Z axis to stroke control
- Loosen bottom clamps and top clamps
- Slowly rise Z\_stroke until able to remove sample
- Remove drainage lines and attach to t-valve
- Weigh sample
- Measure height and diameter
- Remove top cap and membrane
- Place sample in sample moisture content cup
- Weight sample and cup
- Place sample and cup in oven over night
- Take dry weights of trimmings and sample after 24 hours

## MULTI-DIRECTIONAL SIMPLE SHEAR TESTING DATA SHEET AND PROCEDURE CHECKLIST

---

Sample: \_\_\_\_\_ Date: \_\_\_\_\_  
 Soil Depth: \_\_\_\_\_ Water Depth: \_\_\_\_\_  
 Soil Type: \_\_\_\_\_  NC  OC Ratio: \_\_\_\_\_  ?  
 In-situ vertical effective stress: \_\_\_\_\_ In-situ vertical total stress: \_\_\_\_\_  
 Ko assumed: \_\_\_\_\_ In-situ horiz. eff. stress: \_\_\_\_\_ Membrane  Reinforced C: \_\_\_\_\_  Regular

### INITIAL PREPARATION

Dial gauge reading  Membrane  Trimmer  O-Rings  Saturated Caps  
 with \_\_\_\_\_ mm spacer: \_\_\_\_\_ (a)  Moisture tins  Ziplok for trimmings  Filter paper  
 circles

### INITIAL MEASUREMENTS & CONDITIONS (CLAYS)

**TARES:** Wt<sub>w.c. cup</sub> \_\_\_\_\_ No \_\_\_\_\_ Trimmings Wt<sub>saturatedcaps+membrane+orings+filter paper</sub> \_\_\_\_\_  
 Wt<sub>w.c. cup</sub> \_\_\_\_\_ No \_\_\_\_\_ Sample

#### WEIGHTS & CALCS:

Before Test: Wet Wt<sub>sample+saturatedcaps+membrane+orings+filterpaper</sub> : \_\_\_\_\_

Wet Wt. trimmings & cup: \_\_\_\_\_ Dry Wt trim & cup: \_\_\_\_\_

After Test: Wet Wt<sub>sample+csaturateddaps+membrane+oring+filterpaper</sub>: \_\_\_\_\_ Dry Wt sample & cup: \_\_\_\_\_

**INITIAL SAMPLE READINGS:** Dial gauge (w/o suction): \_\_\_\_\_ range (w/o suction) \_\_\_\_\_

Diameter (w/o suction) \_\_\_\_\_ Applied suction \_\_\_\_\_

Dial gauge (w/suction): \_\_\_\_\_ (c) Range: \_\_\_\_\_

Membrane thickness<sup>1</sup>: \_\_\_\_\_ (e) Diameter  
 w/membranes: \_\_\_\_\_ (f) Area<sup>2</sup>: \_\_\_\_\_ (g)

<sup>1</sup> Typically 0.012" or 0.305 mm

<sup>2</sup> Area =  $(\pi (f-2e)^2/4)$

**SAMPLE SEATING CHECKLIST**

Horizontal LVDT centered  X-axis  Y-axis  Top cap secured  Bottom cap secured

Horizontal load cell at 0 load  X-axis  Y-axis

Z-stroke LVDT Readings: \_\_\_\_\_

\_\_\_\_\_ @ \_\_\_\_\_ vertical load

(Z-load)

\_\_\_\_\_

Initial X-stroke LVDT reading: \_\_\_\_\_

Initial Y-stroke LVDT reading: \_\_\_\_\_

**BACK PRESSURE SATURATION**

**Valve open** Max. Effective Stress: \_\_\_\_\_ Min. Effective Stress: \_\_\_\_\_

X-stroke LVDT Reading (before saturation): \_\_\_\_\_ Y-stroke LVDT Reading: \_\_\_\_\_

Z-stroke LVDT Readings: \_\_\_\_\_

Volume Reading: \_\_\_\_\_ X-axis Load \_\_\_\_\_ Y-axis Load \_\_\_\_\_

	Date/Time started					
	A Closed ✓					
	Vertical load					
1	Initial Cell					
2	Initial Eff					
3	Final Cell					
4	Final Eff					
5	$\Delta$ Cell (3-1)					
6	$\Delta$ u (3-1)-(4-2)					
	<b>B-Value</b> (6/5)					
	Values Reset and Valve A Open ✓					
	A	B	C	D	E	

X-stroke LVDT Reading (after saturation): \_\_\_\_\_ Y-stroke LVDT Reading: \_\_\_\_\_

Z-stroke LVDT Reading \_\_\_\_\_

Volume \_\_\_\_\_ X-axis Load \_\_\_\_\_ Y-axis Load \_\_\_\_\_

**CONSOLIDATION**Time/date started: \_\_\_\_\_  HLC zero

Z-load Vert load Initial \_\_\_\_\_ Z-load Vert. load Final \_\_\_\_\_ Volume Initial \_\_\_\_\_

X-stroke LVDT Initial \_\_\_\_\_ Final \_\_\_\_\_ Y-stroke LVDT Initial \_\_\_\_\_ Final \_\_\_\_\_

Z-stroke LVDT Initial \_\_\_\_\_ Final \_\_\_\_\_

Cell pressure \_\_\_\_\_

 One-Step Consolidation Final Stress \_\_\_\_\_ Data File \_\_\_\_\_ Sequenced Consolidation Data File: \_\_\_\_\_

Time	Cell ( $\sigma_{3v}$ )	Z-load ( $\sigma_v$ )	X-stroke	X-load	Y-stroke	Y-load

**CYCLIC/ CIRCULAR/ FIGURE-8 TESTING**

Time/date performed: \_\_\_\_\_

 Horizontal switched to load or displacement control A-valve **CLOSED**  Gain Set

Initial Readings: Cell \_\_\_\_\_ Effective \_\_\_\_\_ Volume \_\_\_\_\_

Test file name: \_\_\_\_\_ Data file name: \_\_\_\_\_

Horizontal Cut-off:  Displacement: \_\_\_\_\_  Stress: \_\_\_\_\_

Frequency: \_\_\_\_\_ Hz No cycles: \_\_\_\_\_

Sampling Rate \_\_\_\_\_

Horizontal Control:  **Stress** Full amplitude load: \_\_\_\_\_ Equiv. Stress: \_\_\_\_\_ **Strain** Full amplitude disp: \_\_\_\_\_ Equiv. strain: \_\_\_\_\_

Initial readings: Vertical LVDT \_\_\_\_\_

Horizontal LVDT \_\_\_\_\_ Cell \_\_\_\_\_

Effective \_\_\_\_\_ Volume \_\_\_\_\_ Diameter \_\_\_\_\_

Vertical :  **Constant load** Dev. Load Setting: \_\_\_\_\_ Deviator stress: \_\_\_\_\_

Total Stress: \_\_\_\_\_

`  **Constant height**

Final readings: Vertical LVDT \_\_\_\_\_

Horizontal LVDT \_\_\_\_\_ Cell \_\_\_\_\_

Effective \_\_\_\_\_ Volume \_\_\_\_\_ Diameter \_\_\_\_\_

NOTES ON TEST:

**MONOTONIC TESTING**

Time/date performed: \_\_\_\_\_

 Horizontal switched to load or displacement control A-valve **CLOSED** Gain Set

Initial Readings: Cell \_\_\_\_\_ Effective \_\_\_\_\_ Volume \_\_\_\_\_

Test file name: \_\_\_\_\_ Data file name: \_\_\_\_\_

Sampling rate \_\_\_\_\_

Horizontal Control:  **Strain** **Stress**

Full amp. Disp: \_\_\_\_\_

Full amp. Load: \_\_\_\_\_

Starting value: \_\_\_\_\_

Starting Value: \_\_\_\_\_

Strain Rate : \_\_\_\_\_

Stress Rate: \_\_\_\_\_

Displacement Rate: \_\_\_\_\_

Load Rate: \_\_\_\_\_

Length of test: \_\_\_\_\_

Length of test: \_\_\_\_\_

Vertical Control:  **Constant load** Dev. Load Setting: \_\_\_\_\_ Deviator stress: \_\_\_\_\_  
Total Stress: \_\_\_\_\_ **Constant height**

Final readings: Vertical LVDT \_\_\_\_\_

Horizontal LVDT \_\_\_\_\_ Cell \_\_\_\_\_

Effective \_\_\_\_\_ Volume \_\_\_\_\_ Diameter \_\_\_\_\_

NOTES ON TEST:



## APPENDIX C

### GULF OF MEXCIO MARINE CLAY TEST RESULTS

Data for the individual tests are presented in this section. Table C.1 summarizes data for each Gulf of Mexico specimen. Table C.2. contains the values of stresses and strains at the end of consolidation for each test. Figures C.1 and C.2 show plots of the  $K_o$  and  $K_\alpha$  consolidation phase of the test. Figures C.3 through C.18 provide plots for each individual undrained shearing test.

**Table C.1.** Summary of Gulf of Mexico specimens.

Test	Depth (m)	Initial Water Content (%)	Final Water Content (%)	Initial Unit Weight (kN/m <sub>3</sub> )
GOM-1	10.59	36.92	35.71	15.3
GOM-2	10.92	38.21		14.6
GOM-3	10.47	39.36	36.68	14.2
GOM-4	10.61	36.98	35.01	14.6
GOM-5	10.45	39.17	36.76	14.8
GOM-6	10.63	37.74	37.68	15.8
GOM-7	10.65	38.37	36.87	15.9
GOM-8	10.86	37.36	36.07	14.6
GOM-9	10.92	38.85		15.1
GOM-10	10.51	38.92	35.85	16.1
GOM-11	10.55	29.13	28.51	16.0
GOM-12	10.67	39.01	38.33	14.3
GOM-13	10.53	35.28	34.92	15.7
GOM-14	10.57	30.37	28.75	15.7
GOM-15	10.88	38.04	37.64	14.2
GOM-16	10.90	39.85	36.81	16.2

**Table C.2.** Consolidation information for all tests on Gulf of Mexico clays.

Test	Final Height (mm)	Vertical Stress (kPa)	End of Consolidation Stress Ratio (kPa)		End of Consolidation Strains (%)		
			$\tau_x/\sigma'_p$	$\tau_y/\sigma'_p$	$\gamma_x$	$\gamma_y$	$\epsilon_v$
GOM-1	19.027	83.6	-0.017	0.004	-0.006	0.007	11.1
GOM-2	18.203	83.9	-0.019	0.012	-0.016	0.210	16.5
GOM-3	19.876	83.7	-0.204	0.002	-13.445	0.010	14.2
GOM-4	17.406	91.4	-0.181	-0.002	-9.362	-0.011	14.5
GOM-5	19.788	83.0	-0.013	0.025	0.011	-0.010	14.9
GOM-6	21.944	82.9	-0.209	0.017	-13.871	0.009	13.5
GOM-7	17.968	84.4	-0.206	-0.012	-20.372	0.017	17.3
GOM-8	18.794	84.7	-0.202	-0.015	-22.751	0.002	24.8
GOM-9	20.145	83.9	-0.019	0.012	-0.016	0.216	13.5
GOM-10	17.753	85.4	0.000	-0.003	0.019	0.011	12.2
GOM-11	20.590	81.0	-0.218	0.051	-9.692	0.017	8.7
GOM-12	15.934	83.2	-0.208	0.007	-12.375	0.002	21.9
GOM-13	18.056	81.3	-0.018	0.020	-0.029	0.007	11.2
GOM-14	17.823	83.9	-0.206	0.005	-15.87	0.026	14.3
GOM-15	15.448	88.6	-0.194	0.004	-11.14	0.016	17.1
GOM-16	16.028	83.4	-0.205	0.013	-18.90	0.004	13.2

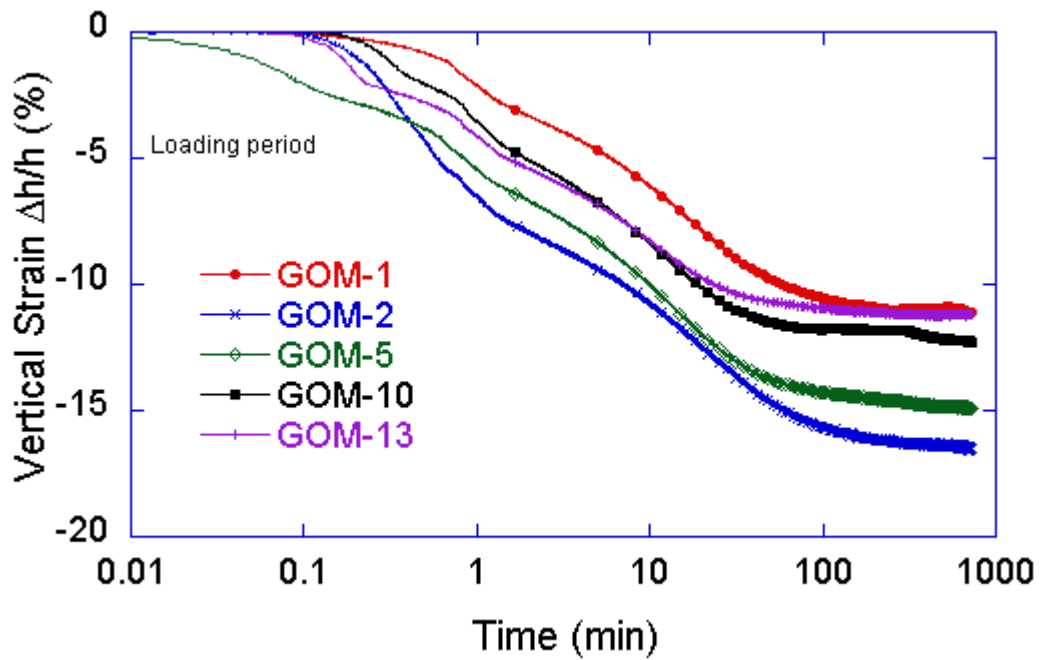


Fig. C.1. Results for all  $CK_0$  consolidated tests.

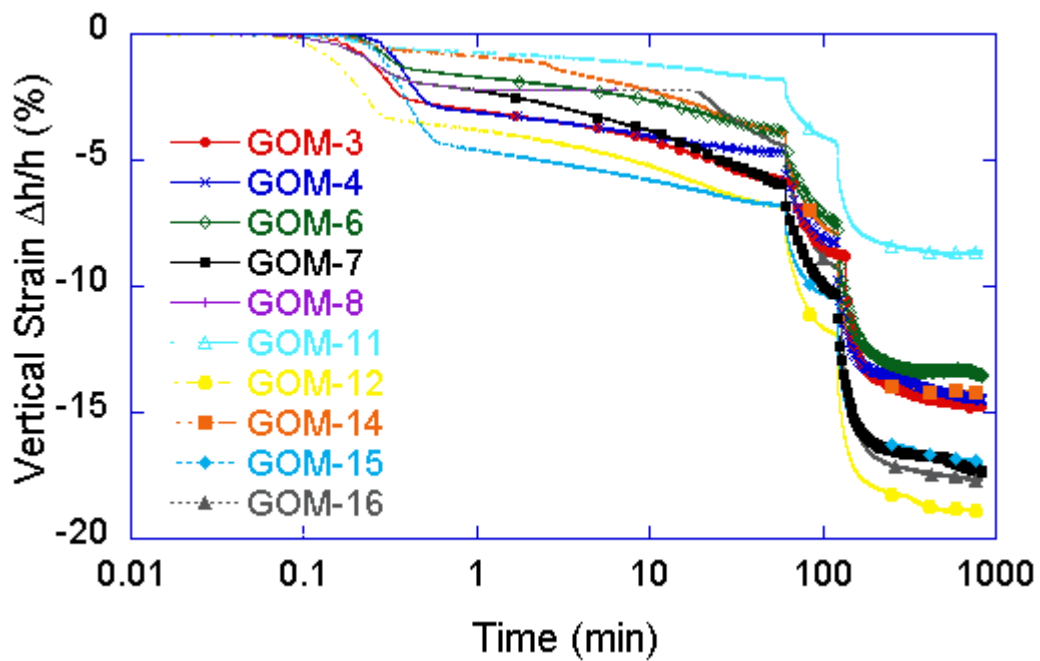
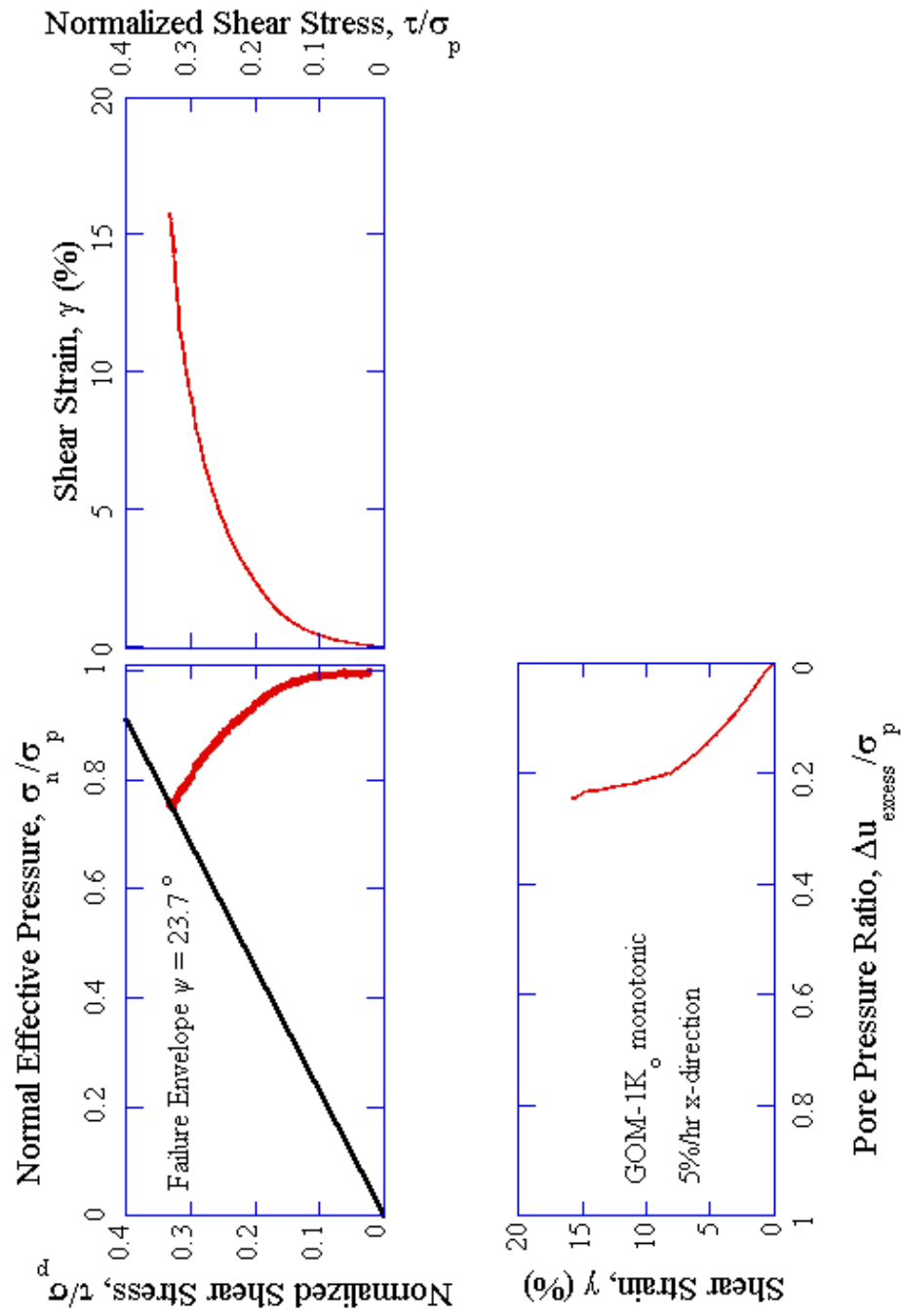


Fig. C.2. Results for all  $CK_\alpha$  consolidated tests.



**Fig. C.3.** GOM-1 CK<sub>0</sub> monotonic x-direction 5%/hr  $\delta = 0^\circ$ .

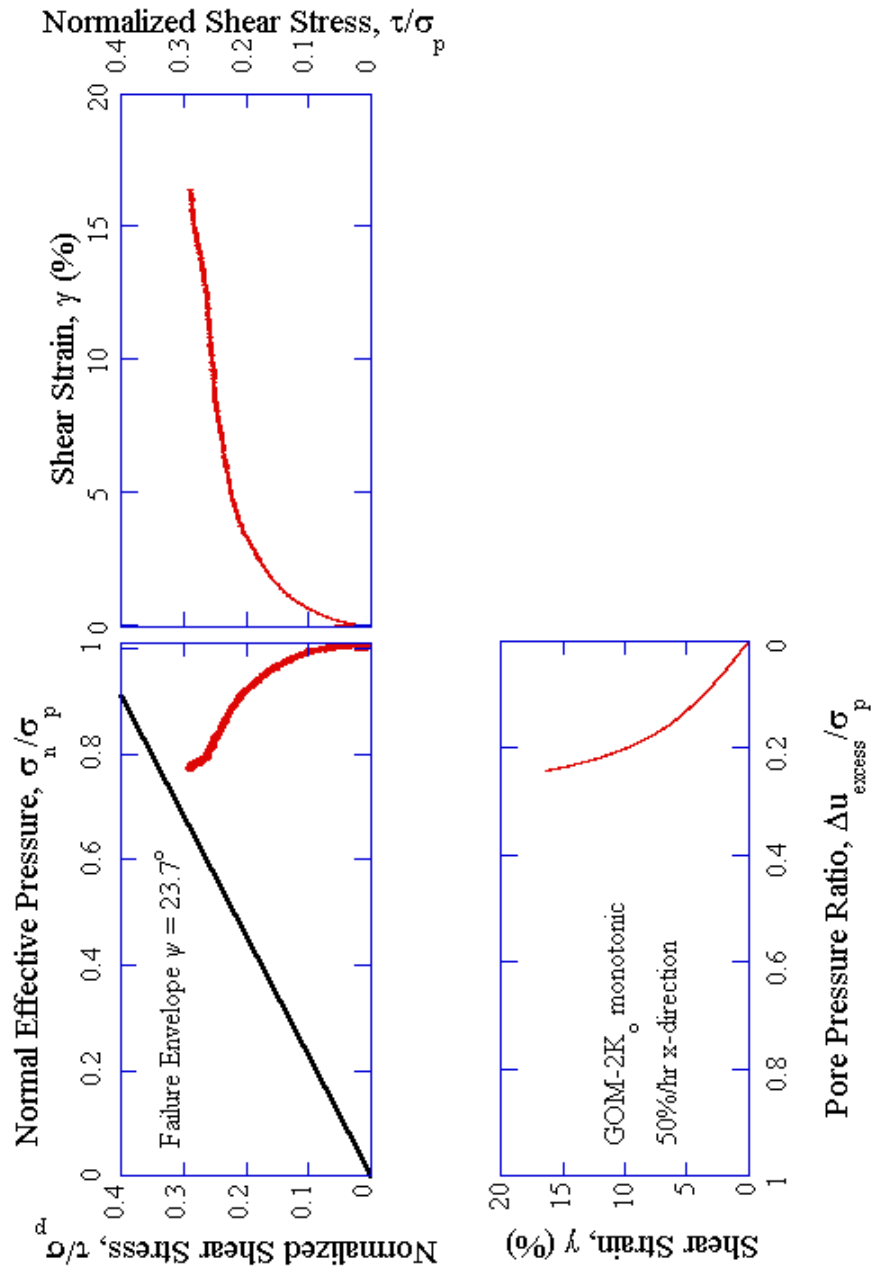


Fig. C.4. GOM-2 CK<sub>0</sub> monotonic x-direction 50%/hr δ = 0°.

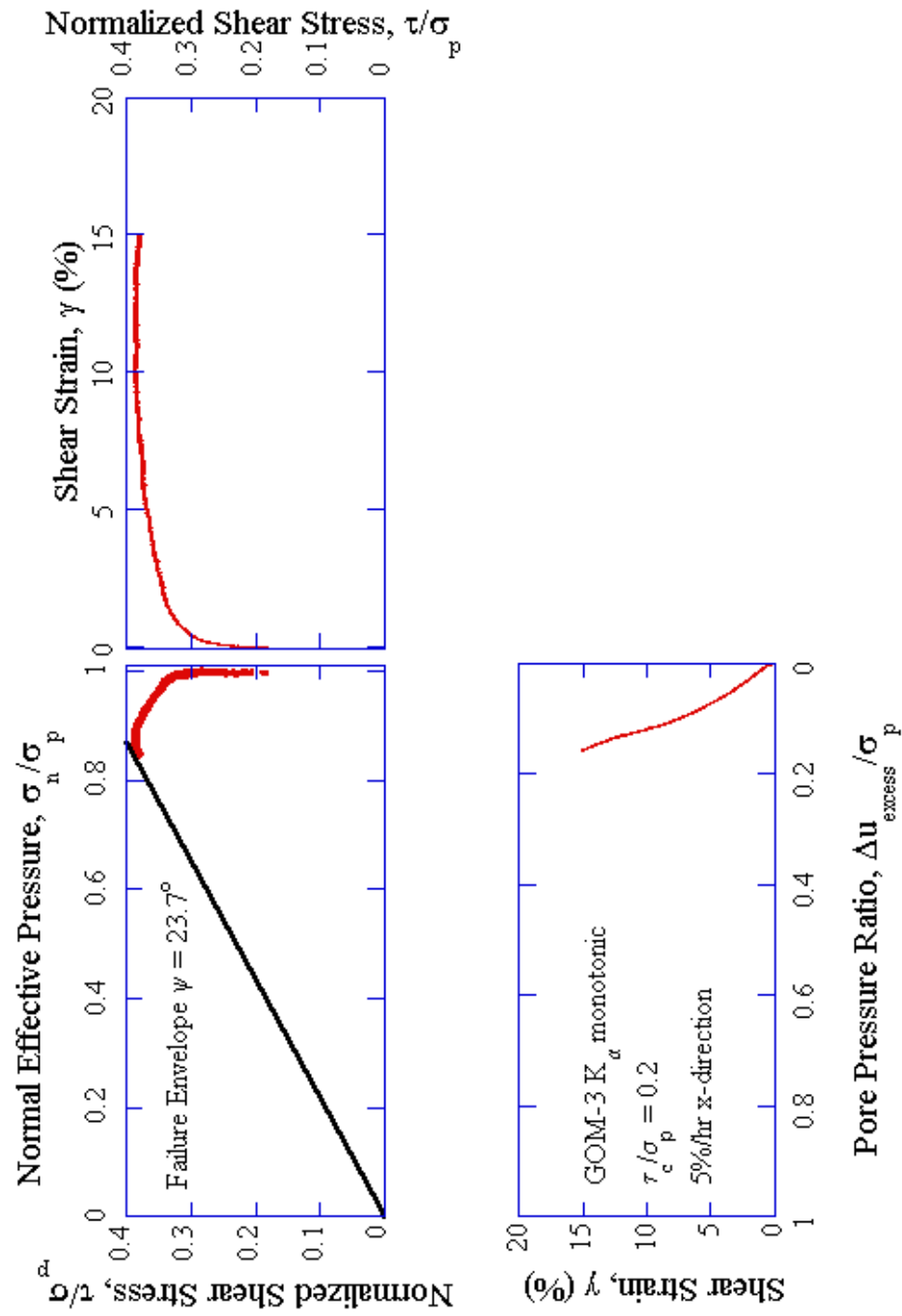
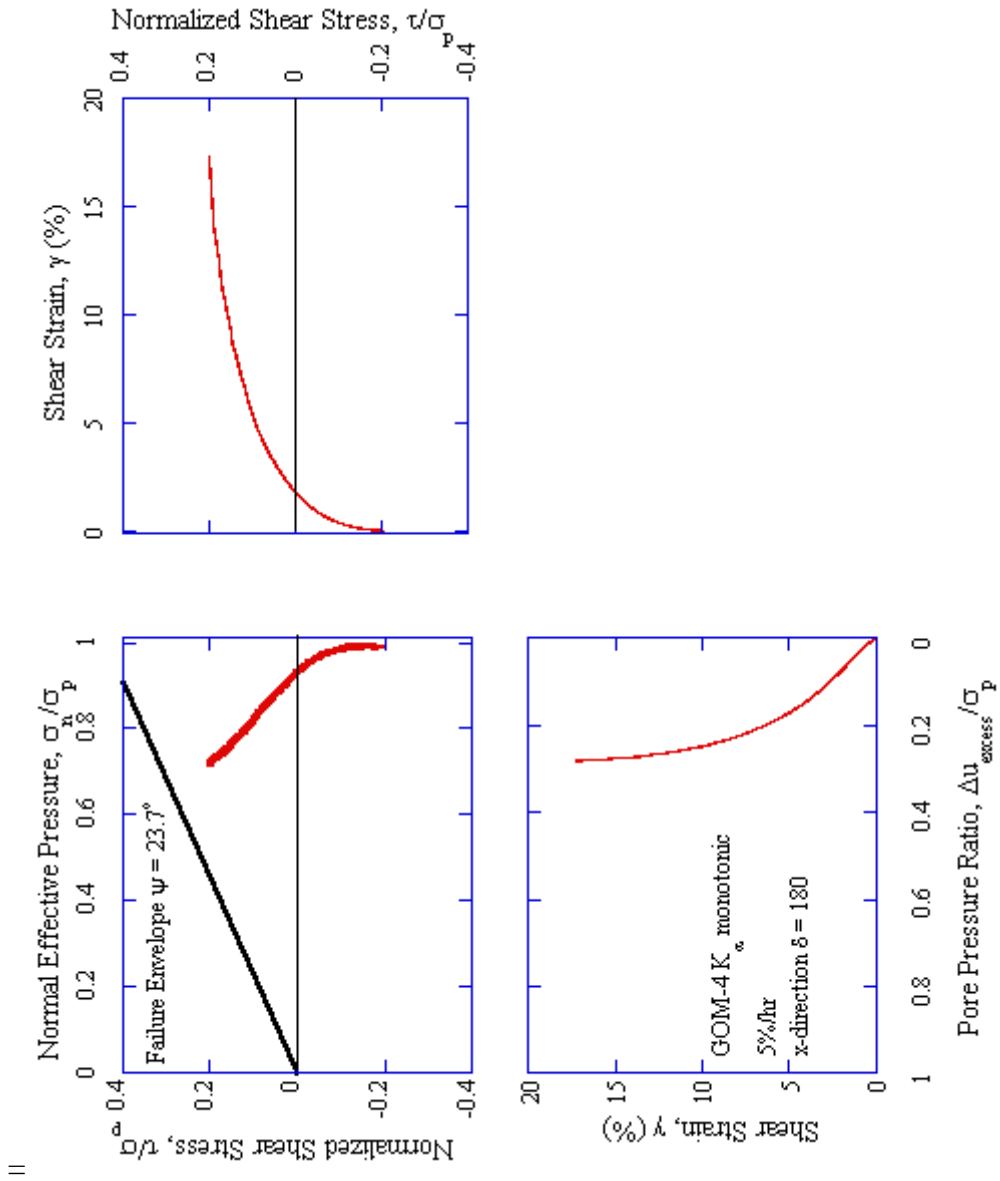


Fig. C.5. GOM-3  $CK_\alpha$  monotonic x-direction 5%/hr  $\delta = 0^\circ$ .



**Fig. C.6.** GOM-4  $CK_{\alpha}$  monotonic x-direction 5%/hr  $\delta = 180^\circ$ .



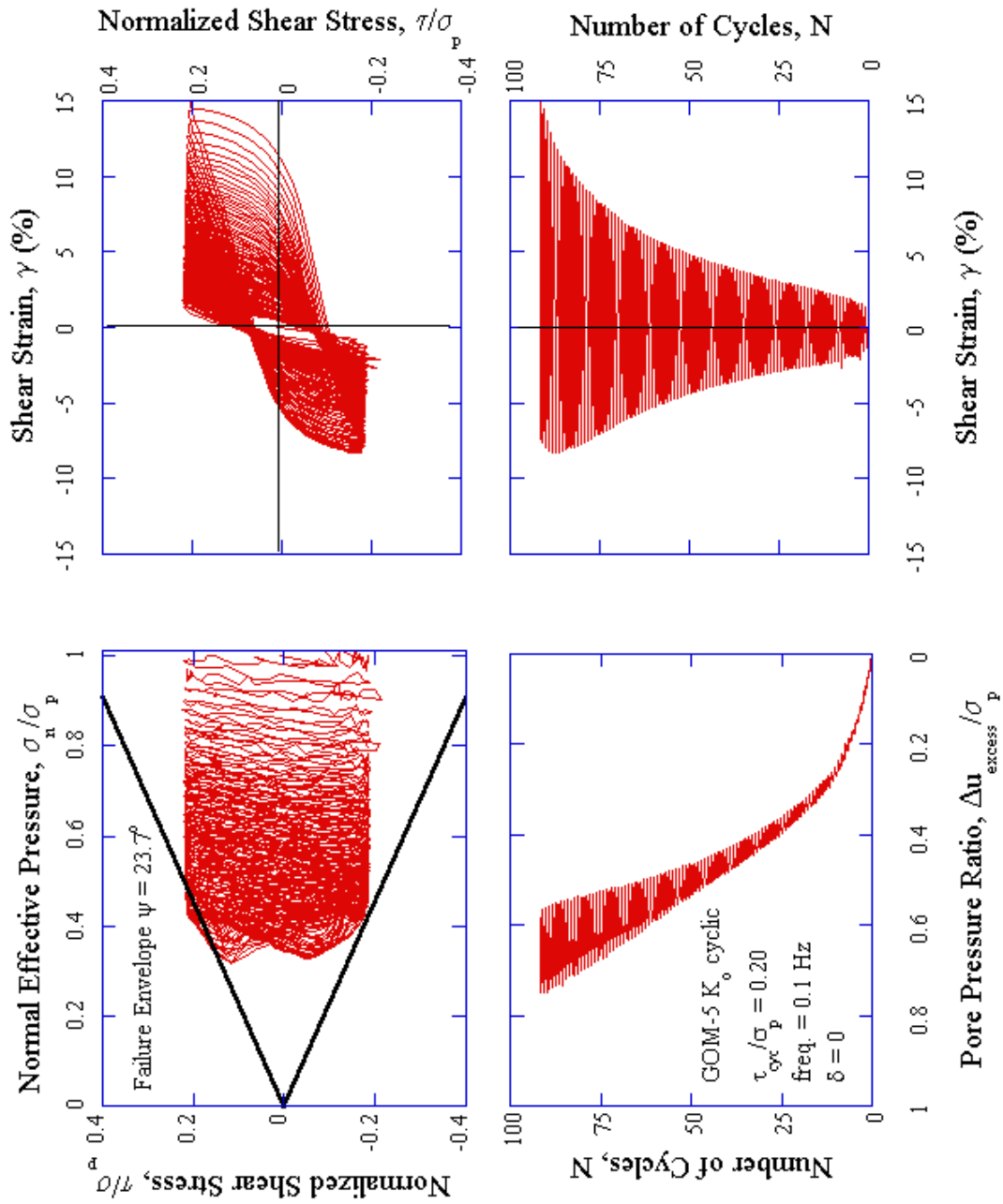
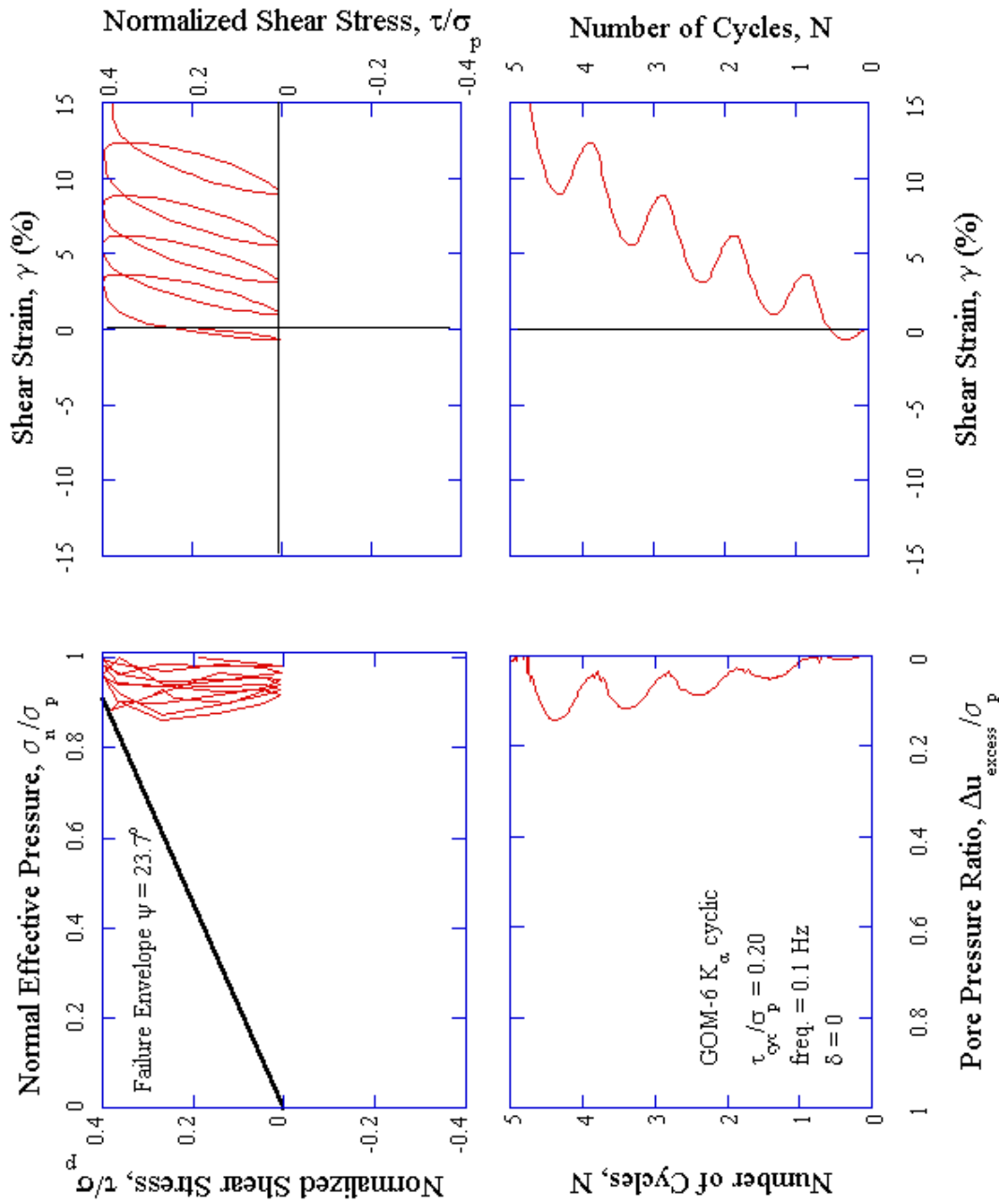


Fig. C.7. GOM-5 CK<sub>0</sub> cyclic x-direction, 0.1 Hz,  $\tau_{cyc} / \sigma'_p = 0.2$ ,  $\delta = 0^\circ$ .



**Fig. C.8.** GOM-6 CK $\alpha$  cyclic x-direction, 0.1 Hz,  $\tau_{cyc} / \sigma'_p = 0.2$ ,  $\delta = 0^\circ$ .

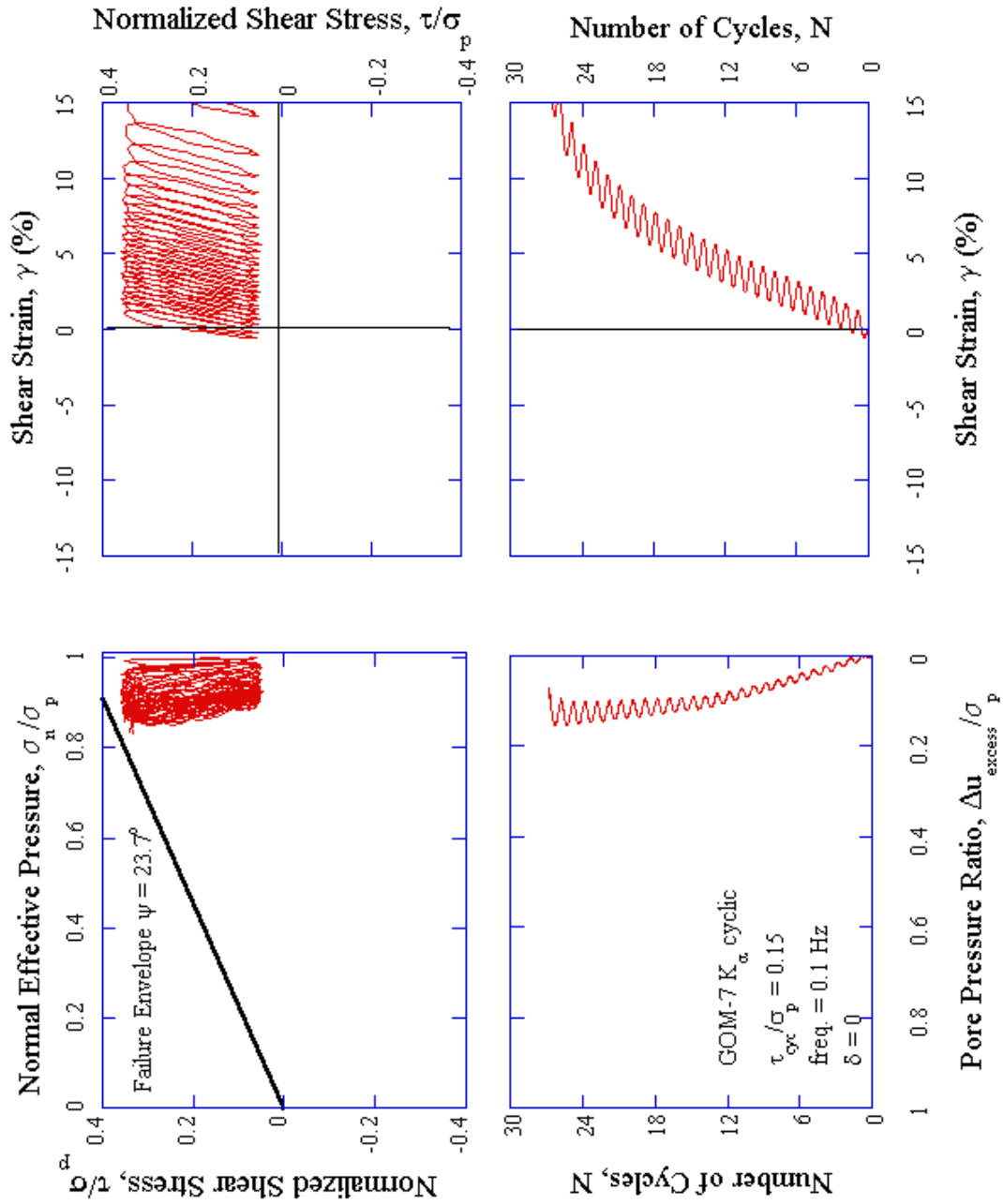


Fig. C.9. GOM-7  $CK_\alpha$  cyclic x-direction, 0.1 Hz,  $\tau_{cyc} / \sigma_p = 0.15$ ,  $\delta = 0^\circ$ .

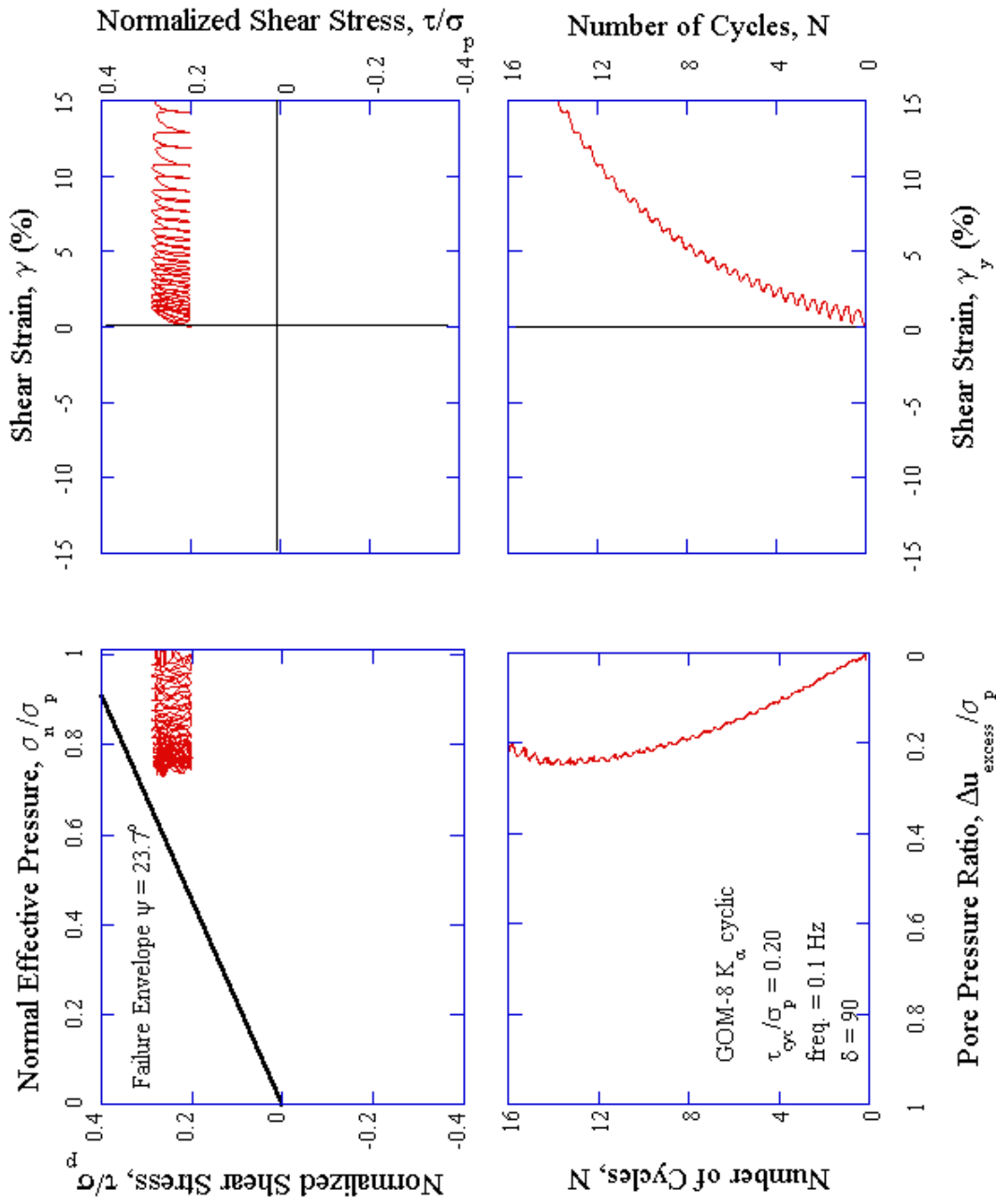


Fig. C.10. GOM-8  $CK_\alpha$  cyclic x-direction, 0.1 Hz,  $\tau_{cyc} / \sigma_p = 0.2$ ,  $\delta = 90^\circ$ .

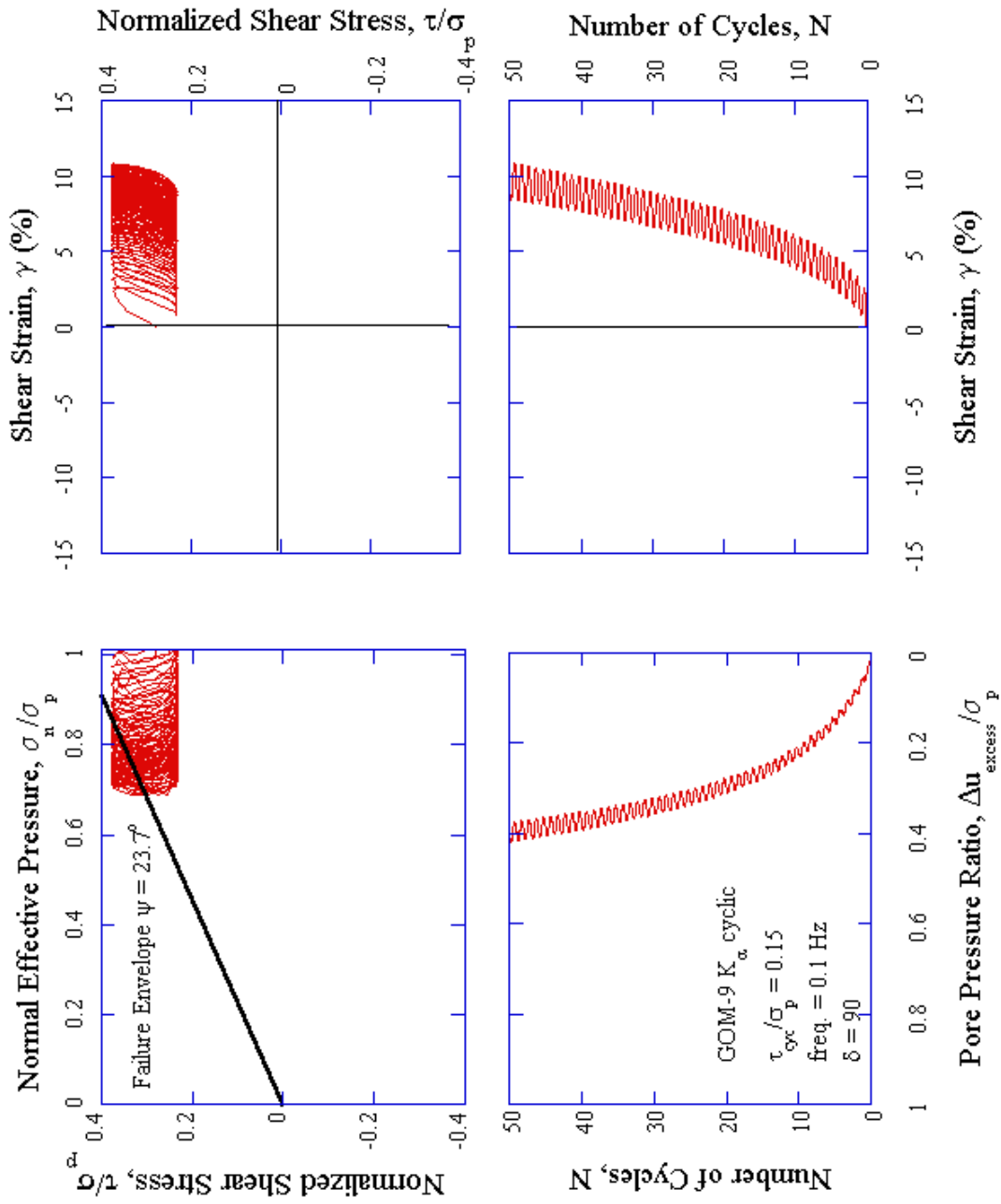


Fig. C.11. GOM-9  $CK_\alpha$  cyclic x-direction, 0.1 Hz,  $\tau_{cyc} / \sigma'_p = 0.15$ ,  $\delta = 90^\circ$ .

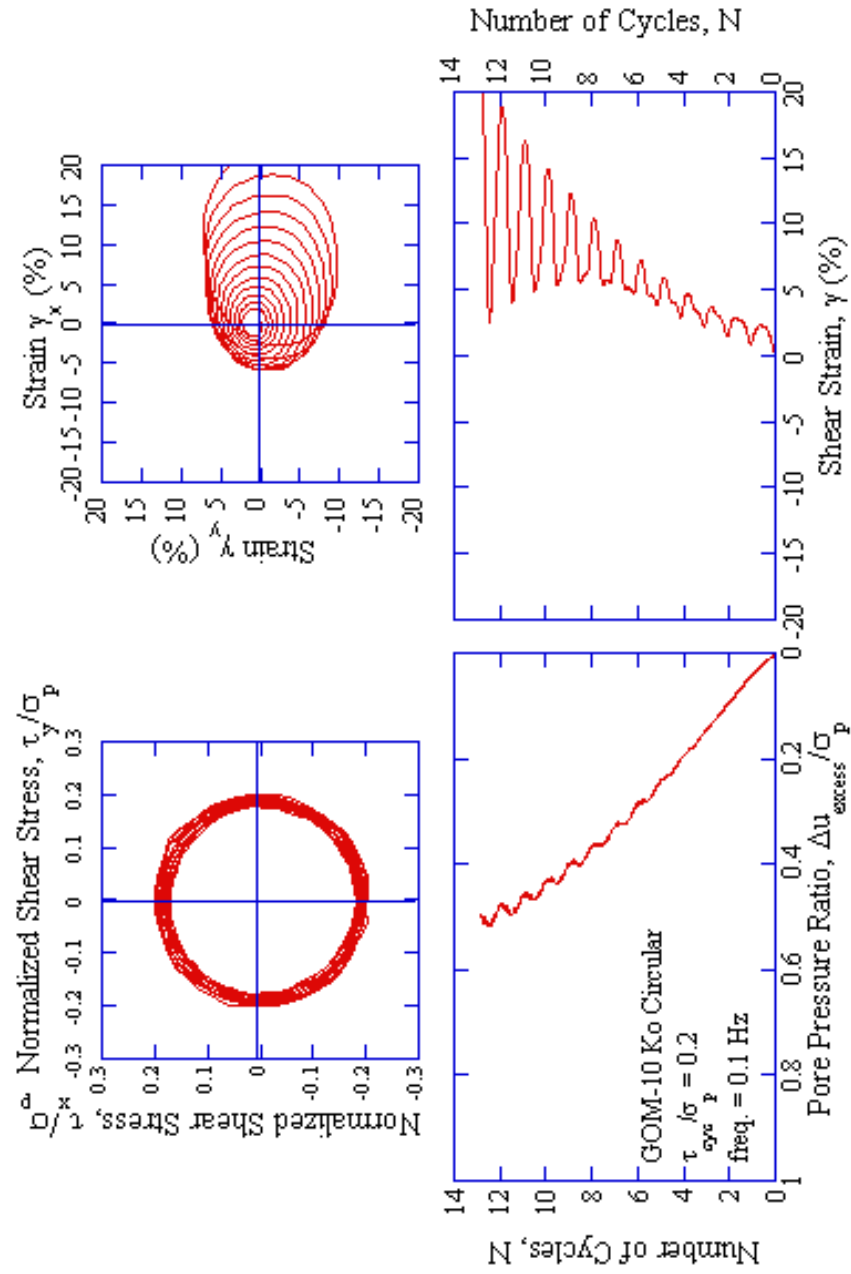


Fig. C.12. GOM-10 CK<sub>o</sub> circular 0.1Hz,  $\tau_{cy}/\sigma'_p = 0.2$ .

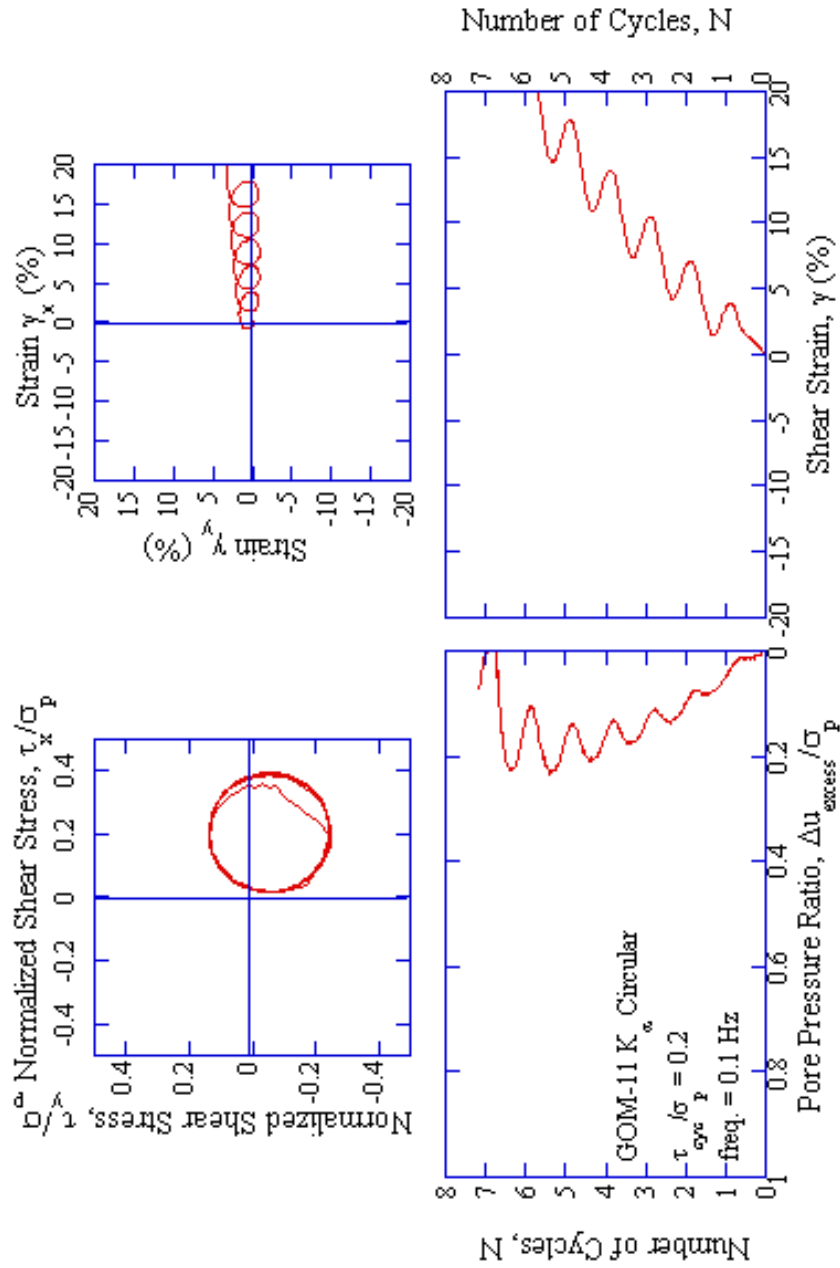


Fig. C.13. GOM-11 CK $_{\alpha}$  circular 0.1Hz,  $\tau_{cyc}/\sigma'_p = 0.2$ .

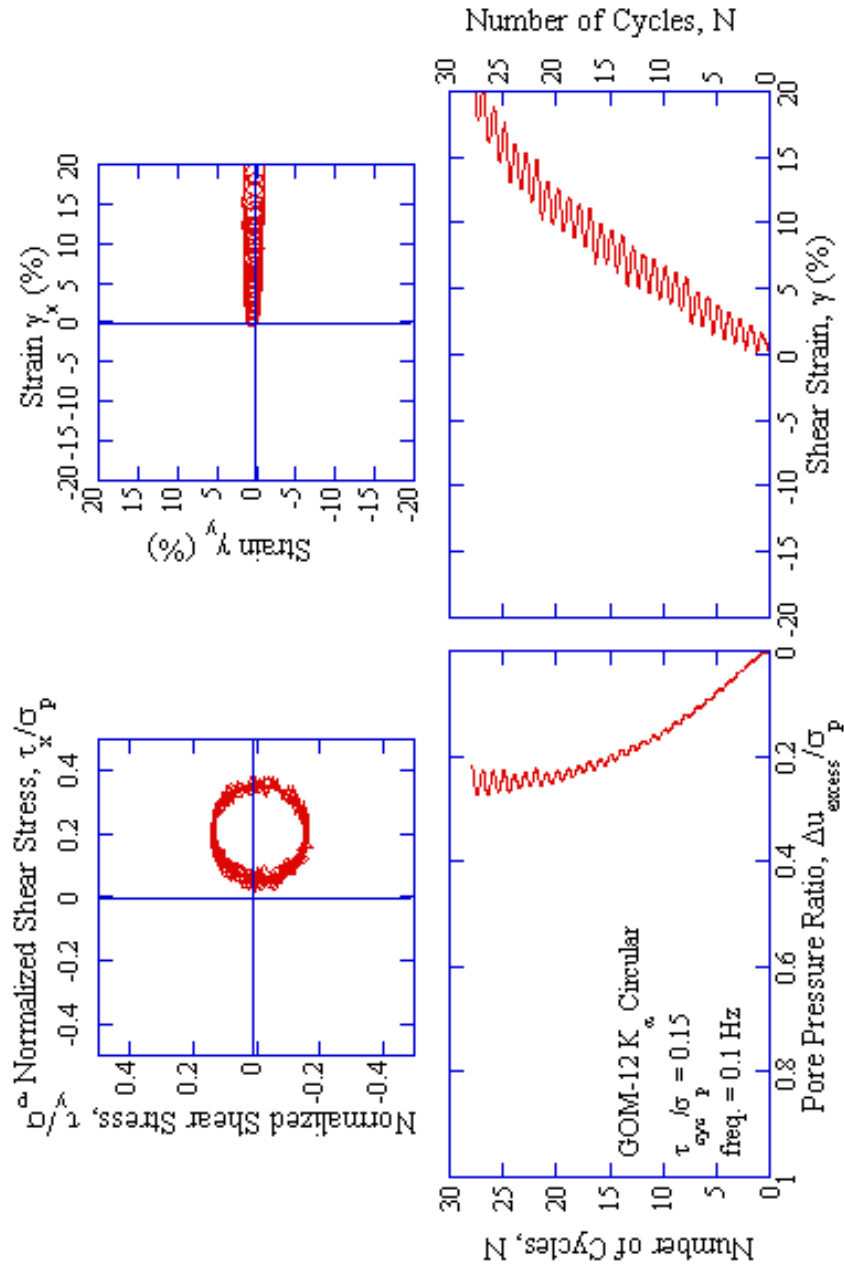
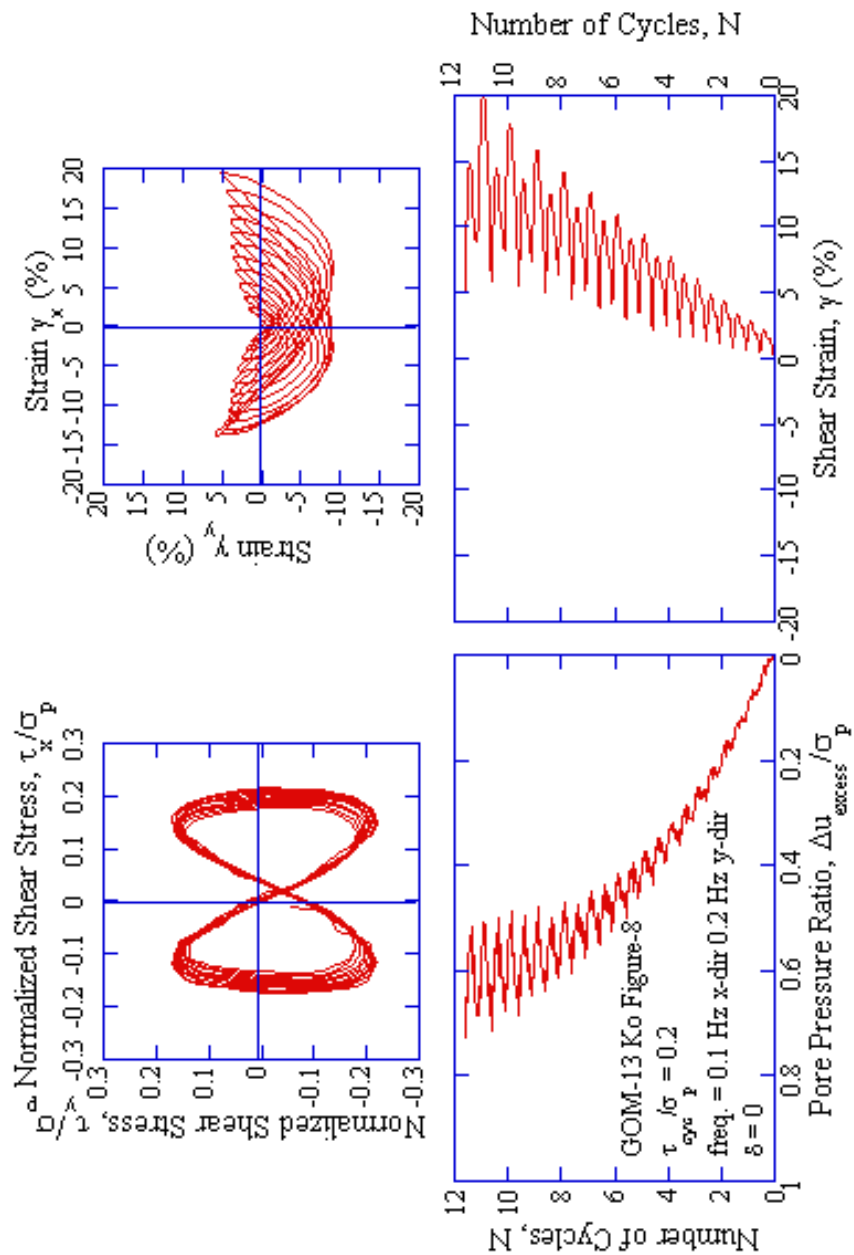


Fig. C.14. GOM-12 CK<sub>α</sub> circular 0.1Hz,  $\tau_{cyc}/\sigma_p = 0.15$ .





**Fig. C.15.** GOM-13 CK<sub>0</sub> figure-8, 0.1 Hz x-direction,  $\tau_{cyc}/\sigma'_p = 0.2$ ,  $\delta = 0^\circ$ .

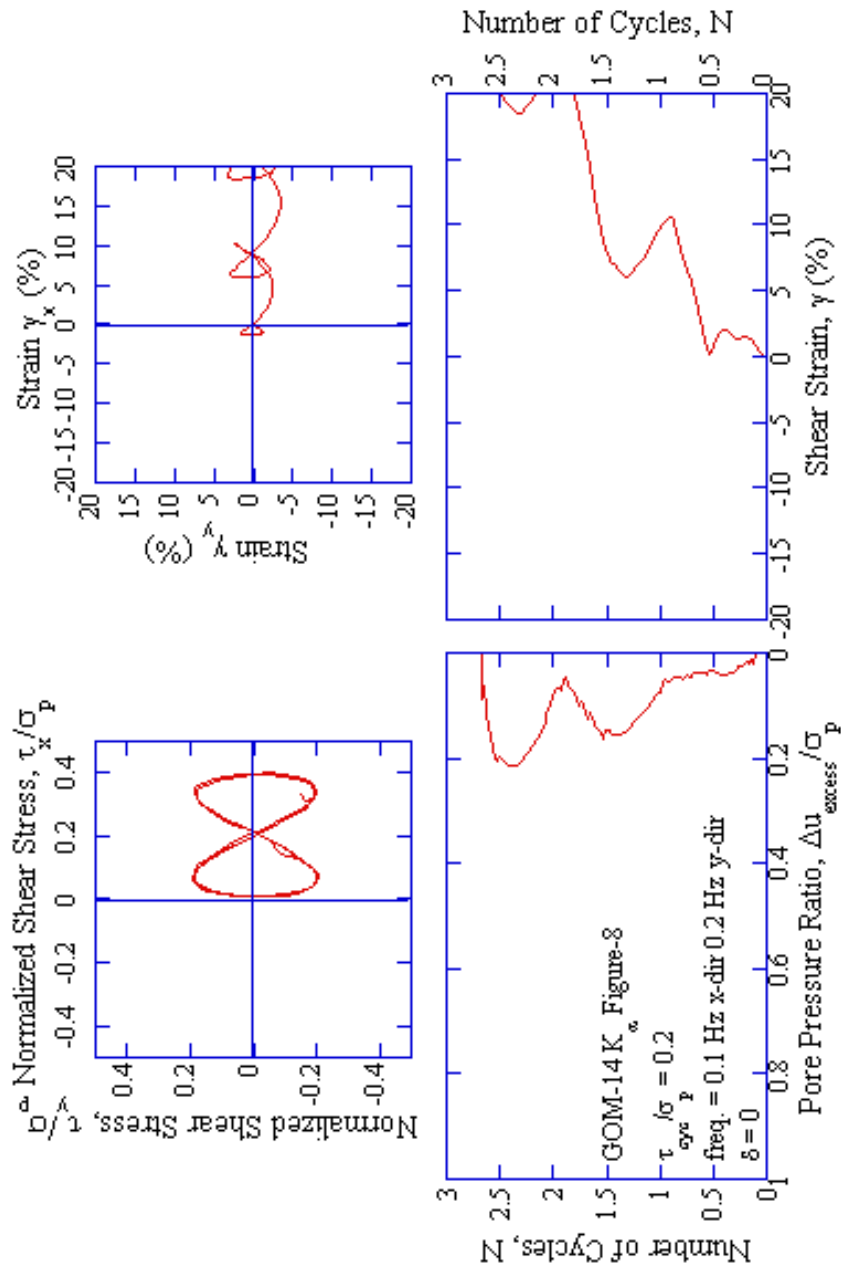
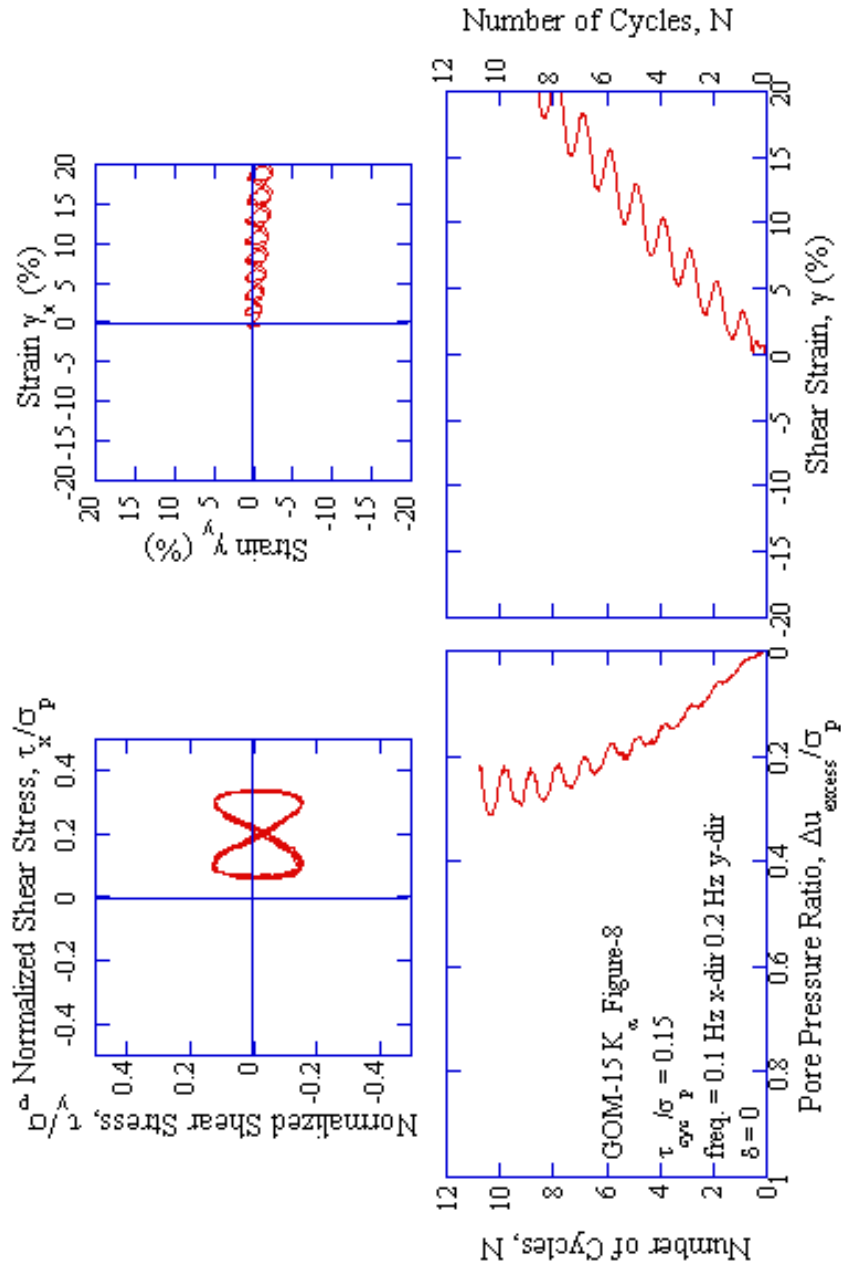
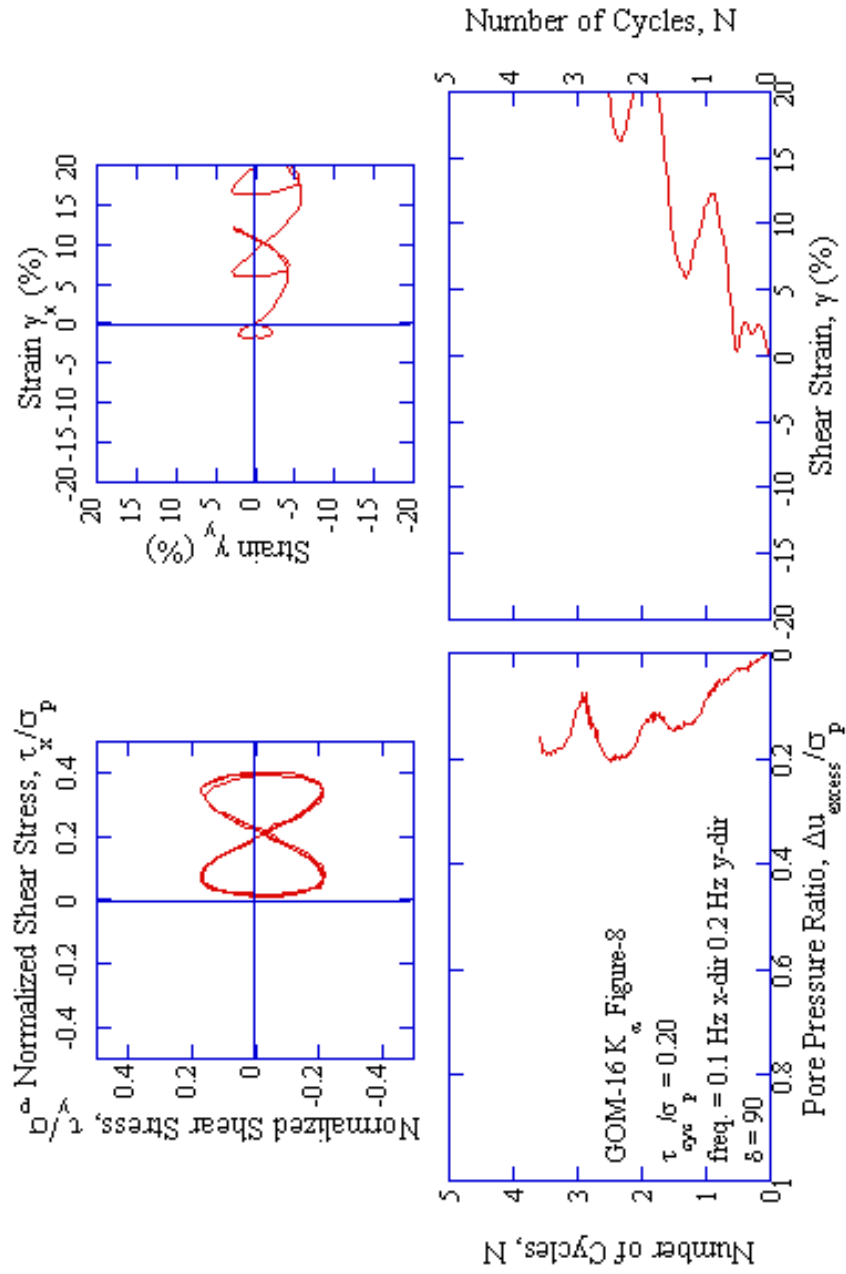


Fig. C.16. GOM-14 CK $_{\alpha}$  figure-8, 0.1 Hz x-direction,  $\tau_{cyc}/\sigma'_p = 0.2$ ,  $\delta = 0^\circ$ .



**Fig. C.17.** GOM-15 CK $_{\alpha}$  figure-8, 0.1 Hz x-direction,  $\tau_{cyc}/\sigma'_p = 0.15$ ,  $\delta = 0^\circ$ .



**Fig. C.18.** GOM-16 CK $_{\alpha}$  figure-8, 0.1 Hz x-direction,  $\tau_{cyc}/\sigma'_p = 0.2$ ,  $\delta = 90^\circ$ .

## APPENDIX D

### MATLAB DATA REDUCTION AND PROCESSING CODE

The data files were processed using the Matlab code below. Three files were used: 1) consol.m for the consolidation phase of the test, 2) mono.m for monotonic undrained shear tests, and 3) cyclic.m for the cyclic, circular and figure-8 undrained shear tests.

#### D.1. Consolidation Program consol.m

```

%%% consolidation processing file
%%% last modified November 27, 2011
%%% Cassie Rutherford

clear all
clc

%%%%% User enters ats data file with extension

atsfile=input('Enter ATS filename with extension:', 's');
atsdata= load (atsfile);% raw data from ats file
rtime = atsdata(:,1); % time in seconds
rStroke_Z=atsdata(:,2); % stroke in z direction in mm
rLoad_Z=atsdata(:,3)* .00444822; % load in z direction converted from
lbs to kilonewtons
rStroke_Y=atsdata(:,4); % stroke in y direction in mm
rLoad_Y=atsdata(:,5)* .00444822; % load in y direction converted from
lbs to kilonewtons
rStroke_X=atsdata(:,6); %stroke in x direction in mm
rLoad_X=atsdata(:,7)* .00444822; % load in x direction converted from
lbs to kilonewtons
rDiff_press=atsdata(:,8)* 6.89475729; % differential pressure between
cell and backpressure converted from psi to kPa
rCell_press=atsdata(:,9)* 6.89475729; % cell pressure converted from
psi to kPa
rVolume=atsdata(:,10); % volume in pipet in cm3

[r,s]=size(atsdata);% size of atsdata matrix

length=length(rtime);% length of time vector

%%%%% sample data user inputs diameter and initial height

diameter=input('Enter diameter in mm:'); % entered by user
area=pi*diameter.^2/4*.000001; % in m^2
hi = input('Enter initial height in mm:'); % entered by user
height(1,1)=hi; % height vector

```

```

%%% calculations for height change and pore pressure

changeStroke_Z(:,1)=rStroke_Z(1)-rStroke_Z;% change in stroke in z
direction
height= hi-changeStroke_Z; % initial height minus change in stroke in z
direction
changeStroke_X(:,1)=rStroke_X(1)-rStroke_X; % change in x-direction
changeStroke_Y(:,1)=rStroke_Y(1)-rStroke_Y; % change in y

dh=-1*changeStroke_Z/hi*100; % delta height in percent

% Change in height in mm from the volume (cm3 to mm3 mult by 1000) and
area
% (m2 to mm2 mult by 1x10^6)
hvol=hi-((rVolume-rVolume(1))*1000)/(area*1000000);

% pore pressure calculation from differential pore pressure transducer
u(1,1)=rDiff_press(1,1);
u = rDiff_press-rDiff_press(1); % kPa

% stress calculations
stress_X=rLoad_X/area; % kPa
stress_Y=rLoad_Y/area; % kPa

verticalpressure=rLoad_Z/area - rDiff_press; % kPa

% strain calculations
strain_X=changeStroke_X./hi*100; % in percent
strain_Y=changeStroke_Y./hi*100; % in percent
strain_Z=changeStroke_Z./hi*100; % in percent

%%%%% Plots %%%%%

% consolidation plots and data save for Kaleidagraph file format

    semilogx(rtime,height)
    xlabel('time (seconds)','FontSize', 20)
    ylabel('height (mm)','FontSize', 20)
    set(gca,'FontSize',18)
    saveas(gcf,'16log_time_height.jpg')

    semilogx(rtime,dh)
    xlabel('time (seconds)','FontSize', 20)
    ylabel('height (mm)','FontSize', 20)
    set(gca,'FontSize',18)
    saveas(gcf,'15log_time_dheight.jpg')

    semilogx(rtime,hvol)
    xlabel('time (s)','FontSize', 20)
    ylabel('height from volume (mm)','FontSize', 20);

```

```

set(gca,'FontSize',18)
saveas(gcf,'13log_time_changeheight.jpg')

plot(strain_X,stress_X)
xlabel('X Shear strain %')
ylabel('X Shear stress (kPa)')
set(gca,'FontSize',18)
saveas(gcf, '13-Strain_xShearStress_X.jpg')

plot(strain_Y,stress_Y)
xlabel('Transverse strain %');ylabel('Transverse Stress (kPa)');
set(gca,'FontSize',18)
saveas(gcf, '14-Strain_yShearStress_Y.jpg')

% Write data file to ,txt file that will be opened in Kaleidagraph

fid=fopen('consolidation.txt','wt');
fprintf(fid,'%s\n','sec sv(kPa) h(mm) hvol(mm) dh(%) u(kPa)
tx(kPa) gx(%) ty(kPa) gy(%)\n');
kaleido=[rtime,verticalpressure,height,hvol,dh,u,stress_X,
strain_X,stress_Y,strain_Y];
fprintf(fid,'%6.1f %4.5f %4.5f %4.5f %4.5f %4.5f %4.5f
%4.5f %4.5f %4.5f\n',kaleido);
st=fclose(fid);

% write final height after consolidation to screen to record on
% datasheet
hf = height(length,1)

%%%%%%%%END%%%%%%%%

```

## D.2. Monotonic Program mono.m

```

%%%%%%%% monotonic processing file
%%%%%%%% last modified November 27, 2011
%%%%%%%% Cassie Rutherford

clear all
clc

%%%%%%%% User enters ats data file with extension

atsfile=input('Enter ATS filename with extension:', 's');
atsdata= load (atsfile);% raw data from ats file
rtime = atsdata(:,1); % time in seconds
rStroke_Z=atsdata(:,2); % stroke in z direction in mm

```

```

rLoad_Z=atsdata(:,3)* .00444822; % load in z direction converted from
lbs to kilonewtons
rStroke_Y=atsdata(:,4); % stroke in y direction in mm
rLoad_Y=atsdata(:,5)* -.00444822; % load in y direction converted from
lbs to kilonewtons
rStroke_X=atsdata(:,6); % stroke in x direction in mm
rLoad_X=atsdata(:,7)* -.00444822; % load in x direction converted from
lbs to kilonewtons
rDiff_press=atsdata(:,8)* 6.89475729; % differential pressure between
cell and backpressure converted from psi to kPa
rCell_press=atsdata(:,9)* 6.89475729; % cell pressure converted from
psi to kPa
rVolume=atsdata(:,10); % volume in pipet in cm3

[r,s]=size(atsdata);%size of atdata matrix

length=length(rtime);% length of time vector

%%%% ATI files
atifile=input('Enter ATI filename with extension:', 's');
atidata= load (atifile);

atitime = atidata(:,1); % time in sec
atiLoad_Y=atidata(:,3)* -.00444822; % convert from lbs to kilonewtons
atiLoad_X=atidata(:,2)* -.00444822; % convert from lbs to kilonewtons
atiLoad_Z=atidata(:,4)* .00444822; % convert from lbs to kilonewtons
atiTorque_Y=atidata(:,5);
atiTorque_X=atidata(:,6);
atiTorque_Z=atidata(:,7);

[rati,sati]=size(atidata);
count=0;

%% zero ATI x and y load cells
atiLoad_Xzero=atiLoad_X-atiLoad_X(1);
atiLoad_Yzero=atiLoad_Y-atiLoad_Y(1);

%%%% sample data user inputs diameter and initial height

diameter=input('Enter diameter in mm:'); %entered by user
area=pi*diameter.^2/4*.000001; % in m^2
hi = input('Enter initial height in mm:'); %entered by user
height(1,1)=hi; %height vector

%% calculations for height change and pore pressure

changeStroke_Z(:,1)=rStroke_Z(1)-rStroke_Z;% change in stroke in z
direction
height= hi-changeStroke_Z; % initial height minus change in stroke in z
direction
changeStroke_X(:,1)=rStroke_X-rStroke_X(1); % change in x-direction
changeStroke_Y(:,1)=rStroke_Y-rStroke_Y(1); % change in y

```



```

% Change in height in mm from the volume (cm3 to mm3 mult by 1000) and
area
% (m2 to mm2 mult by 1x10^6)
hvol=hi-((rVolume-rVolume(1))*1000)/(area*1000000);

% pore pressure calculation from differential pore pressure transducer
u(1,1)=rDiff_press(1,1);
u = rDiff_press-rDiff_press(1); % kPa

% stress calculations
stress_X=rLoad_X/area; % kPa
stress_Y=rLoad_Y/area; % kPa
finestress_X=atiLoad_Xzero/area; % kPa
finestress_Y=atiLoad_Yzero/area; % kPa

verticalpressure=rLoad_Z/area - rDiff_press; % kPa

fineverticalpressure=atiLoad_Z/area - rDiff_press; % kPa

% strain calculations
strain_X=changeStroke_X./hi*100; % in percent
strain_Y=changeStroke_Y./hi*100; % in percent
strain_Z=changeStroke_Z./hi*100; % in percent

% initial normalized parameters for initial test

init_vertical_press=verticalpressure(1);
fine_init_vertical_press=fineverticalpressure(1);
finetcx=finestress_X./fine_init_vertical_press;
finesv=fineverticalpressure/fine_init_vertical_press;
finetcy=finestress_Y./fine_init_vertical_press;
tcx=stress_X./init_vertical_press;
sv=verticalpressure/init_vertical_press;
tcy=stress_Y./init_vertical_press;
gtotal=sqrt(strain_X.^2+strain_Y.^2);
tc=sqrt(tcx.^2+tcy.^2);
Ru = u/init_vertical_press;

%%%%%% Plots monotonic tests

plot(rtime, rStroke_X)
xlabel('Time (seconds)', 'FontSize', 20)
ylabel('Stroke_X (mm)', 'FontSize', 20)
set(gca, 'FontSize', 18)
saveas(gcf, '1-time_Stroke_x.jpg')

plot(rtime, rLoad_X)
xlabel('Time (seconds)', 'FontSize', 20)
ylabel('Load_X (kN)', 'FontSize', 20)
set(gca, 'FontSize', 18)

```

```

saveas(gcf, '2-time_Load_x.jpg')

plot(rtime, atiLoad_Xzero)
xlabel('Time (seconds)','FontSize', 20)
ylabel('fine Load_X (kN)','FontSize', 20)
set(gca,'FontSize',18)
saveas(gcf, '2a-time_fineLoad_x.jpg')

plot(sv, tcx)
xlabel('norm. vertical pressure (sn/sp)','FontSize', 20)
ylabel('norm. shear stress in x-direction (tx/sp)','FontSize', 20)
set(gca,'FontSize',18)
saveas(gcf, '3-vert_stress_xnormshearstress.jpg')

plot(finesv, finetcx)
xlabel('fine norm. vertical pressure (sn/sp)','FontSize', 20)
ylabel('fine norm. shear stress in x-direction (tx/sp)','FontSize', 20)
set(gca,'FontSize',18)
saveas(gcf, '3a-finevert_stress_xnormshearstress.jpg')

plot (strain_X, tcx)
xlabel('Strain in the x-direction','FontSize', 20)
ylabel('norm. shear stress in x-direction (tx/sp)','FontSize', 20)
set(gca,'FontSize',18)
saveas(gcf, '4-xstrain_normshearstress.jpg')

plot (strain_X, finetcx)
xlabel('Strain in the x-direction','FontSize', 20)
ylabel('norm. shear stress in x-direction (tx/sp)','FontSize', 20)
set(gca,'FontSize',18)
saveas(gcf, '4a-xstrain_finenormshearstress.jpg')

plot(strain_X, stress_X)
xlabel('Shear strain in x-direction %','FontSize', 20)
ylabel('Shear stress in x-direction tx (kPa)','FontSize', 20)
set(gca,'FontSize',18)
saveas(gcf, '5-xstrain_xstress.jpg')

plot(strain_X, finestress_X)
xlabel('Shear strain in x-direction %','FontSize', 20)
ylabel('Shear stress in x-direction tx(kPa)','FontSize', 20)
set(gca,'FontSize',18)
saveas(gcf, '5a-xstrain_finexstress.jpg')

plot(rtime, rStroke_Y)
xlabel('Time (seconds)','FontSize', 20)
ylabel('Stroke_Y (mm)','FontSize', 20)
set(gca,'FontSize',18)
saveas(gcf, '6-time_Stroke_y.jpg')

plot(rtime, rLoad_Y)
xlabel('Time (seconds)','FontSize', 20)

```

```

ylabel('Load_Y (kN)', 'FontSize', 20)
set(gca, 'FontSize', 18)
saveas(gcf, '7-time_Load_y.jpg')

plot(rtime, atiLoad_Y)
xlabel('Time (seconds)', 'FontSize', 20)
ylabel('Load_Y (kN)', 'FontSize', 20)
set(gca, 'FontSize', 18)
saveas(gcf, '7a-time_fineLoad_y.jpg')

plot(sv, tcy)
xlabel('norm. vert. pressure (sn/sp)', 'FontSize', 20)
ylabel('norm. shear stress in y-direction (ty/sp)', 'FontSize', 20)
set(gca, 'FontSize', 18)
saveas(gcf, '8-vert_stress_ynormshearstress.jpg')

plot(finesv, finetcy)
xlabel('norm. fine vertical pressure (sn/sp)', 'FontSize', 20)
ylabel('fine norm. shear stress in y-direction (ty/sp)', 'FontSize', 20)
set(gca, 'FontSize', 18)
saveas(gcf, '8a-finevert_stress_ynormshearstress.jpg')

plot(strain_Y, tcy)
xlabel('Strain in the y-direction', 'FontSize', 20)
ylabel('norm. shear stress', 'FontSize', 20)
set(gca, 'FontSize', 18)
saveas(gcf, '9-ystrain_normshearstress.jpg')

plot(strain_Y, finetcy)
xlabel('Strain in the y-direction', 'FontSize', 20)
ylabel('norm. shear stress', 'FontSize', 20)
set(gca, 'FontSize', 18)
saveas(gcf, '9a-ystrain_finenormshearstress.jpg')

plot (strain_Y, stress_Y)
xlabel('Shear strain in y-direction %', 'FontSize', 20)
ylabel('Shear stress in y-direction(kPa)', 'FontSize', 20)
set(gca, 'FontSize', 18)
saveas(gcf, '10-ystrain_ystress.jpg')

plot (strain_Y, finestress_Y)
xlabel('Shear strain in y-direction %', 'FontSize', 20)
ylabel('Shear stress in y-direction(kPa)', 'FontSize', 20)
set(gca, 'FontSize', 18)
saveas(gcf, '10a-ystrain_fineystress.jpg')

plot(Ru, strain_X)
xlabel('Ru', 'FontSize', 20)
ylabel('X Strain %', 'FontSize', 20)
set(gca, 'FontSize', 18)
saveas(gcf, '11-Ru_xstrain.jpg')

```

```

plot(Ru, strain_Y)
xlabel('Ru','FontSize', 20)
ylabel('Y Strain %','FontSize', 20)
set(gca,'FontSize',18)
saveas(gcf, '12-Ru_ystrain.jpg')

% Write data file to Kaleidagraph format file
fid=fopen('monotonic.txt','wt');
fprintf(fid,'%s\n','sec sv(kPa) t(kPa) sv/sp tx/sp gx(%)
u(kPa) ru ty(kPa) ty/sp gy(%) fineLoadx fineLoady fineLoadz finestressX
finestressY finesv finetcx finetcy');
kaleido=[rtime,verticalpressure,stress_X, sv, tcx, strain_X, u,
Ru, stress_Y, tcy, strain_Y, atiLoad_X, atiLoad_Y, atiLoad_Z,
finestress_X, finestress_Y, finesv, finetcx, finetcy];
fprintf(fid,'% -6.1f %4.5f %4.5f %4.5f %4.5f %4.5f %4.5f
%4.5f %4.5f %4.5f %4.5f %4.5f %4.5f %4.5f %4.5f %4.5f %4.5f
%4.5f\n', kaleido);
st=fclose(fid);

%%%%% END %%%%%%

```

### D.3. Cyclic program cyclic.m

```

%%%%% cyclic processing file
%%%%% last modified November 27, 2011
%%%%% Cassie Rutherford

clear all
clc

%% User enters ats data file with extension

atsfile=input('Enter ATS filename with extension:', 's');
atsdata= load (atsfile);%raw data from ats file
rtime = atsdata(:,1); % time in seconds

rStroke_Z=atsdata(:,3); % stroke in z direction in mm
rLoad_Z=atsdata(:,4)* .00444822; % load in z direction converted from
lbs to kilonewtons
rStroke_Y=atsdata(:,5); % stroke in y direction in mm
rLoad_Y=atsdata(:,6)* -.00444822; % load in y direction converted from
lbs to kilonewtons
rStroke_X=atsdata(:,7); %stroke in x direction in mm
rLoad_X=atsdata(:,8)* -.00444822; % load in x direction converted from
lbs to kilonewtons
rDiff_press=atsdata(:,9)* 6.89475729; % differential pressure between
cell and backpressure converted from psi to kPa
rCell_press=atsdata(:,10)* 6.89475729; % cell pressure converted from
psi to kPa
rVolume=atsdata(:,11); % volume in pipet in cm3

```

```

[r,s]=size(atsdata);%size of atsddata matrix

length=length(rtime);% length of time vector

%%% zero stroke data
rStroke_Yzero=rStroke_Y-rStroke_Y(1);
rStroke_Xzero=rStroke_X-rStroke_X(1);

% ATI files
atifile=input('Enter ATI filename with extension:', 's');
ratidata= load (atifile);

%subsample ati data to same length and time interval as ats data
for k=1:length;
  atidata(k,:)=ratidata(2*k-1,:);
end

atitime = atidata(:,1); % time in sec
atiLoad_Y=atidata(:,3)* -.00444822; % convert from lbs to kilonewtons
atiLoad_X=atidata(:,2)* -.00444822; % convert from lbs to kilonewtons
atiLoad_Z=atidata(:,4)* .00444822; % convert from lbs to kilonewtons
atiTorque_Y=atidata(:,5);
atiTorque_X=atidata(:,6);
atiTorque_Z=atidata(:,7);

[rati,sati]=size(atidata);

%%%%% sample data user inputs diameter and initial height

diameter=input('Enter diameter in mm:'); %entered by user
area=pi*diameter.^2/4*.000001; % in m^2
hi = input('Enter initial height in mm:'); %entered by user
height(1,1)=hi; %height vector
freq = input('Enter frequency:'); % entered by user
rnocycles = rtime*freq; %number of cycles

%%% calucations for height change and pore pressure
changeStroke_Z(:,1)=rStroke_Z(1)-rStroke_Z;% change in stroke in z
direction
height= hi-changeStroke_Z; % initial height minus change in stroke in z
direction
changeStroke_X(:,1)=rStroke_Xzero; % change in x-direction
changeStroke_Y(:,1)=rStroke_Yzero; % change in y

% Change in height in mm from the volume (cm3 to mm3 mult by 1000) and
area
% (m2 to mm2 mult by 1x10^6)
hvol=hi-((rVolume-rVolume(1))*1000)/(area*1000000);

% pore pressure calculation from differential pore pressure transducer

```

```

u(1,1)=rDiff_press(1,1);
u = rDiff_press-rDiff_press(1); % kPa

% stress calculations
stress_X=rLoad_X/area; % kPa
stress_Y=rLoad_Y/area; % kPa
finestress_X=atiLoad_X/area; % kPa
finestress_Y=atiLoad_Y/area; % kPa

verticalpressure=rLoad_Z/area - rDiff_press; % kPa

fineverticalpressure=atiLoad_Z/area - rDiff_press; % kPa

% strain calculations
strain_X=changeStroke_X./hi*100; % in percent
strain_Y=changeStroke_Y./hi*100; % in percent
strain_Z=changeStroke_Z./hi*100; % in percent

% initial normalized parameters for initial test

init_vertical_press=verticalpressure(1); % kPa
fine_init_vertical_press=fineverticalpressure(1); % kPa
finetcx=finestress_X./fine_init_vertical_press; %norm. fine load cell
in x-direction
finesv=fineverticalpressure/fine_init_vertical_press; %norm. fine
load cell in z-direction
finetcy=finestress_Y./fine_init_vertical_press; %norm. fine load cell
in y-direction
tcx=stress_X./init_vertical_press; %norm. xload load cell in x-
direction
sv=verticalpressure/init_vertical_press; %norm. load cell in z-
direction
tcy=stress_Y./init_vertical_press; %norm. fine load cell in y-
direction
gtotal=sqrt(strain_X.^2+strain_Y.^2);
tctotal=sqrt(tcx.^2+tcy.^2);
Ru = u/init_vertical_press;

% Plots cyclic tests

plot(rtime, rStroke_Xzero)
xlabel('Time (seconds)', 'FontSize', 20)
ylabel('Stroke_X (mm)', 'FontSize', 20)
set(gca, 'FontSize', 18)
saveas(gcf, '1-time_Stroke_x.jpg')

plot(rtime, rLoad_X)
xlabel('Time (seconds)', 'FontSize', 20)
ylabel('Load_X (kN)', 'FontSize', 20)
set(gca, 'FontSize', 18)
saveas(gcf, '2-time_Load_x.jpg')

```

```

plot(rtime, atiLoad_X)
xlabel('Time (seconds)','FontSize', 20)
ylabel('fine Load_X (kN)','FontSize', 20)
set(gca,'FontSize',18)
saveas(gcf, '2a-time_fineLoad_x.jpg')

plot(sv, tcx)
xlabel('norm. vertical pressure (sn/sp)','FontSize', 20)
ylabel('norm. shear stress in x-direction (tx/sp)','FontSize', 20)
set(gca,'FontSize',18)
saveas(gcf, '3-vert_stress_xnormshearstress.jpg')

plot(finesv, finetcx)
xlabel('fine norm. vertical pressure (sn/sp)','FontSize', 20)
ylabel('fine norm. shear stress in x-direction (tx/sp)','FontSize', 20)
set(gca,'FontSize',18)
saveas(gcf, '3a-finevert_stress_xnormshearstress.jpg')

plot (strain_X, tcx)
xlabel('Strain in the x-direction','FontSize', 20)
ylabel('norm. shear stress in x-direction (tx/sp)','FontSize', 20)
set(gca,'FontSize',18)
saveas(gcf, '4-xstrain_normshearstress.jpg')

plot (strain_X, finetcx)
xlabel('Strain in the x-direction','FontSize', 20)
ylabel('norm. shear stress in x-direction (tx/sp)','FontSize', 20)
set(gca,'FontSize',18)
saveas(gcf, '4a-xstrain_finenormshearstress.jpg')

plot(strain_X, stress_X)
xlabel('Shear strain in x-direction %','FontSize', 20)
ylabel('Shear stress in x-direction tx (kPa)','FontSize', 20)
set(gca,'FontSize',18)
saveas(gcf, '5-xstrain_xstress.jpg')

plot(strain_X, finestress_X)
xlabel('Shear strain in x-direction %','FontSize', 20)
ylabel('Shear stress in x-direction tx(kPa)','FontSize', 20)
set(gca,'FontSize',18)
saveas(gcf, '5a-xstrain_finexstress.jpg')

plot(rtime, rStroke_Y)
xlabel('Time (seconds)','FontSize', 20)
ylabel('Stroke_Y (mm)','FontSize', 20)
set(gca,'FontSize',18)
saveas(gcf, '6-time_Stroke_y.jpg')

plot(rtime, rLoad_Y)
xlabel('Time (seconds)','FontSize', 20)
ylabel('Load_Y (kN)','FontSize', 20)
set(gca,'FontSize',18)

```

```

saveas(gcf, '7-time_Load_y.jpg')

plot(rtime, atiLoad_Y)
xlabel('Time (seconds)','FontSize', 20)
ylabel('Load_Y (kN)','FontSize', 20)
set(gca,'FontSize',18)
saveas(gcf, '7a-time_fineLoad_y.jpg')

plot(sv,tcy)
xlabel('norm. vert. pressure (sn/sp)','FontSize', 20)
ylabel('norm. shear stress in y-direction (ty/sp)','FontSize', 20)
set(gca,'FontSize',18)
saveas(gcf, '8-vert_stress_ynormshearstress.jpg')

plot(finesv,finetcy)
xlabel('norm. fine vertical pressure (sn/sp)','FontSize', 20)
ylabel('fine norm. shear stress in y-direction (ty/sp)','FontSize', 20)
set(gca,'FontSize',18)
saveas(gcf, '8a-finevert_stress_ynormshearstress.jpg')

plot(strain_Y, tcy)
xlabel('Strain in the y-direction','FontSize', 20)
ylabel('norm. shear stress','FontSize', 20)
set(gca,'FontSize',18)
saveas(gcf, '9-ystrain_normshearstress.jpg')

plot(strain_Y, finetcy)
xlabel('Strain in the y-direction','FontSize', 20)
ylabel('norm. shear stress','FontSize', 20)
set(gca,'FontSize',18)
saveas(gcf, '9a-ystrain_finenormshearstress.jpg')

plot (strain_Y, stress_Y)
xlabel('Shear strain in y-direction %','FontSize', 20)
ylabel('Shear stress in y-direction(kPa)','FontSize', 20)
set(gca,'FontSize',18)
saveas(gcf, '10-ystrain_ystress.jpg')

plot (strain_Y, finestress_Y)
xlabel('Shear strain in y-direction %','FontSize', 20)
ylabel('Shear stress in y-direction(kPa)','FontSize', 20)
set(gca,'FontSize',18)
saveas(gcf, '10a-ystrain_fineystress.jpg')

plot(Ru, strain_X)
xlabel('Ru','FontSize', 20)
ylabel('X Strain %','FontSize', 20)
set(gca,'FontSize',18)
saveas(gcf, '11-Ru_xstrain.jpg')

plot(Ru, strain_Y)
xlabel('Ru','FontSize', 20)

```



```

ylabel('Y Strain %','FontSize', 20)
set(gca,'FontSize',18)
saveas(gcf, '12-Ru_ystrain.jpg')

plot(Ru,rnocycles)
xlabel('Ru','FontSize', 20)
ylabel('Number of Cycles','FontSize', 20)
set(gca,'FontSize',18)
saveas(gcf, '13-Ru_cycles.jpg')

    % Write data file to Kaleidagraph format file
    fid=fopen('cyclic.txt','wt');
    fprintf(fid,'%s\n','sec nocy sv(kPa) t(kPa) sv/sp tx/sp gx(%)
u(kPa) ru ty(kPa) ty/sp gy(%) gtotal tctotal finestressX finestressY
finesv finetcx finetcy');
    kaleido=[rtime,rnocycles, verticalpressure,stress_X, sv, tcx,
strain_X, u, Ru, stress_Y, tcy, strain_Y, gtotal, tctotal,
finestress_X, finestress_Y, finesv, finetcx, finetcy];
    fprintf(fid,'% -6.1f %4.5f %4.5f %4.5f %4.5f %4.5f %4.5f
%4.5f %4.5f %4.5f %4.5f %4.5f %4.5f %4.5f %4.5f %4.5f %4.5f
%4.5f\n', kaleido);
    st=fclose(fid);

%%%%%%%%END%%%%%%%%

```

## VITA

Cassandra Janel Rutherford received her Bachelor of Science degree in civil engineering from Texas A&M University in 2002. She continued her studies at the graduate level, earning a Master of Science in civil engineering with a specialty in geotechnical engineering from Texas A&M University in 2004. During the pursuit of her doctoral degree, she taught Introductory to Geotechnical Engineering and guest lectured for many undergraduate and graduate level geotechnical engineering courses. Cassandra received her Ph.D. in 2012.

Cassandra's graduate study has been supported by the National Science Foundation through Dr. Giovanna Biscontin's project titled NSF CAREER: Characterization and modeling of marine clays for slope stability. She has also received financial support from the J. Malon Southerland '65 Aggie Leader Scholarship, Zachry Department of Civil Engineering Graduate Fellowship and Foster Graduate Fellowship.

Cassandra has accepted a position as an Assistant Professor at the University of Illinois in Champaign-Urbana and will start in January 2012.

Cassandra Rutherford can be contacted at [cassie.rutherford@gmail.com](mailto:cassie.rutherford@gmail.com) or at 601 W. Green St., Champaign, IL 61820.